

Faculty of Engineering
Department of Electrical and Electronic Engineering

Considerations on the use of solid material for High Performance, tubular linear motors

Ahmed M. Mohammed, B.Eng. (Hons.), M.Sc. (Elec.)

Submitted to the University of Nottingham for the degree of Doctor of Philosophy

November 2017

Acknowledgments

First and foremost I would like to express my deepest appreciation to my sponsor, the Ministry of Higher Education and Scientific Research, Government of Iraq, for receiving the opportunity to study in the United Kingdome.

I would also thank my supervisors. Professor Chris Gerada, Dr. Michael Galea and Dr. Tom Cox for their guidance, supervision and encouragement throughout my PhD studies period. Further, I also, would like to thank Dr, Michele Degano for his scientific and technical support during my work journey.

Special thanks to all Technicians in the university workshop, and the department workshops, particularly, John Hinchliffe, Colin Blackburn, Kevin Last, Matthew Copper, Guy Thompson, and Ian Medley for their support and effort to make this work success and also providing an excellent work environment.

My appreciation to all my current and former colleagues at the Department of Electrical Engineering, Power Electronics, Machine and Control Group (PEMC) where I spent four years of my life's best time.

Abstract

The last few decades have seen a considerable amount of research and development effort dedicated to linear machines. An important family of linear machines is the tubular, permanent magnet synchronous motor. As for any other machine, such motors are usually developed with laminated cores aimed at reducing core losses. However, for tubular machines, such a configuration requires cores laminated in the axial direction, making for quite expensive and time-consuming manufacturing processes. To address this aspect, this thesis proposes and investigates the use of solid materials for the core structure of the stator of a tubular machine.

The journey to achieve this goal is presented in this thesis. It is shown how through the use of new material characterisation techniques (critical for understanding and modelling structures operating in unconventional magnetic circuits) and new eddy current reduction methods (proposed and validated on representative samples), excellent results in terms of manufacturing costs can be achieved without compromising a machine's performance.

A bench-mark machine comprising a laminated stator is analysed and detailed in the first part of the thesis. The work shows how an equivalent or even better motor (in terms of force density and performance) can be achieved while utilising a solid material for its stator.

List of Contents

1. Introduction....1
1.1 The original Machine....2
1.2 Proposed solution....3
1.3 Aim and Objectives....4
1.4 Thesis Structure....5
1.5 Novelty of the Work....7
1.6 List of publications....8
2. Linear Electromagnetic Actuators; Principles and Applications....9
2.1 introduction....9
2.2 Linear Machine Structure....9
2.3 Linear Motor Topologies....10
2.3.1 Coreless, PM Linear Synchronous Motor....11
2.3.2 Slotted PM Linear Synchronous Motor....12
2.3.3 Slot-less Linear Motors, Toothless....13
2.3.4 Tubular motor....14
2.3.5 High level comparisons of linear machines....15
2.4 Concepts of Cost of Linear Electrical Machines....16

2.5 Manufacturing of TLPM Motor (Overview) 17

2.5.1 Complete lamination Stator 17

2.5.2 Solid (Soft Magnetic Composite) Stator 26

2.5.3 Laminated – Solid Combination 29

2.5.4 Other stator configurations 30

2.5.5 Solid Stator 32

2.6 Conclusions 33

3. Modelling and Analysing of TLPM Motor (Case of Study) 36

3.1 introduction 36

3.2 TLPM Motor “Case Study” 36

3.3 Magnetic Theory and Principles 38

3.3.1 Linear motor: principle of operation 38

3.4 Machine Analyses 40

3.4.1 Air gap flux density 41

3.4.2 No-load induced Voltage (Back *emf*) 53

3.4.3 *A*rmature Reaction and *mmf* distribution 56

3.4.4 Cogging force or Detent force 58

3.4.5 Inductances 62

3.4.6 Thrust Force 64

3.4.7 Thermal model 67

3.5 Finite Element (FE); Modelling, Solving and Analysis 70

3.5.1 Introduction to FE 70

3.5.2 Modelling the Selected Machines with (2D and 3D) 71

3.5.3 Magnetic Field Distribution 74

3.5.4 Machine losses 75

3.5.5 Machine Performance 76

3.6 Different Stator Configurations; Comparison 78

3.6.1 Soft magnetic composites (SMC) stator 78

3.6.2 Blocked Lamination stator configuration 80

3.6.3 Blocked Laminations and solid combination 81

3.6.4 TLPM Motor with Solid Stator 82

3.7 Conclusions 84

4. Material Characterization and its Concepts 87

4.1 introduction 87

4.2 Machines and their Magnetic Circuits 87

4.3 Material Characterization Methods 89

4.3.1 Characterization Methods 90

4.3.2 Characterization Methods for Conventional Magnetic Circuits 90

4.4 proposed characterization methods for unconventional magnetic circuits 99

4.4.1 The concept of the proposed method 99

4.4.2 The proposed test setups 101

4.4.3 Ensuring realistic representation of the application at hand 103

1) Bidirectional Current Condition Set-up 104

2) Unidirectional Current Condition Set-up 106

4.5 Validation and Experimental Results 110

4.6 Considerations on the Characterization Methods 112

4.7 Highlights of the chapter and contribution. 114

4.8 Conclusion 114

5. Eddy Current Reduction Techniques 116

5.1 Introduction 116

5.2 Eddy current behavior in solid materials 116

5.3 Considerations on Winding Configurations and Eddy Currents 120

5.4 Eddy current analyses for different windings 124

5.5 Eddy current reduction techniques....128

5.5.1 The slitting technique 129

5.6 validation of eddy current reduction techniques, the Concepts 132

5.6.1 Method A - Experimental tests of solid ring 135

5.6.2 Method B - One complete slit method....136

5.6.3 Method C – one direction partial slits method 137

5.6.4 Method D – two directions partial slits method. 139

5.7 Further comparisons....140

5.8 Implementation 142

5.8.1 Solid Construction with Radial Complete Slits....142

5.8.2 Solid construction with 1-directional partial slits....143

5.8.3 Solid construction with 2-directional partial slits....144

5.9 Highlights and contributions to research. 146

5.10 Conclusions 146

6. Design of TLPM Motor with Solid Stator....149

6.1 Introduction....149

6.2 Material Selection 150

6.2.1 Material of the Solid Stator....150

6.2.2 Material of the Permanent Magnets 150

6.3 Winding topology Selection 152

6.4 Initial Design Considerations 157

6.5 General Geometrical Sizing 158

6.5.1 Number of turns 159

6.5.2 Slot Current Density 160

6.5.3 Airgap length 161

6.5.4 Magnetic Loading (Magnet Sizing) 161

6.5.5 Stator Sizing 162

6.5.6 The initial design 165

6.6 Fine Tuning the Design with FE 165

6.6.1 Optimising the design 166

6.6.2 Other design considerations 170

6.6.3 Thermal Design 176

6.7 The Final Design's performance 179

6.8 Conclusions 181

7. Manufacturing and Experimental Realization 183

7.1 Introduction 183

7.2 Mechanical Design and Manufacturing 183

7.2.1 Cooling System 183

7.2.2 The coils 184

7.2.3 The stator 185

7.2.4 The mover 190

7.2.5 Final TLPM motor properties 191

7.3 Overall Structure and Assembly 192

7.4 Design of Experiment 194

7.4.1 Machine Static Parameters 194

7.4.2 Short Circuit Fault 194

7.4.3 No load back *emf* 196

7.4.4 Cogging Force 197

7.4.5 Thrust Force 198

7.5 Conclusion and Comparison to Extant Motors 201

8. Conclusions and Future Works 203

8.1 Introduction 203

8.1.1 Material characterization 204

8.1.2 Eddy current reduction techniques 205

8.1.3 Machine design 205

8.2 general comparison 206

8.3 Future Work 207

8.3.1 Motor Design 207

8.3.2 Material Characterization 208

Appendix A I

Appendix B V

Appendix C VII

Appendix D IX

List of Figures

Figure 1-1 TLPM Motor: overview 2
Figure 2-1 Evolution from rotational to tubular concept [20] 10
Figure 2-2 Coreless, PM Linear Synchronous Motor [24] 11
Figure 2-3 single sided slotted linear flat synchronous motor 13
Figure 2-4 double sided slotted PM linear ynchronous motor [27] 13
Figure 2-5 slot-less general structure[22] 14
Figure 2-6 Tubular motor general structure [29] 14
Figure 2-7 the principle of pie-slice structure 18
Figure 2-8 the principle of sunshine structure 20
Figure 2-9 sunshine structure a) inner stator, b) outer stator 20
Figure 2-10 sunshine lamintion structure of [7]. 22
Figure 2-11 structure of staggered lamination stator methode 23
Figure 2-12 the structure of involute lamination stator[39] 24
Figure 2-13 Laminated tubular stators, stacking block [32] 26
Figure 2-14 the construction of blocked lamination stator 26
Figure 2-15 Component elements of a SMC material[46] 27
Figure 2-16 applicable regions for magnetic materials [46] 27
Figure 2-17 Basic design of SMC stator and pre-wound coil [32] 28
Figure 2-18 f_{stack} of lamination and SMC materials [32] 28
Figure 2-19 Construction of laminated-solid combination 29
Figure 2-20 transversal laminated stator 30
Figure 2-21 transversal laminated stator with solid back iron 31
Figure 2-22 slited transversal laminated stator 32
Figure 3-1 the The bench-mark TLPM motor [10] 37

Figure 3-2 TLPM motor with a) SPMs and b) IPMs [13] 42

Figure 3-3 airgap flux density distribution map 44

Figure 3-4 no load airgap flux density 44

Figure 3-5 harmonic spectrum of airgap flux density 45

Figure 3-6 air gap flux density with slot opening effect 45

Figure 3-7 harmonics amplitude of airgap flux density 46

Figure 3-8 Regions of axially magnetised TLPM machine 47

Figure 3-9 Air gap fringing flux 48

Figure 3-10 fundamental and harmonics components of air gap flux density 49

Figure 3-11 subdomains Machine Topology [77]. 49

Figure 3-12 Subdomain Regions of Axial Magnetized TLPM machine [77]. 50

Figure 3-13 distribution of magnetization vector of axially magnetized machine 52

Figure 3-14 normal (radial) component of air gap field distribution 53

Figure 3-15 tangential (axial) component of air gap field distribution 53

Figure 3-16 Comparison of (*emf*) per phase per pole as a function of time 55

Figure 3-17 fundamental and harmonic spectrum of induced emf 56

Figure 3-18 FFT of total airgap mmf generated from three phase current set at t= л/2 57

Figure 3-19 mmf waveform, (a) for each phase (A,B,C), (b) for total mmf waveform at t= л/2 58

Figure 3-20 Single slot cogging force for one complete cycle (pole pair) 60

Figure 3-21 Slotting cogging force of 6 slots for half electrical cycle 61

Figure 3-22 Cogging force of 12 slot/10 pole machine for one pole pair 61

Figure 3-23 Armature current at $I_a = I_d$ and $I_a = I_q$ 63

Figure 3-24 three phase flux linkage at $I_a = 0$, $I_a = I_q$, $I_a = I_d$ 63

Figure 3-25 d-axis and q-axis inductances at armature current = 5 Amp 63

Figure 3-26 Variation of phase d-q inductances with different armature current . 64

Figure 3-27 winding distribution 65

Figure 3-28 Analytical calculation of generated force of the TLPM motor.....66
Figure 3-29 FE calculation of generated force of the TLPM motor.....66
Figure 3-30 Segment of an annulus.[104] 68
Figure 3-31 Independent axial and radial thermal networks [108].....69
Figure 3-32 TLPM motor; (a) 2D model, (b) refine mesh 72
Figure 3-33 TLPM motor; 3D model with lamination stator representation.....73
Figure 3-34 3D flux lines and direction of rotating machines.....75
Figure 3-35 3D flux lines and direction of linear machines 75
Figure 3-36 TLPM motor: eddy current losses of different machine parts 76
Figure 3-37 TLPM motor: generated force with 2D and 3D models 77
Figure 3-38 TLPM Motor: production Force 77
Figure 3-39 TLPM motor: full load phase voltage of 2D and 3D models 78
Figure 3-40 SMC model, force and eddy losses.....79
Figure 3-41 Blocked Lamenated stator configuration.....80
Figure 3-42 Generate force for different laminated block number at rated speed.81
Figure 3-43 Blocked Laminations with solid combination 81
Figure 3-44 Laminated-solid combination, force and eddy losses. 82
Figure 3-45 Force with solid model. 83
Figure 3-46 Eddy current losses with solid model. 84
Figure 3-47 thrust force (P.U) with different stator models. 85
Figure 3-48 Eddy current losses (P.U) with different stator models. 86
Figure 4-1 Standard magnetic circuits of rotating machines; Main flux paths.....88
Figure 4-2 Standard magnetic circuits of rotating machines; Eddy currents.....88
Figure 4-3 Non-standard magnetic circuit; Main flux paths 89
Figure 4-4 Non-standard magnetic circuit; Eddy currents 89
Figure 4-5 Material characterization of lamination stack.....91
Figure 4-6 Standard magnetic characterization method 92

Figure 4-7 Flux direction and eddy current path. 92

Figure 4-8 EN8 solid material ring and toroidal method test set-up 94

Figure 4-9 EN8 material: a.c. B-H curves for different frequencies 95

Figure 4-10 EN8 material: d.c. B-H curve at B_{max} = 1.6T 95

Figure 4-11 EN8 material: d.c. hysteresis loop 95

Figure 4-12 Relative permeability as a function of frequency and B 96

Figure 4-13 Circuit of the wattmeter method 97

Figure 4-14Experimental results of P_{loss} of the ring sample using classical method 98

Figure 4-15 Ring Sample and coils connection diagram with radial flux 100

Figure 4-16 Flux lines inside the ring sample 100

Figure 4-17 Flux lines inside the ring sample (wrong connection) 101

Figure 4-18 B-H loop of ferrite core (0W-48613-TC) 102

Figure 4-19 Magnetic characteristics of Ferrite (0W-48613-TC) at B=0.37 Tesla 102

Figure 4-20 Stator finite edge 103

Figure 4-21 the proposed Bidirectional Current Set-up 104

Figure 4-22 Bidirectional Current Set-up with current direction 104

Figure 4-23 Eddy current pattern of 'Bidirectional Current Set-up' 105

Figure 4-24 single tooth eddy current directions (Bidirectional Condition) 105

Figure 4-25 Bidirectional eddy current setup: FE results of power losses 106

Figure 4-26 the proposed Unidirectional Current Set-up 107

Figure 4-27 Unidirectional Current Set-up with current direction 108

Figure 4-28 Eddy current pattern of Unidirectional Current Set-up 108

Figure 4-29 single tooth eddy current directions (Unidirectional Condition) 108

Figure 4-30 Unidirectional eddy current setup: FE results of power losses 109

Figure 4-31 The experimental set-up components 110

Figure 4-32 The Complete experimental set-up 111

Figure 4-33 Bidirectional eddy current setup: experimental results of power losses 111

Figure 4-34 Unidirectional eddy current setup: experimental results of power losses 111

Figure 4-35 FE and Experimental results of power losses of proposed methods at 50 Hz.....112

Figure 4-36 power losses for three methods, at different B and f = 50Hz 113

Figure 4-37 power losses for three methods, at different f and B=0.7 T.....114

Figure 5-1 the eddy current phenomena 117

Figure 5-2 relative penetration depth of solid tooth 118

Figure 5-3 electromagnetic field vectors in ferromagnetic material[138].....119

Figure 5-4 eddy current direction in single tooth and single coil 121

Figure 5-5 Single layer winding of 12 slot TLPM machine.....122

Figure 5-6 Double layer winding of 12 slot TLPM machine 122

Figure 5-7 instantaneous total slot current for double layer machine 123

Figure 5-8 eddy current map. (a) Single layer (b) Double layer winding 124

Figure 5-9 tooth sides 125

Figure 5-10 Eddy current density (A/mm^2) inside all teeth of single layer, 12 slot TLPM motor.....126

Figure 5-11 Eddy current desity (A/mm^2) inside all teeth of double layer, 12 slot TLPM motor.....127

Figure 5-12 Cross sectional view of eddy current distribution in stator core.....129

Figure 5-13 solid structures with slits.....131

Figure 5-14 Prototype ring samples under test.....133

Figure 5-15 slitting number and its effects.....134

Figure 5-16 the test setup with ring samples 135

Figure 5-17 Power losses of bidirectional eddy current “Method B” 136

Figure 5-18 Power losses of unidirectional eddy current “Method B” 137

Figure 5-19 Power losses of bidirectional eddy current “Method C” 138

Figure 5-20 Power losses of unidirectional eddy current at 0.5 Tesla "Method C" 138

Figure 5-21 Power losses of bidirectional eddy current "Method D" 139

Figure 5-22 Power losses of unidirectional eddy current "Method D" 140

Figure 5-23 Bidirectional eddy current condition setup comparison 141

Figure 5-24 Unidirectional eddy current condition setup comparison 141

Figure 5-25 powerlosses of Bidirectional eddy current, all methods 141

Figure 5-26 Power losses of unidirectional eddy current, all methods 142

Figure 5-27 stator losses with different numbers of complete slits at 17A/mm^2.143

Figure 5-28 TLPM motor: force and losses for different number of slits at 17A/mm^2 and 2.5 Hz.....144

Figure 5-29 force of solid stator vs. 100 slits models at 17A/mm^2 and 2.5 Hz...145

Figure 5-30 losses of solid stator vs. 100 slits models at 17A/mm^2 and 2.5 Hz .145

Figure 6-1 comparison between different permanent magnet types [152].....151

Figure 6-2 electrical shift angle between two adjacent slots 153

Figure 6-3 mmf wave form; ripple and amplitude with different $\Delta\delta$ 154

Figure 6-4 coils and phase distribution of 12 slot machine 155

Figure 6-5 three phase emf phasors of 12 slot/10 pole machine 156

Figure 6-6 TLPM motor: the main parts 157

Figure 6-7 TLPM motor: the main dimensions 158

Figure 6-8 coil temperature with different current density at rated speed of 100mm/sec.....161

Figure 6-9 variation of Air-gap flux density vs. magnet width τ_m for different magnet high h_m 162

Figure 6-10 Output Force versus the split ratio 163

Figure 6-11 variation of generated force at rated current and speed 166

Figure 6-12 force to current ratio with different R_{ext} at rated current and speed.167

Figure 6-13 ripple factor variation with different R_{ext} at rated current and speed 168

Figure 6-14 Cogging force with different Slot Open Ratio at rated current and speed 169

Figure 6-15 Ripple factor with different Slot Open Ratio at rated current and speed 169

Figure 6-16 the THD of back emf with different Slot Open Ratio at rated current and speed 169

Figure 6-17 end faces force variation with different edge length at rated current and speed 171

Figure 6-18 single-side skewing end faces 171

Figure 6-19 3D model for 36 slitted TLPM motor 172

Figure 6-20 force and eddy losses of different slits number 173

Figure 6-21 TLPM motor with different number of slits 173

Figure 6-22 produced force for different number of slits 174

Figure 6-23 Eddy Current Losses for different number of slits 174

Figure 6-24 Force / Losses Ratio at different frequencies. 175

Figure 6-25 Heat path Technique 176

Figure 6-26 coil temperature with natural convection cooling 177

Figure 6-27 coil temperature with water cooled machine 178

Figure 6-28 HPs eddy current losses at rated load current density 179

Figure 6-29 TLPM motor : thrust force 181

Figure 6-30 TLPM motor: FE force production 181

Figure 6-31 TLPM force: comparisonbetween analytical anf FE results 182

Figure 7-1 TLPM motor: Stator housing design 184

Figure 7-2 coil mould 185

Figure 7-3 pre-formed coils 185

Figure 7-4 stator teeth of the TLPM motor before slitting 186

Figure 7-5 Slitted teeth of the TLPM motor 186

Figure 7-6 teeth and end edges arrangement 187

Figure 7-7 end edge slitting technique 187

Figure 7-8 HP losses with different models 188

Figure 7-9 Slited HP (one complete slit + partial slits) 188

Figure 7-10 stator teeth and coil assembly 189

Figure 7-11 stator and housing assembly stage 190

Figure 7-12 TLPM motor: final stator assembly 190

Figure 7-13 TLPM motor: Mover assembling 191

Figure 7-14 TLPM motor: final mover assembly [10] 191

Figure 7-15 TLPM motor: Overall assembled Structure 192

Figure 7-16 TLPM motor: test rig assembling stage 193

Figure 7-17 TLPM motor: complete structure of the test rig 193

Figure 7-18 three phase short circuit fault 195

Figure 7-19 TLPM motor: coil temperature under short circuit fault at rated speed 195

Figure 7-20 TLPM motor: short circuit fault current at rated speed 196

Figure 7-21 TLPM motor: back-EMF, waveform comparison. 197

Figure 7-22 TLPM motor: back-EMF, FFT comparison 197

Figure 7-23 linear load cell trancducer 198

Figure 7-24 TLPM motor: cogging force comparison 198

Figure 7-25 TLPM motor: force capability comparison 200

Figure 7-26 TLPM motor: force density 200

Figure 7-27: Comparison force constant (K_F) of TLPM motor 200

Figure 7-28 produced force for the two versions 201

List of Table

Table 2-1 comparison between different motor topologies 16

Table 2-2 comparison between different stator construction 35

Table 3-1 TLPM motor: main data 37

Table 3-2 TLPM motor: experimental performance data 37

Table 3-3 Material properties of the TLPM motor 74

Table 4-1 properties of EN8 ring sample 94

Table 5-1 Performance Comparisons 147

Table 6-1 General TLPM motor specifications 157

Table 6-2 Materials of the parts of the TLPM 157

Table 6-3 Analytical calculation of machine parameters 165

Table 6-4 TLPM motor, solid stator: final parameters. 180

Table 6-5 TLPM motor, solid stator: final performance 180

Table 6-6 analytical and FE data comparison 182

Table 7-1 final TLPM motor properties 192

Table 7-2 static parameters of the machine at 20Hz 194

Table 7-3 TLPM motor performance chart 199

Table 7-4 differences between the two versions of the TLPM 201

Table 8-1 performance comparison chart 206

Table 8-2 Force density comparison chart 206

List of Abbreviations

2D	*Two dimensions*
3D	*Three dimensions*
AC	*Alternative current*
DC	*Direct current*
EDM	*Electro discharge machining*
ELA	*Electric linear actuator*
EMA	*Electro-mechanical actuator*
emf	*Electro motive force*
FE	*Finite element*
GCD	*Great common divider*
Hc	*Coercive force*
HP	*Heat path*
IPM	*Inset permanent magnet*
LCM	*Least common multiplier*
LIM	*Linear induction motor*
LM	*Linear motor*
LPM	*Linear permanent magnet motor*
mmf	*Magneto motive force*
NdFeB	*Neodymium iron boron*
PM	*Permanent magnet*
rms	*Root mean square*
SMC	*Soft magnetic composite*
SmCo	*Samarium-cobalt*
SPM	*Surface permanent magnet*
SST	*Single sheet tester*
TLM	*Tubular linear machine*
TLPM	*Tubular linear permanent magnet*

List of Symbols

A	electrical loading, magnetic vector potential (Amp/m)
A_{gap}	air gap area (mm^2)
A_{rms}	Rated electrical loading (Amp/m)
B,B_{rms}	magnetic flux density, magnetic loading (Tesla)
B_{g_IPM}	air gap flux density of IPM magnet (Tesla)
B_{g_SPM}	air gap flux density of SPM magnet (Tesla)
B_{g1}	The amplitude of the fundamental component of B_{g_IPM}
BI_0	modified Bessel function, first kind of zero order
BI_1	modified Bessel function, first kind of first order
B_{Ir}	radial component of the flux density in region I (Tesla)
B_{Iz}	axial component of the flux density in region I
BK_0	modified Bessel function, second kind of zero order
BK_1	modified Bessel function, second kind of first order
B_{rem}	remnant flux density of the magnet (Tesla)
C_{c_lam}	cost of the laminated core of the machine
C_{c_solid}	cost of the solid core of the machine
C_{core}	cost of the core material
C_{core}	cost of the core of the machine
C_o	constant cost
C_{PM}	cost of the permanent magnet of the machine
C_{sh}	cost of the shaft of the machine
$C_{winding}$	cost of the winding of the machine
d	distance, thickness (mm)
D	material mass density ($kg/m^{3)}$
f	Frequency (Hz)
F	force (N)
f_{cog}	cogging force (N)
F_{lin}	rated thrust force (N)
f_{ripple}	total ripple factor
f_{stack}	stacking factor
G	Thermal conductance of object
H	magnetic field intensity (Amp/m)

h_{air}	heat transfer coefficient of air (watt/m^{2}K)
h_m	magnet high (mm)
I_{main}	current of the primary winding (volt)
J	current density (Amp/mm^2)
J_{rms}	rated current density (Amp/mm^2)
K_c	Karter coefficient
k_d	winding distribution factor
k_F	force constant (N/Amp)
k_{fill}	copper fill factor
k_{fringe}	flux fringing factor
k_p	winding pitch factor
$k_{saturate}$	saturation factor
k_w	total winding factor
L	length of the body (mm)
$L_{_d}$	inductance of the d_axis (mH)
$L_{_q}$	inductance of the q_axis (mH)
$L_{activet}$	active length (mm)
L_g	air gap length (thickness) (mm)
L_{g_eq}	equivalent air gap length (mm)
m	number of phases
M_z	axial magnetization vector
N_1, N_2	Pimary and secondary number of turns
N_{turn}	number of turns
N_{pole}	number of poles
N_{slot}	number of slots
ω	angular speed of the excitation current/voltage (rad/sec)
P	number of pole pairs
P_e	eddy current losses (watt)
P_h	hysteresis losses (watt)
P_{watt}	power losses (watt)
q	number of slot per phase per pole
r	radius (general) (mm)
R_{depth}	slot depth ratio
R_{ext}	outer radius of the stator (mm)
R_{in}	inner radius of the stator (mm)

R_m	outer radius of the magnet (mm)
R_r	inner radius of the magnets (mm)
R_s	outer radius of the machine slot (mm)
R_{slot}	radius of the slot midline (mm)
R_{split}	split ratio
R_{th}	thermal resistance (Kelvin/watt)
T	Temperature (^{o}C)
T_{max}	maximum temperature of the windings (^{o}C)
v	linear speed (mm/sec)
vs	linear synchronous speed (mm/sec)
$v_{secondary}$	voltage of the secondary winding (volt)
v_{sence}	voltage of the output signal (volt)
x	lamination sheet thickness (mm)
α, α_{slot}	angular displacement of slot (degree)
α_p	magnet span to pole pitch ratio
γ	angular width of the object (rad)
δ	skin depth (penetration depth) (m)
ΔT	temperature difference (^{o}C)
θ_{elec}	position in electrical (rad)
λ	the thermal conductivity (watt/m.kelvin)
μ_o	absolute magnetic permeability of the free space (H/m)
μ_r	relative permeability of the material (H/m)
μ_{rec}	relative permeability of the permanent magnet (H/m)
ρ	electric resistivity (Ω·m)
σ	electric conductivity (S/m)
σ_{Ft}	tangential shear-stress
τ_m	Magnet thickness magnet span (mm)
τ_{pole}	Pole pieces width or pole pitch (mm)
τ_{slot}	slot pitch (slot width + tooth width) (mm)
τ_w	winding width (mm)
Φ	magnet flux linkage (web)
Ψ	Heat flow (watt/m^2)
ω_{elec}	electrical angular speed (rad/sec)
ω_{mech}	angular mechanical speed (rad/sec)

1. INTRODUCTION

Linear electrical machines have been researched quite extensively, for the last 50 years [1, 2]. While they are quite notorious for their inherent lack of system-level force density, however one of their main advantages has always been the fact that a linear thrust force can be achieved without any mechanical connection such as gear-boxes, ball-screws etc.… being required. In this context, they make an ideal solution for applications which require stringent reliability and 'mean time to failure' figures such as in the aerospace industry [3-6].

Recently, the aerospace industry has started to look closely into the feasibility and adaptability of linear machines for linear actuation applications. Being a virtually, jam-free solution to functionalities which traditionally have been achieved via the use of hydraulic and/or mechanical systems or electro-mechanical actuators (EMA) with mechanical gearing or ball screws etc., then this makes linear machines ideal for such applications. Some projects that focus on developing electromagnetic linear actuators (ELA) to replace EMAs include the developments shown in [7-9].

In a recently completed project [7] within the University of Nottingham (UoN), a tubular linear permanent magnet (TLPM) synchronous motor was developed and prototyped for a helicopter application. The machine is shown in Figure 1-1.

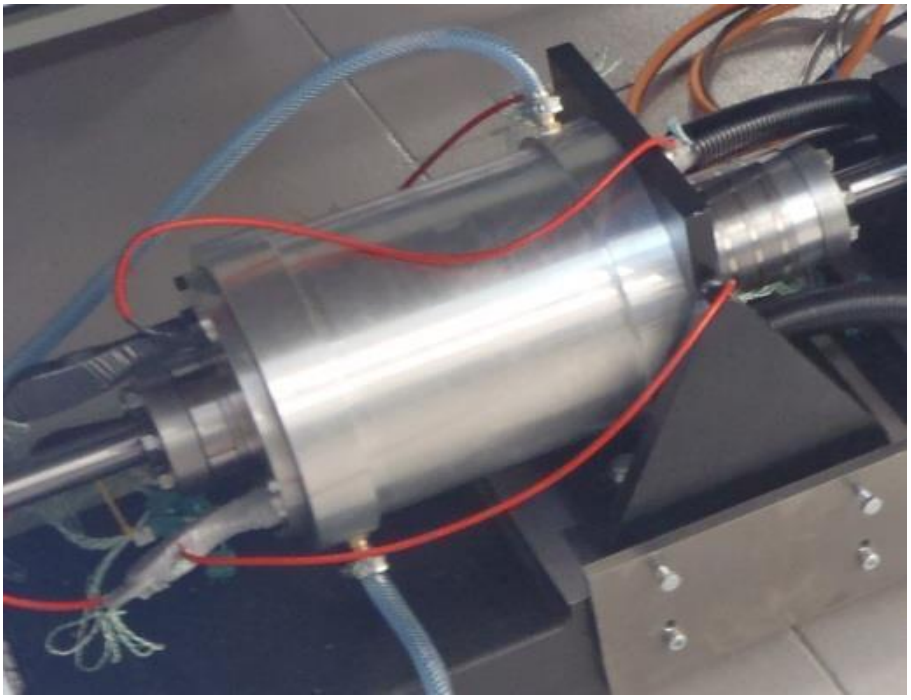


Figure 1-1 TLPM Motor: overview

This TLPM machine, achieved excellent results in terms of force density and efficiency and met almost all the requirement specifications of its relative project. However, one objective that it didn't achieve was the final prototype cost. This was mainly due to the manufacturing costs related to its need for axial laminations. It is therefore the main aim of this project to develop and prototype a TLPM motor for the same specifications as for the original project, where the final cost objective is also achieved. This needs to be done without compromising the performance requirements of the system.

1.1 THE ORIGINAL MACHINE

The TLPM machine shown in Figure 1-1, is a 12-slot, 10-pole, tubular machine whose mover comprises an inset permanent magnet (IPM) configuration with flux-focusing pieces. Detailed specifications of the machine are given in [7, 8, 10] and

are also presented later in Chapter 3. While most of the manufacturing aspects of this machine followed conventional procedures, however an important feature of this particular machine is the laminated, soft magnetic material that makes up its magnetic circuit in the stator. In fact, the stator of the TLPM motor is made up of a series of axial laminations, distributed in a 'sun-shine' structure such as shown in Figure 2-8. While this is ideal in terms of reducing the circulating eddy current losses in the machine, however from a manufacturing point of view, it proved to be a challenging, time-consuming, manual and very expensive step in the prototyping process.

Apart from the manufacturing cost, another perceived disadvantage of this structure is the general reduction of the so-called 'stacking factor (f_{stack})' of the machine, which automatically affects the magnetic circuit of the machine and performance. This is illustrated later in Section 2.5.1.2, Figure 2-8, which shows a representative and simplified laminated stator of the TLPM motor, where for reasons of clarity, the mentioned spaces between the laminations are enlarged.

Considering the above, it is therefore clear that a solution to the 'axial lamination' challenge is required. A cost-friendly alternative that has no negative impact on the machine performance and/or efficiency is needed.

1.2 PROPOSED SOLUTION

In order to address the above, a stator made of solid Ferro-magnetic steel, henceforth known as a 'solid stator' was identified as a potential solution to the manufacturing complexities related to the original laminated configuration. A solid

material manufactured with conventional machining techniques would cost a fraction of the total cost of the laminated stator, used for the bench-mark machine.

However, a solid material structure means a significant increase in core losses, mainly due to the Ohmic eddy current losses. It is therefore the aim of this work to propose a TLPM motor that comprises a stator made of solid material that however does not incur excessive core and eddy current losses.

1.3 AIM AND OBJECTIVES

Thus, the main aim of this work is to propose a new design for the TLPM motor of [7] that comprises a solid stator. As mentioned above, the main perceived challenge with this concept is the core loss requirements. To achieve this aim, this work is built around a set of objectives and deliverables as follows.

- A full understanding of the design and operation principles of the original, bench-mark, TLPM machine is required.
- A full understanding of the mechanisms and phenomena that create the core losses in a machine with an unconventional magnetic circuit such as the TLPM motor is required.
- A full characterisation of the solid material behaviour when applied into unconventional magnetic circuits such as that of a fractional slot per pole, tubular machine is critical for the project at hand. This characterisation exercise results in accurate material property data (that considers all the aspects of the application) that can then inform the design of the TLPM motor with solid material.

- The development and validation of a suite of eddy current reduction techniques, modelled with analytical and numerical methods (based around the accurate material data mentioned above) and experimentally validated on purposely-built test setups able to measure and monitor the core loss of specific specimens. These specimens are designed to reflect the behaviour and needs of the TLPM motor.
- A re-design and development of a new TLPM machine with a solid stator that permits a reduction in the manufacturing costs mentioned above without compromising the performance indicators of the original machine.

1.4 THESIS STRUCTURE

Based on the above, then the thesis is organized as follows:

This Chapter 1 acts as a general project introduction where the main application and its objectives and requirements are presented.

Chapter 2 provides a general literature review of linear machines. The literature review includes detailed considerations on the conventional manufacturing techniques used for tubular machines and also includes various cost reduction techniques used in the manufacturing of TLPM motors

Chapter 3 is focused on the analysis of the original TLPM motor presented in [7]. Analytical and numerical models of the TLPM motor are built and validated against the existing experimental data of the original TLPM

motor. The numerical models are built in 2D and 3D using a commercial software package and used in the rest of the thesis for the development of the proposed eddy current reduction techniques and the re-design of the machine.

Chapter 4 covers the characterization methods of electromagnetic material. Novel characterization methods for the ferro-magnetic material in machines with unconventional magnetic circuits are proposed and validated. Accurate losses maps (relative to the application at hand) are provided at the end of this chapter.

Chapter 5 is the chapter where a focus on eddy currents is prevalent. Detailed analyses of eddy current behaviour in solid material are done in order to achieve a full understanding of this phenomena for the application at hand. Innovative eddy current reduction techniques are then investigated. Finally, the most appropriate method is selected and implemented into the design processes of the new machine.

Chapter 6 is focused on the re-design of the bench-mark TLPM motor into one that comprises a sold stator. The material characterisation of Chapter 4 and the eddy current reduction techniques in Chapter 5 are seamlessly combined into the design procedures of the new TLPM motor in order to achieve the new version of the TLPM motor that respects both performance and manufacturing requirements. Optimisation procedures that consider force density and efficiency as the main objective

functions are also included. The performance of the new design is compared against that of the benchmark machine [7].

Chapter 7 illustrates the manufacturing processes enacted to build the prototype of the new TLPM machine. Thus, all the above technique and design processes are validated against the experimental results illustrated in this chapter.

Chapter 8 summarizes the conclusions of the work and gives recommendations and suggestions for future work.

1.5 NOVELTY OF THE WORK

This thesis presents the following highlights:

- Using solid soft magnetic material instead of laminated soft magnetic material in the stator part of the TLPM machine for manufacturing and cost improvement is challenging. Different stator configurations have been introduced in this work which give an advanced step toward the improvement of machine manufacturing processes.

- A new technique, for eddy current reduction in the solid parts of TLPM machine is introduced. This technique, unlike classical methods found in the literature, keeps the magnetic and thermal characteristics of the machine at its optimal values by keeping the machine f_{stack} at its maximum (unity) value.

Knowledge on the exact materials that can be used for the design and the characteristics estimation of the magnetic loading are necessary inputs for the design process. This work introduces a new step toward extending the domain of material characterization knowledge. With the practical validation, this new characterization method is suitable to be used in the design and optimisation of machines with unconventional magnetic circuits.

1.6 LIST OF PUBLICATIONS

The following publications were originated from this work:

[1]. A. Mohammed, M. Galea, T. Cox, and C. Gerada, "**Considerations for improved design and reduced manufacturing complexity of a PM, Tubular Linear Motor**," in *10th International Symposium on Linear Drives for Industry Applications*, Aachen, Germany, 2015.

[2]. A. M. Mohammed, T. Cox, M. Galea, and C. Gerada, "**A New Method for determining the Magnetic Properties of Solid Materials employed in Unconventional Magnetic Circuits**," *IEEE Transactions on Industrial Electronics,* vol. PP, pp. 1-1, 2016.

[3]. A. M. Mohammed, M. Galea, T. Cox, and C. Gerada, " **Consideration on eddy current Reduction Techniques for Solid Materials Used in Unconventional Magnetic Circuits**," *IEEE Transactions on Industrial Electronics,* **under review**, 2017.

2. LINEAR ELECTROMAGNETIC ACTUATORS; PRINCIPLES AND APPLICATIONS

2.1 INTRODUCTION

This chapter provides a general review of electromagnetic linear actuators and machines. It starts off with a review of linear motor topologies and types. A brief overview of a cost analysis of the machines is also given. The main manufacturing techniques are highlighted, including various cost reduction techniques used in manufacturing of TLPM machines.

2.2 LINEAR MACHINE STRUCTURE

The general structure of a linear machine (LM) is basically similar to that of a rotary motor that has been cut and unrolled to create a linear version, such as shown in Figure 2-1. Thus linear motion along the centre axis is achieved instead of rotary motion. As for any other motor, a linear machine is comprised of two parts, namely the stator and the moving part, which interact with one another to produce a shear stress (δ) in the air-gap when power is applied [11, 12]. As shown in Figure 2-1, either the primary or the secondary can be fixed while the other moves. With this construction, the load is connected directly to the mover part of the motor. These types of motors are known to achieve excellent performances in terms of efficiency, thrust control, position accuracy, fast response, and reliability [13] .

The types and configurations of linear machines reflect the categorisation and families of conventional, rotational machines. In theory, any type of electrical

machine can be re-configured as a linear machine. Depending on the excitation mode, there are two basic types of linear motor: direct current (d.c.) linear motor, such as linear stepping motor and brushless linear d.c. motor, and alternating current (a.c.) linear motor [14]. The most common types of a.c. linear motor, are the linear induction machines (LIMs), linear reluctance motors (LSRs) and the linear PM synchronous machines (LPMs). In several works of literature [15-17], the latter has been shown to be the configuration which can result in the best performances in terms of force density, efficiency and robustness [17-19].

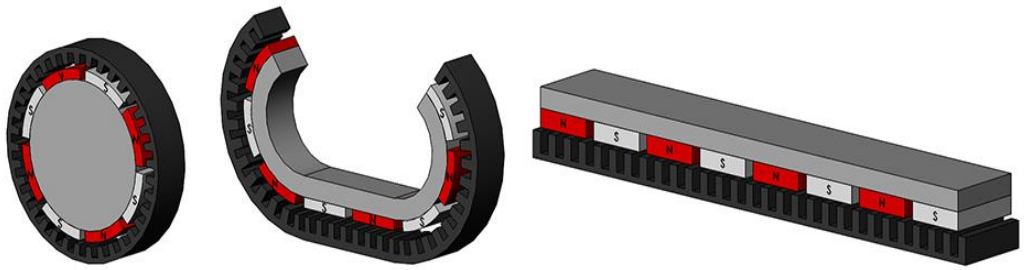


Figure 2-1 Evolution from rotational to tubular concept [20]

2.3 LINEAR MOTOR TOPOLOGIES

This section gives a brief classification of linear motors in order to present an overview of the various possibilities to achieve a linear movement. For all the possible topologies that exist, linear machines can be also classified according to whether they are [12, 21, 22]:-

- Iron-cored or core-less.
- Slotted or slot-less.
- Flat (planar) or tubular (cylindrical).

These various types and topologies give the designer a vast range of different structure types from which the requirements of any application can be achieved [12]. Each type exhibits its inherent advantages and benefits to the user as presented below.

2.3.1 Coreless, PM Linear Synchronous Motor

Coreless machines are also known as “air-core” or “U-channel” motors [22]. Coreless motors consist of a mover (coils) which rides between dual magnet rails as shown in Figure 2-2. The mover does not have any iron laminations in the coils. Instead, the copper windings are encapsulated and located in the air gap between the two rows of magnets. Due to the absence of alignment forces between the stator and the mover, the coreless design has zero cogging force and the attractive force between the stator and the mover parts is zero [23, 24]. Generally, they have lower average thrust force than other types of linear motors. The manufacturing of this motor type is quite easy due to the absence of iron in the mover part, in addition, this type of linear motor has lower mass than iron-core type. Thus, core-less linear motors are ideally suited for extremely high accelerations and applications that require excellent dynamic performances [23], where the force density requirements are not critical.

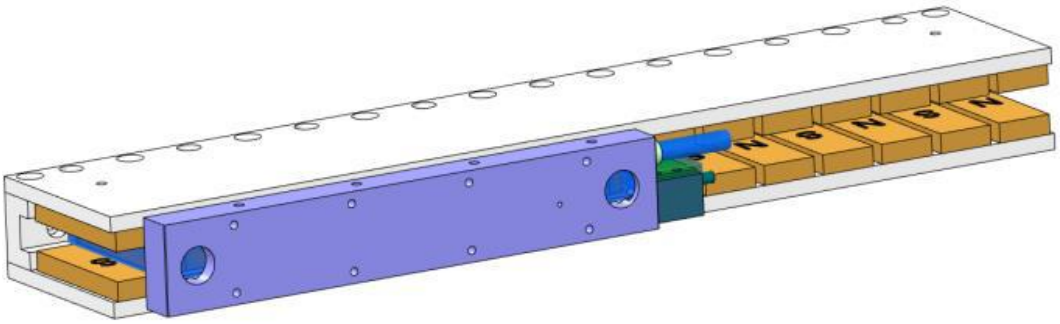


Figure 2-2 Coreless, PM Linear Synchronous Motor [24]

However coreless machines are not very thermally efficient. The intrinsic nature of 'coils in air' and the long thermal path from the winding base to the cooling plate limit the electric loading of these motors [21].

2.3.2 Slotted PM Linear Synchronous Motor

For the more common slotted machine, the iron core provides an efficient path for the magnetic flux to circulate between the motor and the magnet rail. In addition, there is an efficient path for heat dissipation from the motor [11, 12].

From a manufacturing point of view, the slotted design of a linear motor is very economically attractive. Although the structures of iron core, mover, and stator are not complex, the main drawbacks are the presence of the cogging force and the high attractive force between the stator and the magnet track [25]. This high attractive force, which can range from 5 to 13 times the rated force of the motor [21, 26], presents a higher challenge than other linear motor designs [22]. Due to this high attractive force, a robust mechanical guidance system is required to guide the moving parts and to keep a constant air gap. To mitigate this problem, double-sided motors are used. In this design, each side of the double-sided motor produces attractive force opposite to the force in the other side, and then cancel each other out. This is true only when the airgap length in the upper and lower side are equal. However, due to the mechanical tolerance, this construction reduces the attractive force between the stator and mover parts, and does not completely eliminate the problem. Figure 2-3 shows an illustration of a single side linear motor, while Figure 2-4 shows the double sided slotted flat linear motor.

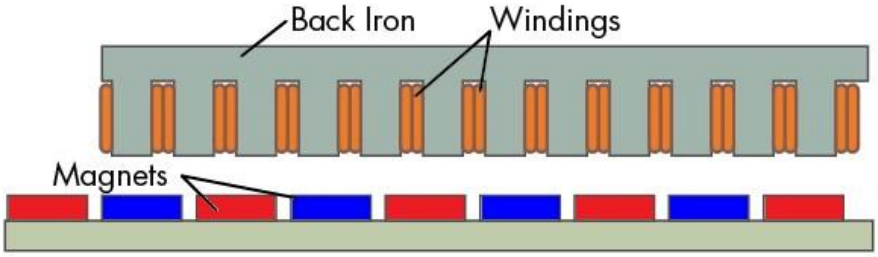


Figure 2-3 single sided slotted linear flat synchronous motor

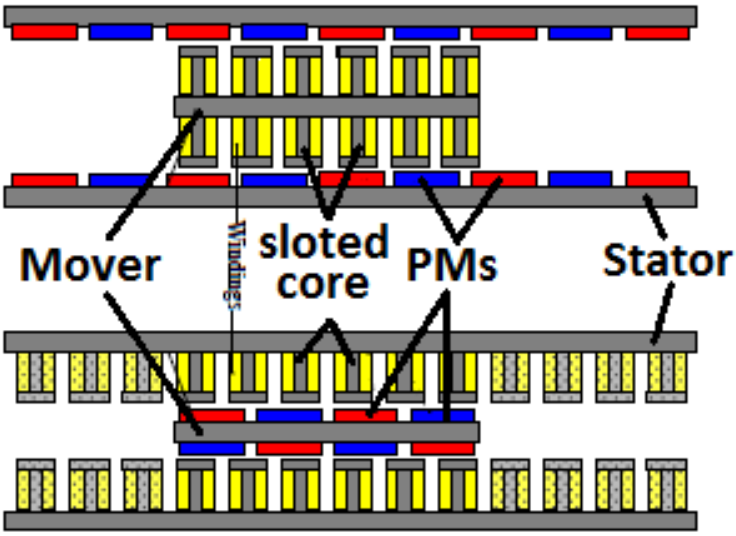


Figure 2-4 double sided slotted PM linear ynchronous motor [27]

2.3.3 Slot-less Linear Motors, Toothless

Slotless motors (see Figure 2-5) are are an alternative type of linear motor which combine several features of cored and coreless motors. In a slotless motor, the stator consist of the back iron part only and has no teeth [22]. The coils are wound without an iron core and are located underneath the back iron part of the stator [12]. Thermally, it has an excellent heat dissipation trait when compared to coreless types due to the shorter heat path length to the cooling base on the outer surface of the back-iron part [21]. However, the main drawback is the equivalent air gap length which results in a considerable decrease in force density when compared to cored slotted types.

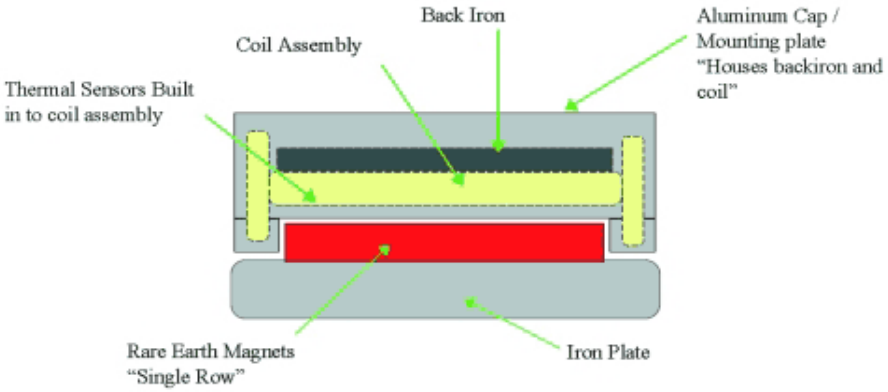
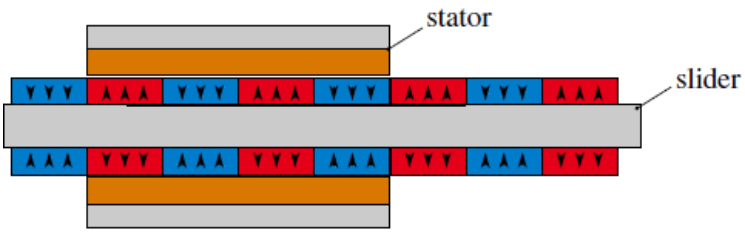


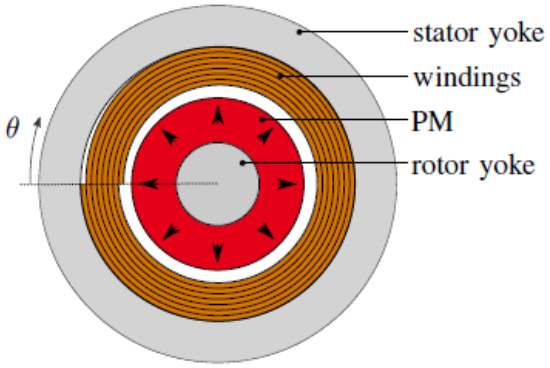
Figure 2-5 slot-less general structure[22]

2.3.4 Tubular motor

Tubular machines (TLM) can be developed from any flat linear machines by rolling them about their longitudinal axis or axis of motion [28], as shown in Figure 2-6. The structure is very attractive for industrial applications thanks to both its closed form, the natural cancellation of radial force between the stator and the mover and the simple circular form of the stator windings [26].



(a) Azimutal cross section and main dimensional parameters of the coreless tubular motor.



(b) Axial cross section of the tubular motor.

Figure 2-6 Tubular motor general structure [29]

TLPM motors enjoy several unique advantages over their linear motor counterparts. These advantages include optimal flux utilisation compared with flat LPM machines within the active length of the machine, balanced radial magnetic fields distribution, and good thermal characteristics due to the providing of radial path for heat dissipation, high thrust density and a good dynamic performance. A very important advantage of tubular machines is the lack of end windings which makes possible a full utilisation of the current carrying conductors [9]. Tubular motors have recently become an optimal choice for precision, high-speed and high-efficiency actuation systems [30, 31].

It is however worth mentioning that similar to any other linear motor, TLPM motors cannot compare in terms of force density to EMAs where a mechanical amplification of produced force is available through a gear-box or a ball-screw. Thus at system level, their force-to-mass and force-to-volume ratios are quite low [7]. Also, they can offer significant challenges in terms of manufacturing complexity, as reported in [32, 33].

2.3.5 High level comparisons of linear machines

The main challenge concerning linear motors is the ratio of output force to mass or to volume. Therefore, in the past few decades there has been much academic and industrial effort to improve the force density values of linear motors. A considerable amount of literature has been published, focused on the performance improvement from a force density point of view. In parallel, there have been several investigations about the cost and manufacturing improvements. Table 2-1

summarises the advantages and disadvantages of the considered motors, which shows the tendency of each type.

Table 2-1 comparison between different motor topologies

Performance	Core-less	Iron-core	Slot-less	Tubular
radial Force	*None*	*High*	*Low*	*None*
Cogging force	*None*	*High*	*Medium*	*High*
Efficiency	*Low*	*Medium*	*Medium*	*Highest*
Force density	*Medium*	*High*	*Medium*	*Highest*
Manufacturability	*Medium*	*High*	*High*	*Lowest*
Cost	*High*	*Medium*	*Low*	*Highest*

2.4 CONCEPTS OF COST OF LINEAR ELECTRICAL MACHINES

Materials and manufacturing costs plays a significant role in typical machine design processes. The overall cost can be divided simplistically into two main parts, namely direct cost and indirect costs. All costs other than direct materials and direct labour costs are related to indirect cost [34]. Mathematically, it is very difficult to find a mathematical expression for the total cost taking into account all dependent factors. Hence, an approximate relation can be written as shown in (2-1) where, $C_{winding}$, C_{core}, C_{PM}, and C_{sh}, are the windings, core, permanent magnets and shaft costs respectively and C_o is constant cost.

$$Cost_{(electric\,machine)} \propto \left(C_{winding} + C_{core} + C_{PM} + C_{sh} + C_o\right) \qquad (2\text{-}1)$$

The parameter C_{core} is the cost of all ferromagnetic materials used in the stator and the mover including the cost of the lamination process of the material and other solid materials and it can be represented in the relation (2-2), where C_{c_lam} and C_{c_solid} are the lamination core and solid core costs respectively.

$$C_{core} \propto \left(C_{c_lam} + C_{c_solid}\right) \quad (2\text{-}2)$$

LPM synchronous motors have found wide applications due to their high power density (compactness), high efficiency, ease of control, high torque-to-inertia ratio and high reliability [35] when compared to LIMs and other linear motor families. Choosing the appropriate PM material further reduces its manufacturing costs and makes the motors costs less vulnerable to increases in magnetic material costs.

2.5 MANUFACTURING OF TLPM MOTOR (OVERVIEW)

In traditional rotary motors, the ferromagnetic cores that make up the stator and the rotor are usually made of insulated laminations. This interrupts the circulation of eddy currents that would form as a result of the time variation of the flow caused by the spatial movement of the magnetic field. For TLPM machines, this concept is the same but the construction is modified because the flow of currents occurs differently from a traditional rotary motor. In this case, eddy currents develop on circumferences laying on a plane that is perpendicular to the main machine axis. The magnetic flux in the motor in many cases is designed to flow in an axial-radial plane that complicates the arrangement of the laminated sheets structure, which needs to be oriented along the flux path [10, 36, 37]. There are different configurations for stator lamination as shown below:

2.5.1 Complete lamination Stator

From a manufacturing point of view, employing this technique into rotating machine is quite easy because the laminated sheets are stacked in a straight

direction. For TLPM machines, it is completely different, as the lamination sheets need to be stacked azimuthally around the axis of motion.

2.5.1.1 Pie-slice lamination stator

In order to successfully construct the tubular linear machine stator with uniformly-distributed lamination sheets, the laminations can be constructed as "pie slice" structure as shown in Figure 2-7, where the thickness of the laminations is varied linearly corresponding to the difference between the inner and outer diameter of the TLPM machine.

Equation 2-3 shows the relationship between the sheet thicknesses (at the two ends) and the machine diameters (inner and outer), where x_1 and x_2 are the thickness of the lamination sheet at the inner and outer ends respectively and R_{in} and R_{ext} are the inner and outer diameter of the machine respectively.

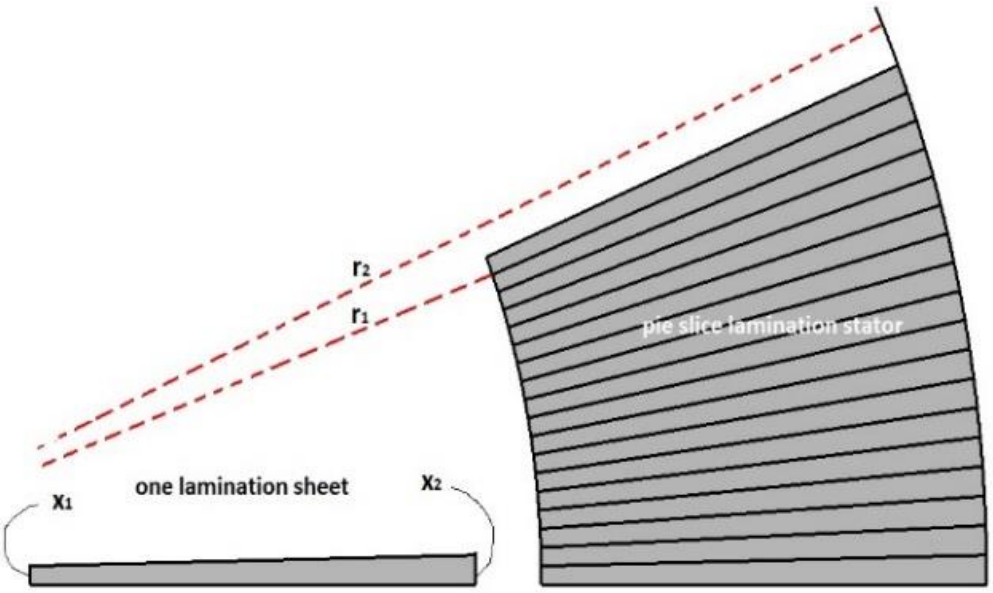


Figure 2-7 the principle of pie-slice structure

In general, the ratio of electrical steel usage in the iron core is called stacking factor (f_{stack}), and it refers to the effective thickness of the lamination sheets along the core active length [18]. In general, the higher f_{stack} is, the better it is for the machine performance. In this case, this structure has good magnetic characteristics due to the high f_{stack} achieved in both, inner and outer stator surfaces.

$$\frac{x_1}{x_2} = \frac{R_{in}}{R_{ext}} \tag{2-3}$$

From a manufacturing point of view, the lamination sheets of the electrical steel are usually manufactured in a uniform thickness, usually less than 1*mm* with a wide range of standards available in markets which can be used by the designer. While for nonstandard or non-uniform sheet thickness as shown in Figure 2-7, for each machine geometry, unique lamination sheets needs to be manufactured. This incurs a significantly high cost and the implementation is practically not applicable.

2.5.1.2 Sunshine lamination stator

The second option for implementing the uniformly distributed lamination sheets is the "sunshine" structure as shown in Figure 2-8. As it can be observed, for outer stator configurations such as in [7], this type of lamination, gives a high f_{stack} at the air gap region at the inner perimeter of the stator. Moving toward the outer perimeter, f_{stack} decreases gradually, and a very low value appears on the outer surface of the stator. On the other hand, when the inner stator configuration has to be used, the lowest value will appear in the air gap region.

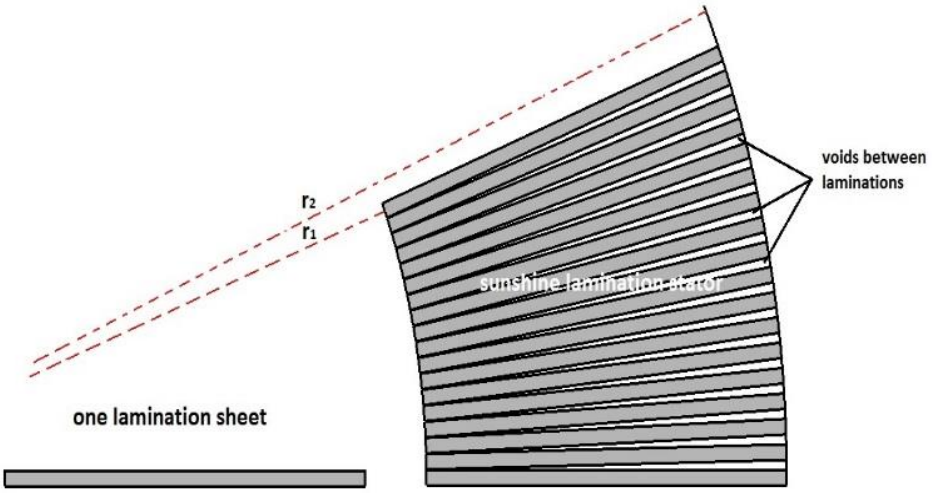


Figure 2-8 the principle of sunshine structure

Considering the two types of stator topologies of a TLPM motor, if the inner stator topology has been used, then the laminations will always suffer from a reduced effective area at the surface facing the machine air gap, and the lamination edges touch each other at the inner diameter of the inner stator as shown in Figure 2-9 (a). If the topology of the outer stator has been used, the lamination sheets density then decreases radially towards the outer surface of the outer stator and the highest value will be achieved at the air-gap region [32] as shown in Figure 2-9 (b).

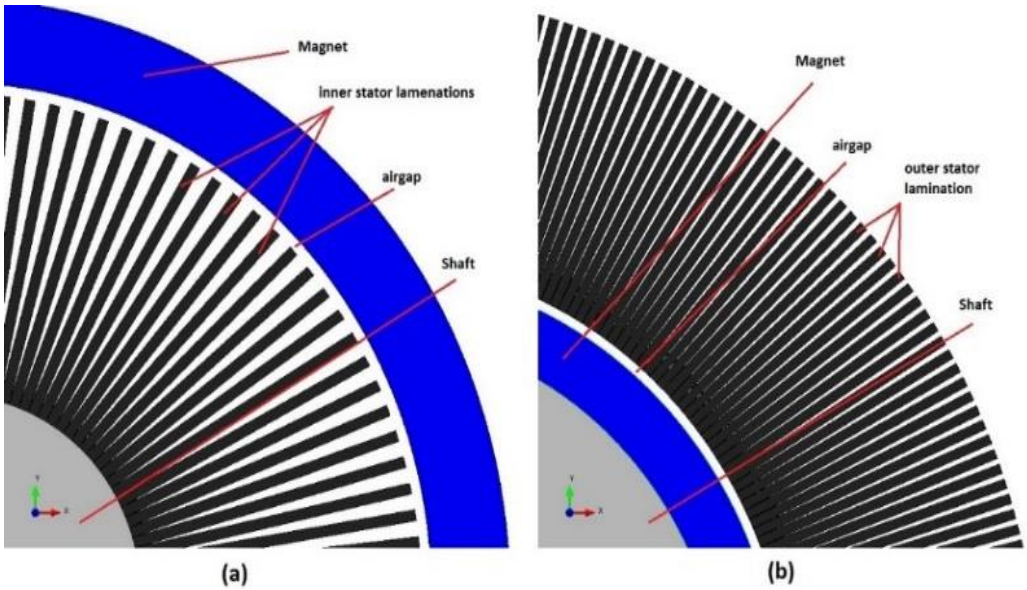


Figure 2-9 sunshine structure a) inner stator, b) outer stator

Generally, the sunshine structure inherently affects the electromagnetic characteristics and thermal behaviour of the TLPM machine. This is due to the voids between the laminated sheets which tend to reduce the mass density of the stator core.

The f_{stack} is strongly dependant on the machine geometry, mainly, on the split ratio R_{split} of the machine geometry, where R_{split} is the stator inner radius to the stator outer radius ratio. (2-4) and (2-5) show the split ratio and its relationship with machine lamination f_{stack}.

$$R_{split} = \frac{R_{in}}{R_{ext}} \tag{2-4}$$

$$f_{stack} = 2 \cdot \frac{(1/R_{split}) - 1}{(1/R_{split})^2 - 1} \tag{2-5}$$

According to Equation (2-5), it is stated that the ratio of the total lamination material's volume to the total stator volume of [7], is 77.3%.

The f_{stack} also affects the thermal behaviour of the machine. Thermal resistance describes the conductive heat transfer along a machine path and it depends on the area of the heat flow direction. When the outer diameter of the TLPM motor increases, then the voids between the lamination are also increased. Assuming that there is no air flow between laminations, then the total effective dissipation area is relatively small and tends to decrease the thermal conductance of the object.



Figure 2-10 sunshine lamintion structure of [7].

From a manufacturing perspective, a TLPM motor is rather difficult, expensive and time-consuming to manufacture with a laminated stator, especially if they are directed in the axial-radial plane [32] as shown above. An important feature is the complexity to position and align the laminations one by one as shown in Figure 2-10. An important aspect is that the excitation coils of a TLPM machine such as that of Figure 2-10 must be previously formed and then each coil will need to be accommodated between two adjacent laminated teeth. This indicates that once the laminations have been assembled as shown in Figure 2-10, then the next step is to 'cut' the stator into these teeth structures so as to allow the assembly of the coils, thus the possibility of misalignment and other damage increase, and the resulting undesirable 'airgaps' between any adjacent teeth incur further reduction in the field of the magnetic circuit.

In [7, 10], it was mentioned that the mechanical structure of such a construction also has low robustness level, because the machine housing part has a series of longitudinal slits in its inner bore into which the laminations were slid as a "sunshine" structure. Not optimal manufacturing techniques such as using glue

were implemented in this machine of Figure 2-10 in order to keep the whole structure together.

2.5.1.3 Staggered lamination stator

A new method to fill the gap of low f_{stack} is proposed in [38]. This can be achieved by using a staggered core lamination method which can facilitate insulation and assembly of a stator core. One tooth with a slot opening interval shaped sheets was built as shown in Figure 2-11. These sheets are arranged and stacked radially to form the stator core. Another advantage of this method is the low core losses at the back iron part of the stator due to the lower flux density achieved with this structure than normal lamination method of [10].

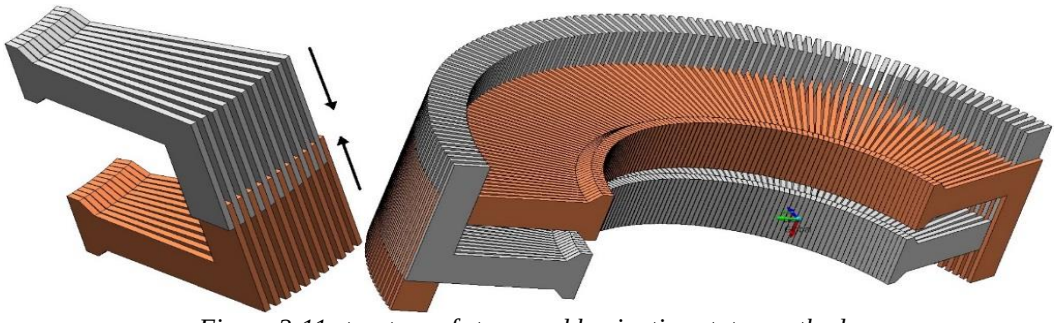


Figure 2-11 structure of staggered lamination stator methode

The f_{stack} for such a construction can be written as in (2-7). This equation shows that both R_{split} and R_{depth} affect the machine f_{stack}, where R_{depth} is the ratio of the slot depth to the stator bore. According to (2-7), the output force of the TLPM machine will be improved by using this construction due to the increasing in the f_{stack}.

$$R_{depth} = \frac{Slot\ \ depth}{Stator\ \ bore} \tag{2-6}$$

$$f_{stack} = 2 \cdot \frac{R_{depth} \cdot (1/R_{split} - 1)}{(R_{depth} \cdot (1/R_{split} - 1) + 1)^2 - 1} \tag{2-7}$$

This method can reduce the fabrication costs to change the slot pitch in order to adapt the length of the magnets and the optimising cost of the slot width ratio by freely setting the interval between two parts. This structure still shows a high level of complexity due to the process of aligning the lamination sheets one by one and the time consumed for this process.

2.5.1.4 Involute lamination stator

In [39], further improvements to the manufacturing of the tubular linear motor are introduced. The lamination sheets of the stator core are involute to one direction. So that, a virtual filled laminated stator is produced and no voids exist between the laminated sheets. This 'filled' stator is achieved by stacking involute laminations of uniform thickness around the inner radius of the stator core. This construction allows for more iron per diameter than non-involute laminations. In this construction, the possibility of misalignment between the lamination of two adjacent part is very low, also it is less sensitive to misalignment of the laminations. Thus, an uninterrupted flux path is possible at the interface of the two adjacent parts. Figure 2-12 shows a simple diagram of this method.

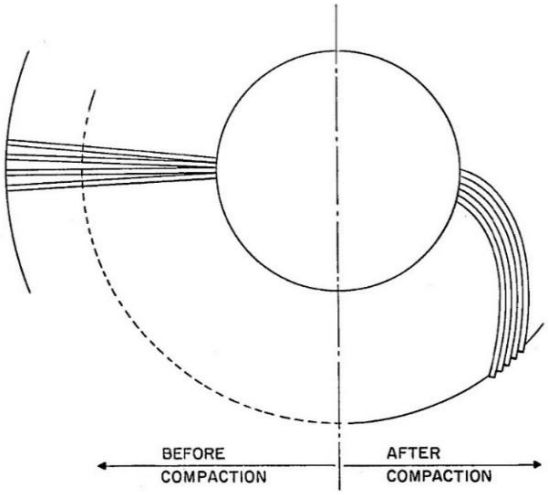


Figure 2-12 the structure of involute lamination stator[39]

From a manufacturing point of view, the challenge is how to keep the outer and/or inner radiuses of the stator fixed. This is due to the radial force which is generated from the bending force or spring back force of involute lamination sheets [40].

2.5.1.5 Blocked Lamination Stator

The stator of a TLPM machine can be constructed by the assembling of multi-blocks of lamination stacks, whose lamination direction is perpendicular to the motion direction.

When lamination sheets are used, the flux is effectively constrained to flow in the two-dimensional plane of the laminations, and regardless of how the laminated tubular stator is constructed, the total cross-sectional areas of the teeth and yoke are equal to the circumference of the inner stator bore multiplied by the tooth width and yoke thickness, respectively, since voids exist [41] and the machine f_{stack} is low.

From a manufacturing point of view, it is more convenient to group the laminations in blocks as shown in Figure 2-13 for the outer stator [32]. It can be considered that each part is quite similar to a one sided linear motor. However, each block of the lamination sheets has varying lengths as shown in Figure 2-14 and this variation inversely depends on the machine's number of blocks and the R_{split} of the machine [32]. Also, the area between each two adjacent blocks can be furnished with an efficient cooling system because direct contacts with coils can be achieved and the current density limit will increase [42].

The choice of the number of blocks is dictated by constructive practicality issues. The larger the circumference is, the greater the number of blocks is, since the

thickness of each sector cannot be too small for mechanical resistance issues. It is also true that if the choice of sectors is too thick in relation to the circumference of the air gap, then this affects the radial distribution of the magnetic flux due to the adopted lamination [32].

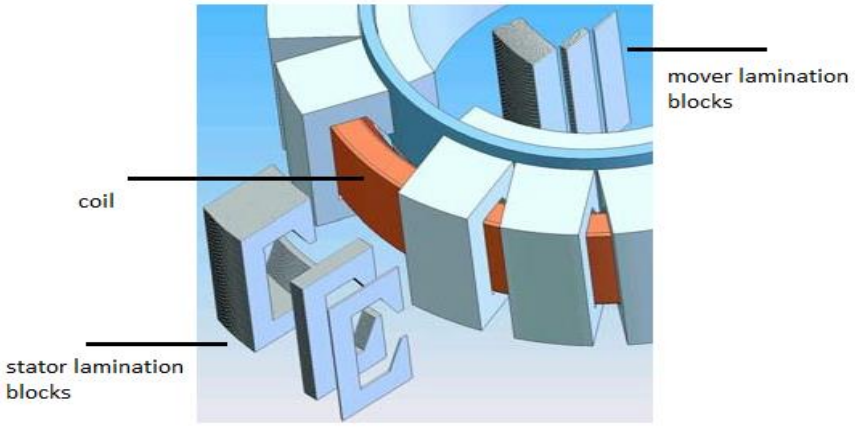


Figure 2-13 Laminated tubular stators, stacking block [32]

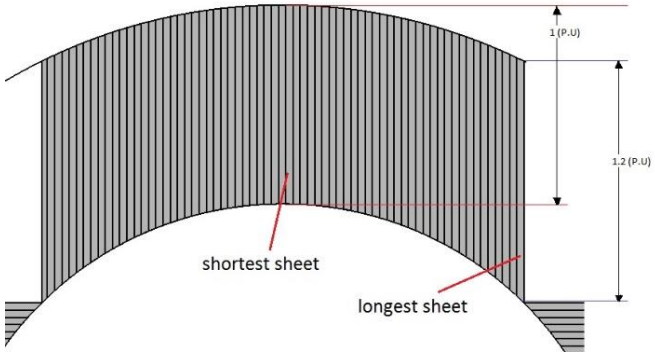


Figure 2-14 the construction of blocked lamination stator

2.5.2 Solid (Soft Magnetic Composite) Stator

Soft Magnetic Composite (SMC) materials are basically iron powder particles separated with an electrically insulated layer [43, 44], as shown in Figure 2-15. It can be considered as an alternative to electrical steels in many applications for a wide range of frequencies as shown in Figure 2-16, such as rotating machines, sensors, tubular and fast switching solenoids [45, 46]. It has several merits including

very low eddy current losses especially at higher frequencies. This holds until the skin depth (δ) becomes comparable with the size of the powder grains (approximately=100μm). The material provides flexibility in machine design and assembly [47].

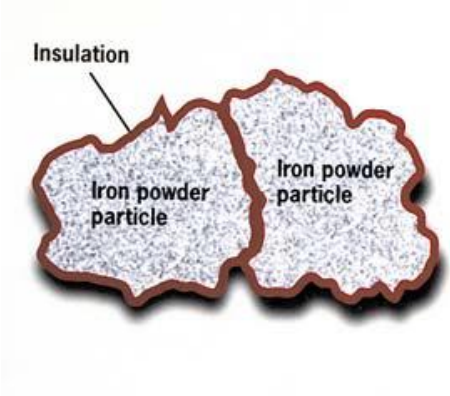


Figure 2-15 Component elements of a SMC material[46]

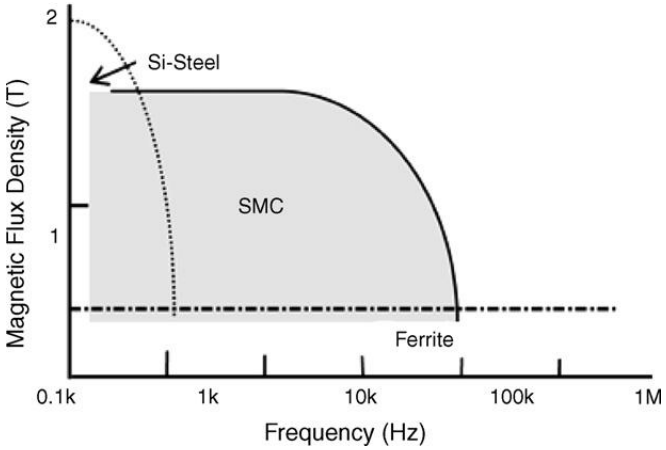


Figure 2-16 applicable regions for magnetic materials [46]

A number of examples employing SMC in electrical machines can be found in literature [32, 41, 43, 48]. In terms of the volumetric efficiency, the available research states that SMC material enables all the available space to be fully utilized and can offer major advantages over the traditional lamination technology. Also, they describe the low manufacturing cost, the simple manufacturing processes and the relatively easy fabrication with complex shapes. SMC materials are cost

effective materials and environmentally friendly, with minimum material waste during the manufacturing process. Figure 2-17 shows the basic design of two outer stator SMC components and a simple pre-wound coil to form one slot of a TLPM machine [32].

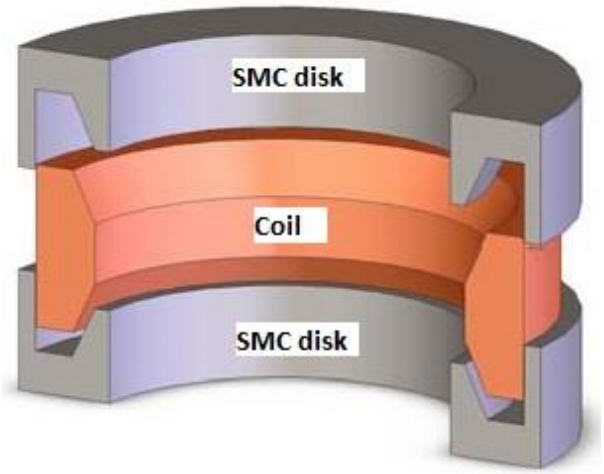


Figure 2-17 Basic design of SMC stator and pre-wound coil [32]

In the application of TLPM machines, [49] claims that SMC represents an ideal material for the stator core material to overcome the lamination problems. SMC components show an overall high f_{stack} that can be well utilised in the design. Figure 2-18 shows the f_{stack} and its dependence on the machine material.

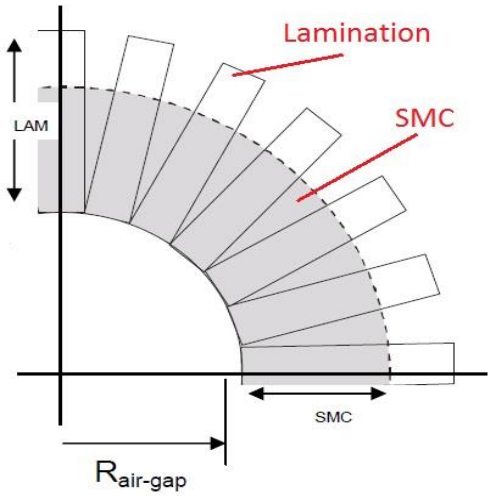


Figure 2-18 f_{stack} of lamination and SMC materials [32]

However, SMC materials do have very poor magnetic properties, namely, the saturation flux density is low, and the unsaturated relative permeability is not high due to the distributed internal air gaps and the non-ferromagnetic coating layer. Thus, using SMC usually results in a lower overall motor performance [43]. In SMC materials, the total loss is dominated by hysteresis loss, which is higher than that of laminated steels due to the particle deformation during compaction [44, 47]. Also, SMC materials have low mechanical strengths especially when high powder density is sought.

2.5.3 Laminated – Solid Combination

This stator configuration consists of a combination of laminated and solid (or even SMC) materials parts within the same stator. It can be simply obtained by applying a simple modification to the configuration mentioned in section 2.5.1.5 by furnishing the 'empty gaps' with a solid material such as solid steel or SMC, as shown in Figure 2-19. It is able to integrate the advantageous of the laminated materials blocks while the voids been filled with ferromagnetic materials, then, the overall magnetic circuit is improved [42].

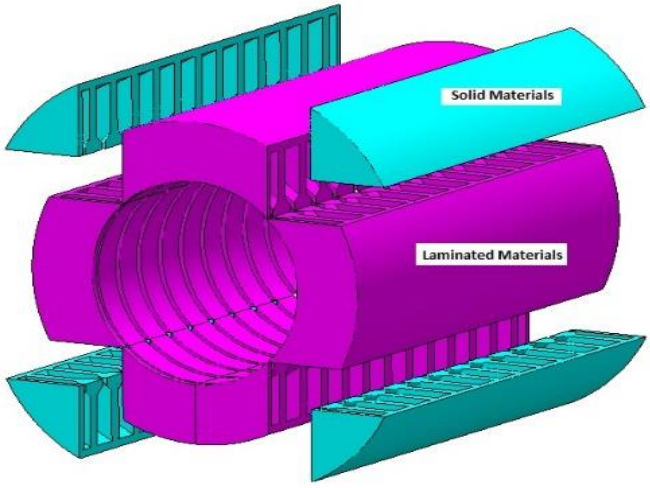


Figure 2-19 Construction of laminated-solid combination.

If a solid ferromagnetic material is used in the corner regions, the machine will suffer from high eddy current losses in these solid parts. This can be mitigated by using SMC materials, but the cost will be highly increased.

From a manufacturing point of view, this configuration increases the degree of machine complexity, where it must be segmented axially for coils windings accommodating. This problem has been addressed in [42].

2.5.4 Other stator configurations

Another configuration of a stator iron core can be built by axially stacking lamination sheets, having hollow disk shape with two different inner radii and equal outer radii and in such a way as to create the stator slots-tooth where the windings are located in. This concept is shown in Figure 2-20. In this structure, the lamination direction is parallel to the translation axis of the movable part of the machine [11, 28, 37].

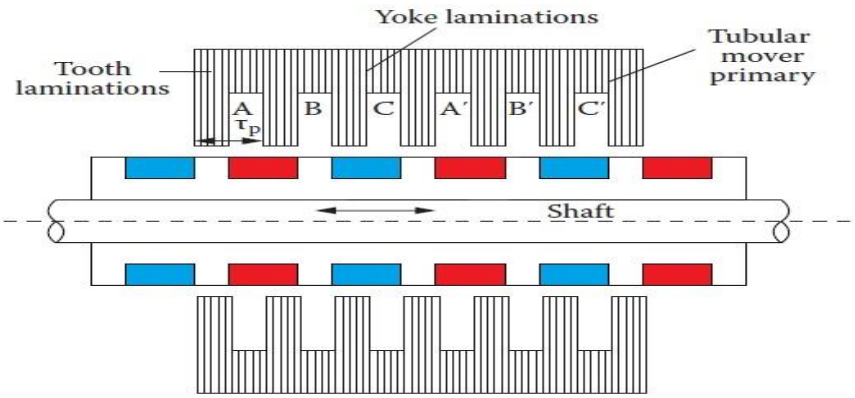


Figure 2-20 transversal laminated stator

In teeth, where the field lines have a radial direction, this type of lamination allows confining the eddy currents in the single sheet volume. On the other hand, this does not occur when the flux has an axial direction as in the stator back iron. Also, this

structure introduces additional air gaps in the path of the axial direction of the field, determining a substantial performance decrease [11].

Another stator configuration of a TLPM machine is described in [37]. A combination of the two lamination structures is used in the stator part. In particular, this structure involves the construction of laminated disks with a vector of rolling parallel to the axis of motion. The size of these disks is equal to the tooth depth. The second part is a block with vector lamination perpendicular to the direction of motion fixed over the first part to form the back iron of the stator, as shown in Figure 2-21.

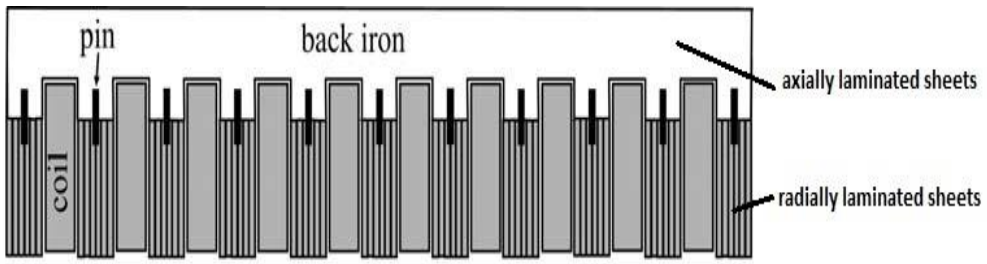


Figure 2-21 transversal laminated stator with solid back iron

Actually, as it can be seen from Figure 2-20 and Figure 2-21, the "transversally laminated core" in this case is almost equivalent to a "solid core." The insulation layers between the laminations only increase the reluctance of the magnetic circuit and there is no resistance increase along the eddy current path and would clearly result in the wrong orientation. However, transversely laminated constructions are much easier and more economical to manufacture [36]. They are quite popular constructions used commercially. The extra eddy current losses may be reduced by adding radial slits as described in [11] and shown in Figure 2-22.

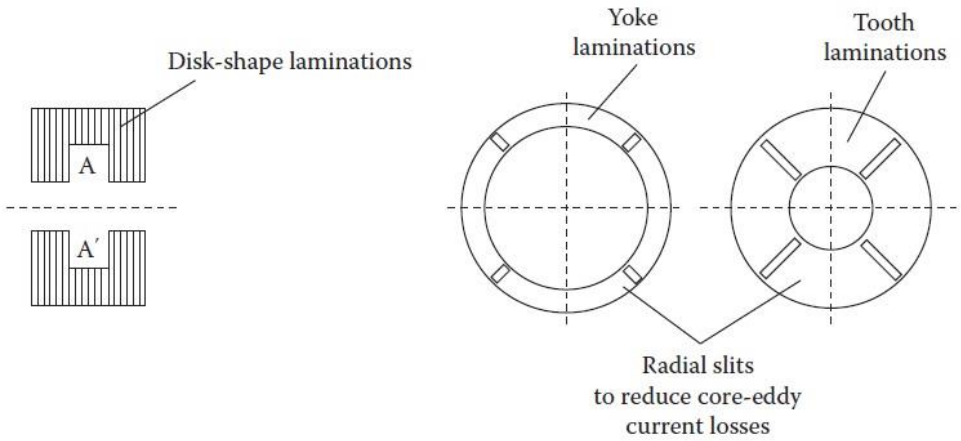


Figure 2-22 slited transversal laminated stator

2.5.5 Solid Stator

Industrial and aerospace applications require miniaturization in the size and the costs. A possible solution consist in using solid iron materials for electrical machines [50]. Solid materials, such as cast steel and cast iron, are used for salient poles, pole shoes, solid rotors of special induction motors and reaction rails of linear motors [12]. For other parts of the machine, the effects of eddy currents and related losses prevent the machine designer from using the solid material in the magnetic parts or even in the nonmagnetic parts facing the time-varying magnetic field. Thus, numerous research efforts have been undertaken on the interaction of PMs magnetic flux with ferromagnetic and nonmagnetic solid materials as in [50-53].

In TLPM machines, for low operating frequencies (less than 25Hz), solid materials can represent a very attractive solution in terms of cost and manufacturing complexity and it is perceived that this solution is by far the better option as in [33, 42]. However, the main drawback of this structure is the high eddy current losses in the motor stator and becoming the main source of power losses in the machine.

2.6 CONCLUSIONS

As well known, the use of laminations significantly reduces eddy current losses in the stator iron as compared to a solid stator construction. Usually alternating current motors including TLPM machines are made with laminated stators. However, various stator configurations and materials (based on solid cores) can be used to reduce the manufacturing cost of TLPM motors. These methods can be illustrated as follows.

(a) Sunshine configuration

While using laminations in conventional rotating machines and even linear PM machines is quite easy and significantly increases the machine efficiency. Implementing laminations in TLPM machines can be done using a 'sunshine' structure, but this structure significantly increases the manufacturing complexity. Also, while the lamination technique decreases the generated eddy currents and related effect, the overall machine performance is decreased due to the low f_{stack} which affects negatively the magnetic and thermal properties.

(b) Blocked lamination configuration

Blocked lamination technique can be used to reduce the complexity of the machine but, from the magnetic properties point of view, it has the same low f_{stack} as "sunshine" configuration. From the machine performance point of view, there is a small improvement in thermal properties.

This configuration, generally, suffers from non-uniform airgap distribution problem because the lamination sheets within the same block have different lengths (as shown in Figure 2-14). This variation results from the difference in

the curvature of the inner and the outer surfaces. Reducing this variation of the lamination sheets length required higher number of blocks and lower R_{split} of the machine.

(c) Lamination with solid combination

A block laminated core with solid corner combinations gives better performance from magnetic characteristics and thermal characteristics points of views due to its high f_{stack}. On the other hand, it has high manufacturing costs and long assembling time.

(d) SMC stator configuration

An SMC stator is the best option for the complex machine and 3D flux directions while the rated speed of the machine is high. However, at low operating speed, the TLPM machine will give a low performance to cost ratio. This is due to the low magnetic permeability and high hysteresis losses when compared with laminated steel.

(e) Solid stator configuration

Solid materials are available with a wide range of mechanical, chemical, electrical and magnetic properties which can be used for a wide range of applications. They enjoy a very low material cost (average price is 2-3 GBPs/Kg) [54] and material availability. Generally, solid materials have isotropic magnetic characteristics and isotropic thermal characteristics which are highly demanded in complex machine designs. From a manufacturing point of view, solid materials do not require costly and customised machining techniques and the manufacturing process is quite simple without any extra special treatments during manufacturing and assembling process.

The main drawback of using solid materials is that, when this solid material subjected to time-varying magnetic fields, an extremely high eddy current will be generated inside these solid parts. As a consequences, and according to Wiedemann-Franz law [55], the eddy current losses in the solid parts will become the main power losses of the machine [53, 56, 57].

Table 2-2 summarizes the differences between the most promising presented stator configurations. It can be seen that, at low operating frequencies, a solid material core can compete with other material used in electrical machines, especially TLPM machines, due to their high manufacturing complexity and cost.

Table 2-2 comparison between different stator construction

Factors\Models	**Laminated steel stator**	**Laminated-Solid stator**	**SMC Solid stator**	**Solid steel stator**
Produced Force	● ●	● ● ●	● ●	● ● ●
Eddy current losses	●	● ●	●	● ● ●
Hysterics losses	●	● ●	● ● ●	● ●
Thermal characteristic	● ●	● ●	●	● ● ●
Magnetic characteristic	● ●	● ● ●	● ●	● ● ●
Mechanical characteristic	● ●	●	● ●	● ● ●
Flux directions	*2-D*	*2-D*	*3-D*	*3-D*
Range of speed	*Low-medium*	*Low-medium*	*High*	*Low*
Cost	● ● ●	● ● ●	● ●	●
Manufacturability	●	●	● ●	● ● ●

3. MODELLING AND ANALYSING OF TLPM MOTOR (CASE OF STUDY)

3.1 INTRODUCTION

Considering that the main aims of this thesis is to improve the cost of the bench-mark machine of [7], by investigating and proposing alternative ways of manufacturing, then a complete and accurate analysis of this bench-mark machine is critical.

Thus, this chapter is dedicated to a careful study of TLPM machine operation, with special focus on the TLPM motor presented in [7]. The chapter starts by developing analytical expressions that describe the TLPM motor and its theory of operation. Two FE models (2D and 3D) of the machine are then built. These models are compared and validated against the existing results from [7] and [10]. Having validated these models, then considerations on the main important features of this work which are the force density and the core losses are given. The idea of a solid stator in order to reduce manufacturing costs is introduced, while the last section introduces and investigates a number of potential methodologies that could be employed to achieve the objectives of this work.

3.2 TLPM MOTOR "CASE STUDY"

The bench-mark TLPM motor is a single air gap, 12-slot/10-pole, PM synchronous machine, with inset permanent magnets (IPM). As reported in [7], its main geometrical parameters are given in Table 3-1, while Table 3-2 presents its main

operation parameters. A general illustration of the motor under study is given in Figure 3-1. This machine was developed to provide the required actuation of a helicopter swash plate angle control system which as can be observed in Table 3-2, requires very low rated speeds.

Table 3-1 TLPM motor: main data

Parameter	**Symbol**	**Value**	**Unit**
Number of poles	N_{pole}	*10*	-
Number of slots	N_{slot}	*12*	-
Machine Active length	L_{axial}	*199.8*	*mm*
Air gap length	L_g	*1*	*mm*
machine outer diameter	R_{ext}	*75*	*mm*
magnet inner diameter	R_r	*39.75*	*mm*
magnet outer diameter	R_m	*46.75*	*mm*
magnet width ratio	τ_m/τ_{pole}	*0.7*	-
R_{split}	R_{in}/R_{ext}	*0.617*	-
Tooth width ratio	T_{tooth}/τ_{slot}	*0. 318*	-

Table 3-2 TLPM motor: experimental performance data

Parameter	*Symbol*	*Value*	*Unit*
Rated electrical loading	A_{rms}	*105.6*	*kA/m*
Rated current density	J_{rms}	*17.68*	A/mm^2
Maximum temperature of the windings	T_{max}	*188*	^oC
Rated thrust force	F_{lin}	*2128.5*	*N*
Mass Force density	-	*91.5*	*N/kg*

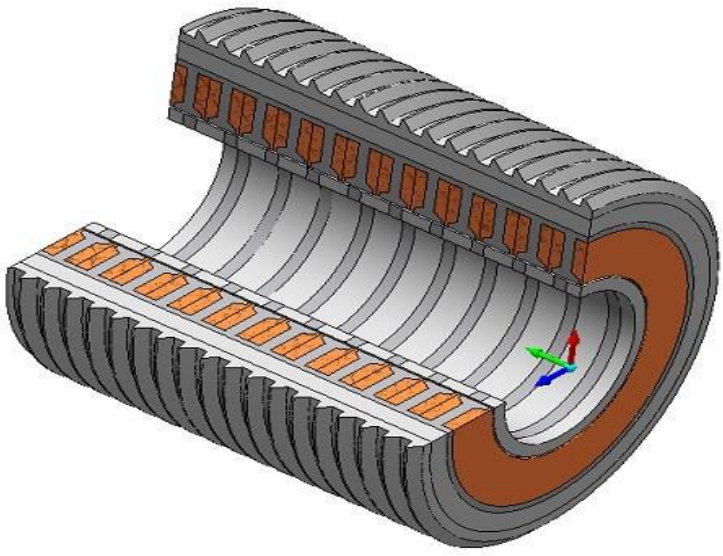


Figure 3-1 the The bench-mark TLPM motor [10]

In the next sub-sections, a detailed and accurate model of the bench-mark machine is developed. The objectives here are multiple and include:

1. A familiarisation exercise with the original machine which results in a complete understanding of the machine
2. The setting up of an accurate modelling tool, which will be validated against the already-existing experimental and FE results of the original machine. This tool will then act as the basic 'bench-mark' from which all the proposed investigations and modifications of this thesis will start.

3.3 MAGNETIC THEORY AND PRINCIPLES

3.3.1 Linear motor: principle of operation

Based on the principles of electromagnetic field, all types of linear electrical machines develop electromagnetic forces. This produced electromagnetic force has two main components, the first one is due to the interaction between the travelling magnetic field of the armature current and the magnetic flux of PMs of the machine which is called synchronous component. The other component is due to the variable reluctance force in d_and_q axes of the machine which is called reluctance component.

For any linear synchronous machine, the speed *v* of the moving part is given in (3-1), which is equal to the synchronous speed *vs* of the travelling magnetic field. As can be observed from (3-1), this speed only depends on the input frequency *f* and the pole pitch (τ_{pole}) [12].

$$v_s = 2 \cdot f \cdot \tau_{pole} = \frac{\omega_{elec}}{\pi} \tau_{pole} \quad (3\text{-}1)$$

Then, the mechanical linear speed v_{mech} is related to the electrical angular speed ω_{elecy}. The mechanical position θ_{linear} of the moving parts traveling in synchronous speed v_s can be calculated using (3-2), where θ_{elec} is the position in electrical radians.

$$\theta_{linear} = \theta_{elec} \cdot \frac{\tau_{pole}}{\pi} \quad (3\text{-}2)$$

By applying Maxwell's stress tensor such as explained in [18, 58], the force and torque production of the machine can be derived. Considering (3-3), it is clear that the interaction of a linear current density *A* and a magnetic induction *B* results in a local tangential shear-stress σ_{Ft} in the machine's air gap. In general machine terms, *B* is also known as the magnetic loading and *A* is also known as the electric loading[18].

$$\sigma_{Ft} = \mu_o H_n H_t = \mu_o H_n A = B_n A \quad (3\text{-}3)$$

Equation (3-3) gives a local time-dependent value for σ_{Ft}, described as the cross product of the local instantaneous values of *A* and *B* on the air-gap surface. From (3-4), it can be seen that, electrical machines are subject to two main constraints, namely the electromagnetic limit and the thermal limit which are imposed by the materials from which its main components (copper, insulation, soft magnetic and hard magnetic materials) are constructed [9]. In fact, B_{rms} is also limited by the non-linearity and the saturation level of the ferromagnetic materials used in the core parts. As the flux density in the magnetic circuit increases, saturation effects, such as increased *mmf* drops across the circuit, become more relevant [59]. On the other

hand, the machine electric loading A_{rms} is in general mainly limited by the thermal limit of the armature windings and/or demagnetization of any eventual magnets [60].

An important element, in terms of the electromagnetic performance, is the air-gap length L_g. Although a smaller L_g would improve the performance [58], its minimum length is however limited by manufacturing and mechanical tolerances [61]. Also, the production of the force is not only depending on B_{rms} and A_{rms}, but is also limited by the air gap area A_{gap} as shown in (3-4).

$$Force = A_{rms} \times B_{rms} \times A_{gap} \tag{3-4}$$

In (3-4), the cross product $B_{rem}\, x\, A_{rem}$ represents local shear stress (δ) or local force. Then, this equation can be solved numerically by integrating the force over the whole area of the air gap of the machine (A_{gap}) [58].

Considering all this, then it is widely noted that assuming standard materials such as copper conductors and classical magnetic materials, the maximum attainable values of δ for a typical standard electrical machines rarely exceed 20 kPa [62, 63]. Pushing these limits forward as much as possible will improve machine performance and is thus the subject of many research efforts, for example [7, 64].

3.4 MACHINE ANALYSES

While the accuracy of the FE method is today universally acknowledged both for 2D and 3D configurations, however the basis of any analysis needs to start from the

fundamental understanding of the system. In this context, a basic analytical model of the TLPM machine, based on its air-gap flux density characterisation is built.

3.4.1 Air gap flux density

The main electric machine parameters such as electromagnetic force, magnetic radial forces, flux-linkage, etc., can be evaluated directly from the magnetic field distribution in the air-gap. The open circuit field distributions in the air-gap can be determined using different calculation methods, e.g. analytically, using a magnetic reluctance network method or subdomain regions method and numerically using finite element method (FE).

TLPM machines can be broadly classified on the basis of the direction of magnetisation of the PMs. Many topologies of PMs can be used in high force density TLPM motors for aerospace and other applications. However, the selection of magnets usually depends on the requirements and constraints of the application of the machine [13, 65].

A. Analytical method

The most common types of magnetic circuits are the radially-magnetised magnet, also known as a surface mounted configuration (SPM) as shown in Figure 3-2(a) and the axially-magnetised magnet with magnetic pole-pieces, also known as inset PMs (IPM) configuration which is shown in Figure 3-2(b).

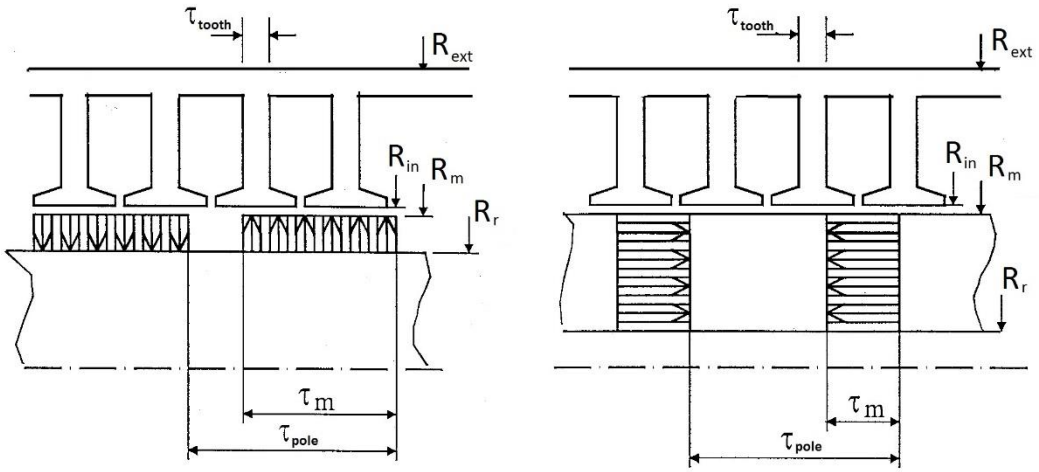


Figure 3-2 TLPM motor with a) SPMs and b) IPMs [13]

Expressions to calculate the no-load airgap flux density have been derived for the SPM and IPM machines types in [7, 11, 66, 67]. The no load airgap flux density of an unsaturated SPM machine can be calculated analytically as in (3-5) and for an IPM as in (3-6). The flux-density distribution in the air gap is assumed to be a quasi-square waveform and the machine is idealized by the following assumptions [11, 13].

1. infinite iron permeability, so that the magnetic drop in the iron is considered null and iron losses are neglected
2. No leakage flux in the shaft region (R_r).

$$B_{g_SPM} = B_{rem}\left[1-\frac{2g_{ac}}{R_{in}}-\frac{\tau_m}{R_{in}}\right]\cdot\frac{1}{1+\frac{\mu_{rec}\cdot g_{ac}}{\tau_m}\left[1-\frac{2g_{ac}}{R_{in}}-\frac{\tau_m}{R_{in}}\right]} \quad (3\text{-}5)$$

$$B_{g_IPM} = \frac{B_{rem}}{2}\cdot\frac{\frac{\tau_m}{\mu_{rec}}\left[1-\left(\frac{R_r}{R_{in}}\right)^2\right]}{g_{ac}\left[1-\left(\frac{R_r}{R_{in}}\right)^2\right]+\frac{\tau_m}{\mu_{rec}}\frac{\tau_{pole}-\tau_m}{R_{in}}} \quad (3\text{-}6)$$

$$g_{ac} = \frac{(R_{in}-R_m)}{2} = \frac{L_g}{2}$$

Where B_{g_SPM} and B_{g_IPM} are the air gap flux density of surface mounted magnet and imbedded mounted magnet configurations respectively. μ_{rec} is the relative permeability of the PM, L_g is the air gap length, B_{rem} is the remnant flux density of the PM, τ_{pole} is the pole pitch of the PM, τ_m, is the PM width (magnet pitch). R_r *and* R_m, are inner and outer radius of the PM respectively. R_{in} is the inner radius of the stator as shown in Figure 3-2.

The amplitude of the fundamental component B_{g1} of the Fourier series expansion of the air gap flux density is directly related to the flux linkage and to the electromechanical generated force for any given current. it can be calculated as shown in (3-7), where α_p is the pole ratio [13].

$$B_{g1} = \frac{4}{\pi} B_{g_IPM} \sin\left(\frac{\pi}{2}(1-\alpha_p)\right) \qquad (3\text{-}7)$$

Where $\alpha_p = \frac{\tau_m}{\tau_{pole}}$

B. Finite Element Method (FE)

The Finite Element (FE) Method is a numerical technique used to solve and analyse nonlinear problems. In many application fields such as, architecture engineering, electrical engineering etc., as well as for electromagnetic analysis purposes. In this method, the field solution can be obtained even in case of time variable nonlinear coefficients, nonlinear material and nonhomogeneous materials field equations, which would be very difficult to solve using other methods. [68-71].

Considering the axial symmetry of the tubular TLPM motor, the problem can be simplified to a 2D axial symmetry model. The FE method allows precise determination of machine parameters through the magnetic field solutions as it takes into account the details of geometry and non-linearity of magnetic materials. Using the FE method, the whole analysis domain is divided into elementary subdomains, which are called finite elements, and the field equations are applied to each of these elements [72]. Figure 3-3 shows an example of the no load FE airgap flux density distribution map, at zero current.

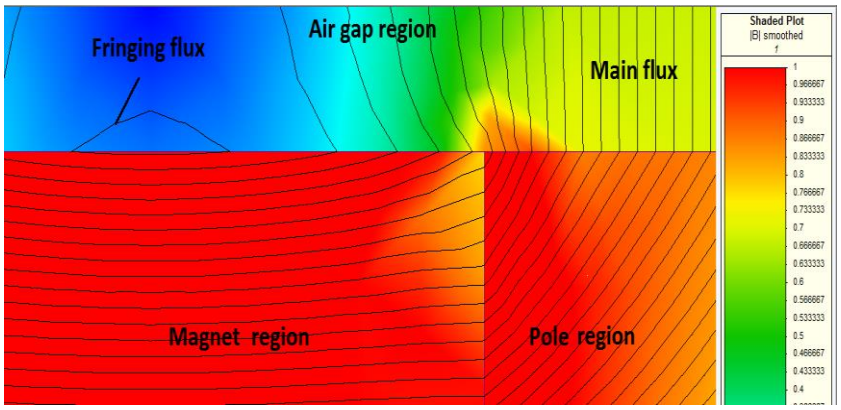


Figure 3-3 airgap flux density distribution map

The spatial air gap flux density distribution contains harmonics as shown in Figure 3-4 and Figure 3-5.

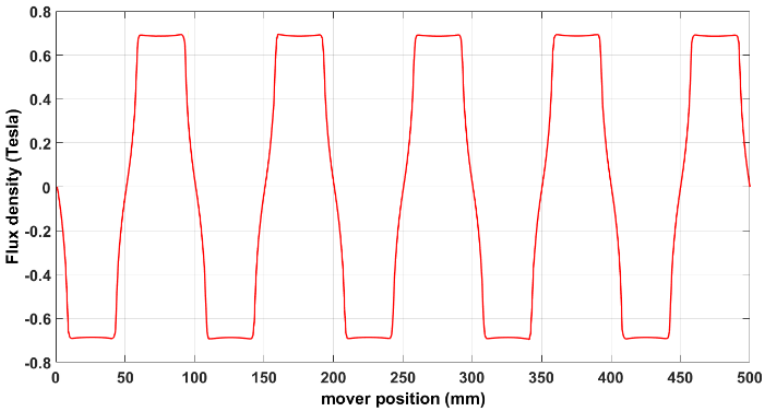


Figure 3-4 no load airgap flux density

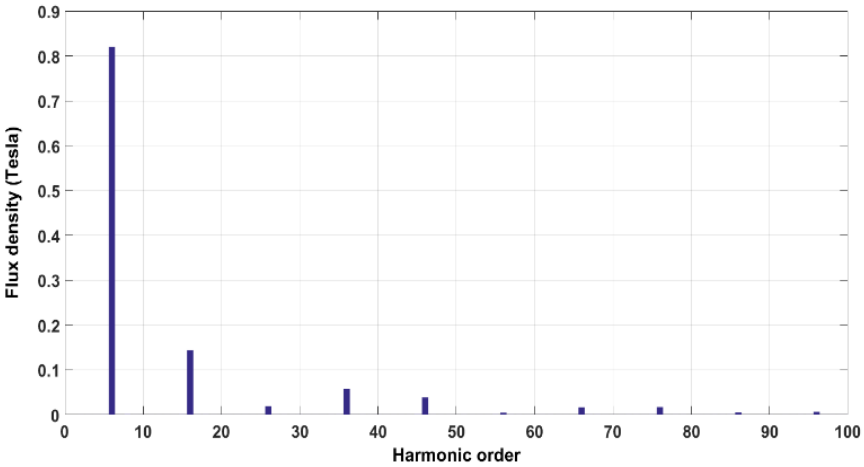


Figure 3-5 harmonic spectrum of airgap flux density

The influence of slot opening is an important factor in an IPM motor topology. For an SPM motor it is less important as the effective air gap is relatively large. Also, the influence of magnetic saturation is larger in IPMs than SPM configurations while the PM fringing flux is comparable [11]. Figure 3-6 shows the air gap flux density with slot opening effect and the harmonic content is shown in Figure 3-7.

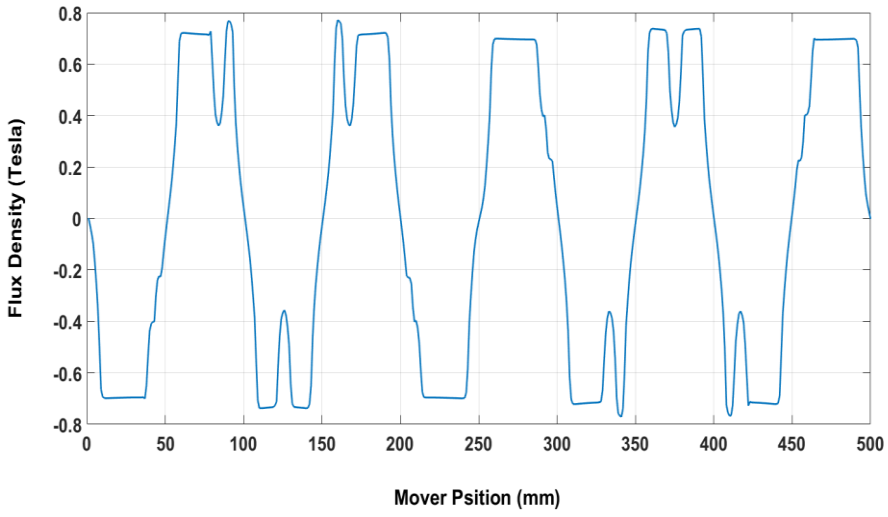


Figure 3-6 air gap flux density with slot opening effect

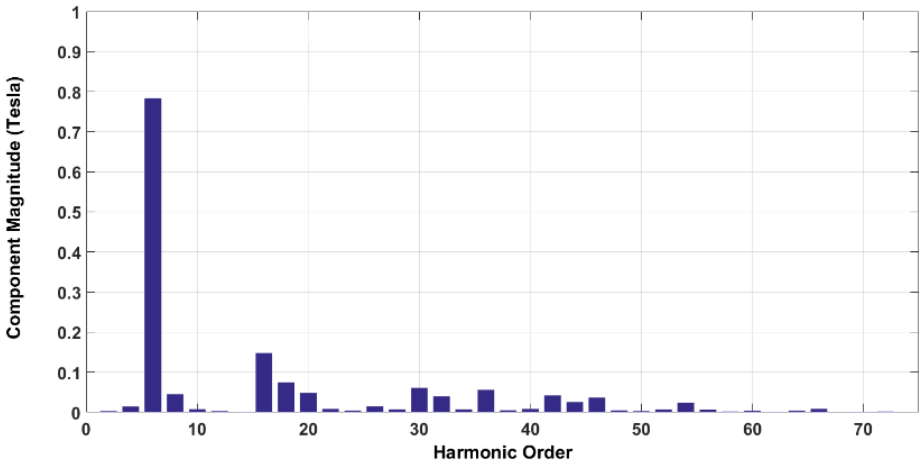


Figure 3-7 harmonics amplitude of airgap flux density

C. Magnetic reluctance network Method

However, while FE analyses methods provide an accurate method for field distribution, with a due account of saturation, non-linearity, etc., it is still considered as a time consuming method. Using analytical methods to solve the electromagnetic field inside the TLPM machine using mathematical model can facilitate the design optimization and procedures. The analytical solutions allow the prediction of the thrust force, the back *emf*, and the winding inductances with an acceptable level of accuracy [73].

Analytically, the magnitude of the air gap flux density can be calculated by using the common method of reluctance network in order to calculate approximattly the average value and the fundamental component of magnetic field density for TLPM machines. The calculation method is mainly based on the assumptions and hypothesis illustrated below [74, 75]:

1. Fringing flux is neglected.
2. Core material permeability (iron permeability) assumed to be infinity.

3. The axial length of the machines is infinite so that the field distribution is axially-symmetric and periodic in the z-direction.
4. The effect of slot opening is neglected.

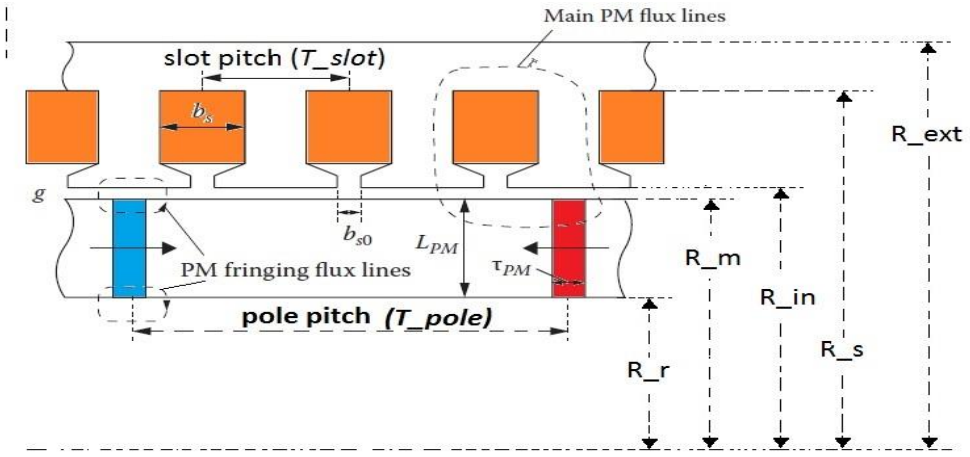


Figure 3-8 Regions of axially magnetised TLPM machine

Thus, considering Figure 3-8, B_{g_IPM} can be derived as shown in (3-8).

$$B_{g_IPM} = \frac{B_{rem}}{\mu_{rec}} \times \frac{\tau_m}{L_g + \left(\tau_m \cdot (\tau_{pole} - \tau_m) \cdot (R_m + R_{in}) / (2 \cdot \mu_{rec} \cdot (R_m^2 - R_r^2))\right)} \qquad (3\text{-}8)$$

In any analytical calculation and in order to avoid error in the calculation of $B_{g_IPM,}$ it becomes important to take the slot opening effects into r consideration. The slot opening may be considered by the Carter coefficient (K_c) (especially for semi-closed slots), and it can be calculated using (3-9). The fringing coefficient k_{fringe} can be successfully calculated by using the FE analysis. To estimate these factors, the TLPM motor of [7] has been modelled as seen in Figure 3-9. From this figure it can be seen that k_{fringe} is approximately equal to 8% of the total PM flux. The saturation coefficient $k_{saturate}$ can be also estimated within the range of 0.1-0.25 [11]. Considering these factors and by substituting (3-9) into (3-8), then (3-10) is obtained.

$$k_c = \frac{1}{1-\sigma_c \cdot \frac{\tau_{slot,open}}{\tau_{slot}}} \qquad (3\text{-}9)$$

$$\sigma_c = \frac{2}{\pi} \cdot \tan^{-1}\left(\frac{\tau_{slot}}{2 * L_g}\right) - \frac{1}{\pi} \cdot \frac{2 \cdot L_g}{\tau_{slot}} \cdot \ln\left(1 + \left(\frac{\tau_{slot}}{2 \cdot L_g}\right)^2\right)$$

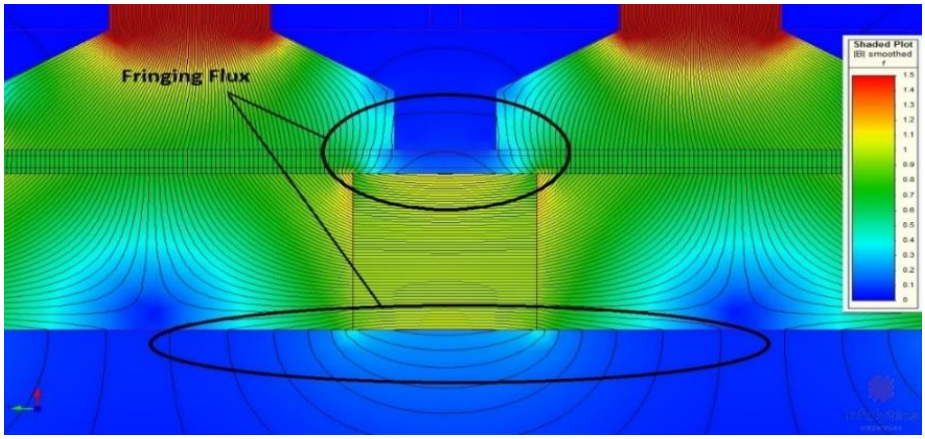


Figure 3-9 Air gap fringing flux

$$B_{g_IPM} = \frac{B_{rem}}{\mu_{rec}} \times \frac{\tau_{pm}}{L_{g_eq} + \left(\tau_m \cdot \tau_c \cdot (R_m + R_{in}) / (2 \cdot \mu_{rrec} \cdot (R_m^2 - R_r^2))\right)} \qquad (3\text{-}10)$$

$$\times \frac{1}{(1 + k_{fringe}) \cdot (1 + k_{saturate})}$$

$$L_{g_eq} = L_g \times k_c$$

The magnetic flux density is supposed to be rectangular shaped and the airgap flux density distribution produced by IPM magnets is approximately a quasi-square wave. The magnitude of the fundamental component B_{g1} can be calculated using (3-7). Consisting of all odd harmonic orders (n), the amplitudes of the flux density of nth order $B_{g(n)}$ can be calculated using (3-11) as shown in Figure 3-10.

$$B_g(n) = \frac{4}{\pi} \cdot B_{g_IPM} \cdot \frac{1}{n} \sin\left(\frac{\pi}{2} \cdot \frac{(\tau_{pole} - \tau_m)}{\tau_{pole}} \cdot n\right) \qquad (3\text{-}11)$$

$$n = 1, 3, 5, 7 \ldots$$

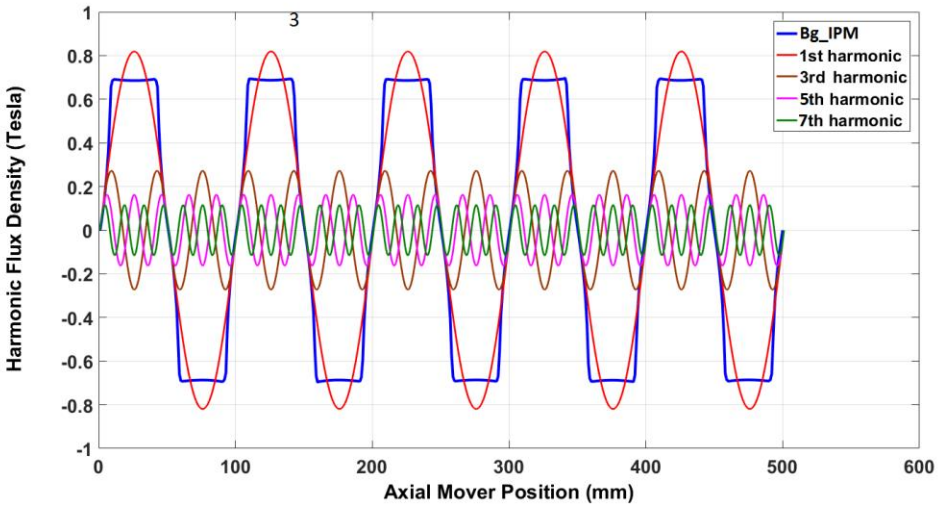


Figure 3-10 fundamental and harmonics components of air gap flux density

D. Subdomain Regions Model Method

For the sake of simplicity, the geometry of the analysed machines is considered to be made up of homogeneous layers or regions [11, 73, 76, 77]. The analysis is simplified by assuming a slot-less structure and the winding coils are located and distributed uniformly along the air gap region. The slot effect can be taken into consideration by considering the carter coefficient as explained in section (C). Figure 3-11 shows this topology with axially magnetized magnets separated by iron pole pieces using the simplification of slot-less structure [77].

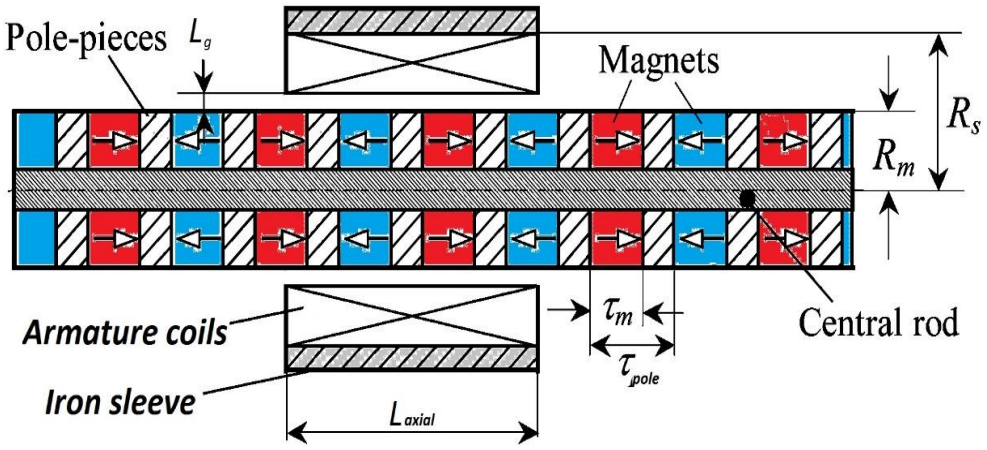


Figure 3-11 subdomains Machine Topology [77].

The magnetic field of the machine is divided into three regions: the air gap or winding region (Region I), the permanent-magnet region (Region II), and the shaft (non-magnetic material) region (Region III), as shown in Figure 3-12.

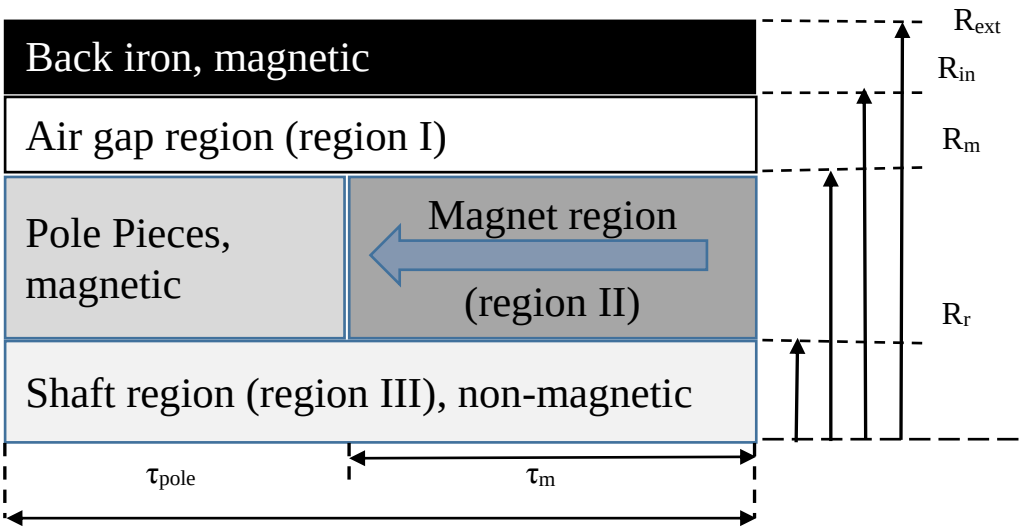


Figure 3-12 Subdomain Regions of Axial Magnetized TLPM machine [77].

The analytical expression of each region is obtained based on the solution of Maxwell differential equations by solving the magnetic vector potential *A* which may be represented in integral form with the hypothesis of no fringing flux, the core permeability is infinity, and the axial length of the machines is infinite.[11, 78-80]:

The governing equations of field distribution for each region in terms of *A* in cylindrical coordinate can be expressed as in (3-12), (3-13) and (3-14), where, M_z is the magnetization vector of the magnet along the z_axis direction and is given in (3-15).

In region I

$$\frac{\partial}{\partial z}\left(\frac{1}{r}\frac{\partial}{\partial z}(rA_{I\theta})\right)+\frac{\partial}{\partial r}\left(\frac{1}{r}\frac{\partial}{\partial r}(rA_{I\theta})\right)=0 \quad (3\text{-}12)$$

In region II

$$\frac{\partial}{\partial z}\left(\frac{1}{r}\frac{\partial}{\partial z}(rA_{II\theta})\right)+\frac{\partial}{\partial r}\left(\frac{1}{r}\frac{\partial}{\partial r}(rA_{II\theta})\right)=-\mu_o\nabla\times\vec{M}_z \quad (3\text{-}13)$$

In region III

$$\frac{\partial}{\partial z}\left(\frac{1}{r}\frac{\partial}{\partial z}(rA_{III\theta})\right)+\frac{\partial}{\partial r}\left(\frac{1}{r}\frac{\partial}{\partial r}(rA_{III\theta})\right)=0 \quad (3\text{-}14)$$

$$\vec{M}_z=\sum_{h=1}^{\infty}4*\frac{B_{rem}}{\mu_o\pi}\cdot\frac{1}{(2\cdot h-1)}\cdot\sin\left((2\cdot h-1)\cdot\frac{\pi}{2}\cdot\alpha_p\right)\cdot\cos\left((2\cdot h-1)\cdot\frac{\pi}{\tau_{pole}}\cdot z\right) \quad (3\text{-}15)$$

Where B_{rem} is the remanence magnetic flux density of the magnet, α_p is the magnet pitch ratio, μ_o is the absolute permeability of the free space and z is the axial position.

These equations are solved analytically for the radial component and axial component of B_g with boundary conditions to satisfy all the equations. The radial B_{Ir} and axial B_{Iz} component of the airgap (region I) flux density expressions are shown in (3-16), where *Besseli* and *Besselk* are the modified Bessel functions of the first kind and second kind respectively. The parameters a_{In} and b_{In} are harmonic dependent coefficients, and *n (n = 1, 2, 3...)* is the harmonic order, given in appendix A.

$$B_{Ir} = \sum_{n=1}^{\infty}\left[a_{In} * besseli\left(1, r\frac{\pi(2n-1)}{\tau_{pole}}\right) + b_{In} \times besselk\left(1, r\frac{\pi(2n-1)}{\tau_{pole}}\right)\right] \times \sin\left(\frac{\pi\ (2n-1)}{\tau_{pole}}\right) \quad (3\text{-}16)$$

$$B_{Iz} = \sum_{n=1}^{\infty}\left[a_{In} \times besseli\left(0, r\frac{\pi(2n-1)}{\tau_{pole}}\right) - b_{In} \times besselk\left(0, r\frac{\pi(2n-1)}{\tau_{pole}}\right)\right] \times \cos\left(\frac{\pi\ (2n-1)}{\tau_{pole}}\right) \quad (3\text{-}17)$$

Figure 3-13 represents the distribution of magnetization vector of the PMs. Figure 3-14, and Figure 3-15 represents the comparison between the analytical results and FE results for the selected machine [7] by applying a periodic boundary condition at the axial direction. It can be seen that, the analytical solutions agree extremely well with the FE results.

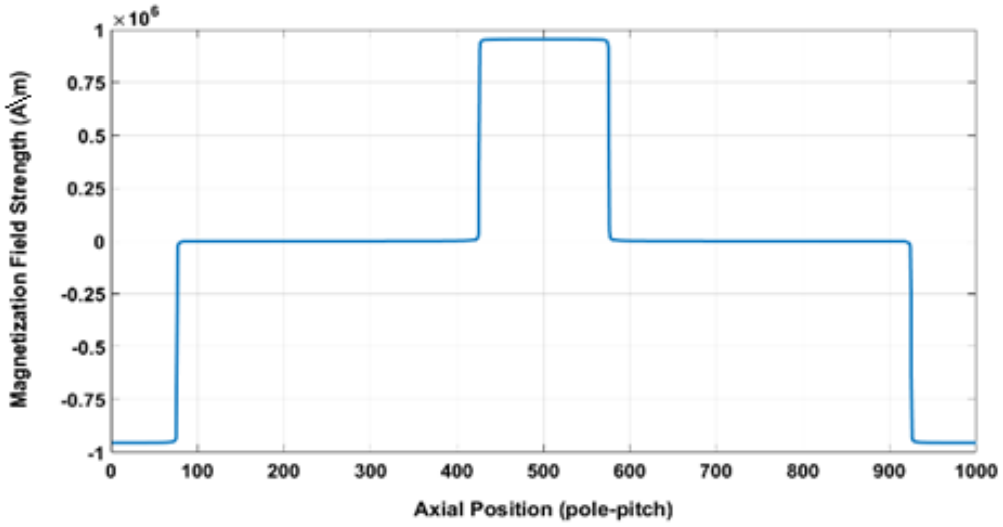


Figure 3-13 distribution of magnetization vector of axially magnetized machine

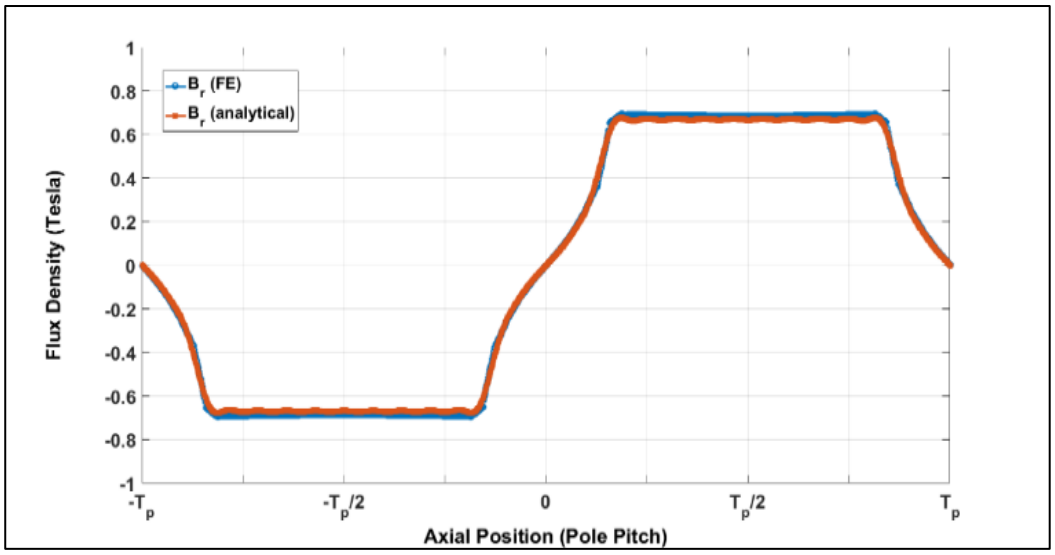


Figure 3-14 normal (radial) component of air gap field distribution

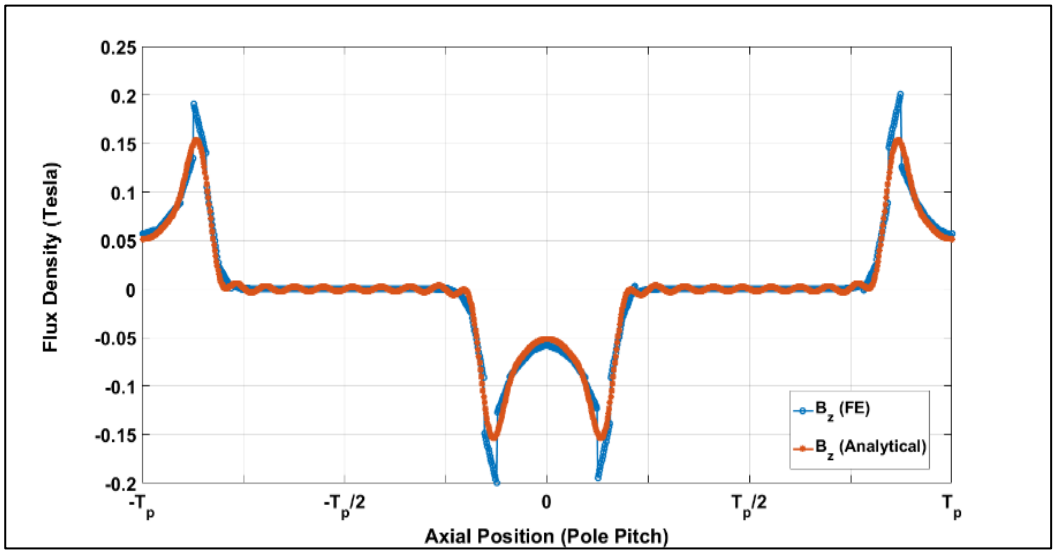


Figure 3-15 tangential (axial) component of air gap field distribution

3.4.2 No-load induced Voltage (Back *emf*)

According to Faraday's law of electromagnetic induction, the rate of change of flux linkage is equal to induced *emf*. This principle of induced voltage under flux variation is expressed as (3-18), where ϕ is the magnetic field in (Wb) and N_{turn} is the number of turns of the coil. The phase voltage can be found by adding the induced voltage of all coils in the phase [81].

$$emf = -N_{turn}\frac{d\phi}{dt} \tag{3-18}$$

Equation (3-19) shows the total induced *emf* , where all the harmonic components (*n*) of the air gap flux density are kept into account for a full pitch winding [82], and *t* is the time. The harmonics content of induced *emf* waveform depend on both the magnet topology and winding configurations.

$$emf = \sum_{n=1,3,5}^{\infty} emf_{coil}(t,n) \tag{3-19}$$

Fractional-slot windings have the advantage of reducing slot harmonics when compared to integral-slot windings [82, 83]. On the other hand, some slot-pole combinations with fractional-slot winding will lead to low fundamental winding factors (k_{w1}) [84, 85], since the induced voltages of the coils within the same phase winding are not identical in magnitude and phase angle. With this case, the scalar sum and the vector sum of coils voltages are not equal. So that, in order to achieve an accurate analytical calculation for the *emf,* the winding factor k_w has to be considered in all voltage calculations. k_w is equal to the product of distribution factor k_d and the coil span factor or pitch factor k_p [81, 83].

The complete analytical expression for no load induced *emf* is given in (3-20), where, k_{dn} and k_{pn} are the winding distribution factor and winding pitch factor of the n^{th} harmonic order and they are expressed in (3-21) and (3-22) respectively. R_{in} and R_s are the inner and outer radii of the coil, N_{turn} is number of series turns in each phase, q is the number of slot per phase per pole, m is the number of phases and τ_w is the width [81-84, 86].

$$emf_{phase} = v \sum_{n=1}^{\infty} \frac{4\pi N_{turn} \cdot k_{pn} \cdot k_{dn}}{(R_s - R_{in})} \cdot k_{rn} \cdot \cos\left(\frac{mn}{2} \cdot (z - \tau_w)\right) \tag{3-20}$$

$$k_{rn} = \int_{R_{in}}^{R_s} r \left[a_{In}\ besseli_1(mn \cdot r) + b_{In}\ besselk_1(mn \cdot r)\, dr\right.$$

$$k_{pn} = \sin\left(n \frac{\pi}{2.m.q}\right) \tag{3-21}$$

$$k_{dn} = \frac{\sin\left[n \cdot \pi \cdot b \cdot \left((m \cdot q - 1)/2 \cdot m \cdot q\right)\right]}{b \cdot \sin\left[n \cdot \pi \cdot \left((m \cdot q - 1)/2 \cdot m \cdot q\right)\right]} \tag{3-22}$$

Figure 3-16 shows the analytical and finite elements representation of the *emf* waveform. Figure 3-17 shows the fundamental component and harmonic spectrum of induced *emf* of one coil for one complete electrical cycle (one pole pair of movement) with mover speed equal to 0.1 m/sec and $N_{turn}=23$ turns as in [7] according to the application of selected machine.

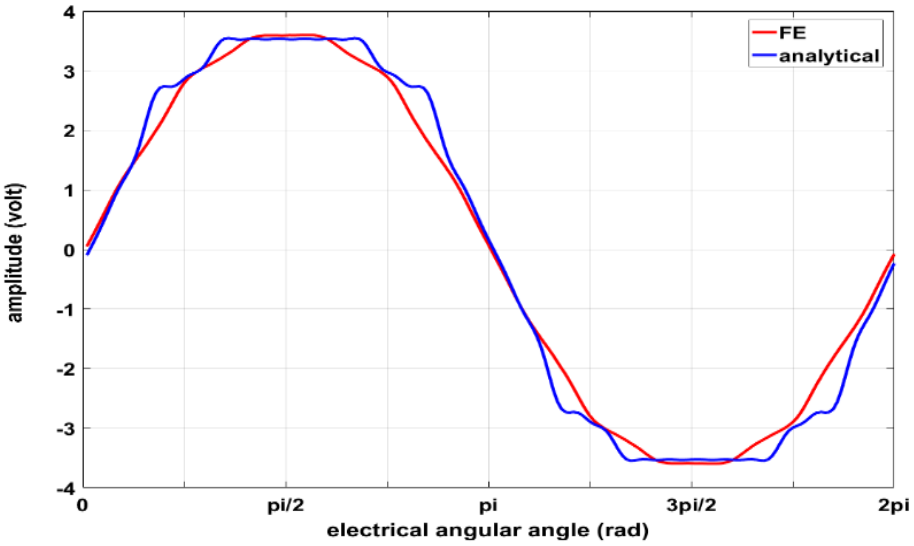


Figure 3-16 Comparison of (emf) *per phase per pole as a function of time*

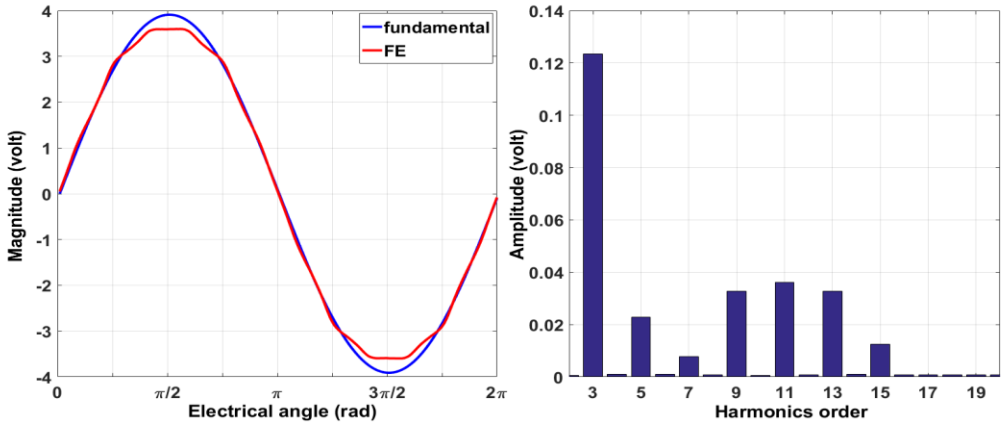


Figure 3-17 fundamental and harmonic spectrum of induced emf

3.4.3 *Armature Reaction and mmf* distribution

In classical machines with integral slot windings, the non-null *mmf* harmonics generated by each phase are generally of order *(2k+1)*, where *k = 1, 2, 3, 4 …* i.e. odd multiples of the number of poles pair [58]. However, this is not the case in machines made with fractional slot winding. In 12_slot, concentrated winding machines, the windings are not sinusoidally distributed and the resulting spatial *mmf* distribution per phase may be far from being sinusoidal [87]. The stator spatial *mmf* is rich in space harmonics [11] as shown in Figure 3-18. The end edge effect on the spatial *mmf* is eliminated, where the machine boundary is assumed to be infinity. When the stator winding is excited with a three-phase balanced set of sinusoidal currents, the stator *mmf* produces forward traveling harmonics of order 1, 4, 7, ... backward traveling harmonics of order 2, 5, 8, ... and zero triplen harmonics of order 0, 3, 6, …[88]. For 10-pole /12-slot machine combination, the thrust force is developed by the interaction of the fundamental component of the stator *mmf* with the fundamental component of the field of the permanent magnets, which is both of 5^{th} order.

The, *mmf* spectrum of the machine [7] has both even and odd harmonics order, far and close to the base frequency. Some of those harmonics which are of a lower frequency than the base frequency of the machine *mmf* are called sub-harmonics [89]. In synchronous TLPM motors, the fundamental component of *mmf,* whose order is equal to the number of pole pair travels synchronously with the mover speed. On the other hand, the asynchronous harmonic components of the *mmf* waveform advance in the air gap in certain speeds different from the mover speed, thus inducing eddy currents in both magnets and mover core [89, 90]. Figure 3-19 shows the *mmf* waveform of the selected machine calculated theoretically. The phase currents values are corresponding to the three phase current set at time instant of л/2. Figure 3-18 shows the *mmf* harmonics content of the selected machine in airgap region. It can be seen that all orders of the harmonic are contained in the *mmf* wave form and the fundamental component is represented in the 5^{th} order. The order of the "fundamental" component is thus equal to the number of pole pairs of the selected machine [91].

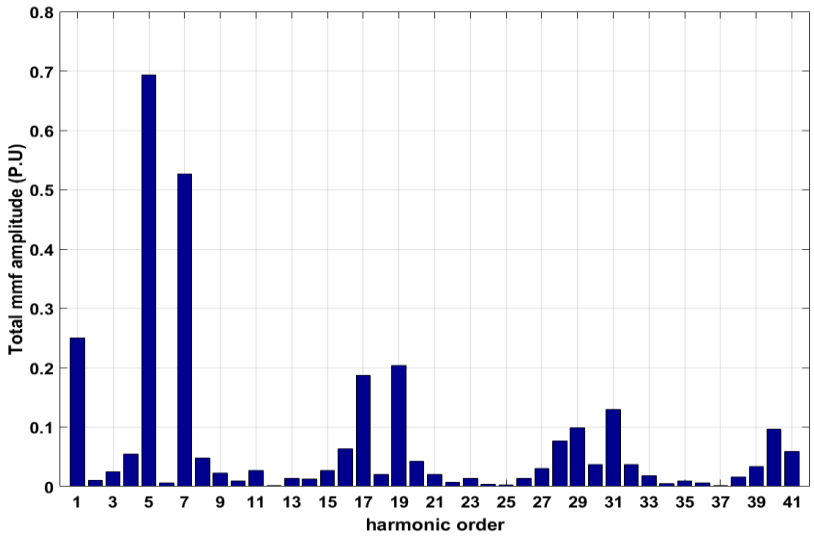


Figure 3-18 FFT of total airgap mmf generated from three phase current set at t= л/2

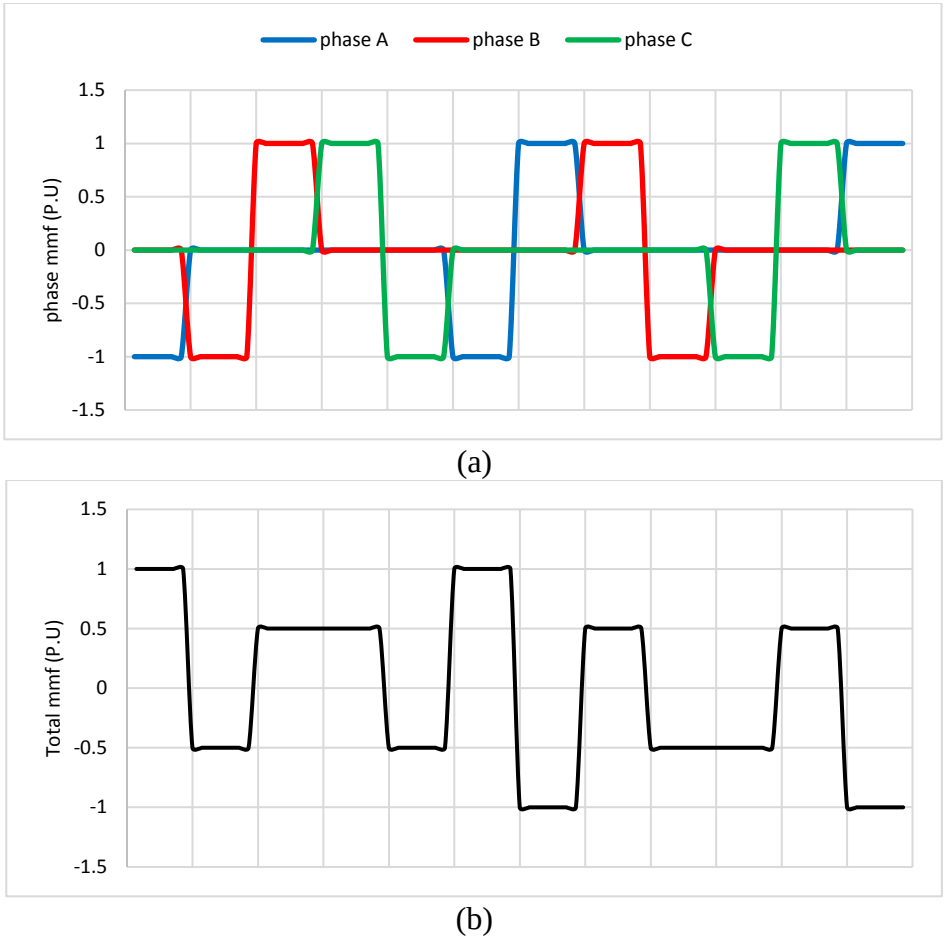


Figure 3-19 mmf waveform, (a) for each phase (A,B,C), (b) for total mmf waveform at t= ᴨ/2

3.4.4 Cogging force or Detent force

Generally, the major drawbacks of slotted TLPM machines are the cogging force and unbalance of the three phase magnetic path due to the finite edge and non-periodic waveform of the magnetic field. These are the main source of the ripple in the generated thrust force of TLPM machines [92] and it is much larger than those in the rotating machines. The cogging force is mainly divided into two main components, namely, the slot effect component and the end edge effect component. The common practice is to reduce the detent force by treating each component individually [93].

For the first component, because it is caused by the attraction force between the mover magnets and the teeth of the primary core. Several techniques have been used to reduce this kind of force ripple. Including the proper slot-pole combinations, it can be reduced by introducing asymmetric arrangements of magnets, magnet skewing factor, teeth skewing factor, semi-closed slot design and air-gap length variation [92]. The reduction of the second component can be achieved by end face modification as in [94, 95].

In fractional slot winding machines, the combination of slot/pole plays a significant role in selecting the desired cogging force amplitude and its frequency. The oscillation order of cogging force (F_{cog}) generated during one complete electrical cycle, i.e. $2\tau_{pole}$ moving distance, can be calculated by the (3-23), where LCM is the *least common multiple* of the number of poles and number of slots.

$$F_{cog} = \frac{LCM(N_{pole}\ ,\ N_{slot})}{N_{pole}/2} \qquad (3\text{-}23)$$

The amplitude of the generated F_{cog} completely depends on the variation of magnetic energy in the airgap due to the change of the magnetic circuit permeance caused by the positional relationship of the poles and slots [89]. The amplitude of the F_{cog} has a direct relationship with the frequency of F_{cog}. When the frequency of the cogging torque increases, the amplitude decreases according to the fact that magnetic power is changing more smoothly along the air gap. Therefore, a higher *least common multiplier LCM* of slot and pole integers determines lower F_{cog} effect [89, 96, 97].

For movement distance x equivalent to 2 τ_{pole}, the variation of F_{cog} acts on the mover shaft and caused by one single slot, can be expressed as in (3-24) [98]. Where $F_{cog(h)}$ is the magnitude of the h^{th} harmonics component of the cogging force, α is the relative angular displacement angle (rad) of the kth slot and ***k*** is the slot number. The single slot generated F_{cog} of the selected machine is shown in Figure 3-20.

$$F_{cog_slot}(x) = \sum_{h=1}^{\infty} F_{cog(h)} \sin\left(\frac{x \cdot h}{\tau_{pole}}\pi + \alpha\right) \qquad (3\text{-}24)$$

$$\alpha = \left[\pi \times \frac{N_{pole}}{N_{slot}}\right] \times k \qquad k = 1, 2, 3.....N_{slot}$$



Figure 3-20 Single slot cogging force for one complete cycle (pole pair)

For 10/12 slot-pole combination machines, the great common divider (*GCD)* value is equal to 2. Thus, the angular displacement angles α of the k^{th} slots of the machine have the relationship of (3-25), which is mean that the slot cogging force of the first ***6*** slots are identical in magnitude and phase with other ***6*** slots. Figure 3-21 shows the cogging force waveform of 1^{st} to 6^{th} slot for half electrical degree.

$$\alpha(k) = \alpha\left(k + \frac{N_{slot}}{GCD_{(10,12)}}\right) \qquad (3\text{-}25)$$

$$k = 1, 2, 3 \ldots \frac{N_{slot}}{GCD(10,12)}$$

The position-varying cogging force generated from ***k*** slots, for a complete electrical period is expressed as:

$$F_{cog} = \sum_{k=1}^{N_{slot}} \sum_{h=1}^{\infty} F_{slot(k,h)}(x) \qquad (3\text{-}26)$$

$$x = \{0 \rightarrow 2 \cdot \tau_{pole}\}$$

The cogging force of a LPM is the summation of these forces due to all slots of the machine [99] as shown in Figure 3-22.

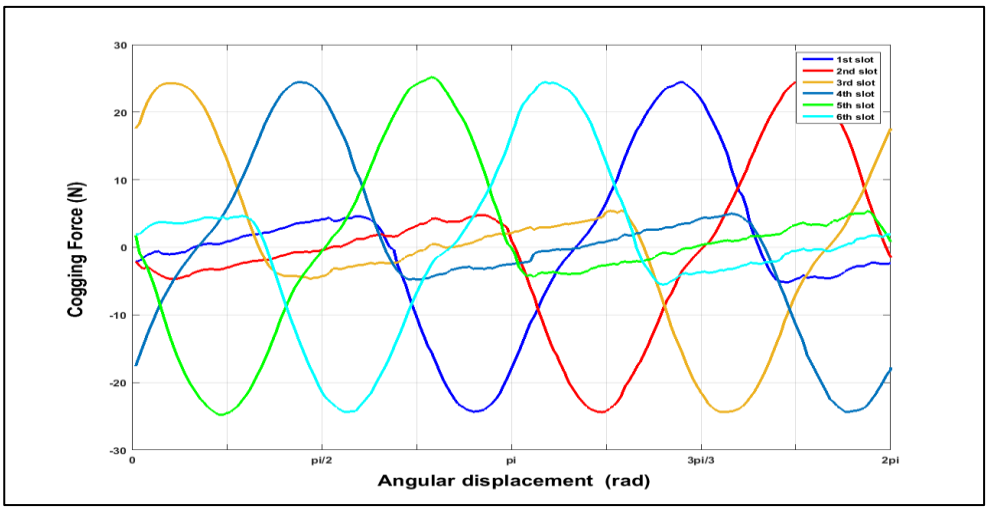


Figure 3-21 Slotting cogging force of 6 slots for half electrical cycle

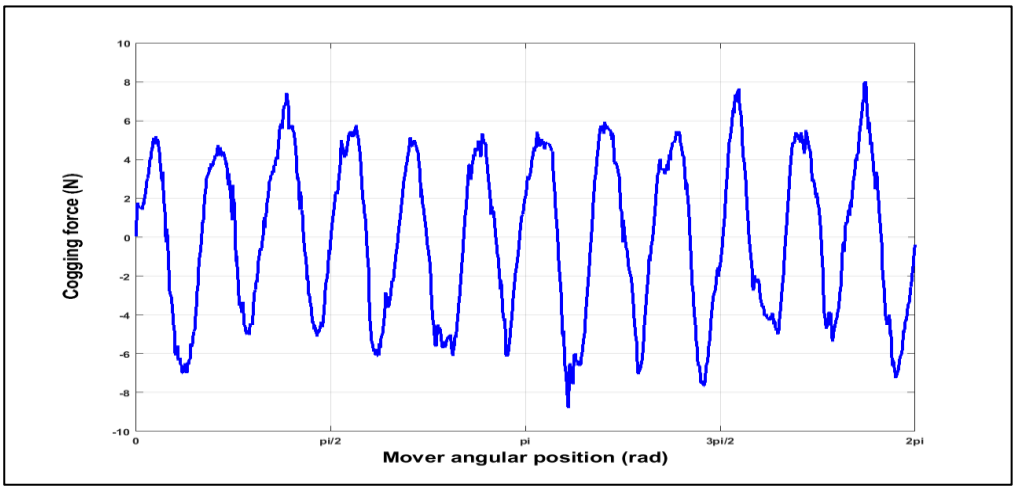


Figure 3-22 Cogging force of 12 slot/10 pole machine for one pole pair

3.4.5 Inductances

To simplify control strategies and to accurately predict the force or torque-speed characteristics of PM machine, various methods of flux linkages and inductances calculation, are available, such as Constant Parameter Method and Partial-Coupling Method [100]. However, although the first method is simple and easy to implement, the error in the calculated performance may be relatively high, especially when the machine is operating under the condition of high electric loading and high magnetic saturation level.

To improve the accuracy of the performance prediction, the second method is used. In this method, the influence of the armature reaction due to q-axis current on the PM flux-linkage is taken into consideration, as well as the influence of the d-axis and q-axis currents on the d-axis and q-axis inductances, respectively and to some extent, the influence of magnetic saturation [100]. Equations (3-27) and (3-28) describe this method for d-axis and q-axis inductances calculation, where $\Psi_q(I_d=0)$ is the q-axis component of the total flux linkage when $I_d=0$ and $\Psi_d(I_q=0)$ is the d-axis component of total flux linkage when $I_q=0$. The parameters $\Psi_{d_PM}(0)$ and $\Psi_{q_PM}(0)$ are the d-axis and q-axis components of the PM flux linkage at no load condition respectively.

$$L_d = \frac{\Psi_d(I_q = 0) - \Psi_{d_PM}(0)}{I_d} \qquad (3\text{-}27)$$

$$L_q = \frac{\Psi_q(I_d = 0) - \Psi_{q_PM}(0)}{I_q} \qquad (3\text{-}28)$$

Figure 3-23, Figure 3-24 and Figure 3-25 show the armature currents, flux linkage, and inductances at machine half load condition respectively. Figure 3-26 shows the variation of the d-axis and q-axis inductances for different armature currents.

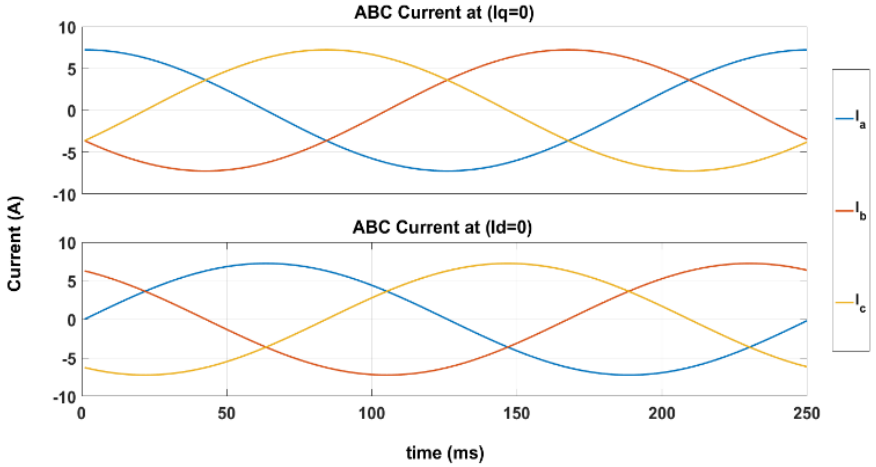


Figure 3-23 Armature current at $I_a = I_d$ and $I_a = I_q$

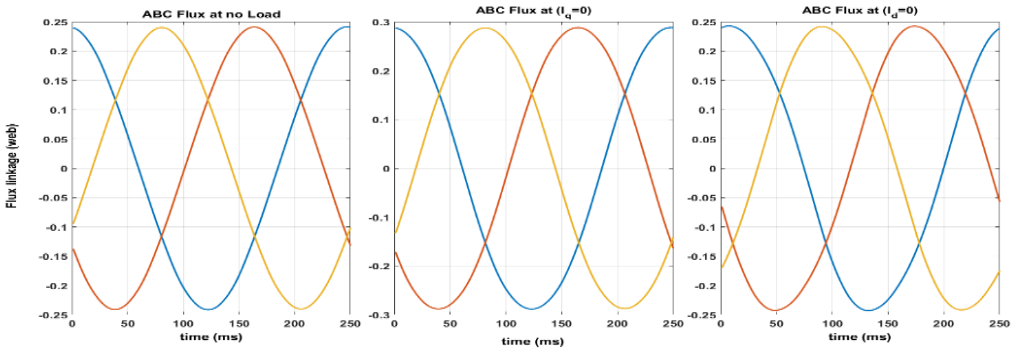


Figure 3-24 three phase flux linkage at $I_a = 0$, $I_a = I_q$, $I_a = I_d$

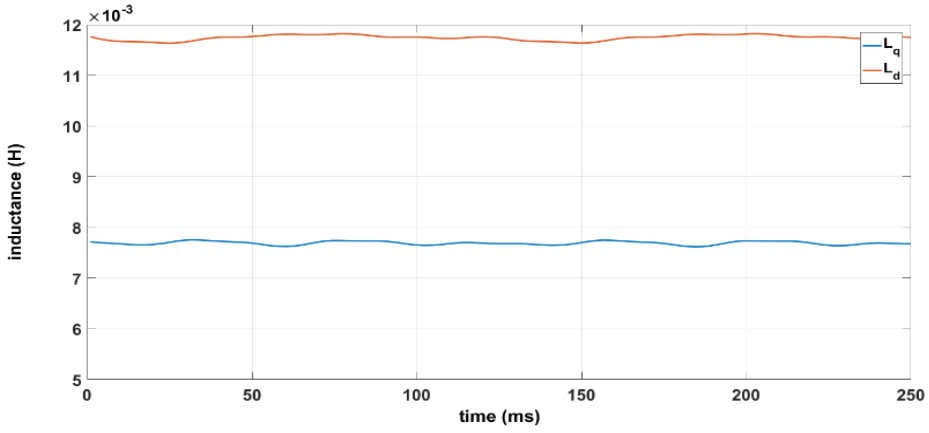


Figure 3-25 d-axis and q-axis inductances at armature current = 5 Amp

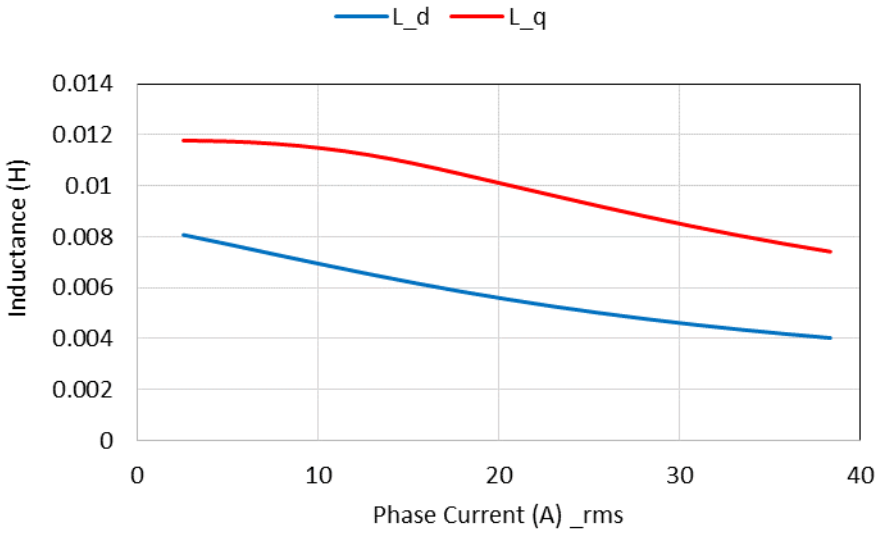


Figure 3-26 Variation of phase d-q inductances with different armature current

3.4.6 Thrust Force

Based on Maxwell stress tensor method, when each phase is fed with a sinusoidal current, the main thrust force acting on the armature or mover results from the interaction between the winding field and the PM field can be calculated [101].

Equation (3-29) represents the principle of the generated force for one coil over the winding volume of the machine for a slot-less machine, where J is the current density of the winding, and V is the coil volume and τ_w is the winding width, the parameters R_{in} and R_{ext} are the inner and outer radii of the stator as shown in Figure 3-27. This permits to determine the shape and the peak force of a motor with mover position (z) [73].

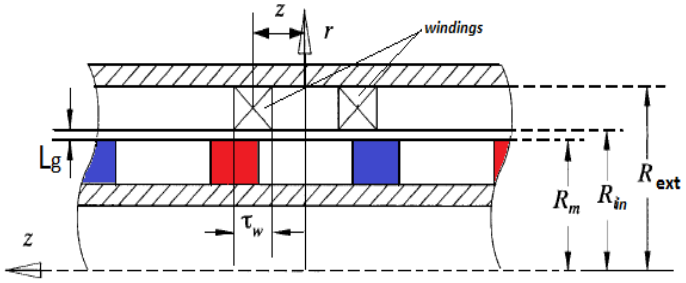


Figure 3-27 winding distribution

$$F = \int_V (J \times B) dV$$

$$F = \int_{z-\tau_w/2}^{z+\tau_w/2} \int_{R_{in}}^{R_{ext}} 2 \cdot \pi \cdot r \cdot J \cdot B_{Ir}(r,z)\, dr\, dz \qquad (3\text{-}29)$$

The analytical expression for force production described in [73, 86, 102] is given in (3-30), where F_1, is the constant thrust force due to the fundamental component of magnetic field and F_n and F_h are the harmonic dependant coefficients given in appendix B, and z is the linear displacement distance.

$$F = F_1 + \sum_n^{\infty} F_n \cos\left[(2n-2)\left(\frac{\pi \cdot z}{\tau_{pole}}\right)\right] + \sum_h^{\infty} F_h \cos\left[(2h-5)\left(\frac{\pi \cdot z}{\tau_{pole}}\right)\right] \qquad (3\text{-}30)$$

$$n = 4, 7, 10, \ldots$$
$$h = 3, 6, 9, \ldots$$

The output force of the TLPM machine is a combination of different components; (1) cogging force, (2) higher harmonics of electromagnetic synchronous force and (3) higher harmonics of electromagnetic reluctance force. These components appear in the force waveform, and they can be represented by a force ripple factor as shown in (3-31) [73, 86, 103].

$$f_{ripple} = \frac{\sqrt{\sum F_k^2}}{F_1} \qquad (3\text{-}31)$$

Figure 3-28 shows the results from analytical calculation for the generated force for the selected TLPM machine according to (3-30), with the assumption of slot-less stator configuration. The total thrust force of the machine given in [7] is shown in Figure 3-29, where the stator slot effects are included, with the assumption of infinite axial length at rated current density and rated speed. The results are calculated over one complete τ_{pole} of movement with balanced three-phase sinusoidal supply currents.

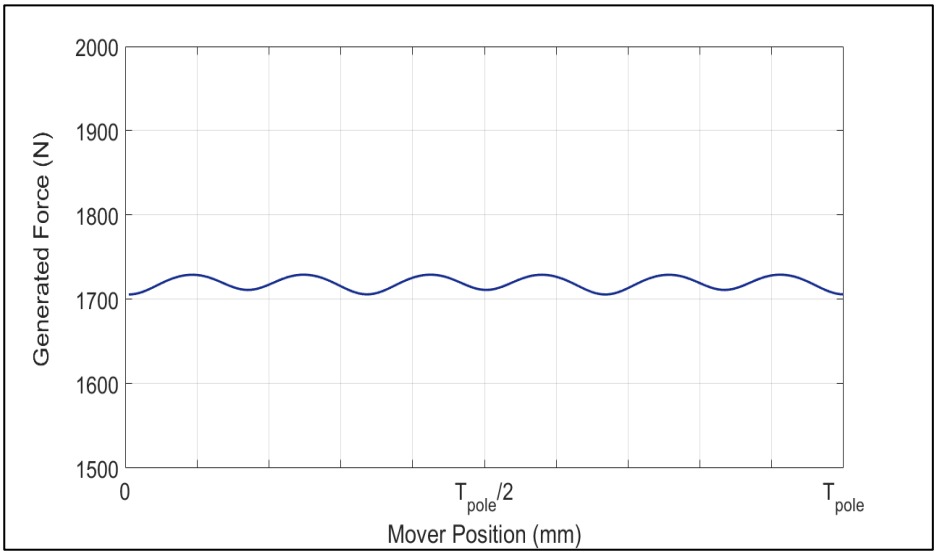


Figure 3-28 Analytical calculation of generated force of the TLPM motor

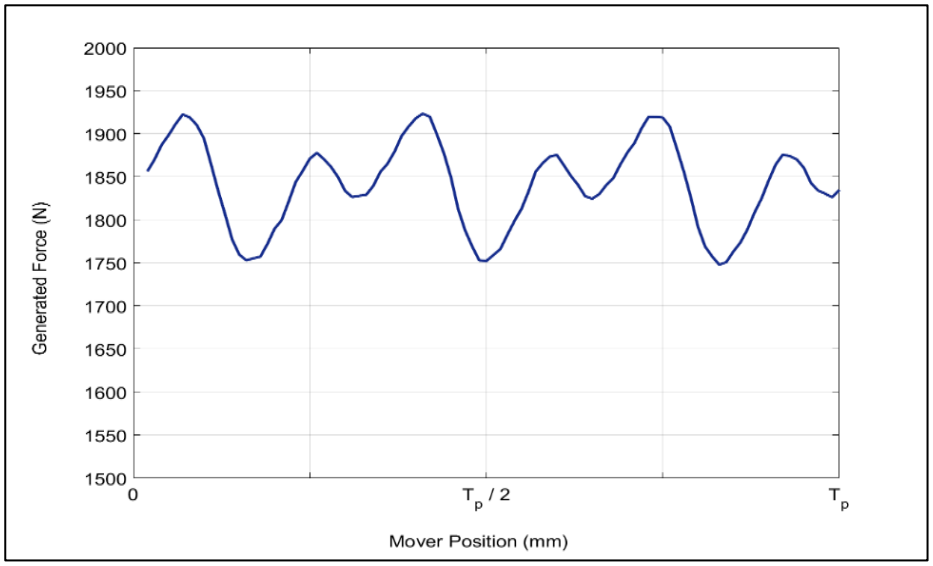


Figure 3-29 FE calculation of generated force of the TLPM motor

3.4.7 Thermal model

The rated power, or the maximum reachable power, of the electrical machines are generally depending on different factors; the area of the outer surface, the cooling method and the thermal class of materials used as well as the rated current and speed on the application. In general, the heat losses of the TLPM machine have to be dissipated through the outer surface of the machine. For a certain volume, the heat flow is limited by the geometrical design and usually define as object specific heat losses. The dissipation surface increases linearly with the machine diameter, which is restricted in most aerospace application [60, 104].

Heat transfer in the solid parts of the TLPM machine is governed by the thermal conductivity factor of these parts with is called heat conduction, while the heat transfer from the machine parts to the surrounding medium is governed by the thermal convection factor of the object which is called heat dissipation due to heat convection [104].

To model the effect of thermal conduction, the TLPM motor structure is simplified in such a way that the thermal conductance of each machine parts are represented by annulus segments. Figure 3-30 shows segment sample for the TLPM machine, where $\dot{\Psi}$ the heat flow or heat dissipation and it can be determined by (3-32), where G is the thermal conductance of the object and ΔT is the temperature difference along the heat flow.

$$\dot{\Psi} = G \times \Delta T \qquad (3\text{-}32)$$

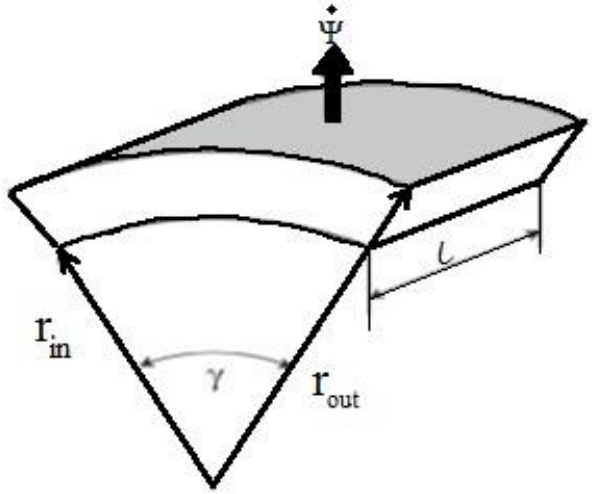


Figure 3-30 Segment of an annulus.[104]

The thermal conductance for a segment of an annulus is given in (3-33), where r_{in} and r_{out} are the inner and outer radii, respectively, and γ is the angular width (in radians) of the annulus.

$$G = \lambda \frac{\gamma \cdot l}{\ln(r_{out}/r_{in})} \qquad (3\text{-}33)$$

Generally, thermal analysis can be divided into two basic model types; analytical (or limped-circuit) model and numerical (FE) model [105-107]. The most important advantages of the analytical model is being very fast to calculate the performance of thermal network. This can be gained with the cost of low accuracy which numerical method can offer. However, finely discretized models can be built to increase the calculation accuracy of the analytical method [108].

The principle of the analytical method is based on the analogy between heat-transfer networks and electrical networks; the analysis consists in the calculation of conduction, convection, and radiation resistances for different parts of the electrical machine construction [104, 105, 108].

The conductive heat transfer network has been modelled in both radial and axial direction with the assumption of no heat flow in the tangential direction. A constant temperature is set at the outer surfaces of the machine as boundary conditions. A symmetry boundary condition is applied in the axial direction at the ends of the one slot pitch (τ_{slot}).

The general form of a thermal resistance R_{th} which describing the conductive heat transfer in one dimension is given in (3-34) [108], where L is the length of the body in the heat flow direction, λ is the thermal conductivity, and A is the cross-sectional area.

$$R_{th} = \frac{L}{\lambda \cdot A} \qquad (3\text{-}34)$$

Generally, the parts of a tubular machine are of cylindrical form, which enables the use of the simplified T-equivalent thermal network circuit that can be used to build and define the multiple-node configurations of thermal resistances [108]. Figure 3-31 shows the T_equivalent thermal network circuit for a single discretised part in two directions (radial and axial).

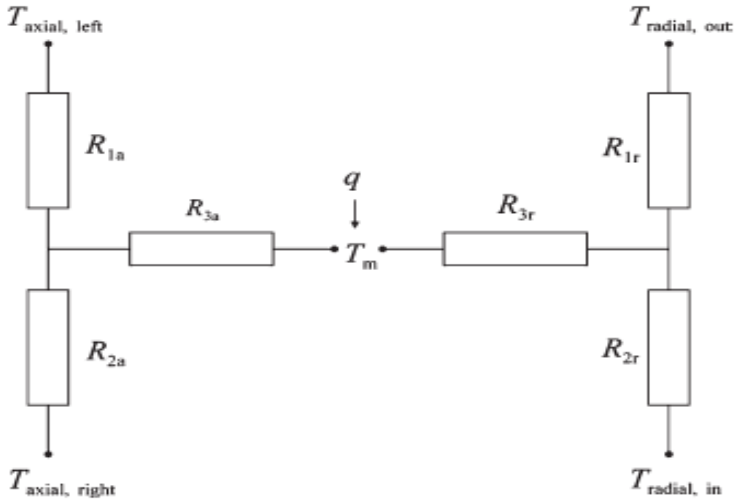


Figure 3-31 Independent axial and radial thermal networks [108].

The water cooled TLPM machine of [7] has been thermally modelled using the T_equivalent network model shown in Figure C-1 given in appendix C. The circuit parameters have been calculated using cylindrical coordinate system for thermal conductivity equations [104].

3.5 FINITE ELEMENT (FE); MODELLING, SOLVING AND ANALYSIS

In the previous section, the selected machine has been modelled and analysed analytically. In this section, more accurate analyses are presented using Finite Element (FE) analyses.

3.5.1 Introduction to FE

The most powerful tool available to simulate the selected machines magnetically is the finite element method, used to compute dynamic and steady state conditions of the machine including two_dimensional (2D) and three_dimensional (3D) analyses. However, the accuracy of the solution depends upon the nature of the magnetic field and many other factors.

2D analysis ideally refers to translational geometry, which means that the object has a constant cross-sectional shape and is generated by translating such shape in a fixed direction (usually in Z-axis). Rotating electrical machines are often represented using this method, and so can many other devices, such as transformers, whenever there are no curved or changes in cross-sectional area of the machine. Generally, such 2D approximation neglects fringing and leakage fields in the third dimension and the end winding effect [71].

Objects with rotational geometry, i.e. which have a shape formed by rotation around an axis of rotation, are usually described in cylindrical coordinates (polar coordinate). The rotated shape is then defined in an (R, Z, θ) system, which is corresponding to X-Y plane in 2D system and makes an angle θ in the 3rd direction with the X-axis. Such shapes require different methods for calculating quantities such as force and inductance. Thus, it is highly recommended to represent and model such structure with a 3D objects, such as TLPM motor [109].

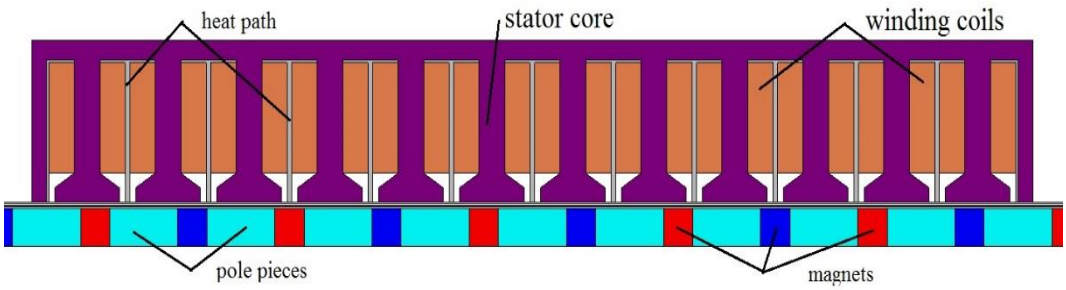
Most published papers present 2D models for TLPM motors, where the electromagnetic field, forces, and motion are analysed easily and efficiently because TLPM motor has naturally no end windings and the tangential component of the magnetic field ($B_{I\theta}$) is approximately equal to zero (in cylindrical coordinate) and the magnetic vector potential $\boldsymbol{A}$, has only the θ component A_{θ}.

However, due to the rotational geometry construction and the axial lamination structure of TLPM motor along the axis of rotation, it is highly recommended to model TLPM motors with a 3D model in order to obtain the representation of lamination sheets and the air voids between sheets which is varying with stator radius, then obtain accurate analyses results. The 3D model offers the ability to represent this actual lamination and any machine with no-axisymmetric bodies of revolution.

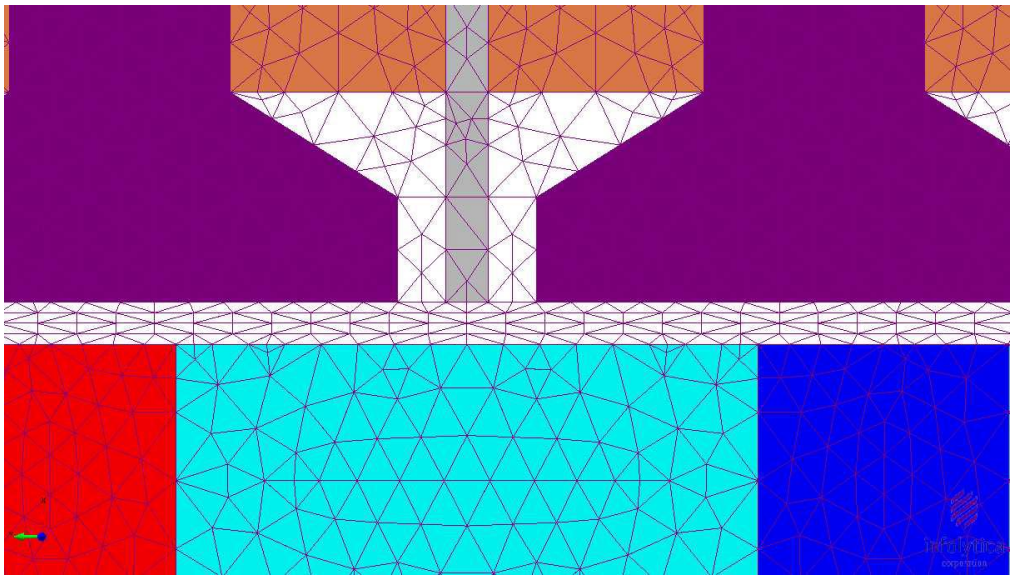
3.5.2 Modelling the Selected Machines with (2D and 3D)

The selected machine of [7] has been modelled with 2D and 3D, FE techniques and a highly refined model in order to deeply investigate the machine performance such

as force density and machine losses. Figure 3-32 (a) shows a cross-section of the 2D model of the bench-mark TLPM motor and Figure 3-32 (b) shows the refine mesh size for the high accurate analyses. Figure 3-33 shows the full 3D model of the machine. In many cases, for the 3D models, the boundary conditions are used to reduce the model size and the solving time. In these analyses and for high realistic results, the 3D model had been built with complete, 360^{o} of model rotation, which that means, the TLPM machine has been modelled completely with the cost of high time consuming. These models are then used for a full analysis of the bench-mark machine as shown in the next sections.



(a)



(b)

Figure 3-32 TLPM motor; (a) 2D model, (b) refine mesh

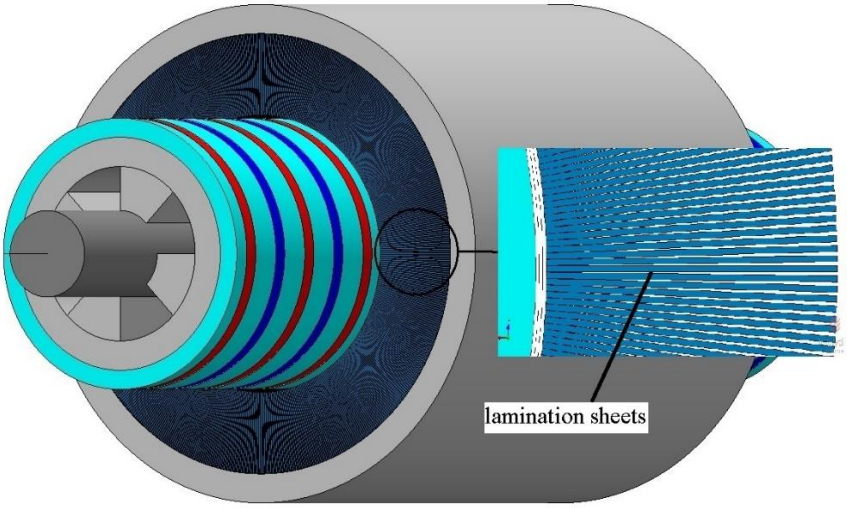


Figure 3-33 TLPM motor; 3D model with lamination stator representation

All the materials included in the model were considered to be isotropic and homogenous. The magnetic and electric properties, such as, resistivity, permeability and specific losses for the materials used in the main machine parts are obtained from experimental tests carried out using high-tech magnetic measurement system "MPG 200 D" [110], and the material samples are provided from the suppliers. The physical properties, such as, specific heat capacity, thermal conductivity and mass density were taken from material data sheets such as [111-113].

The thickness of the lamination sheets plays a significant role in the improving of the machine core losses. On contrast, the manufacturing difficulties are increase directly with the decreases of the stator lamination sheets thickness. Thus, the lamination material of the stator core has been selected base on its high magnetic saturation level, low power losses, low manufacturing difficulties and low cost. The magnetic characteristics of the stator lamination material are reported in appendix D, Table D- 3, Figure D- 2. Table 3-3 shows the physical properties of the materials which are used in this model.

Table 3-3 Material properties of the TLPM motor

Machine part	*material*	*properties*	*Units*
Stator	*LamSteel: Transil270-35*	*Thermal conductivity : 49.8* *Specific heat : 448* *Mass density : 7600* *Sheet thickness : 0.35*	*W/(m.C)* *J /(kg.C)* *kg/m^3* *mm*
Pole pieces	*SolidSteel: EN8*	*Thermal conductivity : 51.9* *Specific heat : 486* *Mass density : 7716* *Electric resistivity@40 : 2.21e-07*	*W/(m.C)* *J/(kg.C)* *kg/m^3* *Ohm.m*
Magnets	*Arnold N40UH*	*Thermal conductivity : 6.3965* *Specific heat : 460.548* *Mass density : 7500* *Electric resistivity@40 : 1.8e-06*	*W/(m.C)* *J/(kg.C)* *kg/m^3* *Ohm.m*
Mover support, stator housing and heat path	*Aluminium*	*Thermal conductivity : 204* *Specific heat : 896* *Mass density : 2707* *Electric resistivity@40 : 2.63e-8*	*W/(m.C)* *J/(kg.C)* *kg/m^3* *Ohm.m*

3.5.3 Magnetic Field Distribution

In electrical machines, the magnetic flux path has different fashions. The magnetic flux travels radially and tangentially in drum type rotating machines, while it travels axially and tangentially in disk type rotating machines. While, the magnetic flux travels radially and axially in tubular type of linear machines. In general, it is finding that in all of machine types, the variation of the magnetic flux is in the same direction of the moving parts. Hence, the variation of the main flux can be considered as a rotating nature of motion such as in rotating machines and axially nature of motion such as that of linear machine [12, 66].

For electrical machines that employ a non-standard configuration such as the tubular machine of Figure 3-33, the magnetic circuit is quite different when compared to standard rotary machines. Figure 3-34 and Figure 3-35 show the magnetic flux direction for the rotating machine and linear machine respectively.

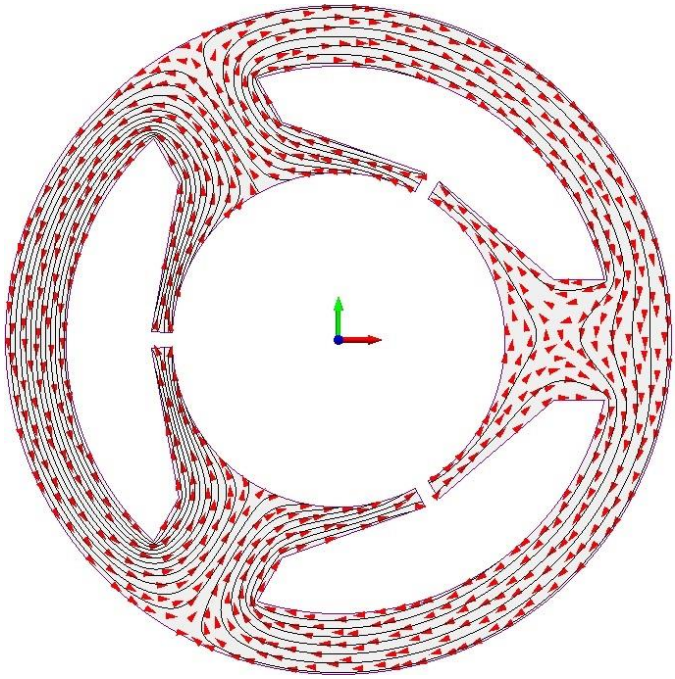


Figure 3-34 3D flux lines and direction of rotating machines

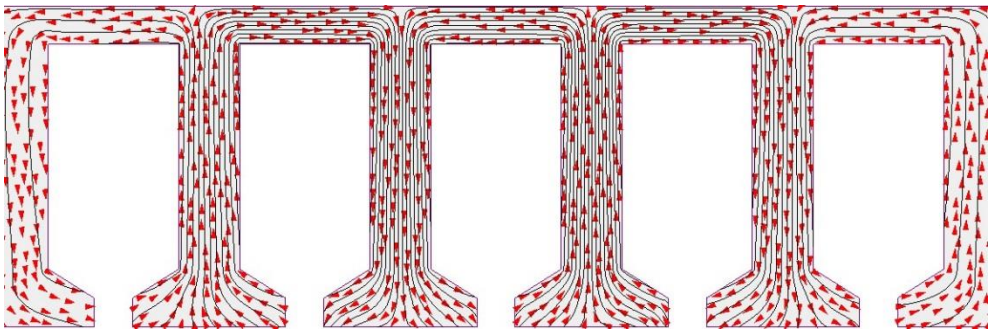


Figure 3-35 3D flux lines and direction of linear machines

3.5.4 Machine losses

The TLPM motor has been modelled and solved using 2D and 3D FE models. For the stator part, the 2D averaged time hysteresis losses is approximately equal to the 3D losses. This similarity gives an indication that, with laminated material, the results are very similar , mainly because they both use the approximated Steinmetz equation and its coefficients are depending on the material specific losses data applied to the FE model [114].

Ohmic losses, due to eddy current, normally appear in solid parts, such as the stator housing and the mover support because they are made from electrically-conductive materials as shown in Table 3-3. Figure 3-36 shows the obtained results of Ohmic losses for these parts of the TLPM machine at rated speed of 100 mm/sec and rated current density of 17 A/mm^2. It can be observed that the 3D results are higher than 2D results. This is true because the eddy current losses inside solid materials is a 3-dimensional problem.

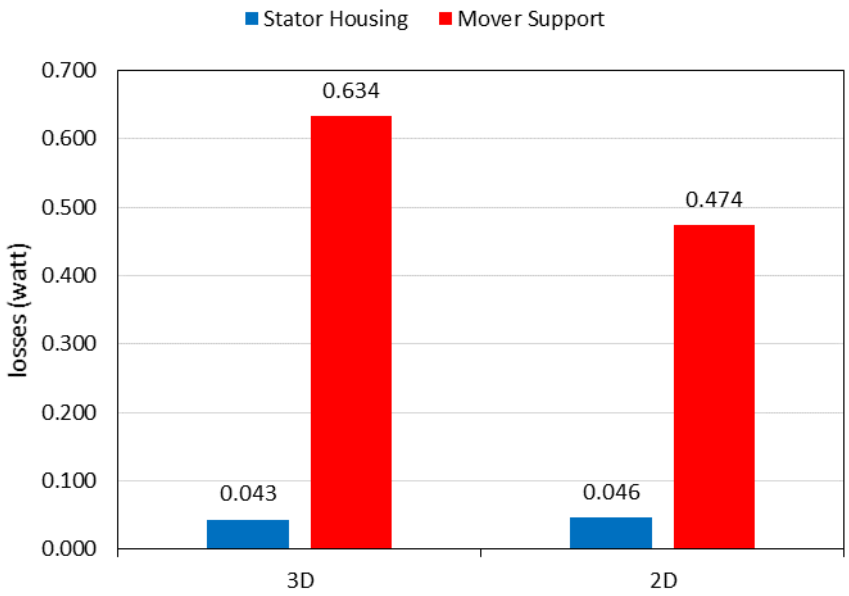


Figure 3-36 TLPM motor: eddy current losses of different machine parts

3.5.5 Machine Performance

As shown in Figure 3-37, the effect of an exact modelling of the electric machine also influences the generated force. The 3D model results in a smaller force; this is mainly due to the effect of the stator f_{stack}, where the effective volume of the stator material cannot be represented in the 2D model, due to the voids exist between the lamination sheets. Figure 3-37 shows the instantaneous generated force obtained

from the 2D and 3D models of the TLPM motor at rated condition of [7, 10]. Figure 3-38 shows the comparison between the simulation results with experimental results of the bench-mark machine at rated current density of 17 A/mm^2. As expected, the 3D results are much closer to the experimental test than the 2D results [114].

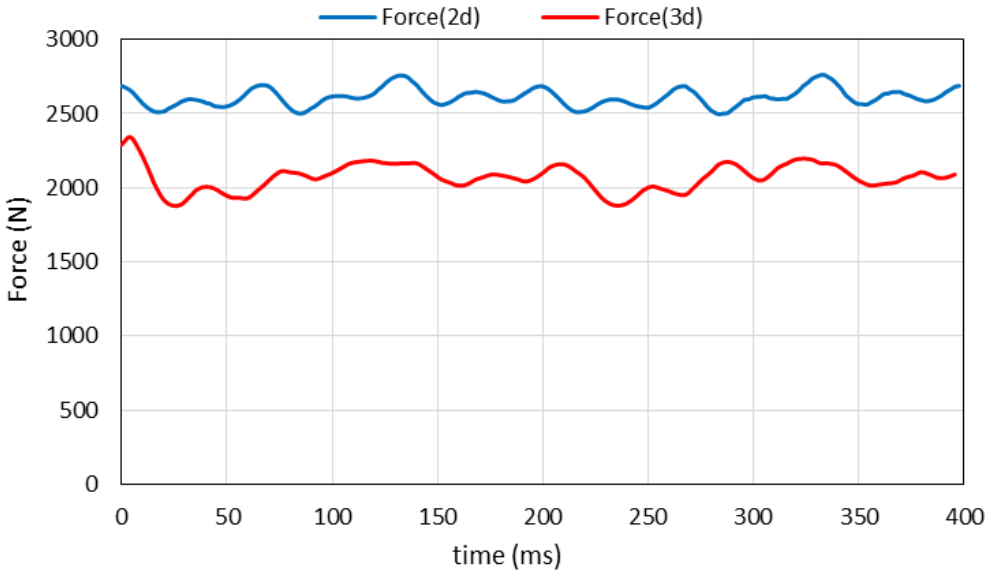


Figure 3-37 TLPM motor: generated force with 2D and 3D models

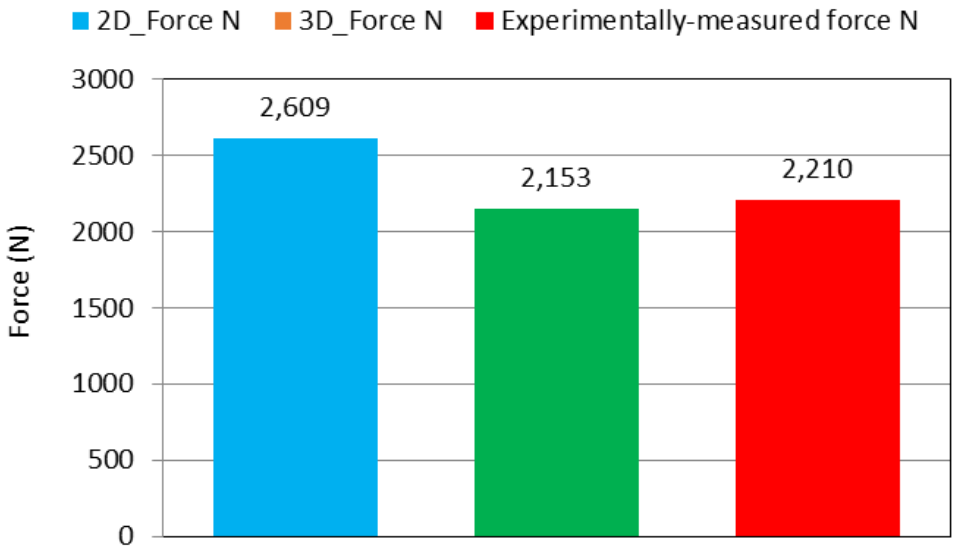


Figure 3-38 TLPM Motor: production Force

The full load voltage, at rated speed of 100 mm/s, and rated current, for both solving methods (2E and 3D), is shown in Figure 3-39. It can be seen that the results are almost the same except for the 3D model gives 4.5% higher in amplitude.

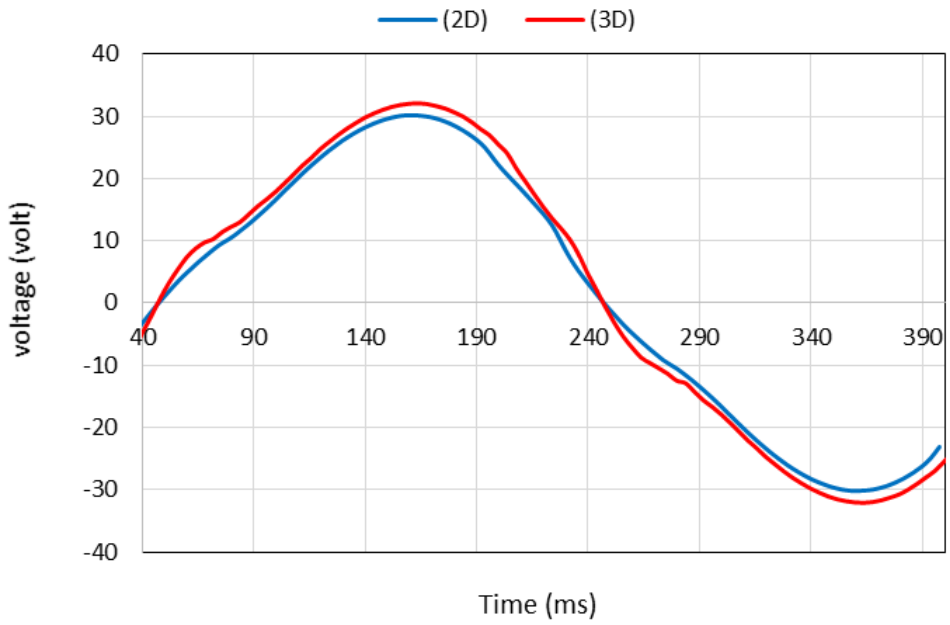


Figure 3-39 TLPM motor: full load phase voltage of 2D and 3D models

3.6 DIFFERENT STATOR CONFIGURATIONS; COMPARISON

In Chapter 2, various stator configurations and materials which can be used to reduce the manufacturing cost and difficulties of TLPM motors were introduced. In this Section, the most promising methods are analysed.

3.6.1 Soft magnetic composites (SMC) stator

To investigate this option, a 3D FE model of the TLPM motor has been built using SMC material called Somaloy 1000 3P for the stator core. The magnetic characteristics and the physical properties of SMC material are given in Table D- 1 and Table D- 2 respectively and given in Appendix D. The model was solved at the

same rated operating current of [7] for different frequencies. The results are shown in Figure 3-40, where the values are normalized with the base values being those of the original laminated configuration. From Figure 3-40, it can be observed that the generated force is very close to that of original machine with a maximum reduction of 2.5%.

While the relative permeability of the SMC is less than that of the laminated material, the generated force is comparable mainly due to the lamination f_{stack} required for the original machine, which is not present when the 'solid' SMC material is used. On the other hand, iron power losses are much lower than for the laminated stator version especially at low frequencies, where negligible values appear. It can be seen from Figure 3-40 that a discrepancy of 20% from the results of the original machine value appear at frequency equal to 25Hz. This indicates the SMC material's potential in terms of its use for the stator of the TLPM motor.

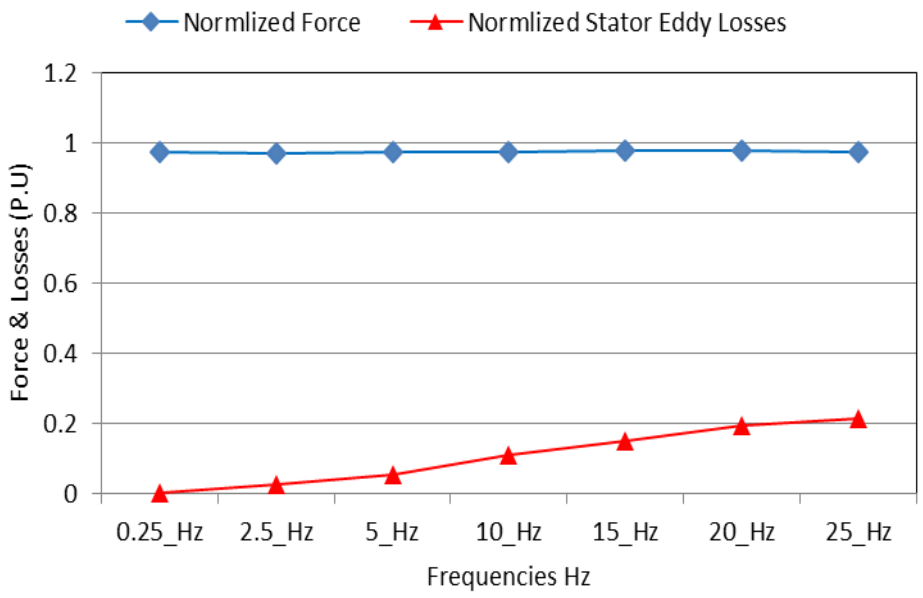
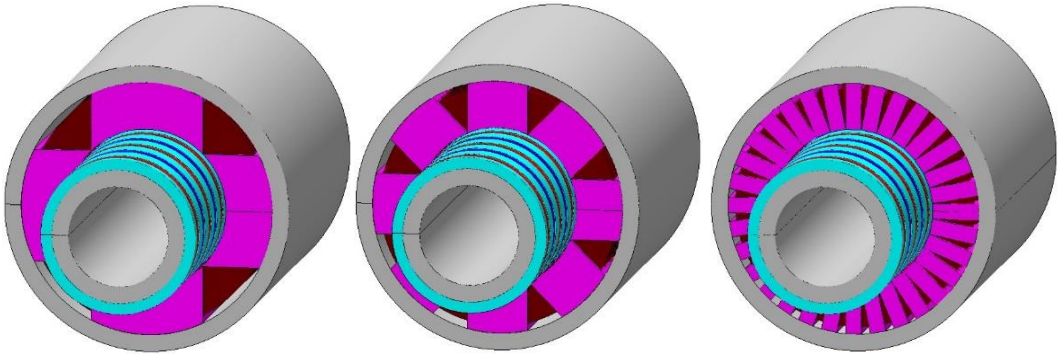


Figure 3-40 SMC model, force and eddy losses.

3.6.2 Blocked Lamination stator configuration

The blocked laminated tubular PM machine under consideration was shown in Figure 2-13 and Figure 2-14. This configuration has been modelled, solved and analysed using different number of blocks with a 3D FE software package. The 4, 8, and 32 blocks versions are shown in Figure 3-41. The performance results are compared with each other and with the original results of the fully laminated stator configuration at rated current density of 17A/mm^2 and rated current of 100mm/sec.



4_Block *8_Blocks* *32_Blocks*

Figure 3-41 Blocked Lamenated stator configuration

From the results, it can be seen that the stator core losses are the same for all number of blocks because it is based on Steinmetz equation. As shown in Figure 3-42, there is no significant change in the produced force for these stator configurations. This can be explained, that the total f_{stack} are the same with all number of blocks, and the small reduction is due to the variation in the lamentation sheets length within the same block, and for the same stator inner area, the magnetic reluctance is little higher than normal laminated stator. These differences tend to be smaller when the number of blocks increase.

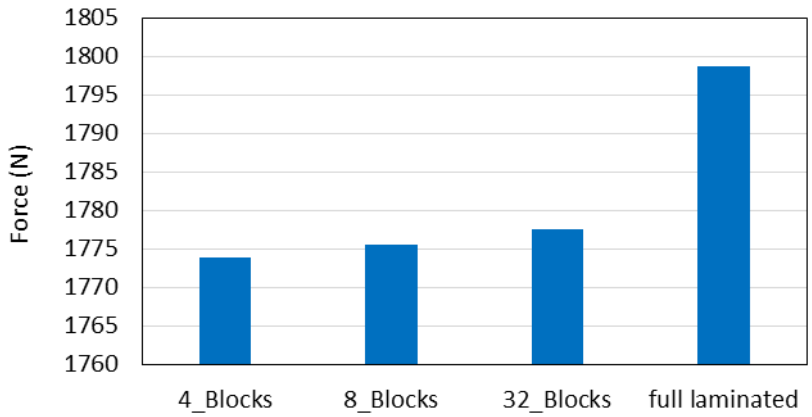


Figure 3-42 Generate force for different laminated block number at rated speed

3.6.3 Blocked Laminations and solid combination

This structure of blocked lamination stator with a solid corner is investigated by building a 3D, FE model, shown in Figure 3-43, where the 'corners' are made of solid steel. The model is again solved for the same conditions as explained in [7]. Figure 3-44 shows that there is a slight improvement in the generated force (around 5-7%), at the cost of a high increasing in the eddy current losses. The losses mainly exist in the solid part; they increase rapidly with the frequency of operation. It is important to note that this configuration while improving the performance still represents a high degree of manufacturing complexity [42].

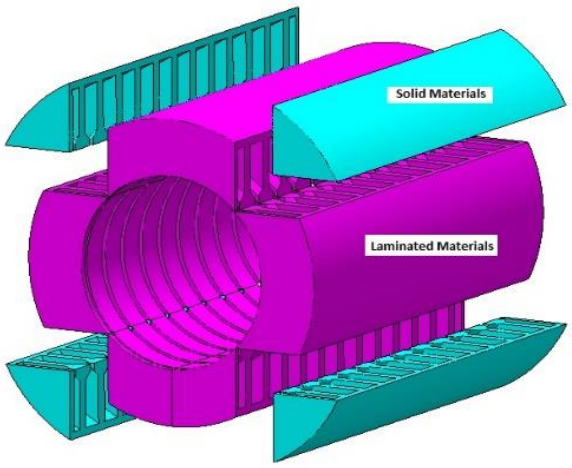


Figure 3-43 Blocked Laminations with solid combination

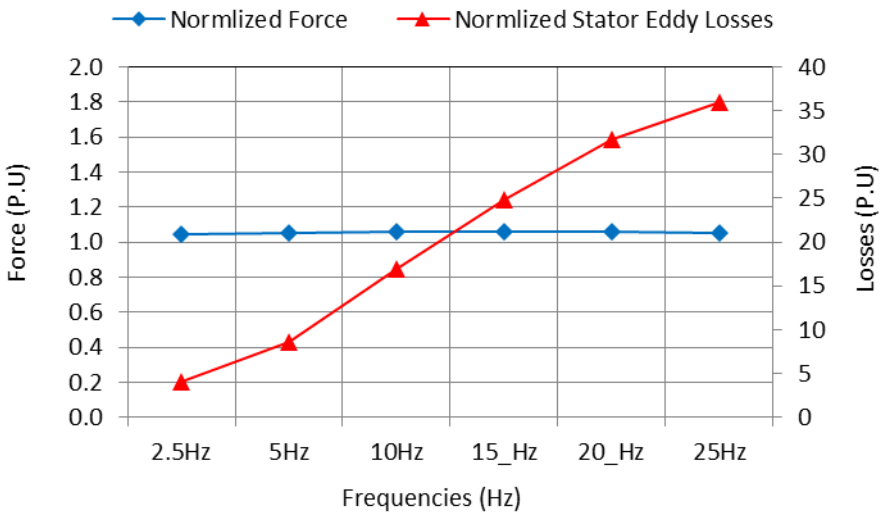


Figure 3-44 Laminated-solid combination, force and eddy losses.

3.6.4 TLPM Motor with Solid Stator

The advantages of implementing solid materials have been used to achieve further reduction in the size and costs. The particular 3D flux directions and complex manufacturing aspects in tubular machines imply that solid core structures can actually represent an optimal solution in terms of performance vs. cost, as given in [9] and [33]. In [33], to reduce the manufacturing cost of the TLPM machine, solid silicon iron has been used instead of laminated silicon steel sheet in the stator core.

In solid materials, eddy currents can result in considerable magnetic reaction and joule losses which compromise the dynamic performance and efficiency of the machine. These losses are eventually turned to heat, so they increase the temperature of the magnetic circuit. Overheating can result in damage to the coils and the magnetic circuit [115]. However for low operating frequencies, where the rated value of the fundamental frequency does not exceed 25Hz, the effect of the extra eddy current losses is quite limited and thus a solid stator core can represent a very attractive solution [7, 33, 116].

The selected TLPM motor has been modelled and solved with a solid stator configuration, where EN8 Carbon Steel (080M40) is selected as the solid material and its properties are given in Table D- 4 and Figure D- 3. EN8 is an unalloyed medium carbon steel grade with reasonable tensile strength and it is widely used for many general engineering applications. The TLPM machine has been solved under rated current condition with different frequencies (speed). The force and losses results are shown in Figure 3-45 and Figure 3-46 respectively, where the values are normalized with the base values being that of the original laminated configuration [7]. From Figure 3-45, it can be observed that the generated force is very similar to the original machine with a maximum force reduction of no more than 2.0% at low operating frequency, up to 10Hz.

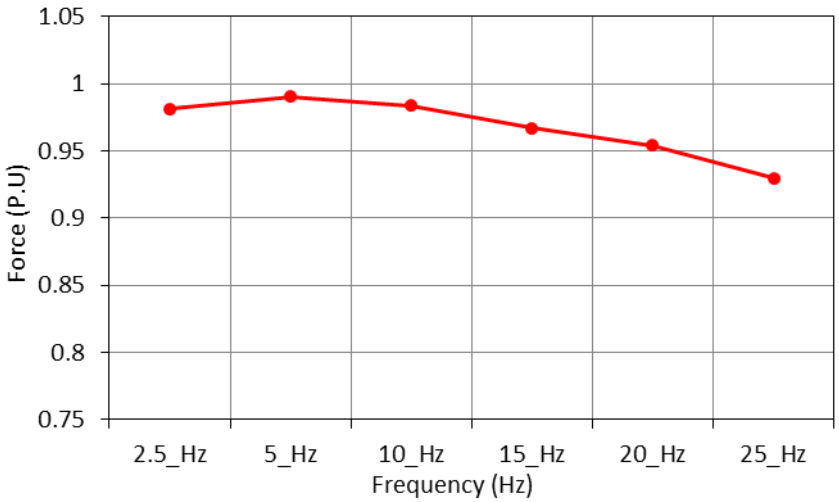


Figure 3-45 Force with solid model.

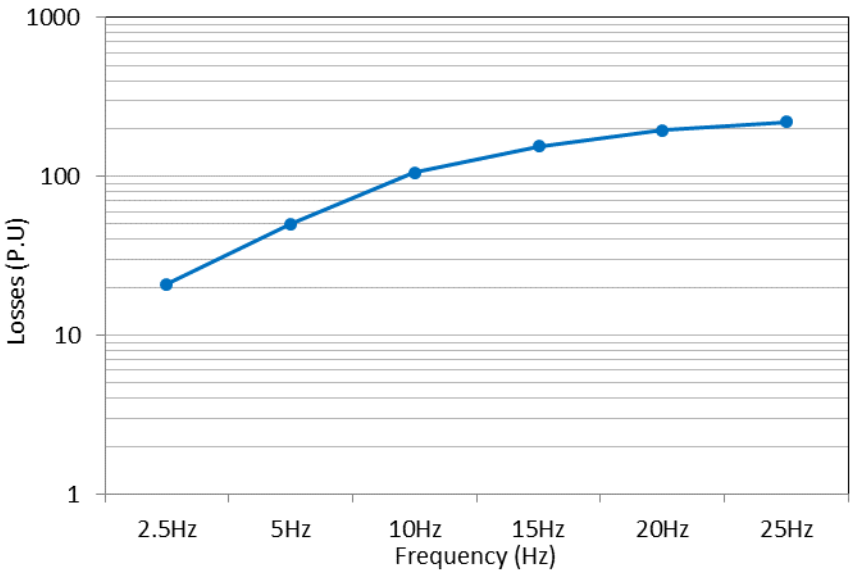


Figure 3-46 Eddy current losses with solid model.

Although the relative permeability of the solid steel (EN8) is less than that of the laminated steel (Transil 270-35) material, reported in appendix D, the generated force is comparable mainly due to the compensation of the lamination f_{stack}, as it is unity in the solid machine. From Figure 3-45, it can be seen that the output force are located within the acceptable limit for frequencies lower than 10Hz, while the output force begin rapidly decay with frequencies higher than 10Hz. The eddy current losses are considerably high in solid materials and they are increasing rapidly with the applied frequency, as shown in Figure 3-46.

3.7 CONCLUSIONS

After a detailed overview of the basic principles of the operation and theory of TLPM machines, this Chapter introduces the formerly-designed, 12-slot/10-pole, bench-mark TLPM motor. Analytical, 2D and 3D FE models of the machine were built and used to analyse the machine operation and performance. The comparisons

between the analytical, FE calculations and the experimental results (from the previous work) show acceptable similarities and thus the built models can be considered validated. However it is clear that the FE analysis result in more accurate at the cost of longer time consuming, when compared to the analytical models.

The last section of this chapter then used these models to investigate a number of TLPM motor configurations (first proposed in Chapter 2) that include solid material considerations. These analyses show that the generated force achieved by the proposed variants are within the expected and required levels, as that of the benchmark machine. However, the solid core machine exhibits a generated force decreasing quite rapidly when the applied frequency exceeds 10Hz. Figure 3-47 compares the overall force performance of the analysed variants, while Figure 3-48 represent the overall losses.

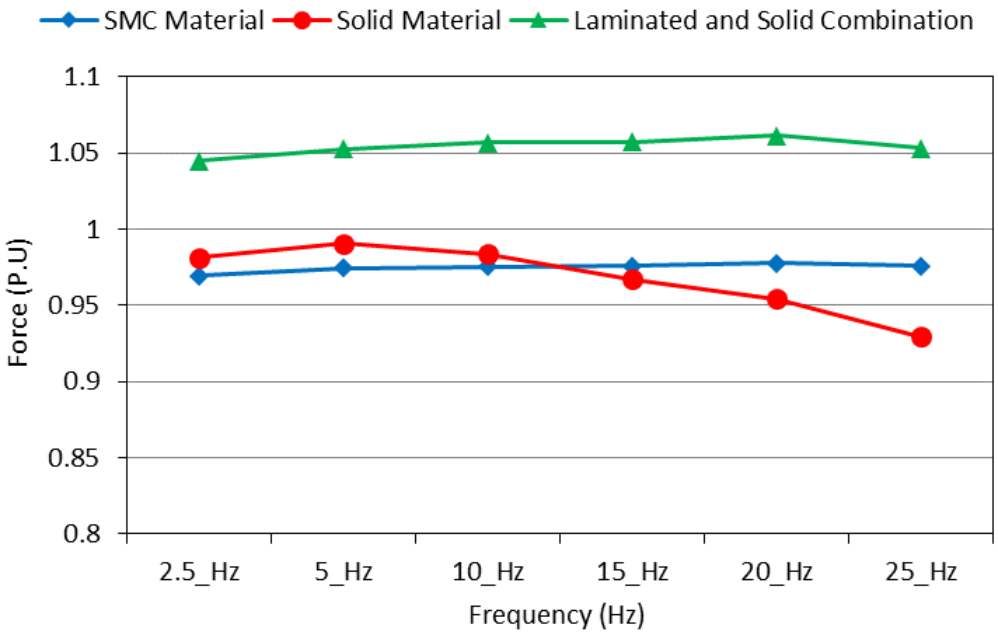


Figure 3-47 thrust force (P.U) with different stator models.

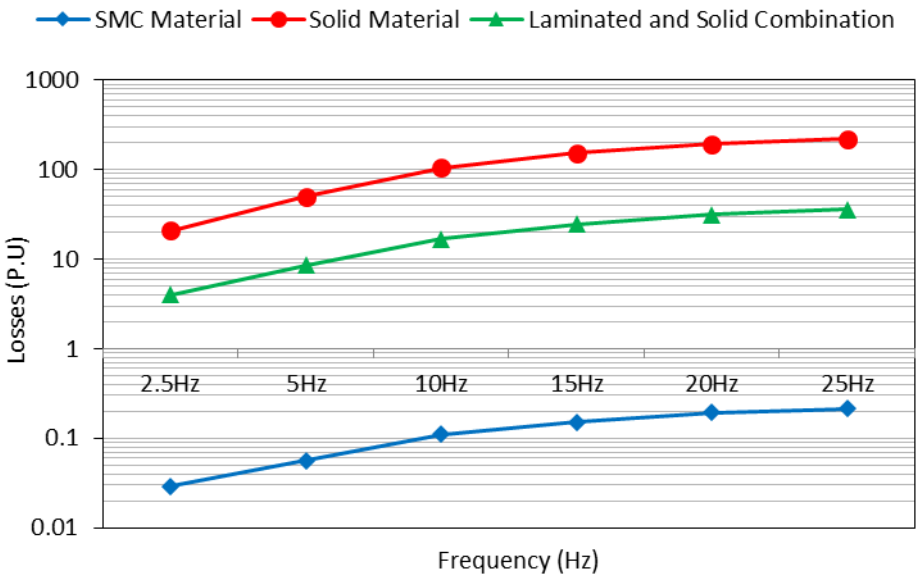


Figure 3-48 Eddy current losses (P.U) with different stator models.

As expected, the main drawback of solid core structures is the high eddy current losses in the motor stator. This matches with previous works as addressed in [33, 36] and indicates that reducing the eddy current losses is a critical issue in the design and manufacturing of a TLPM motor with solid stator structures [36].

Innovative eddy current reduction techniques are proposed and investigated in Chapter 5. However, to achieve this goal, an accurate distribution map for eddy current losses is required and this will be addressed in the next chapter. At this stage, it is important to note that the TLPM motor configuration presented in this work comprises a very unconventional magnetic circuit. Thus, the material data available from standard sources such as the material supplier's data and/or existing material data found in the libraries of commercial FE packages is not 100% representative of the material in the actual system operation. A new technique for the characterisation of the material is presented in the next chapter.

4. MATERIAL CHARACTERIZATION AND ITS CONCEPTS

4.1 INTRODUCTION

In this chapter, the conventional characterization methods of electromagnetic materials are covered and analysed in detail. A new method for the magnetic characterization of solid material used in unconventional magnetic circuits is proposed and investigated with focus on the core power losses. The nature of the so-called unconventional magnetic circuit of the application at hand is also explained. The proposed method involves an experimental set-up capable of characterizing solid materials to be used in non-standard or unconventional magnetic circuits such as that of the tubular machine, where the flux travels axially in the stator yoke. In order to further validate the proposed method, MPG-200D is used and the experimental results are compared with 3D, FE results achieved with time harmonic and transient solvers [110].

4.2 MACHINES AND THEIR MAGNETIC CIRCUITS

Electrical machines can be classified according to many different aspects, such as, the mechanical motion type, the nature of their supply current, the magnetic excitation type… etc. [117]. In this work, a classification method based around their magnetic circuit types and behaviours is used and is listed as follows.

1. Electrical machines with a conventional magnetic circuit, such as for rotating machines. In these machines, the main flux and the eddy currents follow the ‘standard’ paths where the magnetic field is rotating around the

rotational axis of the moving parts and the eddy currents flow in direction that is parallel to the rotation axis of the moving parts. Figure 4-1 and Figure 4-2 respectively show these behaviours.

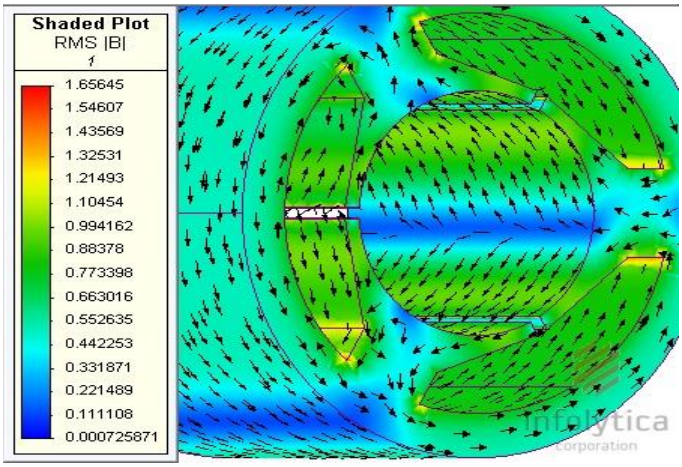


Figure 4-1 Standard magnetic circuits of rotating machines; Main flux paths

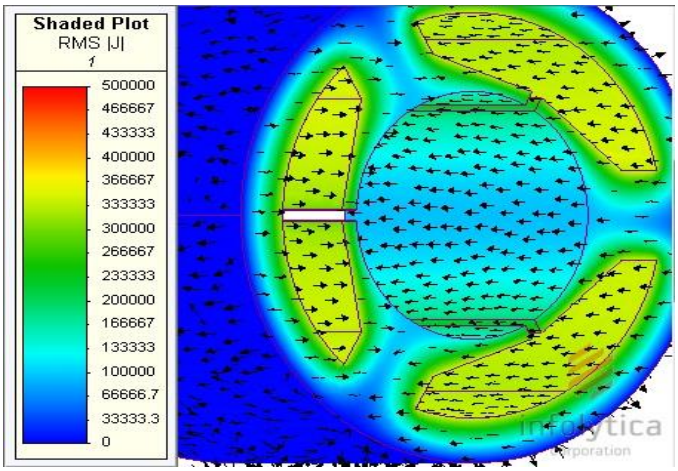


Figure 4-2 Standard magnetic circuits of rotating machines; Eddy currents

2. Electrical machines with unconventional magnetic circuits, such as for TLPM machines. For TLPM machines, the main flux path travels axially along the direction of motion axis, while the eddy current paths are tangential to the circumference of the machine parts and concentric to the motion axis. This is illustrated in Figure 4-3 and Figure 4-4 for the flux density and eddy current behaviour respectively.

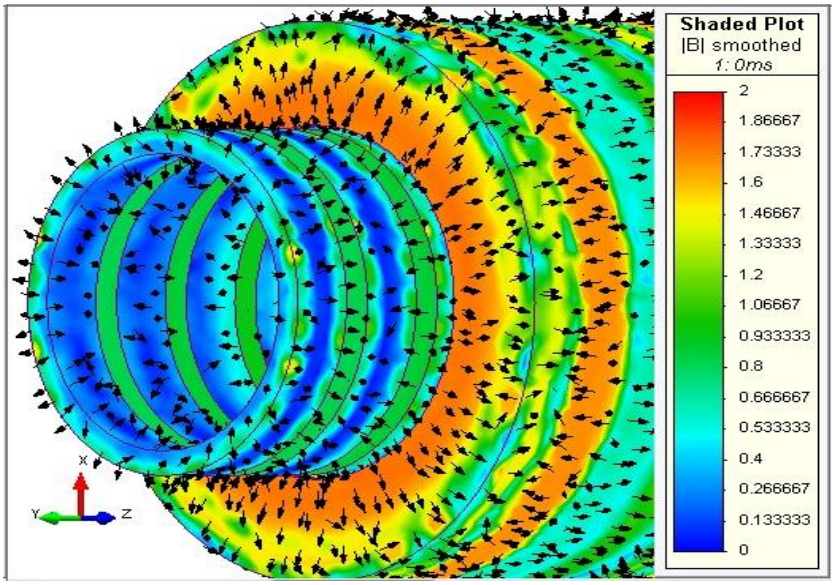


Figure 4-3 Non-standard magnetic circuit; Main flux paths

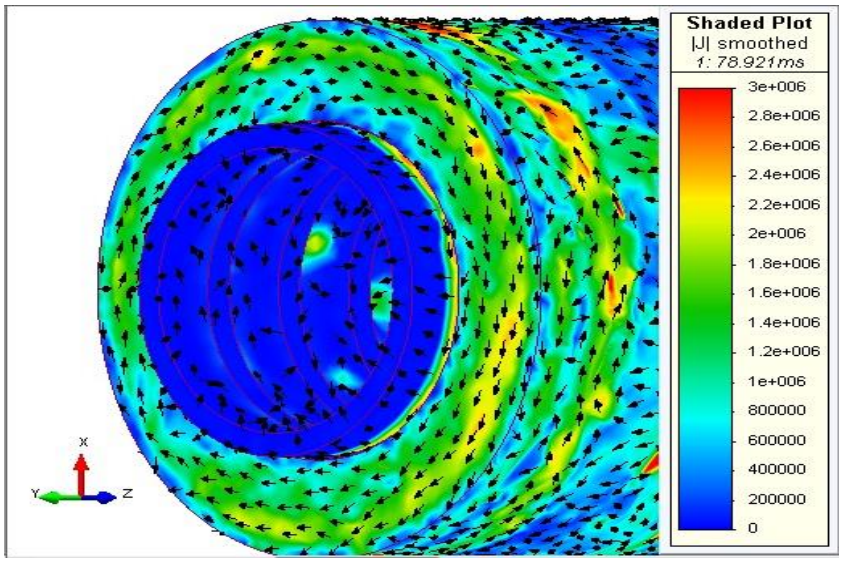


Figure 4-4 Non-standard magnetic circuit; Eddy currents

4.3 MATERIAL CHARACTERIZATION METHODS

Traditionally, the effects of eddy currents iron losses in electrical machines are reduced by employing electrically insulated laminations. However, certain types of machines, such as tubular linear machines [7] can actually benefit from having solid structures for their stator and/or mover parts, although at the cost of extra iron

losses, therefore: a number of methods and techniques have been proposed to mitigate and reduce these core loss effects [42]. These procedures however require accurate mapping of the material characteristics in order to achieve an optimal machine design. Due to the differences in the magnetic circuits types mentioned earlier, it cannot be achieved by the well-known standard procedures for material characterization mentioned in [118], [119] and [120].

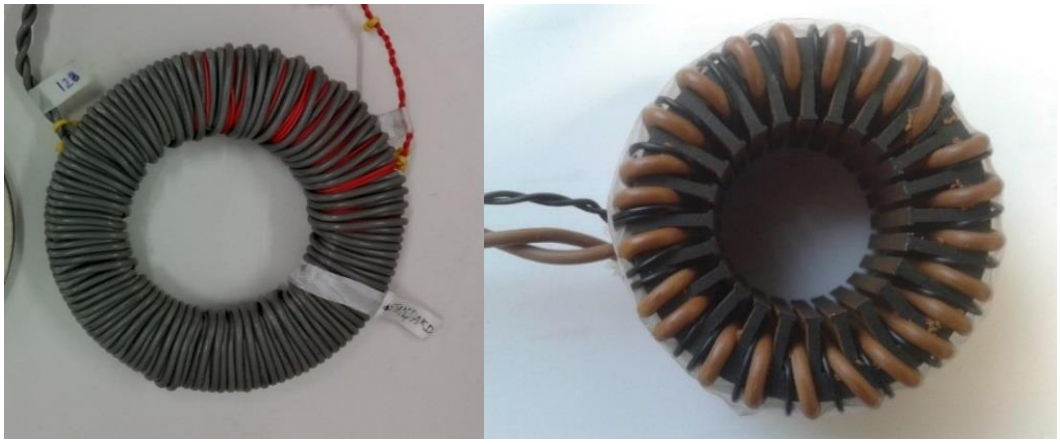
4.3.1 Characterization Methods

This section illustrates how characterization of material employed in standard and nonstandard magnetic circuits can be achieved. Considering a homogenous material structure, then uniform magnetic properties can be assumed.

4.3.2 Characterization Methods for Conventional Magnetic Circuits

4.3.2.1 Laminated materials for conventional arrangements

Today, there is a wealth of literature and data that details the magnetic properties of laminated materials [111]. Alternatively, fast and accurate testing methods for such materials can be achieved by implementing ‘simple’ tests such as the Epstein frame method and the single sheet tester method (SST). The toroidal ring test method allows for stacks of lamination material in the form of circular ring samples to be characterized quite accurately. In some cases, the complete stator part of the machine is used instead of a toroidal ring sample [120] as shown in Figure 4-5 (a) and (b), for toroidal ring and complete stator samples respectively, in order to obtain the closest realistic characterisation of any particular machine.



(a) toroidal ring sample *(b) complete stator*

Figure 4-5 Material characterization of lamination stack

4.3.2.2 Solid materials for conventional arrangements

In terms of solid materials, today there are considerable amounts of freely-available data regarding the mechanical and physical properties of materials such as EN8, SSJ416, … etc. [113, 121, 122]. However, when it comes to the magnetic properties of such solid materials, there is often a considerable lack of information. Even when such data is available [111], it is generally incomplete and does not provide all the information that is required by electrical machine designers.

In order to mitigate these issues, there are a number of testing procedures that can be used to characterizing the magnetic properties of solid materials [118]. Such procedures are usually limited to applications where the magnetic circuit of the machine is standard as for example for conventional rotary electrical machines.

A typical method consists in the using of a ring sample setup with two windings as shown in Figure 4-6, where the main winding creates the magnetic field intensity *H* and the secondary winding is used to measure the *B* in the ferromagnetic core.

N_{main}, N_{sense}

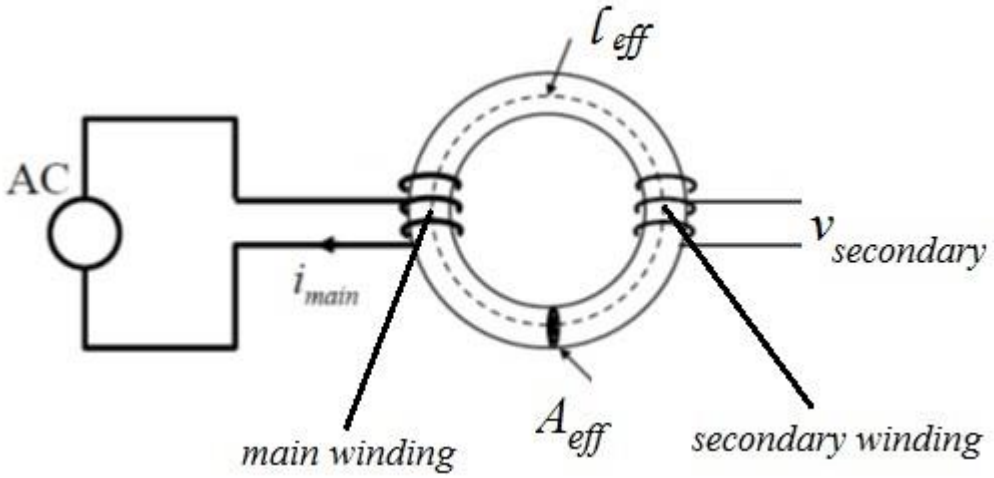


Figure 4-6 Standard magnetic characterization method

Considering this setup, then according to the right hand rule, the generated eddy current is circulating in the X-Y plane only as shown in Figure 4-7. Thus, it is quite easy to identify the desired direction for the metal lamination in order to reduce these eddy currents and losses. The material characteristics obtained from this test can be employed successfully in rotating electrical machines, where the magnetic flux is approximated to a circulating fashion and the eddy current is in the axial direction and perpendicular to flux vector, which is not the case of TLPM motor.

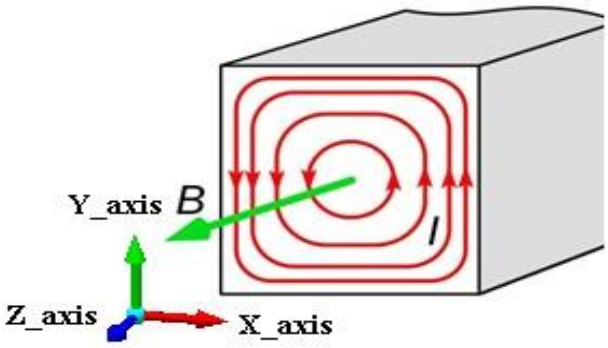


Figure 4-7 Flux direction and eddy current path.

The objective of the above-mentioned test is to calculate the amplitude relative permeability μ_r and the AC losses of the material at different frequencies and

different flux densities. The maximum values of H and B can be computed from (4-1) and (4-2), where $v_{secondary}$ is the average or DC value of the output signal measured by an average-type voltmeter. Root mean square (*rms*) voltmeter type could also be used when the form factor of the output voltage of the secondary winding is kept at 1.1107 which indicates a pure sinusoidal B in the ring sample, as discussed in [119]. Then, μ_r can be calculated by (4-3), where μ_o is the absolute permeability of free space, N_{main} is the number of turns of the primary coil and $N_{secondary}$ is the number of turns of the secondary windings. L_{eff} and A_{eff} are the effective length and cross-sectional area of ring sample respectively.

$$H_{\max} = \frac{N_{main} \cdot I_{\max}}{l_{eff}} \qquad (4\text{-}1)$$

$$B_{\max} = \frac{v_{seeondary_\max}}{4\, f\, N_{seeondary}} \qquad (4\text{-}2)$$

$$\mu_r = \frac{B_{\max}}{\mu_o \cdot H_{\max}} \qquad (4\text{-}3)$$

Figure 4-8 illustrates a test set-up of an EN8 solid steel that involves a toroidal ring sample with uniform cross-sectional area, [118], [119]. The geometry of the test specimens and their actual dimensions has been presented in Table 4-1. The dimensions of the sample have been selected based on the desired aspect ratios AR which is given in 4-4), where D_{out} is the outer diameter, D_{in} is the inner diameter and h is the high (thickness) of the ring sample [123].

$$AR = \frac{(D_{out} - D_{in})/2}{h} \qquad (4\text{-}4)$$

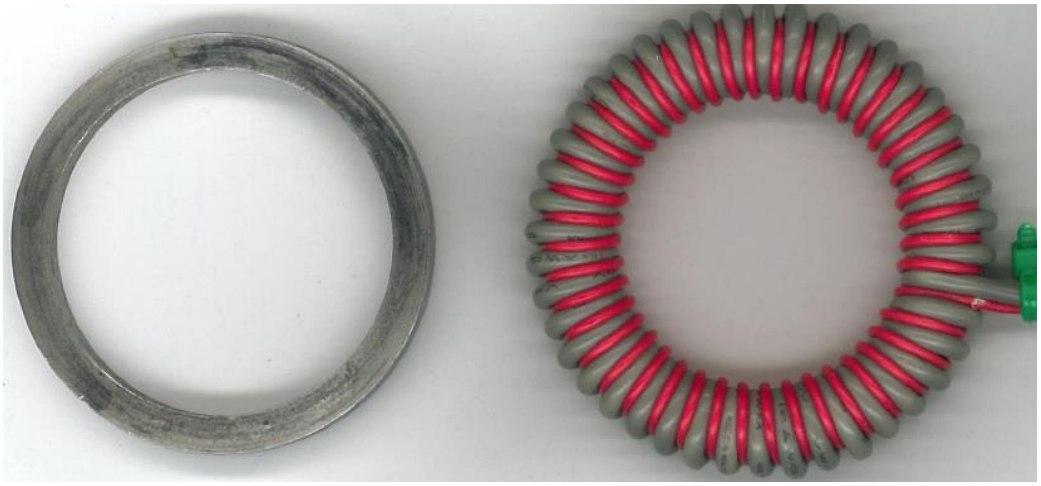


Figure 4-8 EN8 solid material ring and toroidal method test set-up

Considering a purely sinusoidal *B* inside the ring sample, which can be achieved by using a closed loop control system to control the form factor of the secondary voltage waveform as a function of *B*, the *B-H* curves of an *EN8* solid steel ring sample whose parameters are shown in Table 4-1, is obtained through the closed loop magnetic measurements system of [110]. The characterization has been carried out with frequency range of 2.5Hz to 50Hz. The resulting curves in Figure 4-9 shows the AC magnetization loop at different frequencies and maximum flux density of 1.6 Tesla, Figure 4-10 shows the d.c. magnetization curve of EN8 and Figure 4-11 shows the d.c. hysteresis loop of EN8.

Table 4-1 properties of EN8 ring sample

Parameter	*Value*	*Parameter*	*Value*
Ring Height (h)	*5 mm*	*Sample mass*	*30 G*
Inner Diameter (D_{in})	*45 mm*	*Material mass Density*	*7840 Kg/m^3*
Outer Diameter (D_{out})	*55 mm*	*Material resistivity(20^o C)*	*2.21e-007 Ω.m*
number of turns of Primary Coil	*80*	*number of turns of Secondary Coil*	*75*

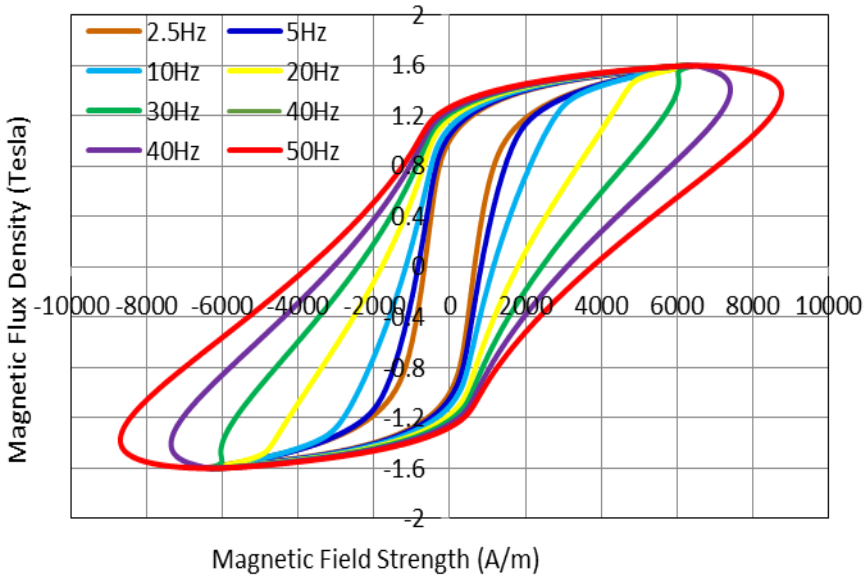


Figure 4-9 EN8 material: a.c. B-H curves for different frequencies

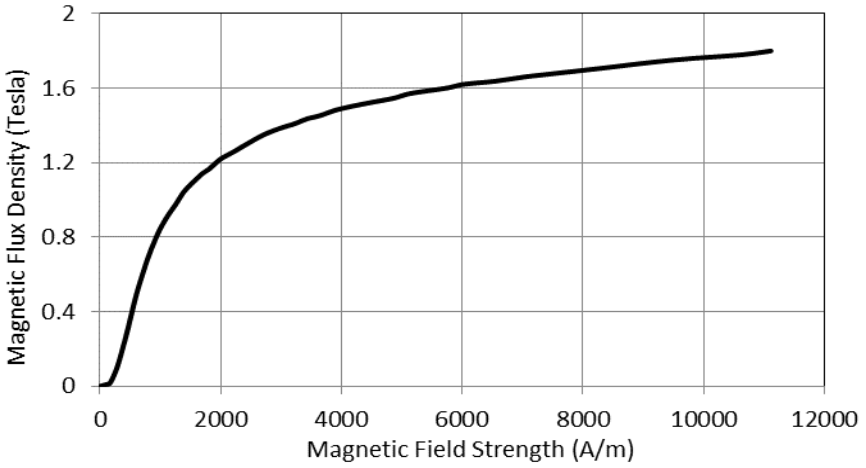


Figure 4-10 EN8 material: d.c. B-H curve at B_{max} = 1.6T

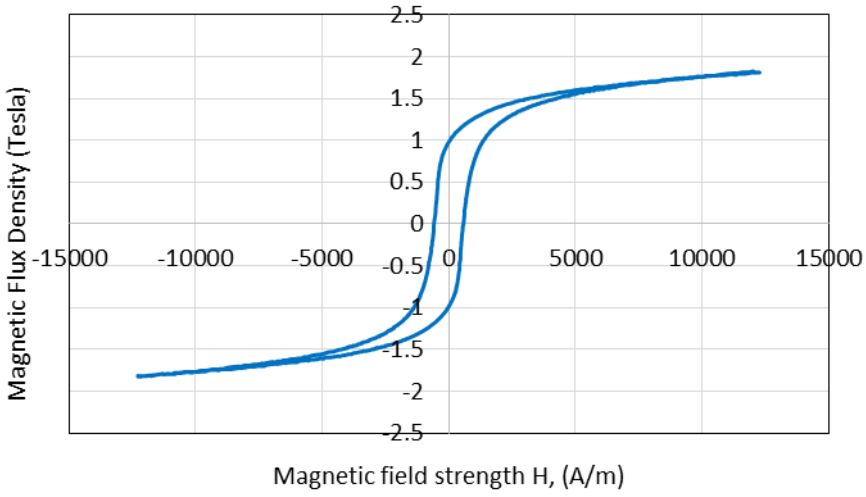


Figure 4-11 EN8 material: d.c. hysteresis loop

Figure 4-12 shows the relative permeability μ_r of EN8, where relationship between μ_r and B at different applied frequencies has been obtained from (4-1), (4-2) and (4-3). It can be clearly observed how μ_r of the material is strongly dependent on the frequency and flux density. A higher μ_r appears at the lower frequencies, reaching its maximum values when the flux density is equal to 0.7T at 2.5Hz. Generally, at very low frequencies, the a.c. μ_r is approximately identical to the d.c. value of μ_r [124].

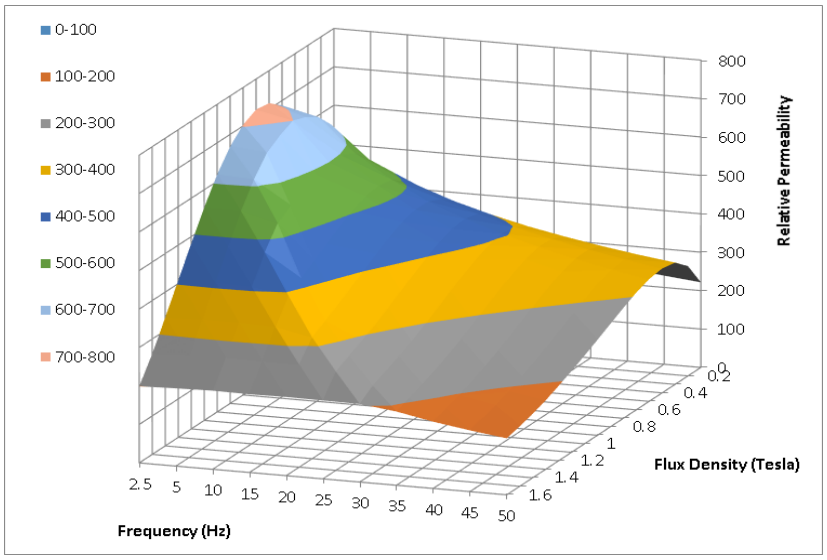


Figure 4-12 Relative permeability as a function of frequency and B

In this work, the total core power loss P_{loss} of the ring sample is measured by using the single-phase wattmeter method. The current sensor of the wattmeter is connected in series with the main winding (excitation coil) of the toroidal ring test setup and the voltage sensor of the wattmeter is connected in parallel with the secondary winding as shown in Figure 4-13. Equation (4-5) is then used to compute the total core power losses P_{loss}, where P_{watt} is the wattmeter reading, N_1 is the number of turns of the primary winding and N_2 is the number of turns of the secondary winding as shown in Figure 4-13. It is important to note that the copper

loss has no effect on the wattmeter reading because only the main current is measured in the primary side [119].

$$P_{loss} = \frac{N_1}{N_2} P_{watt} \tag{4-5}$$

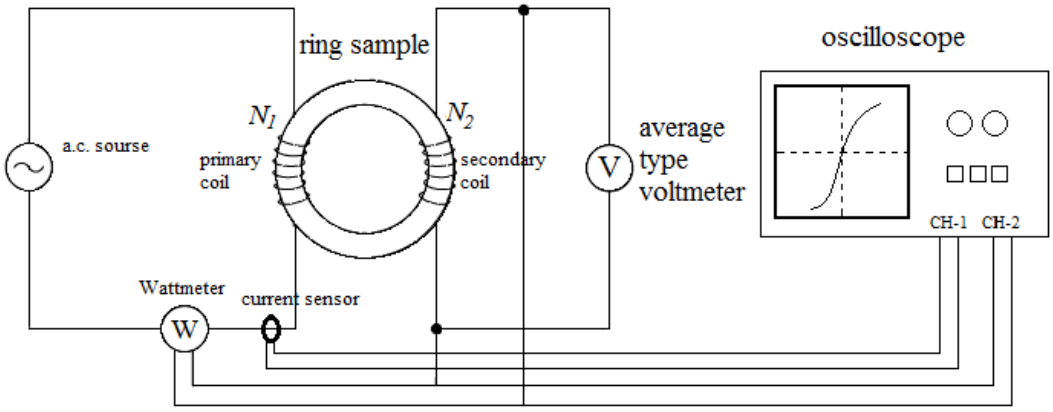


Figure 4-13 Circuit of the wattmeter method

The total loss over one complete electrical cycle can be computed by (4-6) by using digital acquisition system with uniform sampling period, where *k* is the sampling number per complete electrical cycle, as described in [125]

$$P_{loss} = \frac{N_1}{N_2} \cdot \frac{1}{K} \sum_{k=1}^{K} i_{primery}[k].v_{secondary}[k] \tag{4-6}$$

The iron losses calculated from (4-6) can be categorized into three types of losses, namely eddy current losses, hysteresis loss and excess (abnormal) loss. The latter 'abnormal' loss is considered as part of the total eddy current losses [126, 127].

Hysteresis loss P_h is associated with the phenomena of hysteresis and is an expression of the fact when ferromagnetic material is involved, not all the energy of the magnetic field is returned to the circuit when *mmf* is removed. It is known as hysteresis loss. While eddy current losses P_e arise from the fact that the core itself

is composed of conducting material, so that the voltage induced in it by the varying flux produces circulating currents in the material [128].

Generally, hysteresis losses increase linearly with the applied frequency, while the eddy current losses increase with the square of the frequency [127]. Then, these losses can be 'separated' by using (4-7) and (4-8), where $P_{(f1)}$ and $P_{(f2)}$ are the total iron power loss at frequencies f_1 and f_2 respectively, P_e is the eddy current power loss and P_h is the hysteresis power loss.

$$P_h = \frac{P_{(f1)}}{f_1} + f_1 \cdot \left[\frac{(P_{(f_2)} / f_2) - (P_{(f_1)} / f_1)}{f_1 - f_2} \right] \qquad (4\text{-}7)$$

$$P_e = P_{total} - P_h \qquad (4\text{-}8)$$

Thus, the actual core losses in the ring sample can be identified. For the ring sample discussed above, Figure 4-14 shows the total losses of the toroidal ring sample obtained from experimental tests at different frequencies and flux densities.

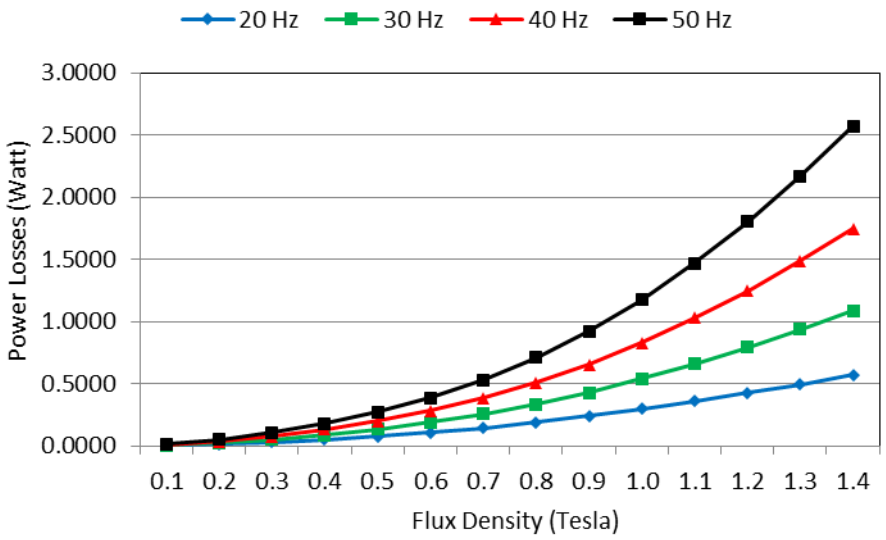


Figure 4-14Experimental results of P_{loss} of the ring sample using classical method

4.3.2.3 Discussion

All the above are well-noted and well-known methods used to analyse and characterise materials and their properties in conventional machines and magnetic circuits. However such methods are not fully appropriate to the unconventional magnetic circuits described in Section 4.2. Therefore in the next sections, a new method for these situations is proposed and investigated.

4.4 PROPOSED CHARACTERIZATION METHODS FOR UNCONVENTIONAL MAGNETIC CIRCUITS

For electrical machines that employ a non-standard configuration such as the tubular machine of [7], the magnetic circuit is quite different from a standard rotary machine. In such an electrical machine, the magnetic flux travels in the same direction of the moving parts [66]. This indicates that common material characterization methods, such as the one highlighted in Figure 4-6 do not accurately represent the true flux and eddy current conditions in this configuration. If such methods are used, this can result in non-accurate values and in non-optimal design of electrical machines constructed from solid magnetic materials.

4.4.1 The concept of the proposed method

In order to characterize material that is used in machines with unconventional magnetic circuits, a flux pattern/behaviour such as that of the real machine (during operation) needs to be generated within the sample under test. The proposed method is therefore based on the generating of a magnetic flux passing radially through a representative ring sample (emulating the actual TLPM motor structure) from the

inner surface to the outer surface, as shown in Figure 4-15 and Figure 4-16. The selected ring sample has the same properties of the toroidal ring sample given in Table 4-1.

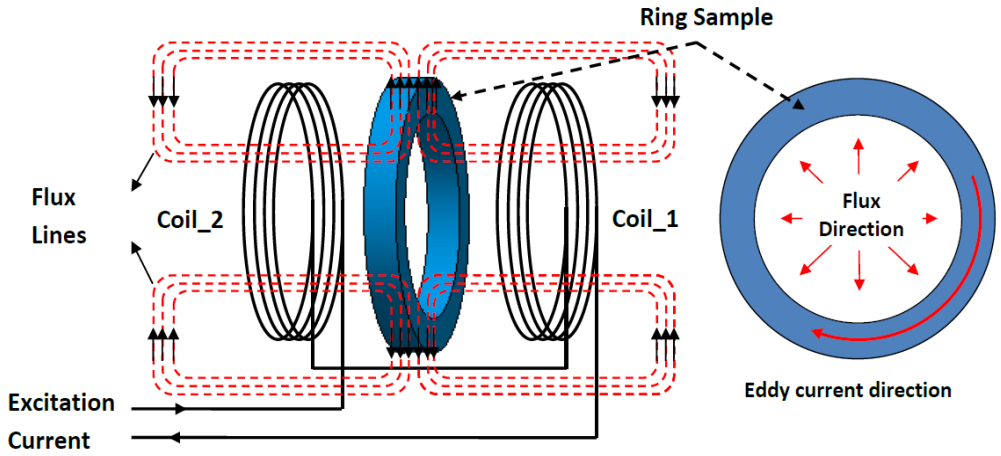


Figure 4-15 Ring Sample and coils connection diagram with radial flux

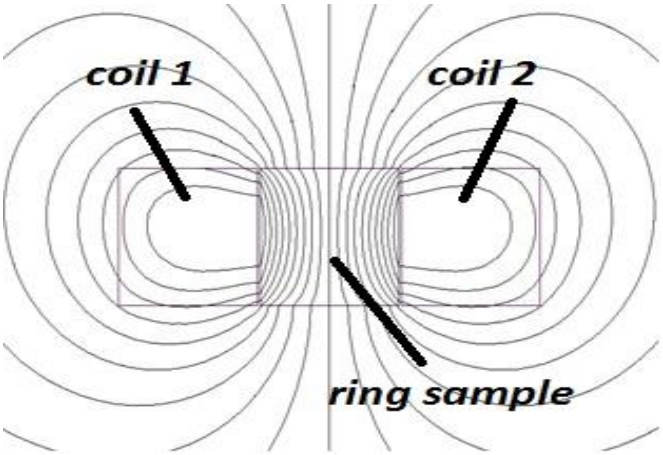


Figure 4-16 Flux lines inside the ring sample

To generate the particular field required to emulate the TLPM machine flux pattern, two coils connected in series are accommodated on both sides of the ring sample. The direction of the current flow in the first main coil should have a 180º phase shift to the second main coil, otherwise only leakage flux would pass through the ring sample as shown in Figure 4-17.

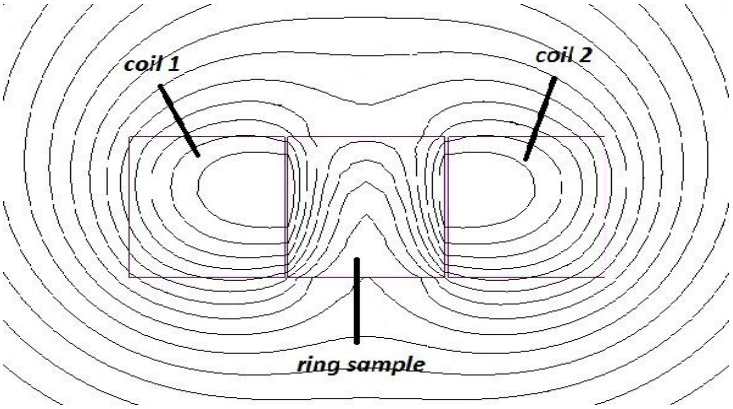


Figure 4-17 Flux lines inside the ring sample (wrong connection)

By combining this proposed method with the 'standard' toroidal ring test method of Figure 4-6, it is then possible to provide a complete magnetic characterisation for any magnetic circuit. This can be implemented to 'cater' for all the known types of electric machines including rotating machines, axial flux machines and radial flux machines.

4.4.2 The proposed test setups

The objective of the proposed set-up is to generate the non-standard magnetic flux direction that was described in Section 4.2. The ring sample is fitted with two primary and two secondary coils, because very high current densities are required to obtain the desired flux density ***B*** in the ring sample under the test. To further aid the increase of magnetic flux for a given current in the main windings, a high permeability, ferrite magnetic material, known as 0W-48613-TC, is used as the outer core and the inner core to complete the magnetic circuit of the flux generated by the excitation coils shown in Figure 4-15. This 0W-48613-TC ferrite material exhibits very low magnetic losses at high frequencies while it enjoys negligible losses at low frequencies in addition to its linear μ_r [129]. The main challenge with

this particular material is its relatively low saturation level, which is approximately 0.4Tesla as shown in Figure 4-18.

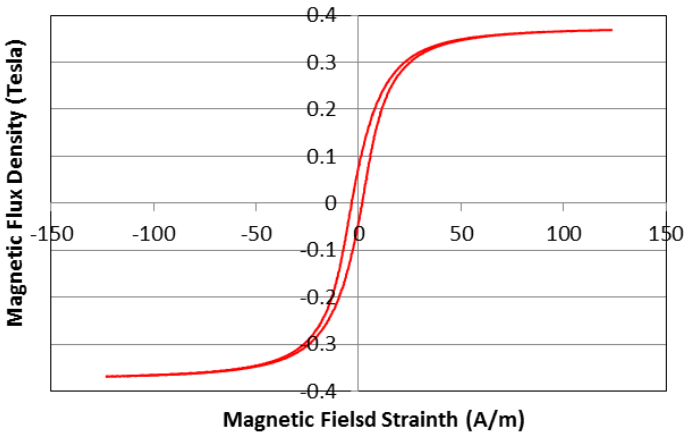


Figure 4-18 B-H loop of ferrite core (0W-48613-TC)

To investigate the magnetic properties of the selected ferrite core, Figure 4-19 shows the experimental results including μ_r, eddy current losses and the hysteresis losses, when a sample of ferrite core is tested using the set-up shown in Figure 4-13. The total losses of the ferrite core represents less than 0.02% of the total power losses of the complete setup, at the highest frequency. Having such low values of losses justifies neglecting the ferrite core losses in the proposed model and experimental setup.

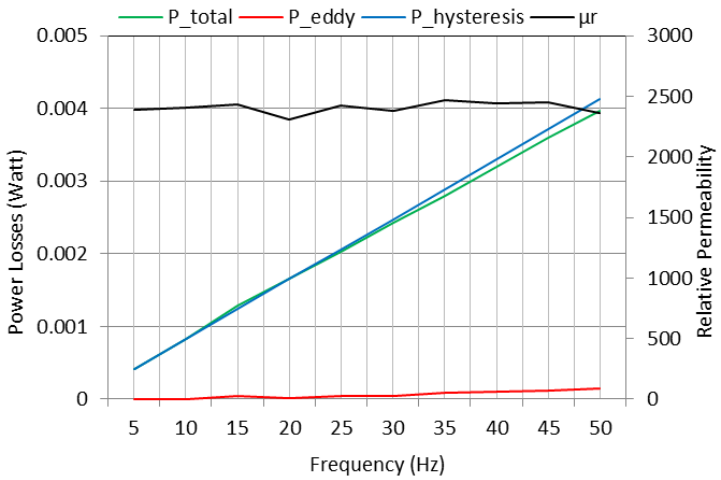


Figure 4-19 Magnetic characteristics of Ferrite (0W-48613-TC) at B=0.37 Tesla

4.4.3 Ensuring realistic representation of the application at hand

While the general concept shown in Figure 4-15 does provide the required flux distribution, it was however felt important to consider certain aspects of the application right from the start. An important aspect of tubular machines is the extra length at the ends of the stator yoke, as shown in Figure 4-20, in order to reduce the end faces cogging force due to the finite edges [130]. The resulting eddy current in these parts behaves in a different manner from the rest of the magnetic circuit, mainly due to this part not being completely wound like the machine teeth [33]. Also, in the 'active part' of the machine itself, the teeth of the machine are not always facing the same current conditions as those of the adjacent coils. . Considering this, it was then decided to examine two variations of the proposed set-up, one to consider the parts (corresponding to teeth) that lie between coils carrying current in the opposite directions and the other to consider the parts that lie between coils carrying current in the same direction.

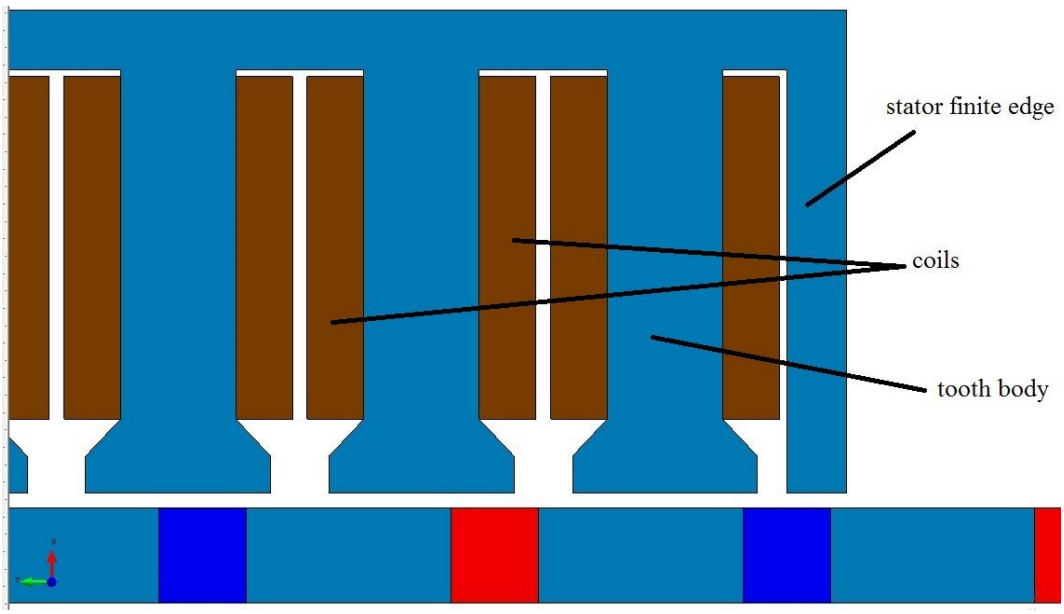


Figure 4-20 Stator finite edge

1) Bidirectional Current Condition Set-up

The first set-up is aimed to characterize the material used for the TLPM machine's teeth which lie under the condition of two opposite directions of currents in each side (slot). A 3D, FE model of the proposed set-up is shown in Figure 4-21, where the tooth of the TLPM machine is represented by the ring sample. The ring sample is fitted between two primary coils and two secondary coils connected in series. It is important to set the correct polarity of the coils, in order to generate the correct direction of the *mmf* of the excitation coils. Figure 4-22 shows the mesh size and the current density and its direction inside each coil side and the eddy current density inside the ring sample.

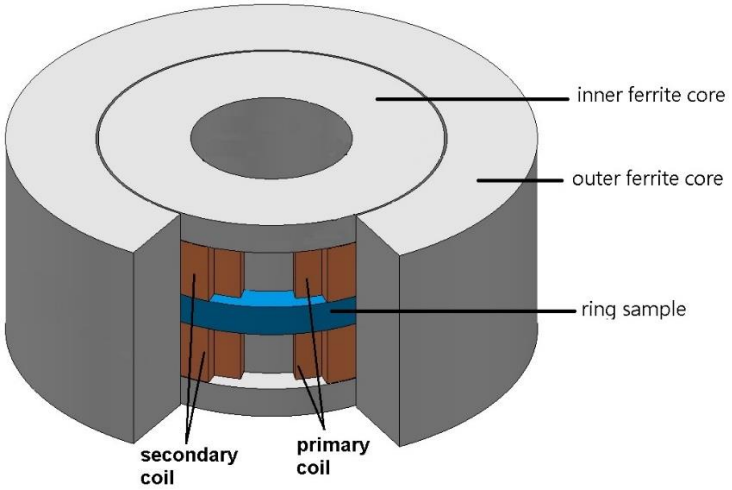


Figure 4-21 the proposed Bidirectional Current Set-up

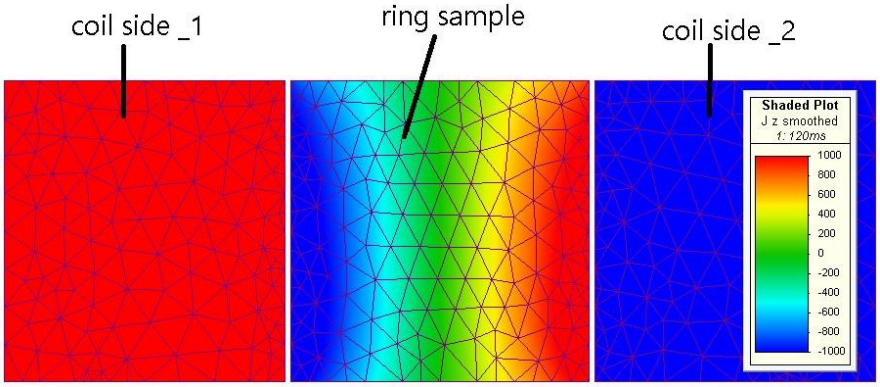


Figure 4-22 Bidirectional Current Set-up with current direction

Considering the eddy current directions in solid material, as shown in Figure 5-3 and in Figure 4-15 and according to the analyses given in [33], it can be shown that the eddy currents inside the ring sample behave as two components rotating in opposite directions, where the direction of each component is opposing the direction of the excitation current in the adjacent coils on each ring-side. Figure 4-23 shows clearly the directions of the generated eddy current which is quite similar to the eddy current inside the tooth of the TLPM machine at rated condition of [7], as shown in Figure 4-24.

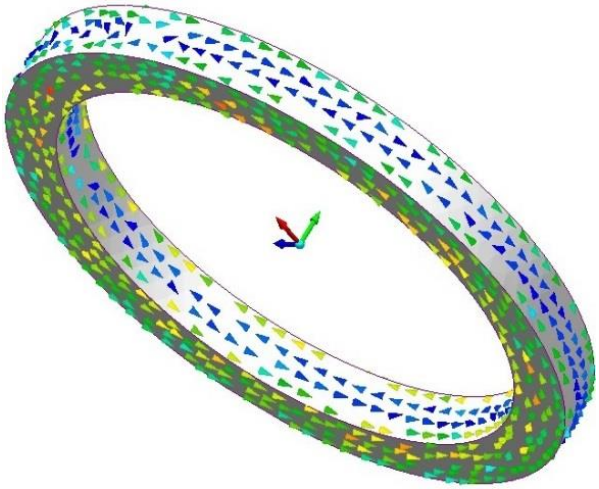


Figure 4-23 Eddy current pattern of 'Bidirectional Current Set-up'

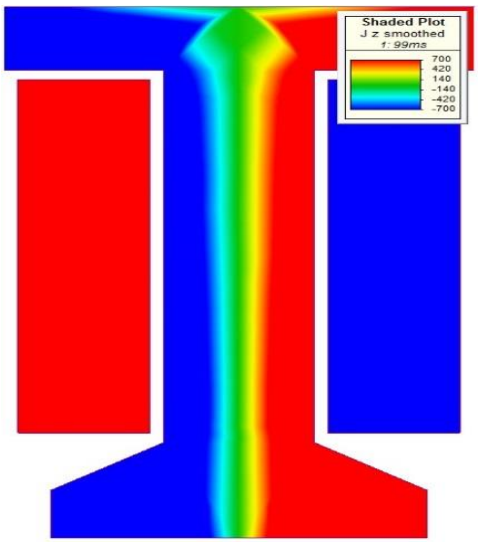


Figure 4-24 single tooth eddy current directions (Bidirectional Condition)

The 3D, FE model is then used to assess the validity of the proposed method for predicting the eddy current loss in the ring sample. The model is solved for a range of frequencies and flux densities. Figure 4-25 showing the resulting eddy current losses as a function of applied *f* and *B*.

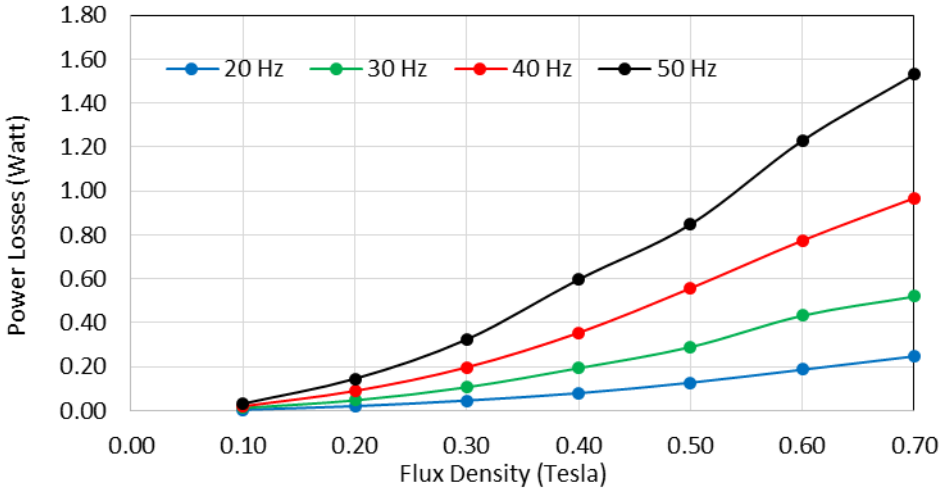


Figure 4-25 Bidirectional eddy current setup: FE results of power losses

Considering Figure 4-25, it is important to mention that with the Bidirectional Current Condition Set-up, the eddy current losses are higher than that of Figure 4-14 when a classical characterization method is used. These extra losses are incurred due to the eddy current pulsations between the two sides of the ring sample, resulting from the 180^{o} phase shift between the eddy current components, generated in each side of the ring sample. This can potentially result in a relatively higher loss than for the toroidal method.

2) Unidirectional Current Condition Set-up

The second proposed set-up is used to characterize the solid material of the tooth that lie between two coils carrying currents in the same direction or a tooth with a current carrying coil only on one side. In this case, the eddy current is a one-

component flow in one direction. Thus, this eddy current is facing a lower electrical resistance of the eddy current path. In the TLPM motor application, this can represent a single layer winding configuration or the finite edge parts of the tubular machine. A FE model of the 'Unidirectional Current Condition Set-up' is shown in Figure 4-26, where it can be observed how the ring sample is no longer positioned between two coils. Figure 4-27 shows the mesh size and the current density and its direction inside each coil side and the eddy current density inside the ring sample. Figure 4-28 shows the behaviour of the eddy currents that travel only in one direction around the ring sample. Figure 4-29 shows the eddy current behaviour inside the tooth of TLPM motor with the same direction of the excitation currents of the proposed, unidirectional current condition, set-up.

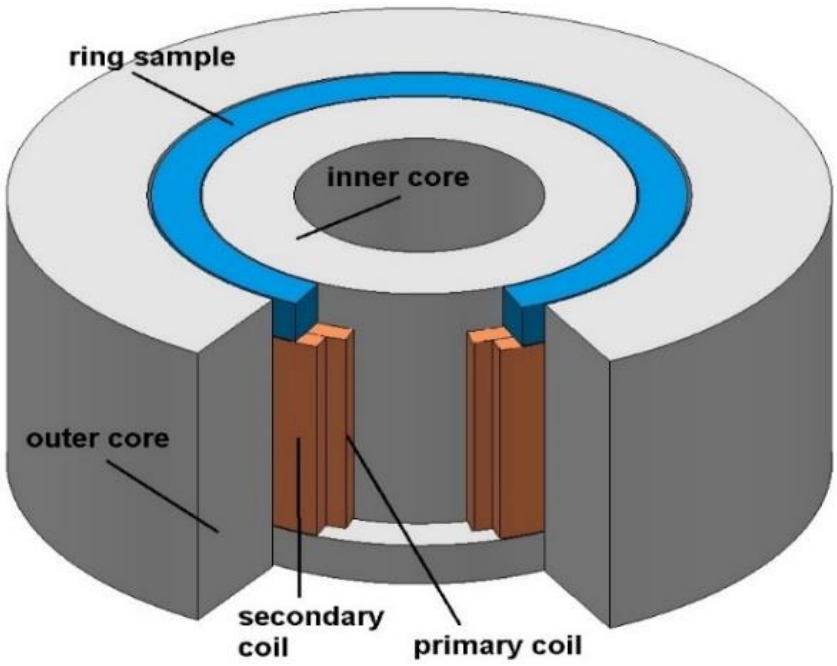


Figure 4-26 the proposed Unidirectional Current Set-up

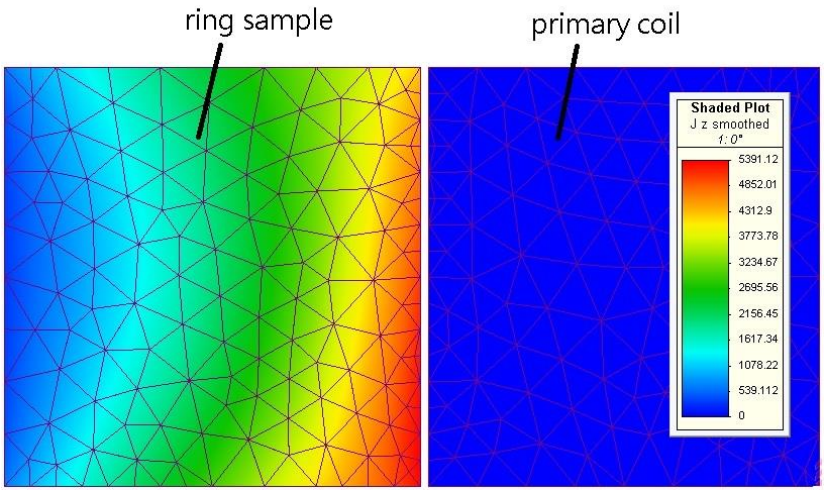


Figure 4-27 Unidirectional Current Set-up with current direction

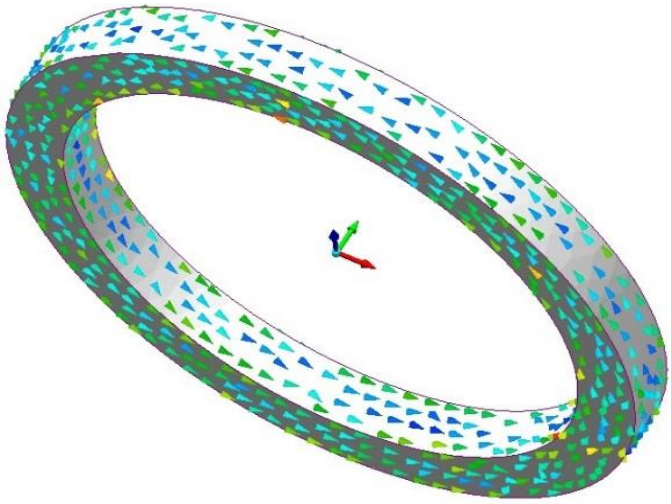


Figure 4-28 Eddy current pattern of Unidirectional Current Set-up

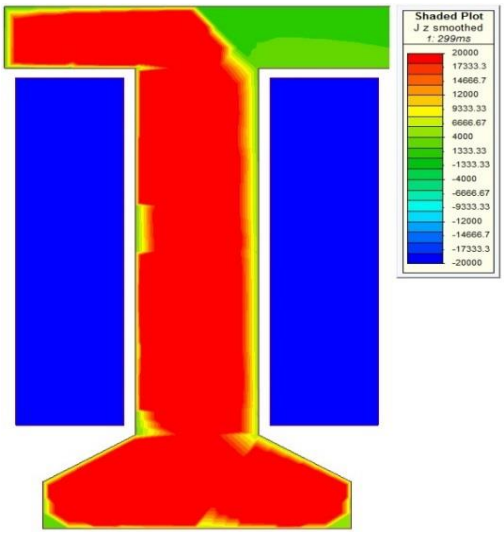


Figure 4-29 single tooth eddy current directions (Unidirectional Condition)

Figure 4-30 shows the eddy current losses obtained from this 3D, FE model as a function of applied frequency and ***B***, where ***B*** is limited by the saturation level of the ferrite core used in frame material of the proposed set-up. From Figure 4-30, it can be observed that the losses in the Unidirectional Current Condition Set-up are significantly higher than those of classical (toroidal) Set-up and the Bidirectional Set-up. This is mainly due to the unidirectional component of eddy current that passing completely through a larger effective cross-sectional area A_{eff} which has a much lower effective Ohmic resistance. Considering (4-9), where J is the eddy current density, σ is the conductivity and ω is the angular speed, then it can be concluded that for a fixed B, the eddy current density is directly proportional to the electrical conductivity of the material. This means that the eddy loss is also directly proportional to the A_{eff} of the ring sample, resulting in an increase in the magnitude of the eddy current itself and therefore an increase in power losses.

$$\nabla \times J = -j\ \omega\ \sigma\ B \tag{4-9}$$

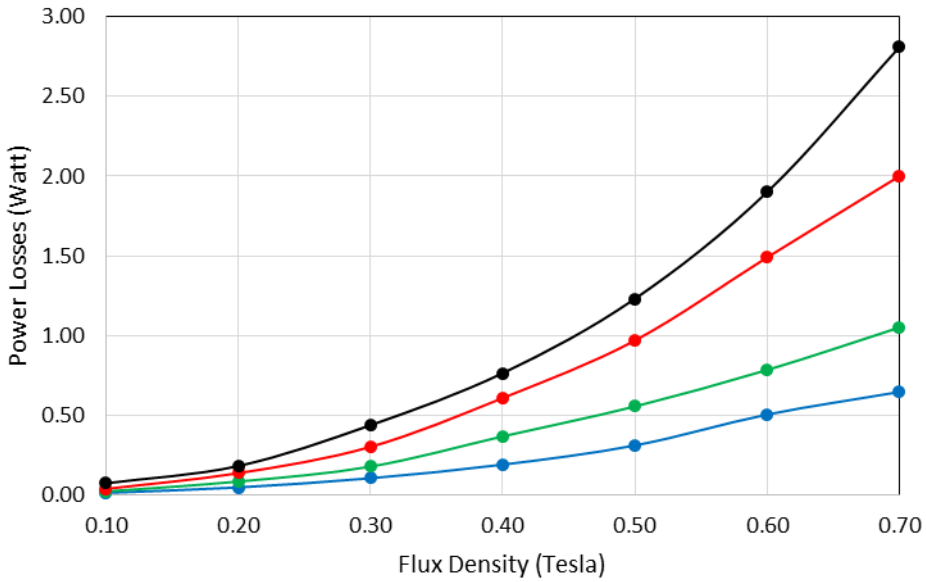


Figure 4-30 Unidirectional eddy current setup: FE results of power losses

4.5 VALIDATION AND EXPERIMENTAL RESULTS

In order to validate the proposed methods, a purposely-built experimental set-up is manufactured. This is shown in Figure 4-31, where the set-up components can be observed and the overall scheme is shown in Figure 4-32.

The material characterization for the two configurations explained in Section 4.4.2 is thus performed experimentally on the setups shown in Figure 4-32. Both the Unidirectional Current Condition Set-up and the Bidirectional Current Condition Set-up are tested in order to characterize the required material to be used for the design and optimisation stages of the TLPM motor development.

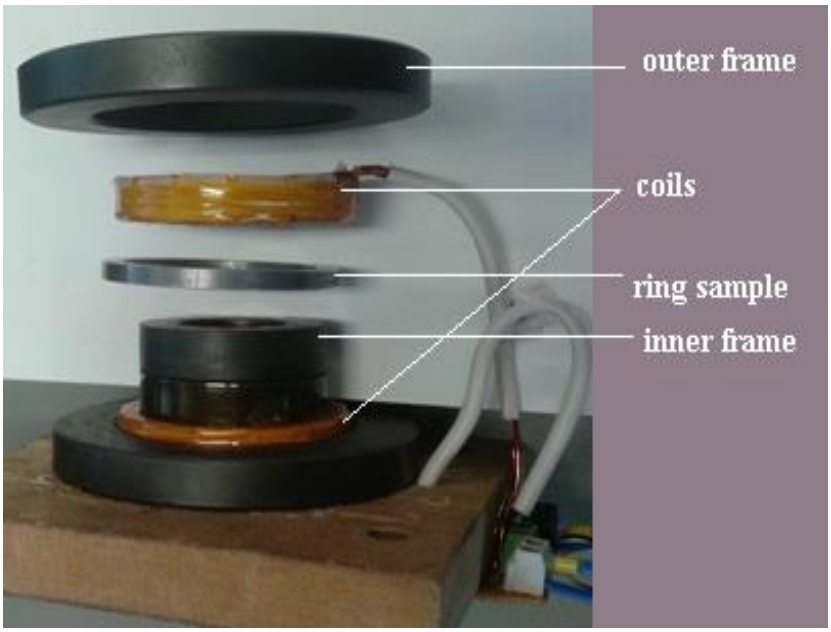


Figure 4-31 The experimental set-up components

The core losses that are experimentally obtained for the ring sample which represents the 'tooth material' by the Bidirectional Current Condition Set-up are shown in Figure 4-33. Figure 4-34 illustrates the core losses of the machine 'edges sections' obtained by the Unidirectional Current Condition Set-up.

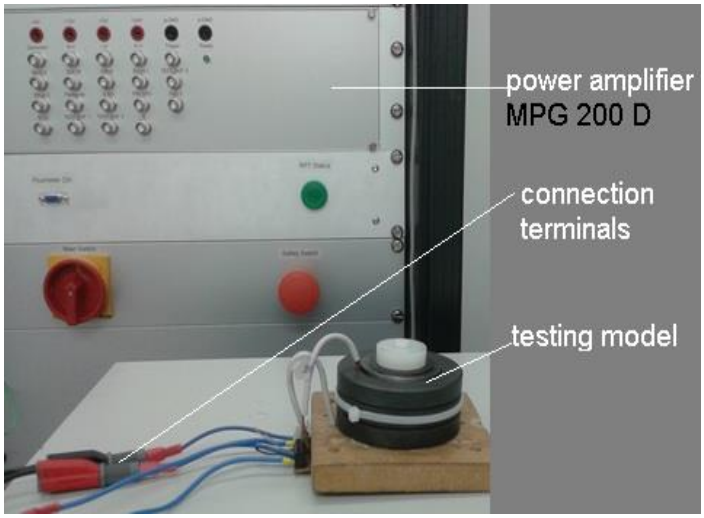


Figure 4-32 The Complete experimental set-up

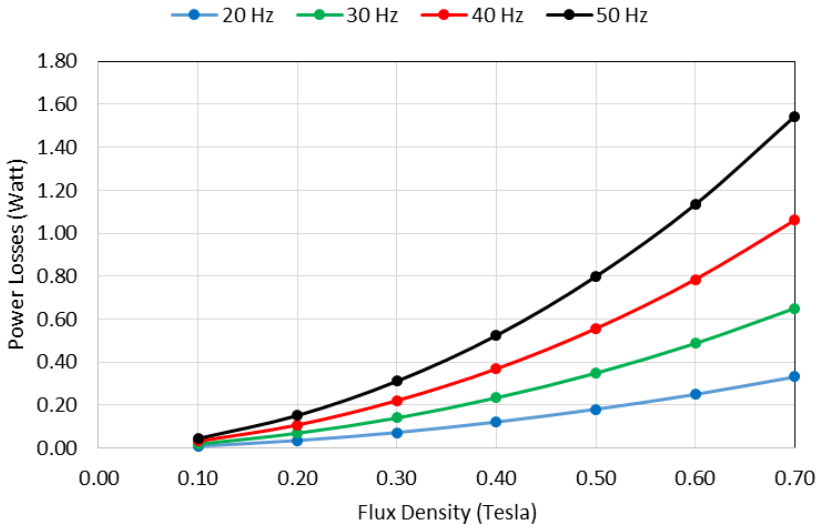


Figure 4-33 Bidirectional eddy current setup: experimental results of power losses

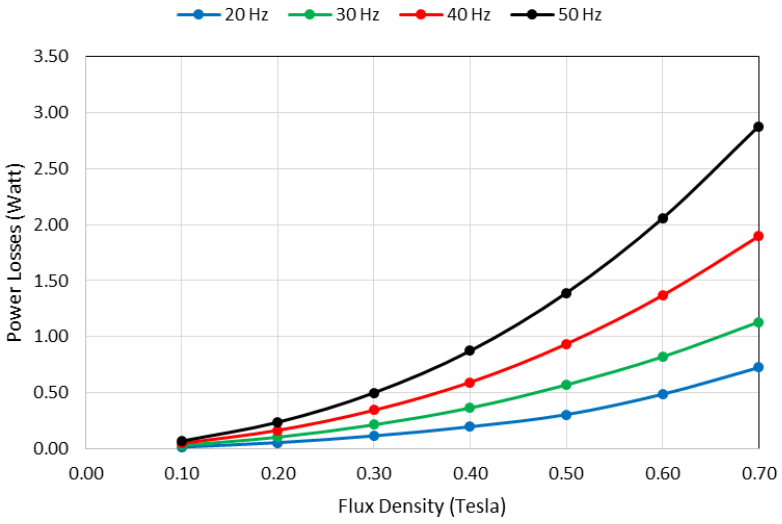


Figure 4-34 Unidirectional eddy current setup: experimental results of power losses

Figure 4-35 compares the results obtained from the 3D, FE models with those achieved experimentally. Excellent similarity is achieved, thus validating the proposed models.

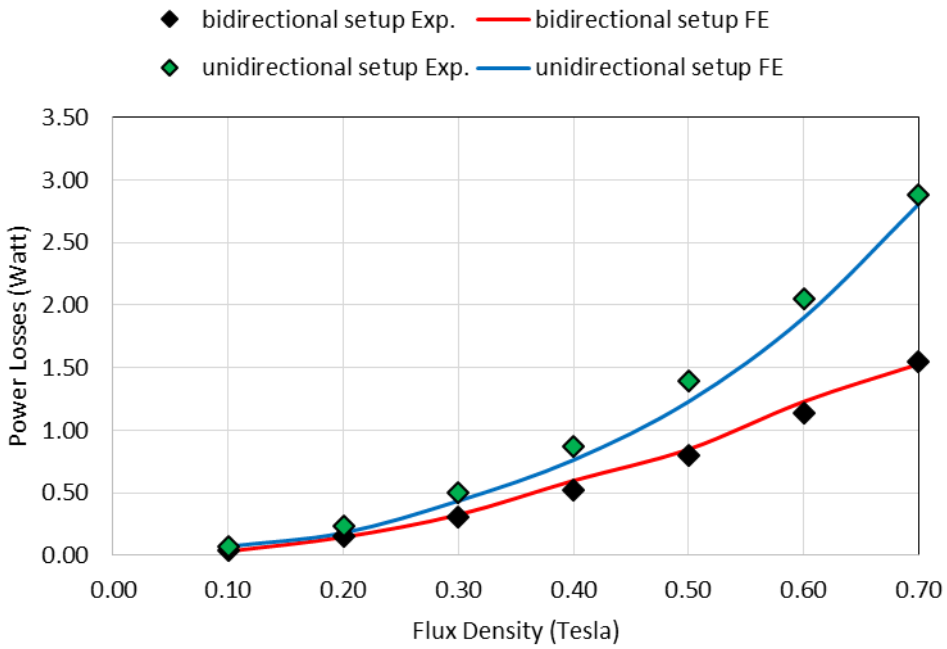


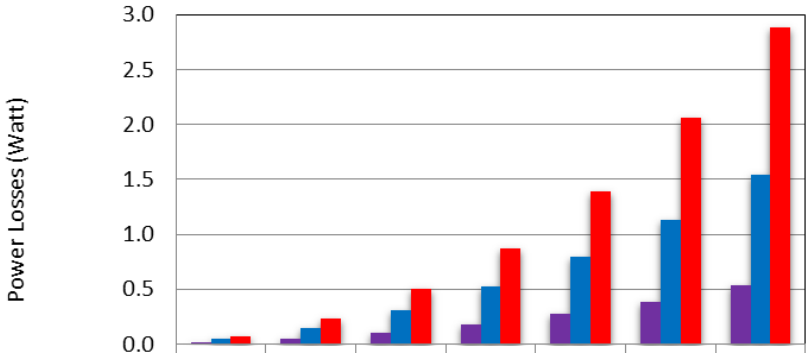
Figure 4-35 FE and Experimental results of power losses of proposed methods at 50 Hz

4.6 CONSIDERATIONS ON THE CHARACTERIZATION METHODS

In order to fully appreciate the significance of the proposed methods, a comparison between the resulting eddy current losses from the above-mentioned methods is illustrated in Figure 4-36. The objective of this is to illustrate and emphasize the difference in the losses calculations that arise from using inaccurate material data based on inappropriate characterisation methods.

The eddy currents losses depend not only on physical factors, such as magnetic and electrical characteristics, but also on the geometrical shape and size [131].

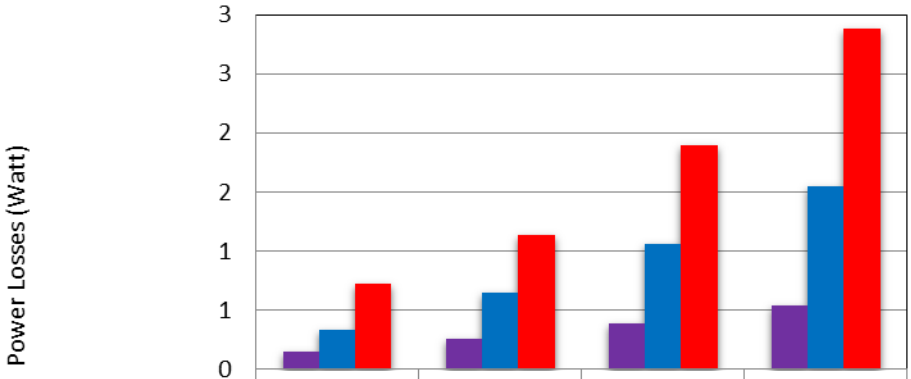
Moreover, the resistance of the eddy current path depends strongly on the sample shape and aspect ratio AR, given in (4-4).



	0.1	0.2	0.3	0.4	0.5	0.6	0.7
Conventional method	0.01	0.05	0.11	0.18	0.27	0.39	0.53
Two directions condition	0.04	0.15	0.31	0.52	0.80	1.13	1.54
one direction condition	0.07	0.24	0.50	0.87	1.39	2.06	2.88

Figure 4-36 power losses for three methods, at different B and f = 50Hz

The classical toroidal method of Figure 4-6 results in a very low eddy current loss, while the proposed methods of Figure 4-15 indicate a much greater component of eddy current loss. This illustrates the significant under-estimation of eddy current losses if traditional methods are used to test and characterize materials being used in unconventional magnetic circuits. In traditional method, the eddy currents circulate in the plane which is perpendicular to flux lines. Obviously, such an error in the correct estimation of losses can have a severe impact on the design of an electrical machine that makes use of an unconventional magnetic circuit. Figure 4-37 shows the relation between the eddy current losses of all the mentioned methods for different frequencies but at a fixed *B* of 0.7T.



	20 Hz	30 Hz	40 Hz	50 Hz
Conventional method	0.15	0.26	0.39	0.53
bidirectional eddy current	0.33	0.65	1.06	1.54
unidirectional eddy current	0.72	1.13	1.90	2.88

Figure 4-37 power losses for three methods, at different f and B=0.7 T

4.7 HIGHLIGHTS OF THE CHAPTER AND CONTRIBUTION.

The main highlights and contribution to research from this chapter can be summarised in the following list:

- A detailed analysis of core losses in magnetic circuits that have conventional and unconventional flux behaviour.
- A new method to characterise solid material being used in unconventional magnetic circuits.
- Numerical and experimental validation of this new method.

4.8 CONCLUSION

In this chapter, a new method of magnetic material characterization was proposed which provides more accurate results for losses prediction and accurate characterization of solid magnetic materials used in unconventional electrical machines.

The new method significantly improves on the conventional method by its ability to map the full losses developed from non-standard flux and eddy current behaviour, which have been shown to be significantly higher than predicted by existing methods. The implementation of this technique has also highlighted the significant under-estimation of losses that the ‘classical’, toroidal ring method provides when non-standard flux and eddy current distributions are present.

As a final remark on the proposed methods, it is clear that significant eddy current loss is identified when using the Unidirectional Current Set-up, with lower loss resulting from the Bidirectional Current Set-up. However, both methods have been shown to result in significant improvements in terms of accuracy related to predicting core losses in unconventional magnetic circuits, over the classical toroidal ring set-up. Note that there is a relative difference between the measured losses of the proposed methods and the real machine due to the differences in scale and shape.

5. EDDY CURRENT REDUCTION TECHNIQUES

5.1 INTRODUCTION

In this chapter, the eddy current distribution of the tubular machine of [7], when the laminated stator has been replaced with a solid stator, is analyzed. As mentioned above, the use of a solid material comes at the cost of an increased eddy current loss. Thus, this chapter is focused on proposing a number of eddy current reduction techniques for solid core materials that will reduce the impact of such materials on losses and efficiency. These techniques are illustrated and analyzed using FE models, after which experimental validation work was carried out to validate and identify the optimal method which can be employed in TLPM machines.

A dedicated apparatus, MPG 200D, combined with the new material characterization method described in Section 4.4 is used to test and investigate the validation of the proposed methods. Then, these eddy current reduction techniques are implemented into the design process of the selected machine using 3D analysis.

5.2 EDDY CURRENT BEHAVIOR IN SOLID MATERIALS

Ferromagnetic metallic materials such as iron *Fe* feature a relatively high electrical conductivity, which makes them unsuitable for high frequency *a.c.* applications in solid form [132].Virtually, all types of electromagnetic devices are subject to Ohmic losses due to induced eddy currents in electrically conductive materials. These eddy currents are generally caused by an external time varying current [133]. The key problem is that the prediction eddy currents generated inside any solid

electrically connective materials is highly complicated. It is practically affected by the part shape and skin effect in addition to the flux linkage, frequency, permeability and material resistivity [131, 134, 135].

The skin effect is found in all conductors subjected to *a.c.* magnetic field, but is much more pronounced for ferromagnetic conductors than for a non-ferromagnetic conductors for the same conductivity. Equation (5-1) shows the penetration depth $\delta_{(m)}$ (or skin depth) of the eddy currents. It can be seen that it is inversely proportional to the square root of electrical conductivity $\boldsymbol{\sigma}$, magnetic permeability μ and the frequency of the exciting current f [136, 137]. The penetration depth is shown in Figure 5-1.

In solid materials, the eddy current is strongest at the surface of the material and decrease in strength below the surface. The standard depth of penetration or skin depth can be defined as the depth that the eddy currents are only 37% as strong as they are on the surface.



Figure 5-1 the eddy current phenomena

$$\delta = \sqrt{\frac{1}{\pi \cdot f \cdot \mu \cdot \sigma}} \quad (m) \qquad (5\text{-}1)$$

Bu using (5-1), the relative penetration depth, or penetration depth ratio, of the flux inside the tooth of solid material under a time varying field is shown in Figure 5-2, which represents the penetration depth normalized to the tooth width, this figure highlights the penetration depth variation as a function of frequency *f* and $\mu(B)$, where $\mu(B)$ is the material permeability measured at different flux density *B*. In this calculation the nonlinearity of magnetic permeability was taken into consideration. The results have been normalized vs. the width of the tooth measured from the middle centre line of the tooth.

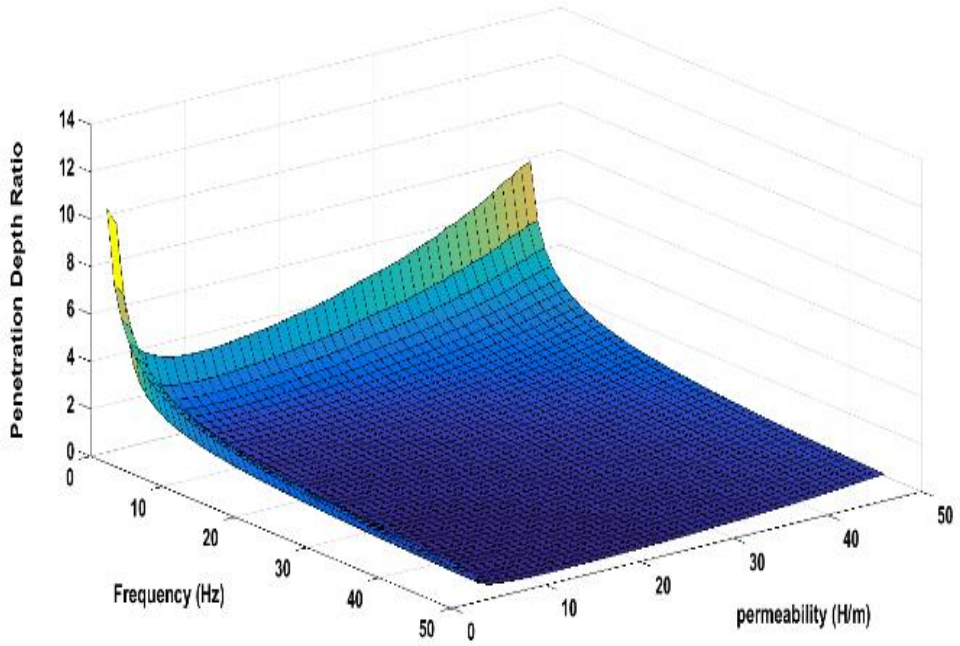


Figure 5-2 relative penetration depth of solid tooth

The distribution of magnetic field, electric field and eddy current direction inside sold material with thickness ***d*** are given in [138] and shown in Figure 5-3, where H_x and E_x are the magnetic field strength and electrical field strength in z-axis and y-axis directions respectively.

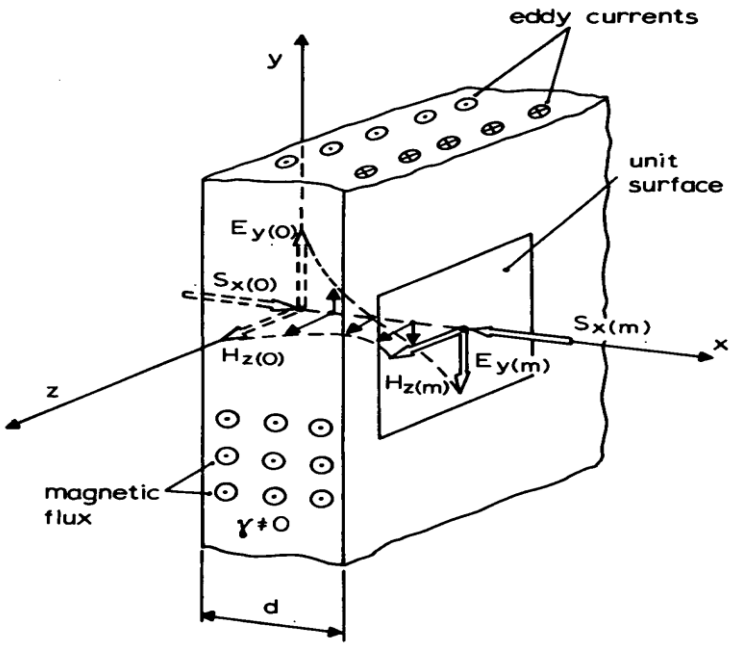


Figure 5-3 electromagnetic field vectors in ferromagnetic material[138]

With certain assumption of uniform magnetic distribution along the z-axis (no skin effect) and uniform material, the power losses due to the eddy current P_e per unit mass can be calculated using (5-2), Where ***D*** is the material mass density and *d* is the sample thickness, ρ is the material resistivity.

$$P_e = \frac{\pi^2}{6} \cdot \frac{B^2 \cdot d^2 \cdot f^2}{\rho \cdot D} \qquad (5\text{-}2)$$

The eddy current of TLPM motor can be mathematically described by using Maxwell's equations. In general, coils with time varying currents produce an alternating *H* in the direction which can be identified by the right hand rule. This field induces eddy currents in an electrically conducting magnetic material in the opposite direction of the excitation current [139]. By expanding Maxwell's equation of induced eddy current (5-3) into cylindrical coordinates (5-4) [18].

$$\nabla \times \mathrm{H} = J \qquad (5\text{-}3)$$

$$J = a_r\left(\frac{1}{r}\frac{\partial \mathrm{H}_z}{\partial\theta} - \frac{\partial \mathrm{H}_\theta}{\partial \mathrm{z}}\right) + a_\phi\left(\frac{\partial \mathrm{H}_r}{\partial \mathrm{z}} - \frac{\partial \mathrm{H}_z}{\partial r}\right) + a_z\left(\frac{1}{r}\frac{\partial (r\mathrm{H}_\theta)}{\partial r} - \frac{1}{r}\frac{\partial \mathrm{H}_r}{\partial\theta}\right) \qquad (5\text{-}4)$$

Assuming that the eddy current is rotating tangentially in θ direction only, then (5-4) can be simplified to (5-5).

$$J_{ring} = a_\theta\left(\frac{\partial \mathrm{H}_{r,ring}}{\partial \mathrm{z}} - \frac{\partial \mathrm{H}_{z,ring}}{\partial r}\right) \qquad (5\text{-}5)$$

5.3 CONSIDERATIONS ON WINDING CONFIGURATIONS AND EDDY CURRENTS

In distributed winding configurations, high-order time harmonics in the stator current waveform and space harmonics are often considered to be negligible. However, concentrated-winding topologies are recently becoming more popular even for machines such as the TLPM motor at hand, due to a number of perceived advantages over the more common, distributed winding configuration. The stator winding of such a machine differs from that of distributed-wound TLPM machines in that each phase comprises a number of concentrated coils which are disposed adjacent to each other, which clearly can be seen in Figure 5-5 and Figure 5-6. This results in a small number of slots for a given number of poles [88] and leads to machines that are relatively inexpensive to wind [140] as the coils can be pre-wound and inserted into the slots individually. Each single tooth inside the machine has two coils, one coil in each side. These coils have currents flowing in opposite directions. Thus it can be easily deduced that the induced eddy currents in each side of the tooth have 180^o phase shift in direction between the each other and opposite to the coil current direction as shown in Figure 5-4. In this figure a single tooth has

been represented and accommodated with two coil sides, each coil carrying current in opposite direction to the other.

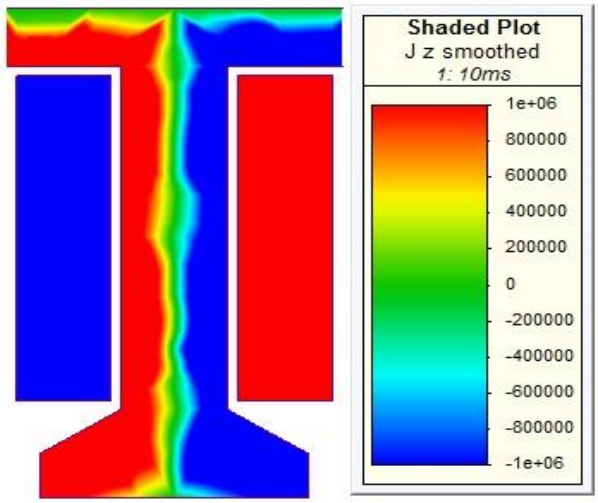


Figure 5-4 eddy current direction in single tooth and single coil

In general, there are two main types of machine windings, namely the single layer winding and the double layer winding configuration. For high performance multiphase electrical machines, multilayer concentrated windings are also used. The sequential arrangement of coils around the stator teeth is different for each types of windings. These various topologies are used in order to increase efficiency and fault tolerance, and to decrease size and manufacturing complexity [140-142].

For single layer windings, the complete slot is occupied only by one coil side. For the TLPM machine winding configurations such as that of Figure 5-5, it can be seen that each tooth may lie between two coil sides that carry currents for the same phase or different phases. This leads to the condition that some teeth may lie between two coil sides carrying currents in the same or opposite directions with equal or different magnitudes during specific time instants.

For a double layer winding, each slot hosts two identical coils, displayed either in the top and bottom halves or in the right and left halves of the slot. Coils located at the two sides of a tooth connected in series as shown in Figure 5-6. This figure showing the coil arrangement of the double layer winding of the TLPM motor. Thus, each tooth always lies between two coil sides that carry current in the same magnitude and opposite directions for the same phase. In modern multi-layer winding configuration machines [143], some teeth might lie between coils carrying currents for more than two phases.

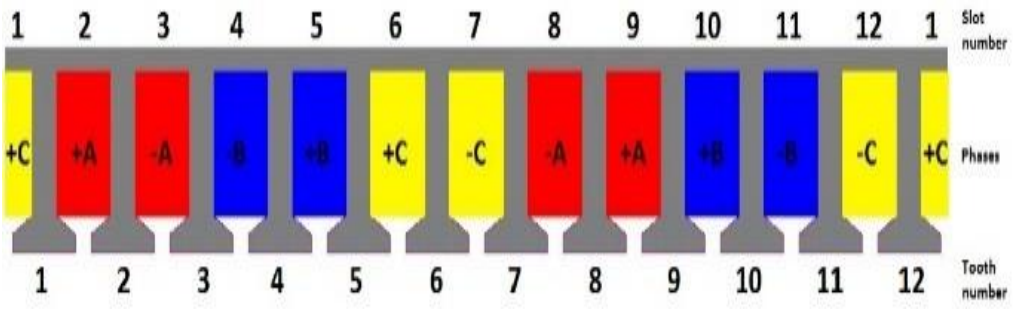


Figure 5-5 Single layer winding of 12 slot TLPM machine

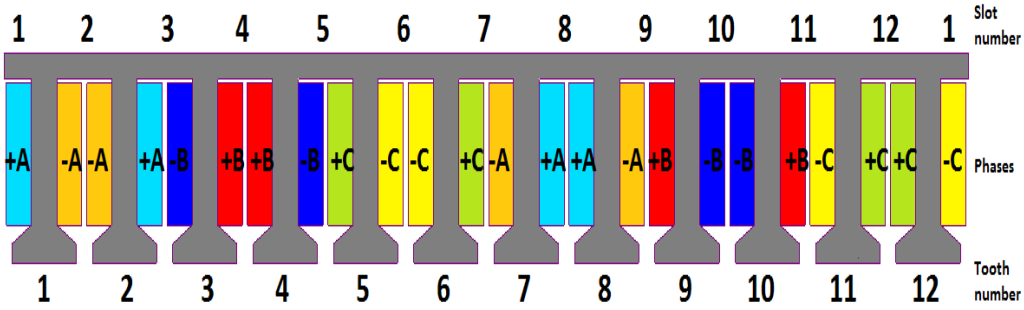


Figure 5-6 Double layer winding of 12 slot TLPM machine

The instantaneous total current flowing in each slot is equal to the summation of the instantaneous total currents passing through each coil side inside the slot. Assuming the three phase machine windings are supplied with balanced three phase sinusoidal currents, as described in (5-6), then (5-7) shows the general form, derived

for the representation of the total current inside each slot, for example, for a double layer winding configuration; $i_{slot(3)}(t) = i_{phase(a)}(t) + i_{phase(b)}(t)$. In the case of single layer windings, the total current in each slot is the same as the phase current of the slot. It is important to note that the TLPM machine is assumed to be infinite length.

$$i_{phase}(t) = I_{\max} \sin(\omega t + \vartheta)$$

$$\begin{aligned} Where\ \vartheta &= 0 \quad for\ phase\ A \\ &= 2\pi/3 \quad for\ phase\ B \\ &= 4\pi/3. \quad for\ phases\ C \end{aligned} \tag{5-6}$$

$$i_{slot(n)} = \sqrt{3}.I_{\max}.\cos(\omega t - \frac{(n+1)}{2}.\frac{\pi}{3}).$$

$$where\ n = 1, 3, 5, \ldots. \tag{5-7}$$

$$i_{slot(m)} = -2.I_{\max}.\sin(\omega t - \frac{(m-2)}{2}.\frac{\pi}{3}).$$

$$where\ m = 2, 4, 6, \ldots.$$

Considering (5-6) and (5-7), the total current follow in each slot is as shown in Figure 5-7. Basically, the total currents flowing through the 7th-to-12th slots are similar to those of the 1st-to-6th slots with a phase shift equal to π.

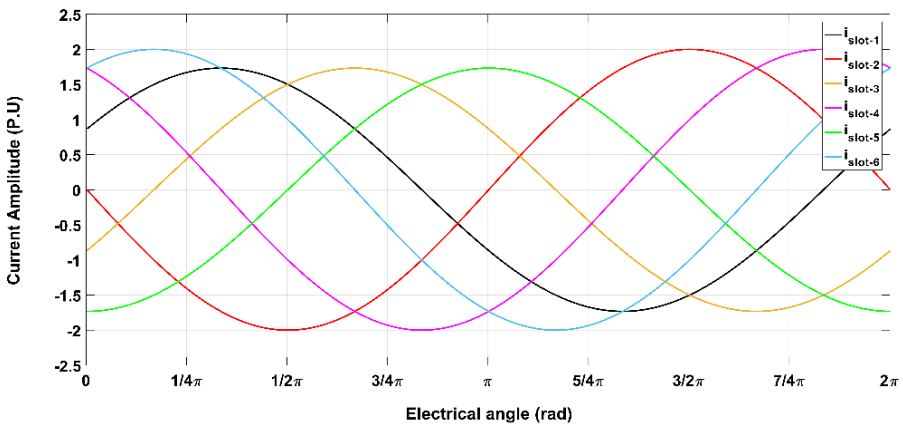


Figure 5-7 instantaneous total slot current for double layer machine

Based on (5-6), (5-7) and Figure 5-7, it can be seen that for every complete electrical cycle, each tooth situated between two coils sides will face a magnetic field strength *H* with magnitude and direction governed by the net *mmf* produced by the total current passing through coils inside the slot at each side. The generated eddy currents circulate in each tooth side in directions opposite to the inducing slots currents and this direction is varying depending on the time instant of the electrical cycle. (5-8) shows the direction of eddy current.

$$\left(\frac{\partial H_r}{\partial z}-\frac{\partial H_z}{\partial r}\right)\vec{1}_\theta = J_\theta \qquad (5\text{-}8)$$

5.4 EDDY CURRENT ANALYSES FOR DIFFERENT WINDINGS

2D FE models of the machine configurations shown in Figure 5-5 and Figure 5-6 are built and solved to investigate the eddy current behavior in each machine. Figure 5-8 shows the FE eddy current distribution map in each tooth of the selected TLPM motor for the same specific time instant, where Figure 5-8 (a) represents the single layer concentrated winding set-up and Figure 5-8 (b) represents the eddy current distribution map of a double layer concentrated winding configuration.

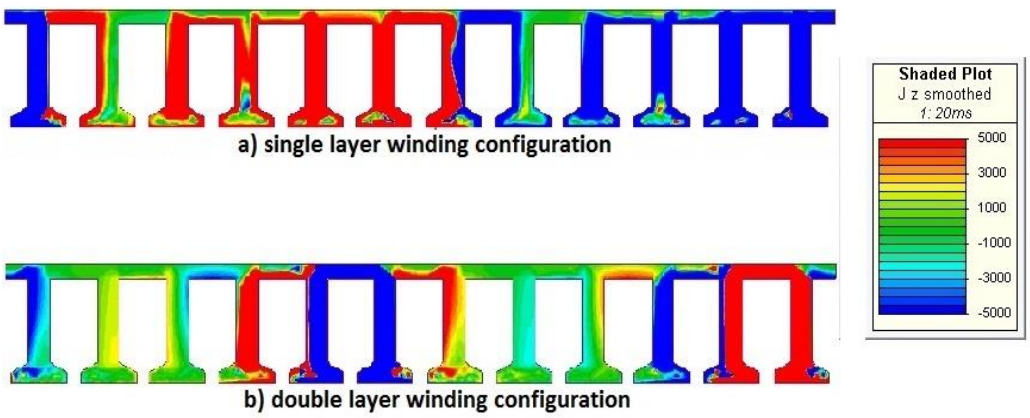


Figure 5-8 eddy current map. (a) Single layer (b) Double layer winding

Figure 5-10 and Figure 5-11 show the results of these simulations, highlighting the eddy current values and directions inside each tooth of double layer winding and single layer winding machine respectively. These figures show the eddy current variation with time inside each tooth side, shown in Figure 5-9. As described above, it can be easily observed that there are two eddy current conditions, namely the unidirectional eddy current condition, where the eddy current in both tooth sides are circulating in one direction and a bidirectional eddy current condition where the eddy current components in each tooth side have two opposite directions.

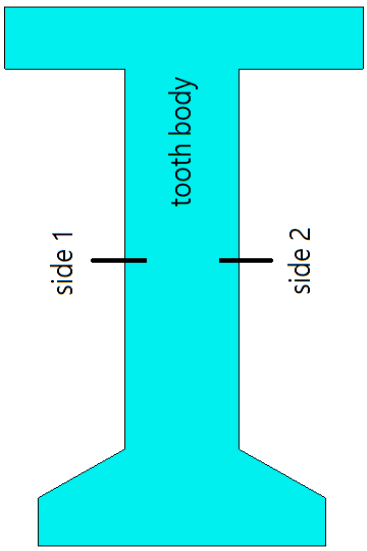


Figure 5-9 tooth sides

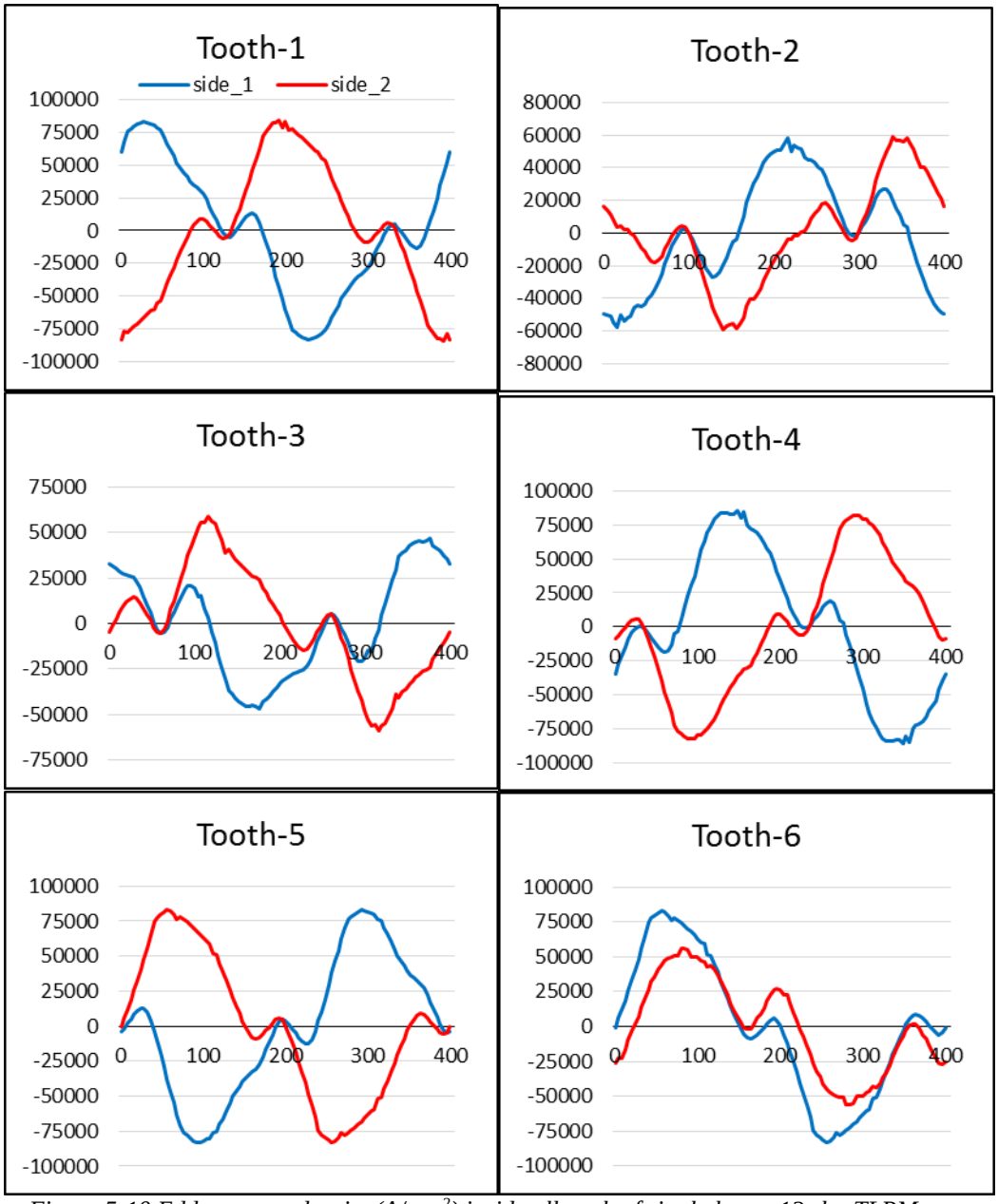


Figure 5-10 Eddy current density (A/mm^2) inside all teeth of single layer, 12 slot TLPM motor

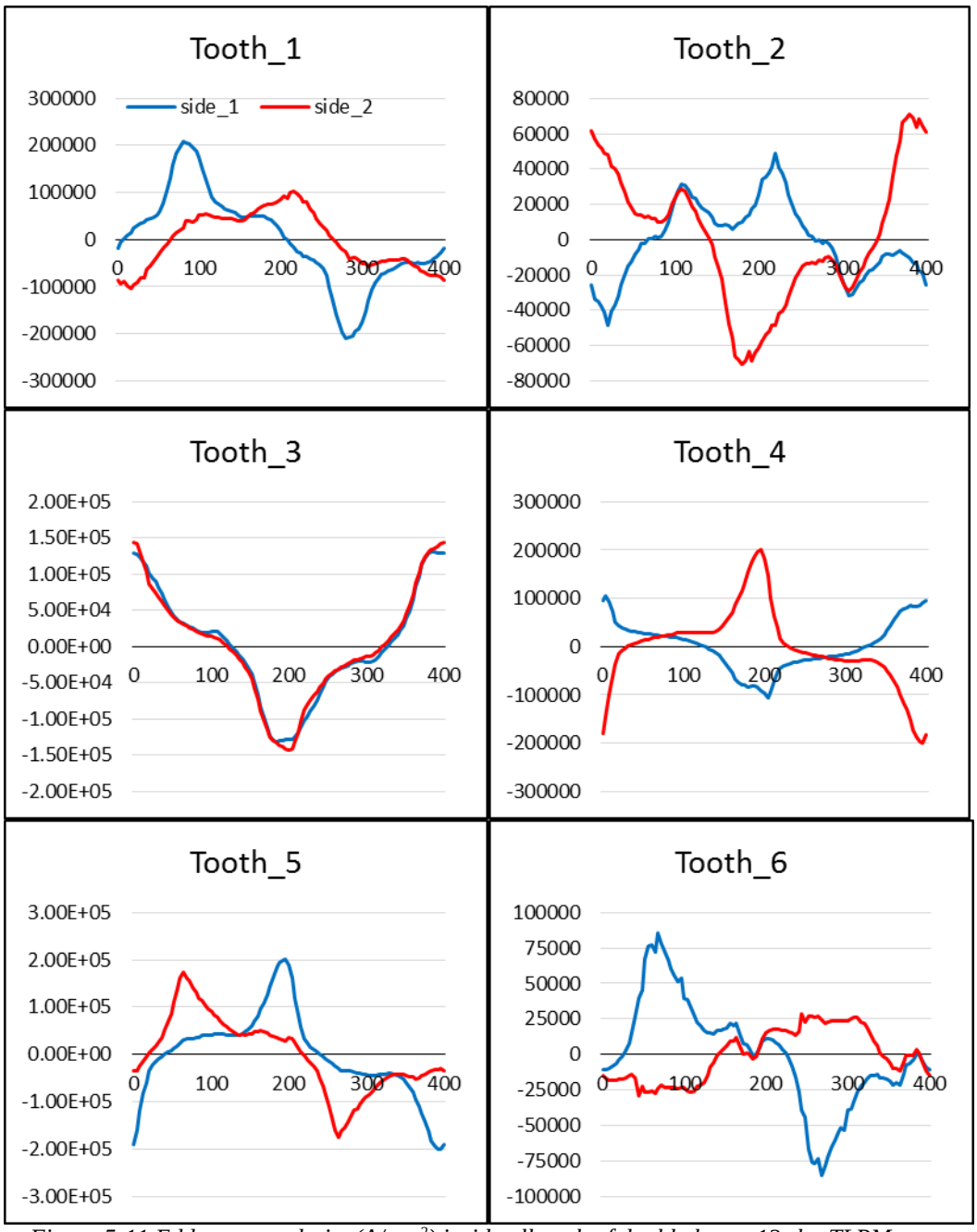


Figure 5-11 Eddy current desity (A/mm^2) inside all teeth of double layer, 12 slot TLPM motor

As can be observed in Figure 5-8, the eddy current in each tooth can be divided into two components. These components are rotating either in the same direction or in the opposite direction to each other, depending on the time instant of the phase current. Thus, the generated losses in each tooth are strongly affected by the eddy current behavior and path.

In the case of bidirectional eddy currents (the two eddy current component are rotating in the opposite direction), the two 'out of phase' eddy current components will generate losses due to two factors, namely;

1) Losses produced by the main two components of the eddy current.
2) Losses produced by the leakage current pulsating between these two main components.

For the case of unidirectional eddy currents, the eddy current losses will be generated by the complete eddy currents circulate completely in one direction inside the tooth. Then the eddy current losses of unidirectional eddy current case is predicted to be larger than the case of bidirectional eddy current. This is mainly due to the fact that the total path resistance is much lower due to the larger cross section of the effective area [144].

5.5 EDDY CURRENT REDUCTION TECHNIQUES

From Figure 5-12, It can be seen that transversely laminating a tubular machine core gives an eddy current path almost equivalent to a solid core, as it will increase the reluctance of the magnetic circuit on the motor back iron which has to be crossed by the flux between tooth segments [36]. An axially laminated core will significantly increase the resistance along the direction of the eddy current path, with a relative reduction in the stator's stack factor.

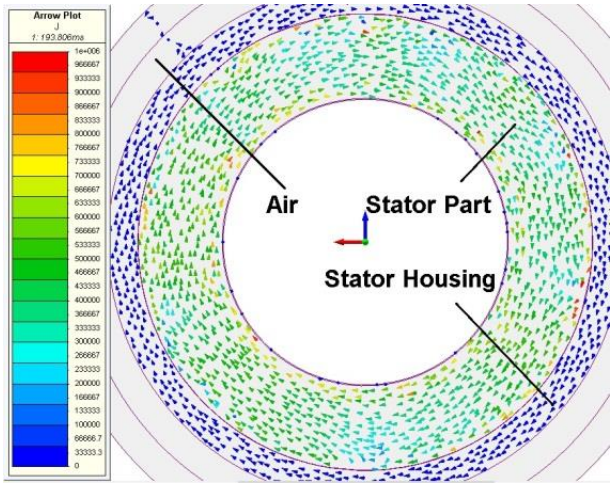


Figure 5-12 Cross sectional view of eddy current distribution in stator core

In literature, methods which are used to reduce eddy current losses in solid parts of electrical machines exist. For example, the reduction of eddy current inside the stator part of the machine can be found in [33, 36, 42], for the mover magnets in [145] and for other parts embedded inside the machine such as heat paths (HP) which are used to improve the heat dissipation of slot coils as proposed in [8].

5.5.1 The slitting technique

An effective method for eddy current reduction techniques needs to be used in this machine. The principle of such a method needs to be based on an increase of the eddy current path resistance. This can be achieved by increasing the effective length of this path without affecting the path of the main flux, which, in this case, is radial inside the tooth and axial inside the yoke part.

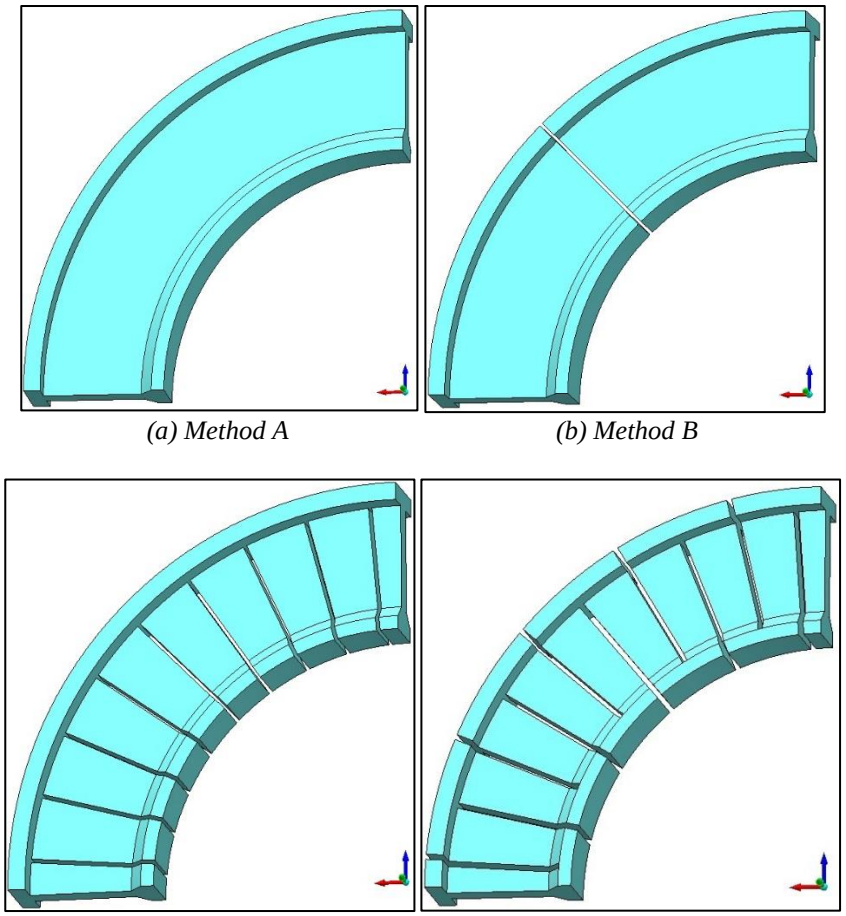
A number of such eddy current reduction methods are based on the principle of the so-called slitting technique. The stator teeth are slitted in various ways in order to implement one or more narrow ‘air-gaps’ radially along the direction of motion [11, 33, 42].

The basic concept of this methodology, relative to the TLPM motor application at hand, is illustrated according to the slitting numbers and slitting directions as shown below.

1. Figure 5-13 (a) shows the 'original', solid stator tooth. This method is referred as "Method A" (for clarity) in which the machine is constructed completely from solid material.
2. Figure 5-13 (b) shows the stator tooth when it has been cut with one radial complete slit "Method B".
3. Figure 5-13 (c) shows the unidirectional partial slit "Method C" where the stator has been slitted radially with partial slits starting from the inner surface of the tooth face.
4. The slitting technique of "Method C" has been upgraded, where a simple modification to the slitting direction been proposed and a bidirectional partial slits "Method D" introduced, as shown in Figure 5-13 (d).

"Method B", is completely different from "Method C", where in the last one a non-complete radial slits along the inner radius have been made and distributed uniformly along the inner surface in sunshine style. The reason for the uniform distribution is to keep the attractive force between the mover and the stator of the TLPM motor balanced and the radial force equal to zero.

"Method D" is very similar to "Method C" but aims to further increase the eddy current path length through applying inner-outer slits.



(a) Method A *(b) Method B*

(c) Method C *(d) Method D*

Figure 5-13 solid structures with slits

Combinations of more than one method and/or increasing the number of slits will lead to further improvements in the eddy current losses but will also increase the manufacturing complexity and cost as well as reduce the mechanical structure strength of the stator. For example, more than one-complete slit of "Method A" will considerably increase the structure complexity and will also require an external structure for mechanical support.

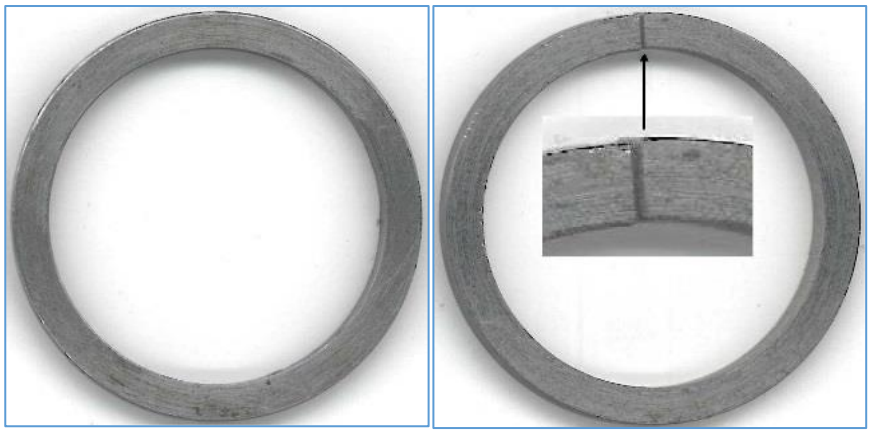
The slitting techniques of "Method B" and "Method C" are similar to those firstly proposed in [33], where a 9-slot/10-pole TLPM motor was constructed from solid material. In [33], a full transversal slit across the axisymmetric plane of the T-Shape teeth has also been added to prevent circulating currents around the entire ring. This

full slit forces the induced eddy current to be contained within the 'half tooth' and hence reduces the loss.

The main advantage of using solid material with the slitting techniques methods mentioned above (with limited number of slits) is that it has less manufacturing complexity, a higher force production at low frequencies, a high stator f_{stack}, good thermal dissipation and a good mechanical structure when compared with lamination model [33, 42]. In general, it can be easily understood that a higher number of slits results in reduced eddy current loss, but it is also important to note that the generated thrust force will also be reduced due to the consequent reduction of stator magnetic material and active area which affects the total f_{stack} of the stator part in addition to the reduction in the mechanical properties.

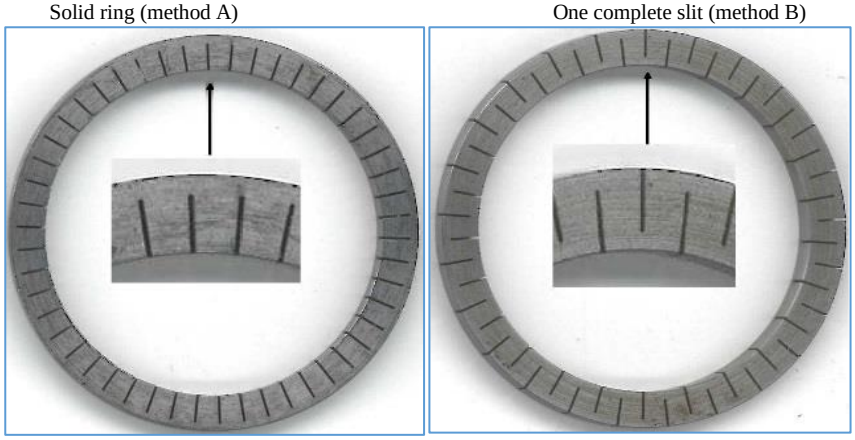
5.6 VALIDATION OF EDDY CURRENT REDUCTION TECHNIQUES, THE CONCEPTS

In order to validate the proposed eddy current reduction techniques, four EN8 ring samples were manufactured. The main specifications and material properties are illustrated in Table 4-1. These ring samples are shown in Figure 5-14, where; Figure 5-14(a) represents a solid ring, corresponding to "Method A", Figure 5-14(b) represents a solid ring with one-complete slit, corresponding to "Method B", Figure 5-14(c) represents a solid ring with 50 one directional partial slit, corresponding to "Method C", and Figure 5-14(d) represents a solid ring with 50 two directional partial slits, corresponding to "Method D".



(a) Solid ring (method A)

(b) One complete slit (method B)



(c) Unidirectional partial slit (method C)

(d) Bidirectional partial slit (method D)

Figure 5-14 Prototype ring samples under test

As mentioned earlier, the number of slits is limited by the mechanical considerations. From a magnetic properties point of view, increasing the number of slits affects positively the eddy current losses reduction at the cost of a reduction in machine performance. To evaluate the optimum number of slits of the ring samples, two factors have been taken into consideration. The first factor is the effect on the total electrical resistance along the azimuth direction (eddy current path) of the proposed slitting. This factor is calculated from on the basic equation of electrical conductance of any conductor given in (5-9), where G is the conductance of the object in Siemens, $\boldsymbol{\sigma}$ is the electrical conductivity of the material in

Siemens/meter, L_{eff} is the effective length of the ring in meter and A_{eff} is the effective area of the ring in meter^2.

$$G = \frac{\sigma \cdot A_{eff}}{L_{eff}} \tag{5-9}$$

The second factor is the total reduction in the inner surface area of the ring sample under investigation when the slitting is implemented. This is equivalent to the reduction on the active area of inner stator surface of the TLPM motor where the force is produced, as shown in (3-4).

Figure 5-15 shows the variation of these two factors with the slitting number, normalized to the standard solid ring values. It indicates that a slit number of approximately 50 to 60 is the optimal value, when considering the relationship between the two factors mentioned above.

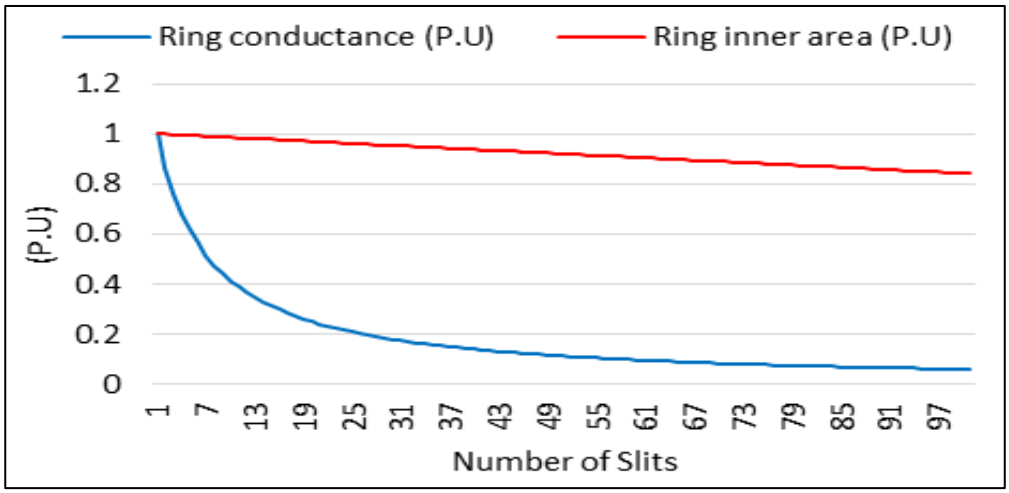


Figure 5-15 slitting number and its effects

The samples have been tested with the procedure shown in Section 4.4.2 and the eddy current losses recorded using MPG 200 D described in [110]. The tests were

conducted with the “bidirectional eddy current ring set-up” and “unidirectional eddy current ring set-up”. A photo of the test setup is shown in Figure 5-16.

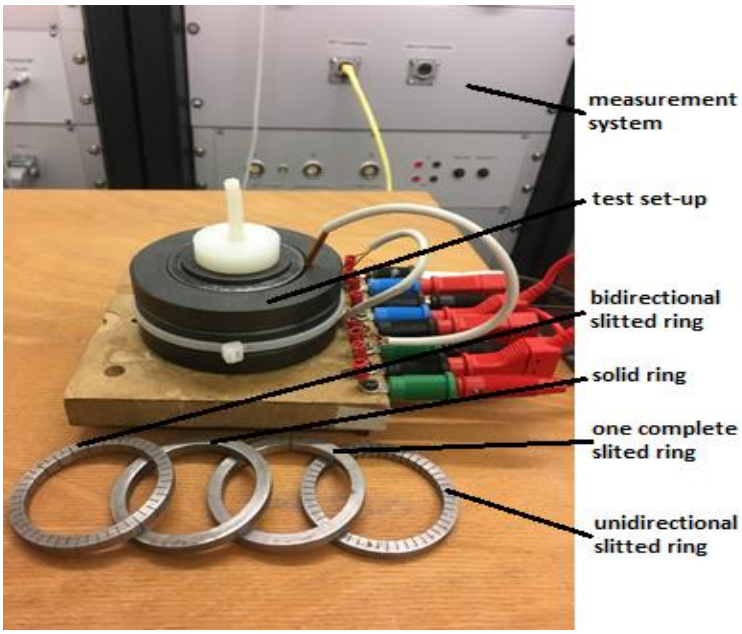


Figure 5-16 the test setup with ring samples

5.6.1 Method A - Experimental tests of solid ring

The eddy current losses of a solid ring (without slitting), using the two set-ups, with different frequencies is shown in Figure 4-21 and Figure 4-26, Chapter 4. It can be seen that there is a variation in the measured eddy current losses between the two methods. This is because, in the unidirectional ring set-up, the eddy current is passing through a larger effective cross-sectional area which in turn, directly increases the ring conductance. As explained in [144], this is done to indicate the different nature of the eddy current paths according to which tooth of the TLPM motor is being considered.

5.6.2 Method B - One complete slit method

Considering the extra losses being incurred due to eddy current pulsations "leakage current" between the two components inside the ring sample tested with 'bidirectional eddy current set-up', adding one complete slit will only slightly affect the main eddy current path. In fact, this method will tend to increase the "leakage current" between these two components of the eddy current which causes an overall increase in eddy current losses. This behaviour is clearly recognized in Figure 5-17. In this figure, the 'Method B' is compared with the original solid results. It can be seen that at 50 Hz, the eddy current losses is increases by 10% and 22% at 25 Hz.

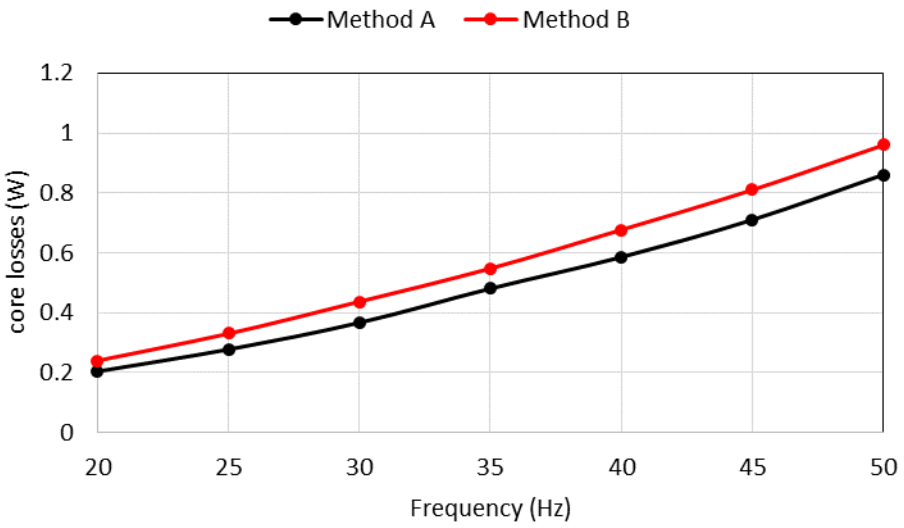


Figure 5-17 Power losses of bidirectional eddy current "Method B"

For the same sample, when the "unidirectional eddy current condition" is applied, the eddy currents rotate only in one direction facing lower resistance. Thus, the losses inside this ring sample will be much higher than the first condition [144]. Therefore, adding one-complete slit will force the eddy current to find a return path, and greatly decrease the eddy current loss due to increasing the effective length of the eddy current path. Figure 5-18 shows that with the "one complete slit" method

a reduction of losses by 64% and 72% has been achieved at 50*Hz* and 25*Hz* respectively, when it is compared with the solid ring results.

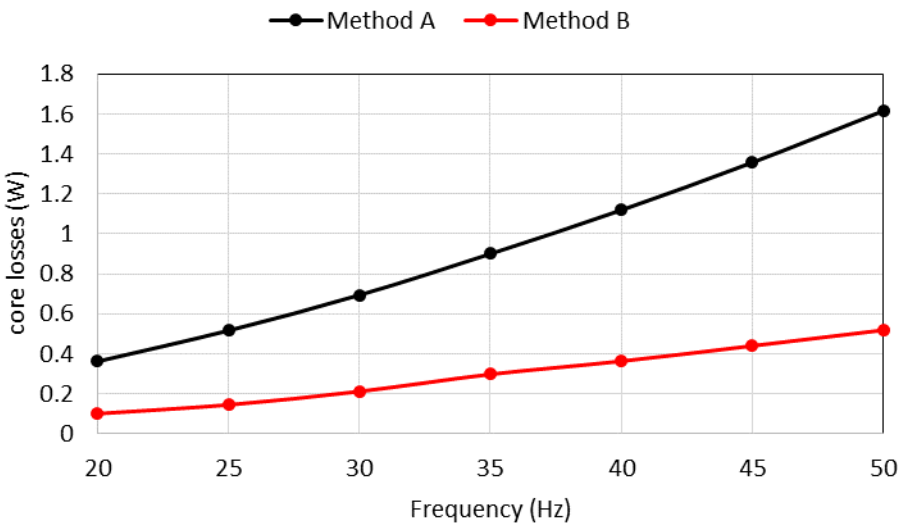


Figure 5-18 Power losses of unidirectional eddy current "Method B"

5.6.3 Method C – one direction partial slits method

Both eddy current conditions have been applied to test the eddy current losses of the ring sample shown in Figure 5-14 (c) with 50 uniformly distributed radial partial slits. It can be seen that this method is very effective when both eddy current conditions of [144] have been applied. Considering the "two direction eddy current condition", the advantage of this method is to increase the effective resistance of the ring sample. While the "leakage current" is increased, however the main two components of the eddy current are also greatly decreased. For the other case of "one direction eddy current condition", this method is also very effective because there is no "leakage current" and the eddy current faces a high resistance along the circulating path around the ring sample.

These eddy current losses improvements can be observed in Figure 5-19, where for the “two direction eddy current condition” test, improvements of 34% and 29% over the solid ring concept have been achieved at 50Hz and 25Hz respectively. The resulting benefits are further increased when the “one direction eddy current condition” is applied for the same operating frequencies, where 60% and 57% losses reduction are achieved, relative to the solid ring losses as shown in Figure 5-20.

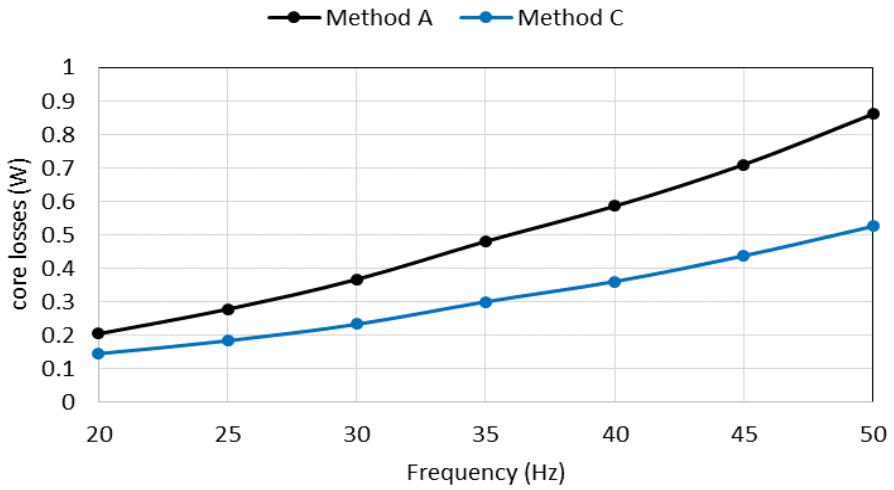


Figure 5-19 Power losses of bidirectional eddy current “Method C”

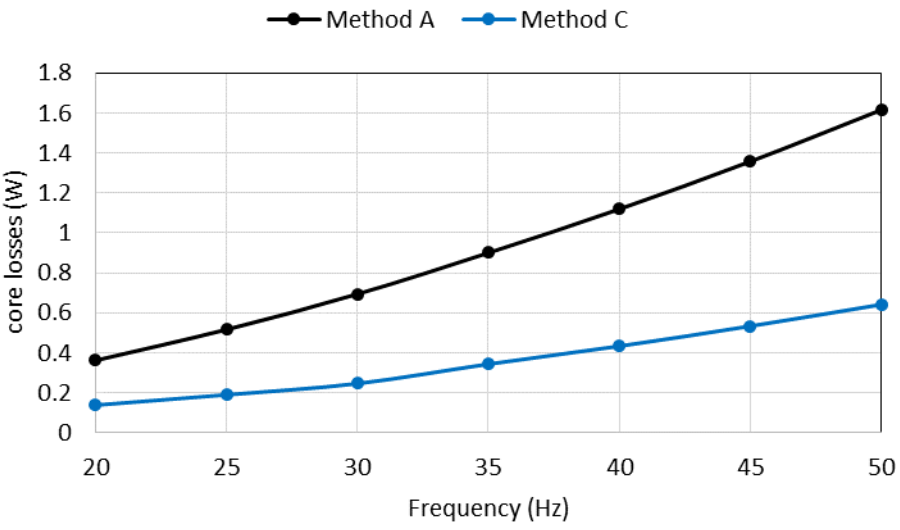


Figure 5-20 Power losses of unidirectional eddy current at 0.5 Tesla “Method C”

5.6.4 Method D – two directions partial slits method.

The bi-directional slitting method with 25-inner slits and 25-outer slits alternating along the sample circumference is presented and shown in Figure 5-14 (d). This configuration is very similar to the model described in "Method C", but aims to further increases in the length of the eddy current path. Even though the actual difference between the parts in Figure 5-14 (c) and Figure 5-14 (d) is minimal, however an incremental improvement can still be achieved with the "two direction partial slits" method. This is due the fact that in "Method C", the eddy current has a clear path on the outer surface of the ring sample, while in "Method D", the eddy current path is also interrupted by the outer slits.

As can be seen in Figure 5-21 and Figure 5-22, comparing this "Method D " with "Method C", the eddy current losses for the "first testing condition" have been reduced by approximately 12% at all frequencies. While, for the second condition, the improvement is increased by 16% and 10% at 50Hz and 25Hz respectively.

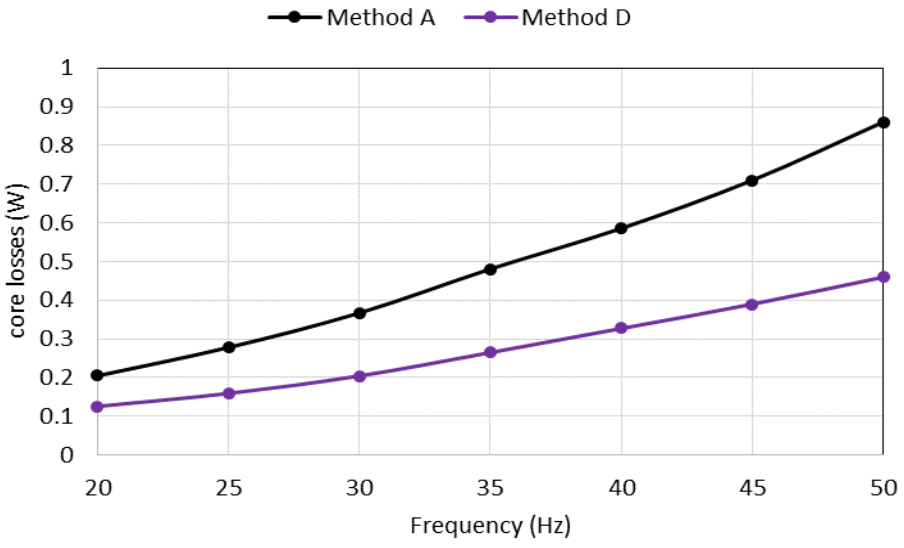


Figure 5-21 Power losses of bidirectional eddy current "Method D"

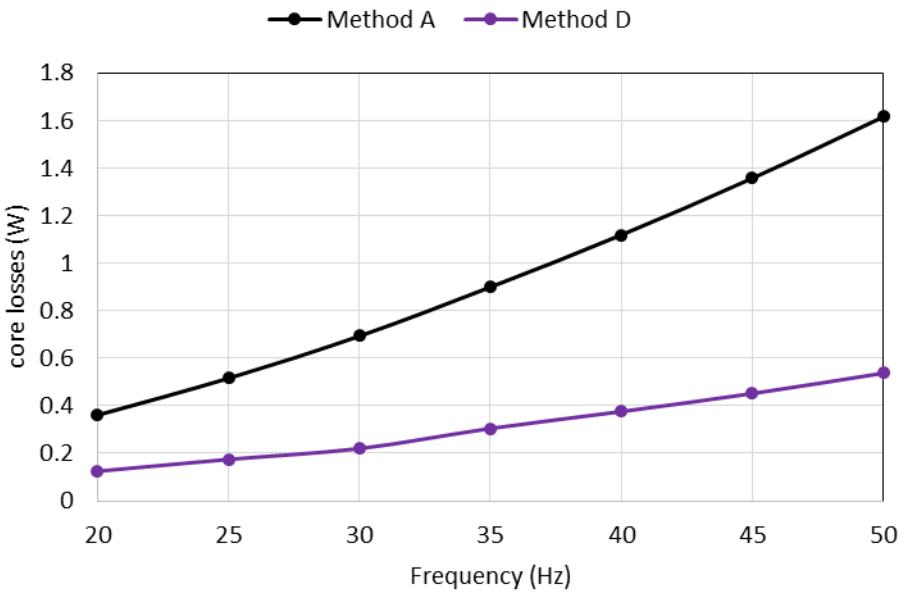


Figure 5-22 Power losses of unidirectional eddy current "Method D"

5.7 FURTHER COMPARISONS

Figure 5-23 and Figure 5-24 show the overall compression of all methods at excitation frequency equal to 25 Hz and flux density of 0.5 Tesla for both proposed set-ups. A final investigative study aimed at an in-detail comparison of the methods described above was finally done. The same ring samples were also tested for different flux densities (while maintaining the same current conditions). Figure 5-25 and Figure 5-26 show the eddy current loss measurements for all the slitting methods at fixed frequencies (50Hz) and different flux densities. As can be observed, this indicates that all slitting methods demonstrate the same behavior, even with different flux densities.

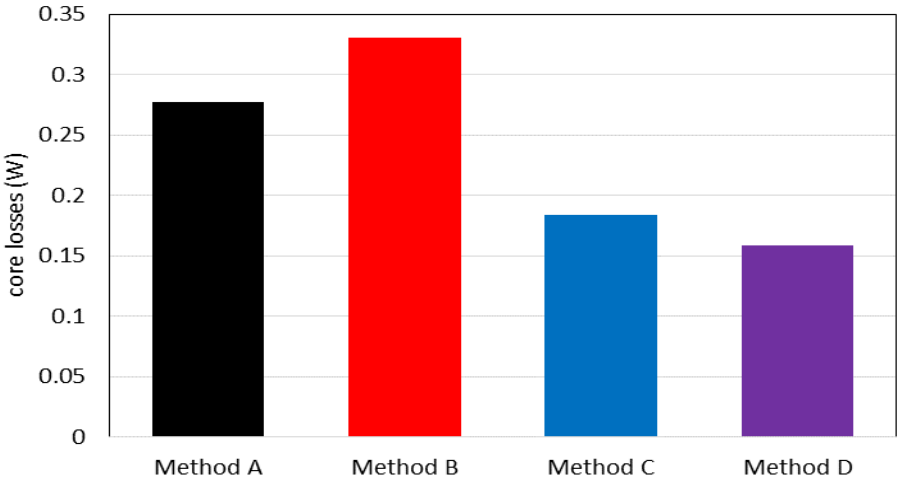


Figure 5-23 Bidirectional eddy current condition setup comparison

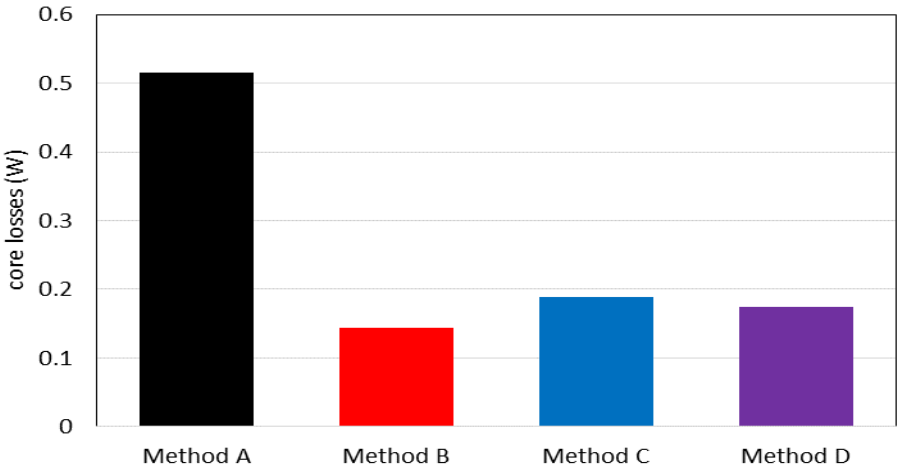


Figure 5-24 Unidirectional eddy current condition setup comparison

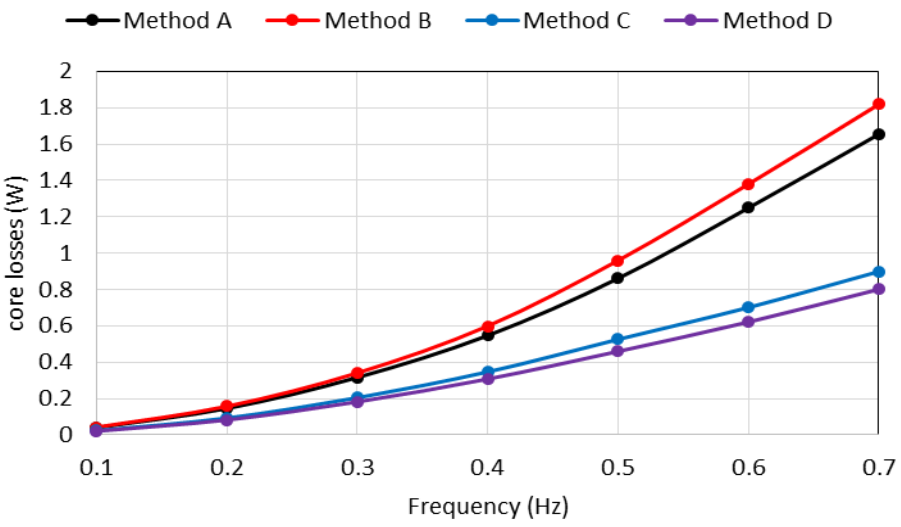


Figure 5-25 powerlosses of Bidirectional eddy current, all methods

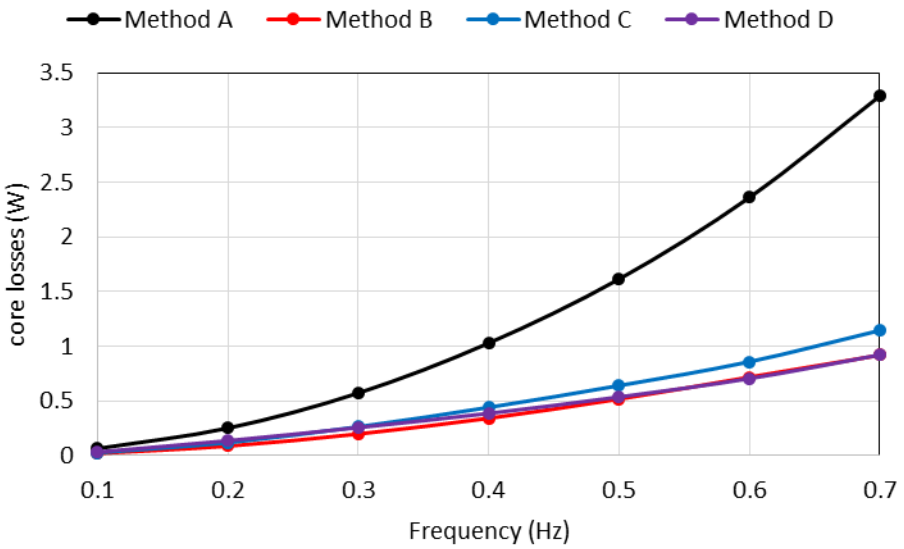


Figure 5-26 Power losses of unidirectional eddy current, all methods

5.8 IMPLEMENTATION

Having achieved a full characterization of the loss and magnetic properties of the material being implemented with such techniques as described above, then all the information and data is imported into the materials libraries in the FE software used for the design process of the TLPM motor in [7]. The machine models with the updated information and the eddy current reduction techniques implemented were then tested for the same ratings and operating points as for the original machine. This provides the basis for a careful comparison of performance in terms of the generated thrust force and machine losses.

5.8.1 Solid Construction with Radial Complete Slits

Figure 5-27 compares the results of TLPM motor when different number of complete slit is applied, i.e. one complete slit given in Figure 5-13 (b), two complete slits, four complete slits and solid core machine at different frequencies and current

density of 17 A/mm^2. From these results it can be observed that the largest losses reduction with respect to the solid configuration losses can be achieved when the 'one complete slit' is applied. Adding more than one slit will tend to increase the improvement but increasing the number of complete slits will also tend to increase the cost and manufacturing complexity and thus defeat the scope of this work.

It is wise to highlight that this method is mainly effective for each tooth that is under the condition of a unidirectional eddy current. Its effect is negative for the objectives at hand, when the tooth is under the bidirectional eddy current condition.

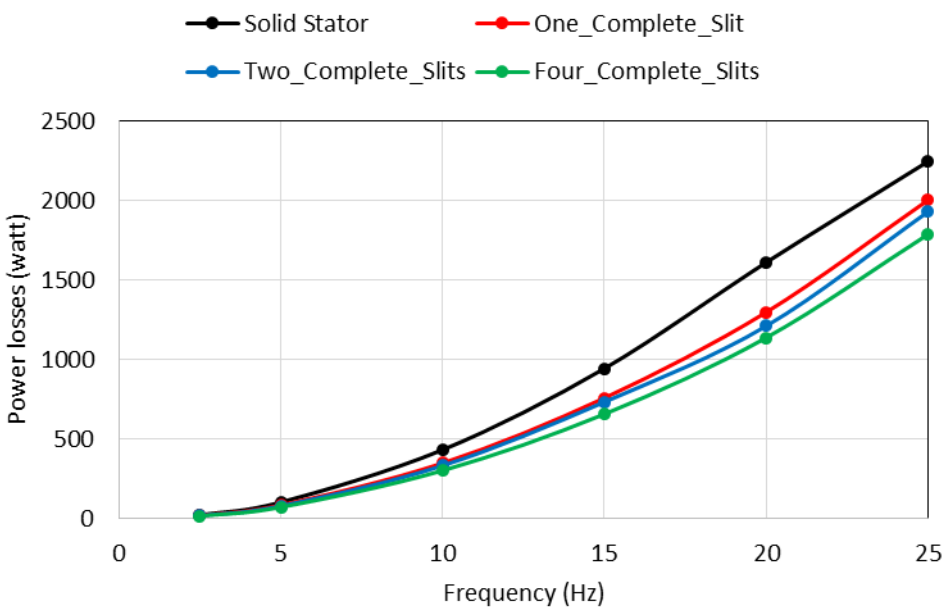


Figure 5-27 stator losses with different numbers of complete slits at 17A/mm^2

5.8.2 Solid construction with 1-directional partial slits

This configuration is shown in Figure 5-13 (c). The stator of the TLPM motor is slitted radially and not completely from the inner surface of the stator toward the outer direction along the slot radius. Using high precession Electric Discharge Machine EDM, 0.3mm slits thickness has been achieved. To investigate the potency

of this method, 3D model for this structure is built and solved for different number of slits at rated current density 17A/mm^2 and rated frequency 2.5Hz. According to Figure 5-28, increasing the number of silts will affect positively on the losses and negatively on the force generation. Various configurations (mainly in terms of the number of slits used) are investigated, from 0 slits (solid stator) to 100 slits as maximum. Figure 5-28 shows the TLPM motor behaviour with different number of slits normalized to the solid model without slitting technique. Regarding the two factors; the generated force and the power loss, the partial number of slits need to be optimized based on these two factors as will be given in Chapter 6 of the machine design.

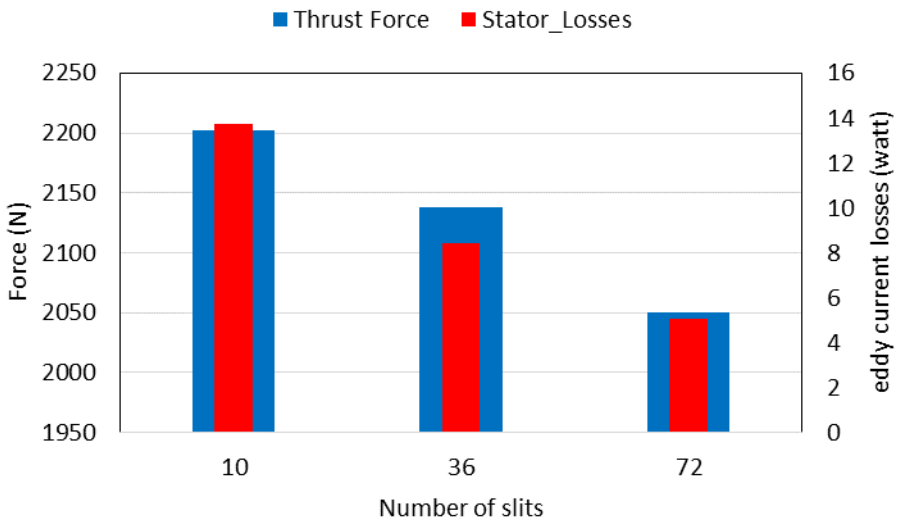


Figure 5-28 TLPM motor: force and losses for different number of slits at 17A/mm^2 and 2.5 Hz

5.8.3 Solid construction with 2-directional partial slits

This configuration, shown in Figure 5-13 (d), is very similar to the model described in section 5.8.2, but aims to further increase the eddy current path length. The main advantage of this structure is that contrasts the circulation of eddy currents in both the tooth body and the back iron part of the stator.

To investigate this method a 100 partial slits (50 inner slits and 50 outer) are implemented into 3D FE model of the TLPM motor and solved at rated current density 17A/mm^2 and rated frequency 2.5Hz. A comparison with the solid stator model, comprising 1-directional partial slits, and this model is presented in Figure 5-29 and Figure 5-30 for force and power losses respectively. These results indicate 56 % losses reduction with only 1.5 % force reduction. This is indeed a very good result for the objectives of this part of the work, since the effectiveness of the proposed slitting techniques can be easily observed.

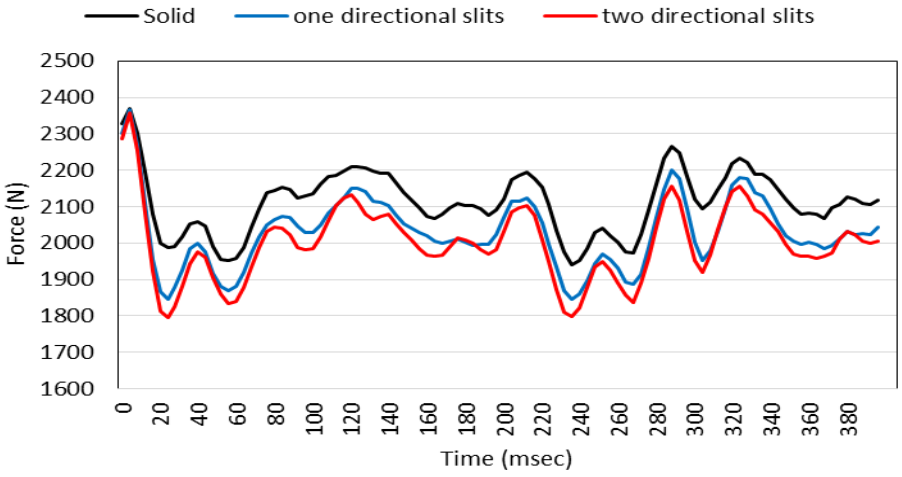


Figure 5-29 force of solid stator vs. 100 slits models at 17A/mm^2 and 2.5 Hz

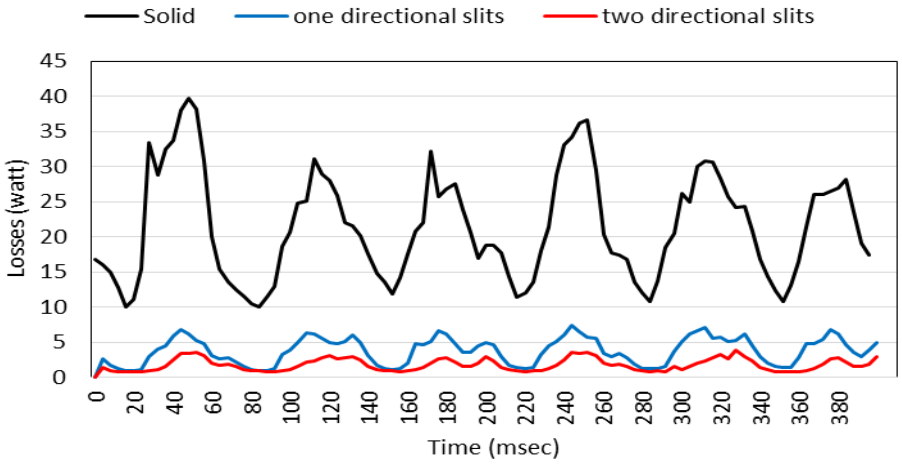


Figure 5-30 losses of solid stator vs. 100 slits models at 17A/mm^2 and 2.5 Hz

5.9 HIGHLIGHTS AND CONTRIBUTIONS TO RESEARCH.

The main highlights and innovation for this chapter can be summarised in the following list:

- A detailed analysis of eddy current behaviour in solid materials employed in magnetic circuits that have unconventional flux behaviour.
- Investigation of different eddy current reduction techniques or methods.
- A detailed investigation of the slot current condition and its effect on the eddy current reduction techniques
- Experimental validation of these methods

5.10 CONCLUSIONS

In this chapter, a detailed analysis with experimental validation of eddy current reduction techniques for solid ferromagnetic materials used in unconventional magnetic circuits has been presented. Analytical and FE analyses of eddy current behavior inside single layer and double layer concentrated windings have been presented. It has been concluded that for the TLPM machine in question with a concentrated, 12-slot, 10-pole configuration, the eddy current behavior varies according to the particular tooth position and the condition of the excitation current waveform. It also depends on the time instant, the winding configuration used and the actual position of the tooth. For clarity, the testing results described above are tabulated in Table 5-1 in order to easily compare all the methods for rated condition of operation of the machine in [7].

Table 5-1 Performance Comparisons

Eddy current reduction method	Thrust Force (N)	Difference %	Eddy Loss (Watt)	Difference %
Solid (Method A)	*2112*	-	*21.34*	-
one slit (Method B)	*2222*	*5.2*↑	*17.66*	*17*↓
two slits (Method B)	*2215*	*4.8*↑	*16.74*	*21*↓
four slits (Method B)	*2102*	*4.7*↓	*14.2*	*33*↓
10 slits (Method C)	*2202*	*4.2*↑	*13.74*	*35*↓
36 slits (Method C)	*2137*	*1.1*↑	*8.398*	*60*↓
100 slits (Method C)	*2029*	*4.0*↓	*3.782*	*82*↓
100 slits (Method D)	*1999*	*5.4*↓	*1.782*	*90*↓

As can be observed in Table 5-1, all the methods described above tend to decrease the eddy current losses, but obviously with varying results. However, it is also clear that some of these methods have a negative effect on the generated force. While the one complete slit of Method (B) causes an increase in the output force, adding more than two slits will tend to decrease the output force. The same behaviour is found with the partial slits of method (C). Adding more than 36 slits will give the same negative effect on the generated force. To explain this behaviour, it is important to note that the eddy currents have their highest values when the solid model (method A) being used. In this case each tooth represents a current carrying conductor ring. Thus, this eddy current, according to the Lorentz Force law, produces a negative force which is opposite to the main force [146]. Considering method (B), adding more than one complete-slit will lead to small changes in the eddy current losses due to the same concept as described in the first tests shown in Section 5.6.2, i.e. the length of the effective eddy current path will not change. In addition, adding more than one complete slit will tend to reduce the mechanical structure and an external supporting structure will be required.

Considering the slitting technique of method (D), the high radial force which normally exists in TLPM machines means that from a structural perspective, this

stator configuration can be represented as a circular ring under radial pressure. This radial force leads, in turn, to a circumference force and as a consequence, because of this slitting structure, the radius of the stator teeth will be increased or decreased depending on the force direction [147]. Thus Method D is not considered any further in this work.

All the above indicates “Method C” as the optimal solution for eddy current reduction while allowing for appropriate levels of structural and mechanical integrity. The selection is based on the balancing between the eddy current losses, mechanical structure and manufacturing complexity.

6. DESIGN OF TLPM MOTOR WITH SOLID STATOR

6.1 INTRODUCTION

Considering the application, the main objective of this design procedure is to focus on the force density capability of the machine, within the given space constraints and performance requirements. For the special case of the solid stator, the core losses need to be within an acceptable level. Analytical models are used in combination with accurate FE models in order to minimise computational resources. These design procedures need to not only resolve the conflict for space between iron, copper, insulation and coolant but also to optimize the cost of the manufacturing process.

In this chapter, as a first step of machine design, the PMs and solid material of the machine cores will be specified based on the information provided from the material characterisation datasheets. The selection of the winding configuration of the TLPM motor and the slot pole combination is also given. The designed machine will be geometrically optimized based on the maximum achievable power density with minimum allowable power losses, using analytical, 2D and 3D FE solving methods.

This chapter is focused on the design of the TLPM machine with a solid stator. Details of manufacturing processes are then presented in Chapter 7.

6.2 MATERIAL SELECTION

6.2.1 Material of the Solid Stator

Several solid materials are readily today available for use in electrical machines, however it is important to note that such materials and other new ones are always in constant development and upgrading [148-150].

Generally, an appropriate material selection depends on a range of aspects, such as the physical properties, chemical properties, magnetic properties and very importantly cost. Such characteristics can usually be obtained from different sources such as manufacturer datasheets or other official documents. Based on a high level comparison around these aspects, the EN8 material has been selected. EN8 is a popular steel in industry. It is an unalloyed medium carbon steel which is usually used in applications where better properties than mild steel are required but where the costs do not justify the purchase of a steel alloy [151]. The magnetic characteristic of EN8 is determined when it is employed in machines with conventional and unconventional magnetic circuits. The full characterization procedures, given in chapter 4, Figures 4-9, 4-10, 4-11, 4-13,4-28 and 4-29, is used to develop an accurate FE model with realistic data for the material to be used in solid structure of the TLPM motor.

6.2.2 Material of the Permanent Magnets

Selecting an appropriate PM material always requires a careful investigation. The most popular types include Neodymium Iron Boron (NdFeB), Samarium-Cobalt (SmCo), Alnico, and Ceramic Ferrites. Each prospective magnet material offers

unique characteristics that are ideal to specific applications. Figure 6-1 shows a comparison between magnet types based around their more important characteristics relative to electrical machine applications.

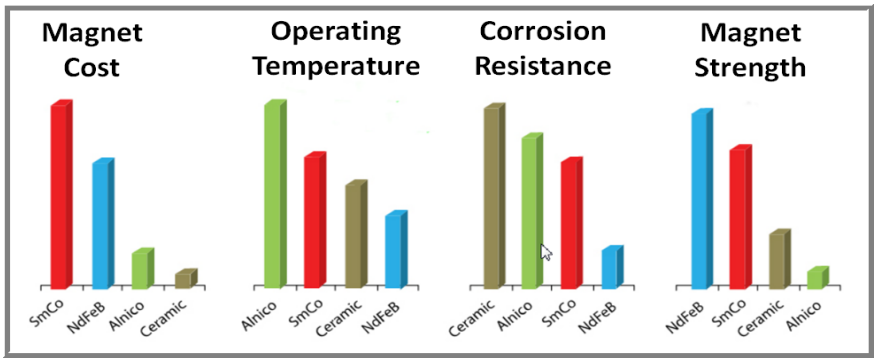


Figure 6-1 comparison between different permanent magnet types [152]

Ceramic magnets have moderate energy density and are low cost. From an operating temperature point of view, Alnico provides the highest level among all magnetic materials. However there are limitations to its performance because it is inherently has a low coercive force (*Hc*) [153]. Samarium Cobalt PMs can today withstand elevated temperatures and also have the second highest available energy density but a PM grade that combines those two aspects usually comes at relatively high cost.

From all the PMs available today on the market, NdFeB PMs have the highest energy density values, high remanence, high coercive force, high energy product and high performance/cost ratio and exist in a variety of grades. These grades not only vary in magnetic output performance but they also vary with temperature rating. The maximum recommended temperature of operation for the "NdFeB" magnets is +200 to +230^{o}C, although the exact limit is actually dependent on the magnet shape and the total magnetic circuit [152-154].

When considering all the above, it was decided to employ NdFeB PMs for the application at hand. This strategy is based on the following points.

- The main objective function of the design is a high force density, indicating that the highest energy density possible is desirable for the application.
- The new TLPM machine will be implemented with a powerful water-based cooling system. A reliable temperature control is therefore available, indicating that choosing SmCo PMs for their temperature ratings would be over-engineering.

6.3 WINDING TOPOLOGY SELECTION

Slot/pole ratio (SPR) is defined as the ratio of slot number to pole number for feasible slot/pole combinations [155]. For fair comparison between the first version of the TLPM designed in [7] and the new version designed in this work, the same number of slots has been selected. Although there are various possible stator winding configurations for three-phase tubular modular PM machines based on the feasible slot/pole number combinations given in [89, 156, 157], the most appropriate configuration, for a given slot/pole combination, is that which yields the maximum k_w for the working space harmonic *mmf* and results in no dc *mmf* component of [158].

Since the windings and the PMs of the machine are distributed uniformly along the machine axis, then, the electrical angle difference between any two neighbour slots $\Delta\delta$ is given in 6-1):-

$$\Delta\delta = \delta - 180$$
$$\delta = \frac{180 \times N_{pole}}{N_{slot}} \quad (6\text{-}1)$$

According to the assumption that the direct axis of the first PM of the mover part is aligned with centre of the first slot of the stator part, the individual electric degree shift will be as (0, Δδ, 2Δδ, 3Δδ, …, 11Δδ). And because a two layer winding configuration is used, then, $\Delta\delta$ is valid for both coils sharing the same slot number. Figure 6-2 shows a simple representation for (6-1).

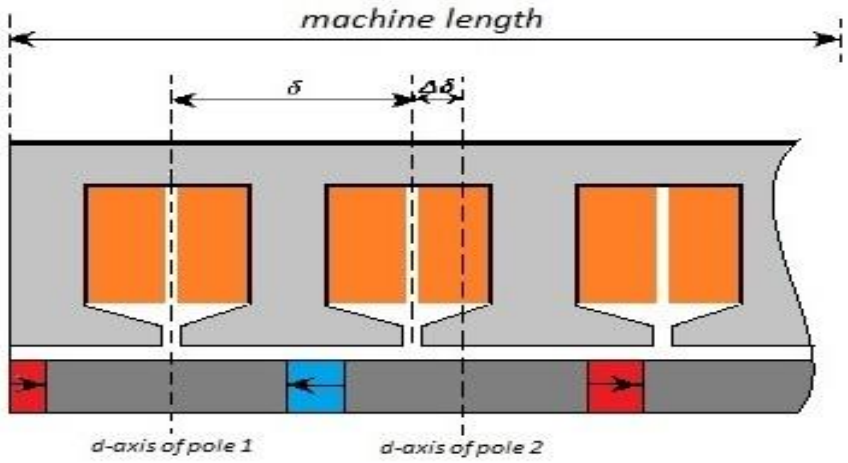


Figure 6-2 electrical shift angle between two adjacent slots

The SPR can be calculated using the form shown in (6-2) [155]. Thus, it can be understood that the number of poles N_{pole} corresponding to a selected number of slots N_{slot} can be written as a function of $\Delta\delta$ as in (6-3).

$$_{slot/\,pole} = \frac{180}{180 + \Delta\delta} \quad (6\text{-}2)$$
$$N_{pole} = N_{slot} + \frac{N_{slot} \times \Delta\delta}{N_{slot}} \quad (6\text{-}3)$$

In order to maximise machine performance and minimise *mmf* harmonic content, $\Delta\delta$ need to be optimized.

For a balanced three phase system, the supply currents are expressed as in equation (5-6). According to this, each coil inside each slot will generate an *mmf* waveform and for the purpose of steady synchronous movement, *mmf* ripple should be as small as possible and the *mmf* amplitude should be as great as possible, to achieve maximum thrust.

The fundamental component of the generated *mmf* of the three phase armature current as a function of $\Delta\delta$ and time is shown in (6-4).

$$mmf = N_turn \cdot \left\{ \begin{array}{l} +\sum_{k=1}^{4}(-1)^{(k-1)}\left[i_a \cdot \cos(0\cdot\Delta\delta + 6(k-1)\cdot\Delta\delta + \omega t\right] \\ -\sum_{k=1}^{4}(-1)^{(k-1)}\left[-i_a \cdot \cos(1\cdot\Delta\delta + 6(k-1)\cdot\Delta\delta + \omega t\right] \\ +\sum_{k=1}^{4}(-1)^{(k-1)}\left[i_b \cdot \cos(2\cdot\Delta\delta + 6(k-1)\cdot\Delta\delta + \omega t\right] \\ -\sum_{k=1}^{4}(-1)^{(k-1)}\left[i_b \cdot \cos(3\cdot\Delta\delta + 6(k-1)\cdot\Delta\delta + \omega t\right] \\ +\sum_{k=1}^{4}(-1)^{(k-1)}\left[i_c \cdot \cos(4\cdot\Delta\delta + 6(k-1)\cdot\Delta\delta + \omega t\right] \\ -\sum_{k=1}^{4}(-1)^{(k-1)}\left[-i_c \cdot \cos(5\cdot\Delta\delta + 6(k-1)\cdot\Delta\delta + \omega t\right] \end{array} \right\} \quad (6\text{-}4)$$

The variation of *mmf* ripple and *mmf* amplitude as a function of $\Delta\delta$ are shown in (6-2).

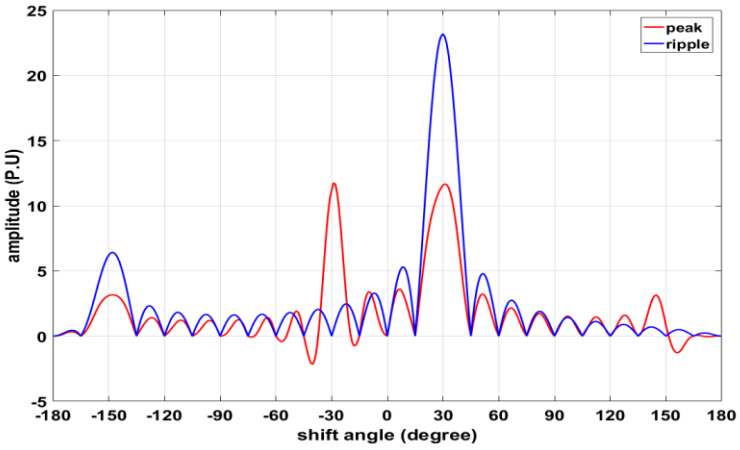


Figure 6-3 mmf wave form; ripple and amplitude with different $\Delta\delta$

With full range of $\Delta\delta$ variation (360°), it can be seen that the minimum ripple and maximum amplitude are obtained when $\Delta\delta = -30$. Using (6-3), the optimal pole number can be found, and it is equal to 10 poles.

After the pole number is calculated, for a 10-pole/12-slot modular machine, the number of slots per phase ($N_{slot}/3$) is an even number, and equal to 4, and in order to maximize the k_w for the working space-harmonic *mmf*, the phase winding can be subdivided into two sections, each having two slots and displaced from each other by five pole pitches, as shown in Figure 6-4.

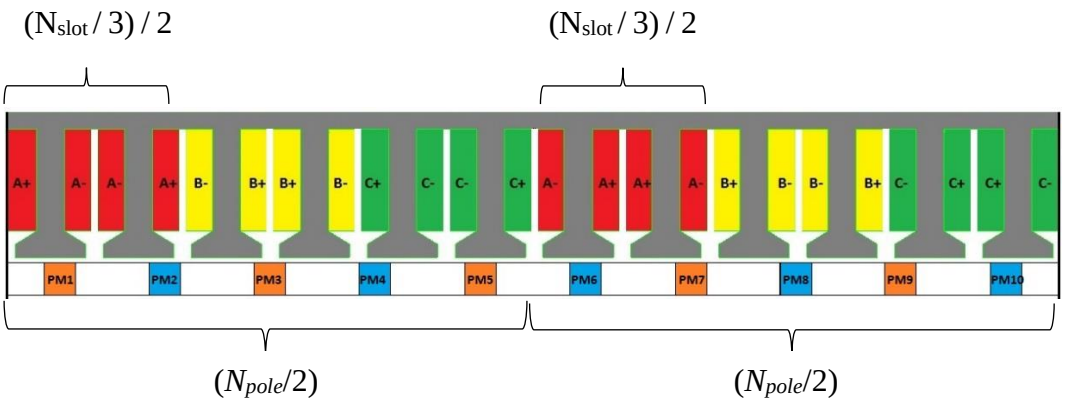


Figure 6-4 coils and phase distribution of 12 slot machine

The fundamental k_w is calculated using the electromotive force *emf* phasors for all coils as shown in (6-5) and the phasor quantity of the *emf* of each coil ($\vec{E}_{coil}$) is given by (6-6) [84].

$$k_w = \frac{\left| \sum_{1}^{2 \cdot N_{slot}/3} \vec{E}_{coil} \right|}{2 \cdot N_{slot}/3} \tag{6-5}$$

$$\vec{E}_{coil} = e^{j\frac{\pi \cdot N_{pole}}{N_{slot}} \cdot S_{(coil)}} \tag{6-6}$$

Where $S_{(coil)}$ is the order of coils with current direction (+ or -) of one phase. This can be easily obtained from (6-3). Considering the two layer winding, the number of coils in each phase is equal to $(2 \cdot N_{slot} / 3)$, two coils in each slot. $S_{(coil)}$ is shown below for phase (a).

$$S_{(coil)}phase(a) = [\underset{coil_1}{1} \quad \underset{coil_2}{-2} \quad \underset{coil_3}{-2} \quad \underset{coil_4}{3} \quad \underset{coil_5}{-7} \quad \underset{coil_6}{8} \quad \underset{coil_7}{8} \quad \underset{coil_8}{-9}\ ]$$

Figure 6-5 shows graphically the *emf* vectors for the three phase of 12-slot/10-pole TLPM machine. Basically, k_w can be calculated from the vector summation of the *emf* of all coils divided by the algebraic summation of them. Using (6-5), the fundamental k_w for the selected machine is equal to (0.933).

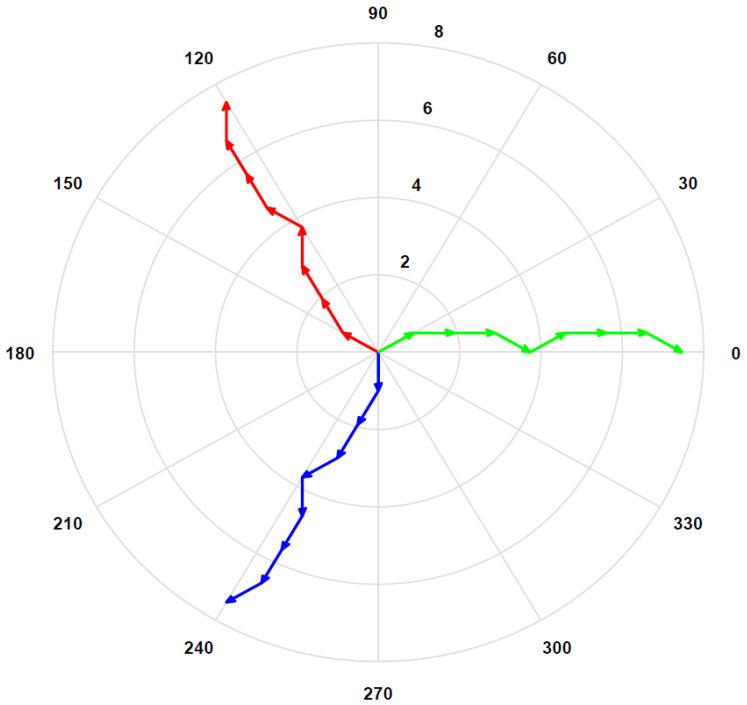


Figure 6-5 three phase emf phasors of 12 slot/10 pole machine

6.4 INITIAL DESIGN CONSIDERATIONS

Before designing the machine, certain design specifications and constraints were defined. These constraints gave the basic framework for the design to evolve into a working TLPM motor. The TLPM motor specifications and material specifications are summarized in Table 6-1 and Table 6-2, while the main parts and dimensions of the TLPM machine are shown in Figure 6-6 and Figure 6-7, where the external dimensions $L_{activet}$ and R_{in} are fixed by the application envelope.

Table 6-1 General TLPM motor specifications

Number of phases (m)	m	*3*	-
Number of slot	N_{slot}	*12*	-
Number of poles	N_{pole}	*10*	-
Active length	L_{active}	*199.8*	*mm*
Mechanical rated speed	V_{lin}	*100*	*mm/s*
Ambient temperature	T_{amb}	*40*	℃
Max. slot (coil) temperature	T_{max}	*180*	℃
Mover outer radius	R_m	*46.25*	*mm*

Table 6-2 Materials of the parts of the TLPM

Stator iron core	*EN8 silicon steel*
Mover poles pieces	*EN8 silicon steel*
Permanent magnet	*Neodymium Iron Boron (NdFeB); N40UH*
Coil	*Copper*
Machine housing	*Aluminium*
mover support	*Aluminium*

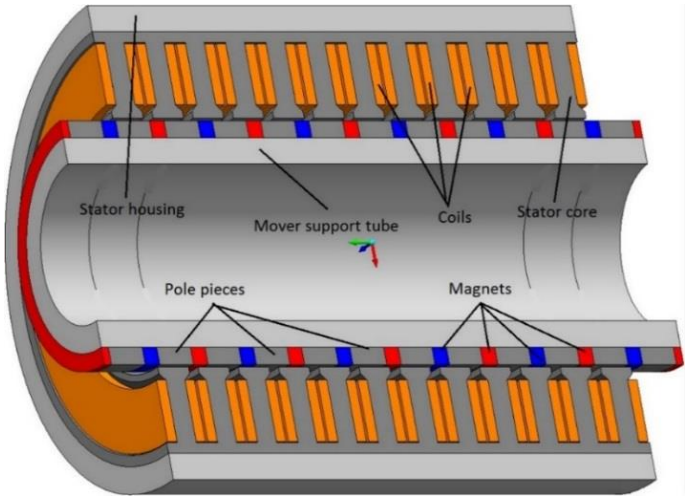


Figure 6-6 TLPM motor: the main parts

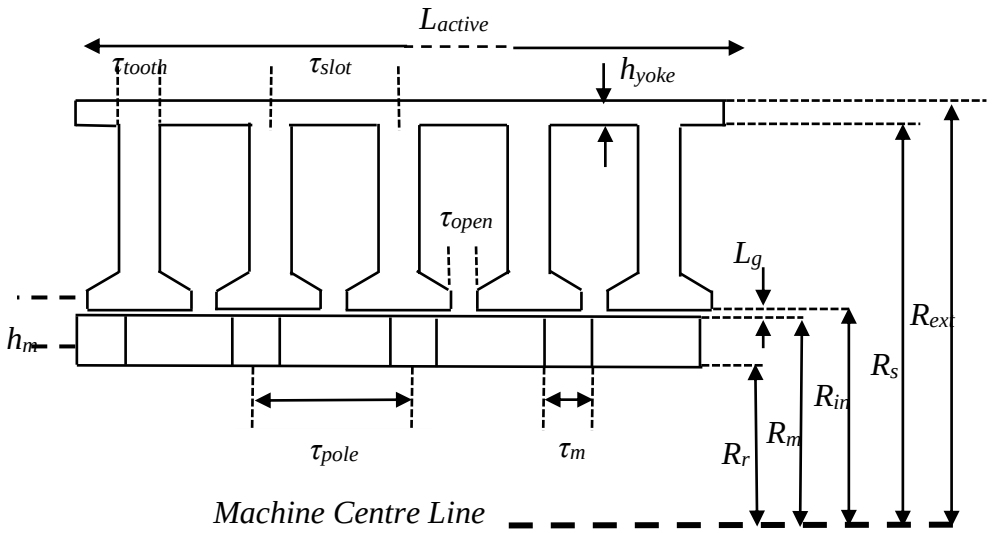


Figure 6-7 TLPM motor: the main dimensions

The maximum allowable temperature in Table 6-1 was calculated corresponding to the maximum limit of the temperature of the coil's insulation and the maximum allowable temperature limit for the machine's PM material.

6.5 GENERAL GEOMETRICAL SIZING

In this section, the physical size of the electrical machine is primarily determined using the most general equations for force production. The calculations are based on the most common known design equations, such as magnetic field equation, thermal equations, Maxwell Stress Tensor and machine volume. These initial values can be used as a base point for the next step of accurate designing processes, where 2D and 3D FE optimization will be used.

6.5.1 Number of turns

Based on the winding factor of the machine k_w, to estimate the number of armature turns per phase and the cross-sectional area of the armature conductors, the following factors should be considered: -

1- The total no-load phase $back_emf$ at rated speed.

2- The maximum achievable slot copper fill factor.

The no-load *rms* voltage induced in one phase of the stator winding emf_{rms} by the PMs flux Φ_{PM} of the mover and frequency f is shown in (6-7) [18].

$$emf_{rms} = \pi \times f \times \sqrt{2} \times N_{turn} \times k_w \times \Phi_{PM} \tag{6-7}$$

Then, the number of turn can be calculated using (6-8).

$$N_{turn} = \frac{emf_{rms}}{\pi \times f \times k_w \times \Phi_{PM}} \tag{6-8}$$

The number of turns N_{turn} can also be calculated using the common basic equation of conductor cross sectional area as in (6-9).

$$N_{turn} = \frac{A_{slot} \times k_{fill}}{A_{cond}} \tag{6-9}$$

For design purposes, where A_{slot} is the slot area and k_{fill} is slot filling factor, and it has been empirically calculated and it is equal to 0.48. The conductor cross sectional area A_{cond} equal to 0.5 mm^2, then, the number of turns per phase can be known.

6.5.2 Slot Current Density

An important aspect that defines a machine's design and operation is the slot current density J_{rms}. A common practice is to set a maximum value of J_{rms} that corresponds to the thermal limit of the machine. Knowing the maximum permissible winding temperature T_{max}, the maximum value of copper losses P_{cu} for each coil can then be calculated depending on the principle of heat convection area of the electrical machine as shown in (6-10). Then, the maximum value of J_{rms} and A_{rms} can be calculated, as in (6-11), where h_{air} is the heat transfer coefficient of air in $watt/m^2.K$, ρ_{cu} is the resistivity of copper at a given winding temperature, R_{ext} is the external radius of the stator and R_{slot} is the midline radius of the slot [7].

$$P_{cu} = h_{air} \times (T_{\max} + 273.15) \times 2 \times \pi \times R_{ext} \times L_{active} \qquad (6\text{-}10)$$

$$P_{cu} = J_{rms}^2 \times A_{slot} \times k_{fill} \times \rho_{cu} \times R_{slot} \times 2\pi \qquad (6\text{-}11)$$

In the design and optimization stage, J_{rms} is selected to be equal to $14\ A/mm^2$, corresponding to the maximum temperature rise with normal cooling conditions without any use of heat dissipation parts, such as stator housing. Figure 6-8 shows the variation of the coil temperature with different values of J_{rms} at rated speed of 100mm/sec and ambient temperature equal to 40°C.

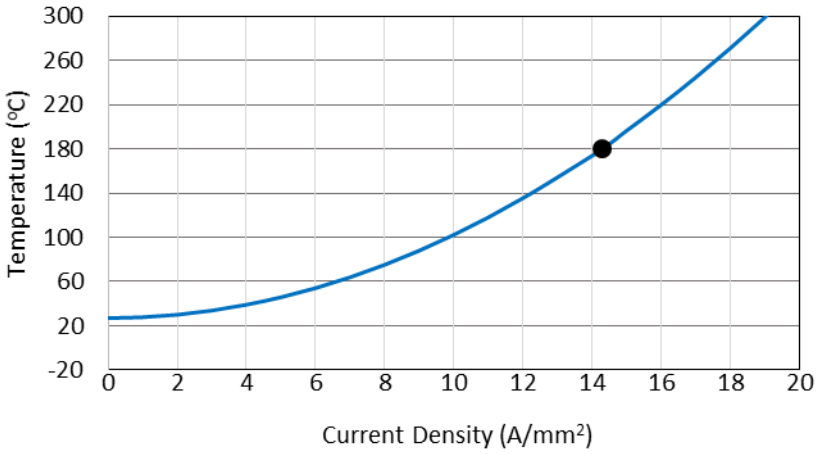


Figure 6-8 coil temperature with different current density at rated speed of 100mm/sec

6.5.3 Airgap length

The air-gap length L_g is considered to be 1 mm. While a smaller air-gap length tends to improve performance, it is however limited by manufacturing tolerances as well as the stiffness and the static and dynamic radial run-out of the moving-magnet armature [61].

6.5.4 Magnetic Loading (Magnet Sizing)

For the PM configuration shown in Figure 3-1(b), the key dimensions are 1) the pole width, τ_{pole}, 2) the magnet width (magnet span, τ_m) and 3) the PM inner and outer radii (magnet thickness, h_m). These parameters are shown in Figure 6-7.

In general, the performance improves as h_m is increased. However, cost is also increased as the volume of rare-earth PM material increases and results in heavier moving parts, which are usually undesirable for a moving-magnet machine. In this study therefore, the magnet thickness is selected so that to produce an acceptable air-gap flux density at around 0.8T, while providing the required demagnetization withstand capability [10].

According to its direct effect on the flux linkage and its major contribution to the electromagnetic force of the machine, the most important parameter is τ_m. using analytical calculation, to select the optimum value of τ_m, the flux density distribution in the air gap is assumed to be a quasi-square waveform [66]. Considering the PM field only, B_{g_IPM} can be computed by using (3-12). Equation (3-13) represents the fundamental component of the Fourier series expansion B_{g1}. The optimum value can be found by finding the maximum value of B_{g1} with respect to the remnant flux density of the magnet, i.e. B_{g1}/B_{rem} with different τ_m. The optimum value for the magnet thickness can be determined from Figure 6-9. For different value of h_m, the maximum B_{g1}/B_{rem} is achieved when the ratio is approximately equal to 0.71. Then τ_m/τ_{pole} can be known.

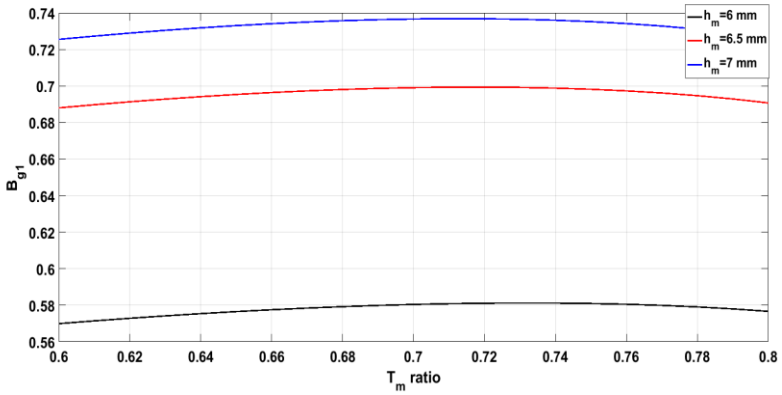


Figure 6-9 variation of Air-gap flux density vs. magnet width τ_m for different magnet high h_m

6.5.5 Stator Sizing

Once the magnetic loading, the electrical loading and the slot current density are known, it become possible to define the general machine sizing parameters. These parameter can be recognized manly into three main parameters. These are; (1) the split ratio (R_{split}) of the machine, which the ratio of inner diameter to the outer

diameter of the stator, (2) the tooth width (τ_{tooth}), which represents the balance between the electrical loading and the magnetic loading and can be represented by τ_{tooth}/τ_{slot}, (3) the stator back iron thickness, which also known as stator yoke (h_{yoke}).

R_{split} has a direct effect on the machine performance due to its relationship with the electrical loading of the machine [159]. Considering (3-4), and for fix outer diameter (R_s), A_{rms} and hence the shear stress δ decreases linearly with the increasing of the Split ratio, while the active airgap area A_{gap} increases linearly with this ratio. Thus (6-12) and (6-13) can be derived and they represent the electrical loading and output force relationship with the inner stator diameter (R_{in}).

The tooth width to slot pitch ratio which is called tooth width ratio τ_{tooth}/τ_{slot} has a significant effect on machine performance because it represents the balance between the magnetic loading and electrical loading of the machine.

$$A_{rms} \propto \left(1 - R_{split}\right) \tag{6-12}$$

$$Force \propto (1 - R_{split}) \times R_{split} \tag{6-13}$$

The output force relationship obtained from (6-13) is shown in Figure 6-10. Where the initial value corresponding to the maximum force is equal to 0.5.

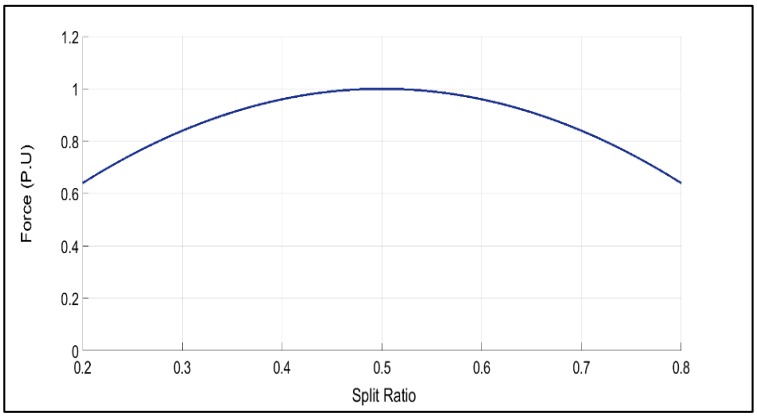


Figure 6-10 Output Force versus the split ratio

In order to calculate τ_{tooth} and h_{yoke}, shown in Figure 6-7, it is wise recalling that they are depending on the magnitude of the air-gap flux density and the maximum permissible flux density in the stator material [61]. Then, the initial values for these variables can be calculated using the ratio of the average value of air gap flux density B_{avg} to the maximum possible value of the flux density inside the tooth B_{tooth} and the back iron B_{yoke} parts, as shown in (6-15) and (6-16), where L_{active} is the active length of the machine, N_{pole} and N_{slot} are the number of poles and the number of slot respectively. B_{avg} is calculated from (6-14), where B_{Ir} is the radial components of air gap flux density[159].

$$B_{avg} = \frac{1}{\tau_{pole}} \int_{-\tau_{pole}/2}^{\tau_{pole}/2} B_{Ir} \cdot dz \qquad (6\text{-}14)$$

$$h_{yoke} = \frac{B_{avg}}{B_{yoke}} \times \frac{L_{active}}{N_{pole}} \times \frac{1}{2} \qquad (6\text{-}15)$$

$$\tau_{tooth} = \frac{B_{avg}}{B_{tooth}} \times \frac{L_{active}}{N_{slot}} \qquad (6\text{-}16)$$

As can be seen in (6-15), increasing N_{pole} significantly reduces the stator yoke thickness but at the cost of higher stator iron losses. In fact, for a given operating magnetic flux density the iron loss density is roughly proportional to the square of the electrical frequency and hence also related to the pole number [159].

6.5.6 The initial design

Considering all the above and based on the analytical models presented in this section, an initial, first-cut design of the TLPM motor with a solid stator is achieved. The main parameters are tabulated in Table 6-3.

Table 6-3 Analytical calculation of machine parameters

Number of phases	m	*3*	-
Number of poles	N_{pole}	*10*	-
Number of slot	N_{slot}	*12*	-
Active length	L_{active}	*199.8*	*mm*
Pole_pitch	τ_{pole}	*19.98*	*mm*
Slot_pitch	T_{slot}	*16.65*	*mm*
Magnet pitch (magnet span)	T_m	*6*	*mm*
Air gap length	L_g	*1*	*mm*
Pole ratio (magnet width ratio)	τ_m/τ_{pole}	*~0.29*	-
Tooth width ratio	τ_{tooth}/τ_{pole}	*~0.5*	-
Split ratio	R_{in}/R_s	*~0.5*	-
Back iron thickness	h_{yoke}	*~3.0*	*mm*
Magnet outer radius	R_m	*46.25*	*mm*
Current density	J_{rms}	*14*	*Amp*
Slot Fill Factor	k_{fill}	*0.48*	-
Winding Factor	k_w	*0.933*	-

6.6 FINE TUNING THE DESIGN WITH FE

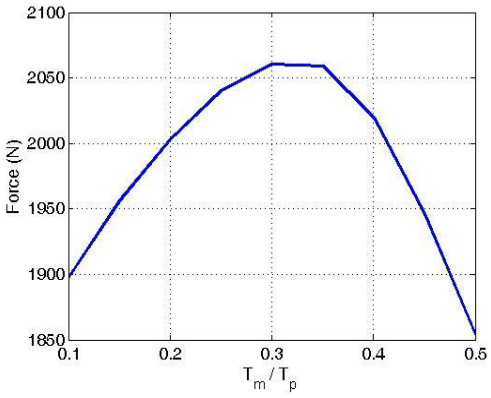
In this section, the work follows the optimisation procedures of the design of the motor, whose initial design parameters are given in Table 6-3. The optimisation is performed through accurate FE models and analyses. The main objective function is to achieve the maximum force possible for the specific space available with minimum weight while meeting all the other requirements and constraints.

The main dimensions that are most influential on the performance of the TLPM motor, are the PM thickness (h_m), pole ratio (τ_m/τ_{pole}), split ratio (R_{in}/R_{ext}) or (R_{ext}/τ_{pole}) ratio, and tooth width ratio (τ_{tooth}/τ_{slot}) [61].

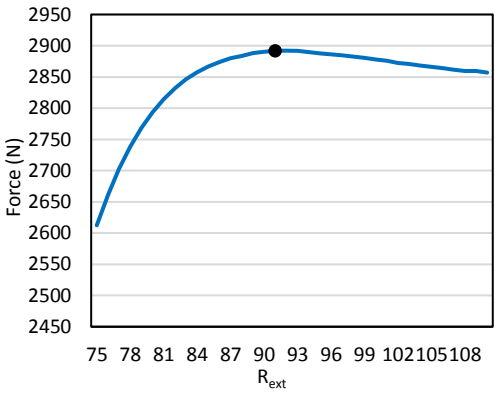
6.6.1 Optimising the design

A detailed, 2D FE model of the machine was built. The processes and methodologies for the development of the models has already been given in Section 2.5.5 and Section 3.6.4. The model here is built on similar concepts. For the same specifications and operating ranges as given above for the analytical models, the FE model was then used to perform sensitivity analyses and optimisation of the machine.

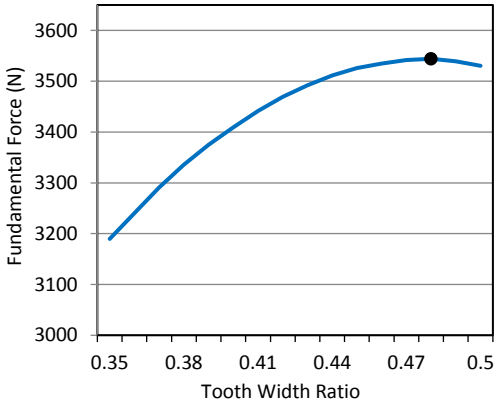
Figure 6-11 (a), (b), (c) and (d) show the optimization results of produced force with respect to τ_m/τ_{pole}, R_{ext}, τ_{tooth} and h_{yoke}. The optimization has been carried out based on solving the TLPM motor at rated current and rated speed.



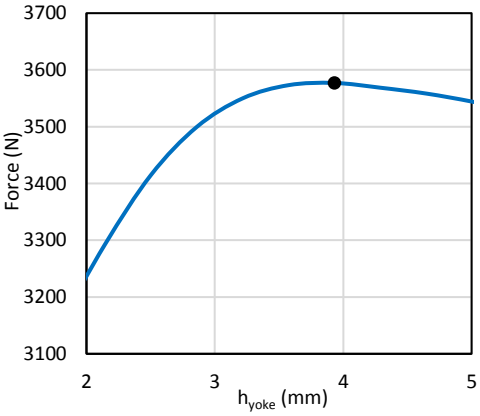
(a) Force with τ_m/τ_{pole} ratio [10]



(b)Force with R_{ext}



(c) Force with Tooth Width Ratio



(d) Force with hyoke

Figure 6-11 variation of generated force at rated current and speed

Although, for the fixed current density J_{rms}, the electrical loading A_{rms} is increased linearly with R_{ext}, it can be seen that force to losses ratio and force to current ratio decrease with R_{ext}. Figure 6-12 shows the variation of force to current ratio with R_{ext}.

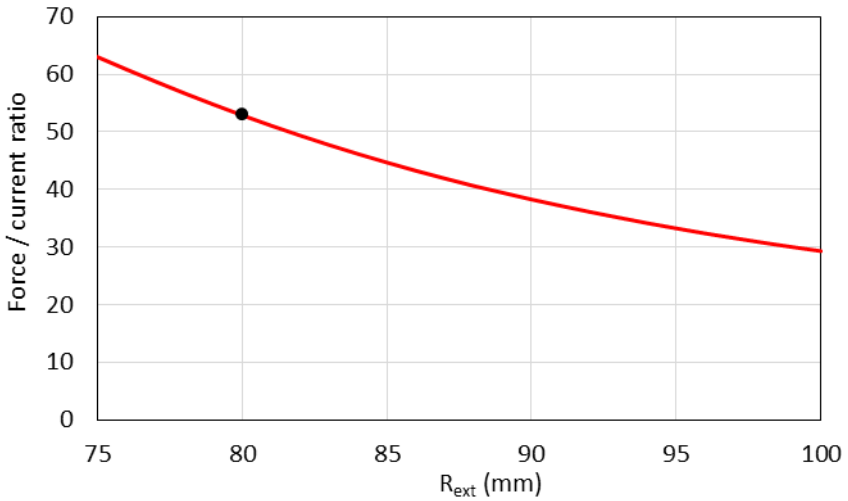


Figure 6-12 force to current ratio with different R_{ext} at rated current and speed

Increasing the external diameter with the fixed internal diameter will tend to increase the magnetic reluctance of the magnetic circuit. Also, increasing the outer diameter with the same τ_{pole} will give faster decay of the magnetic flux density inside the tooth body and increase the leakage flux which ultimately will decrease the machines performance.

Reluctance force or alignment force is experienced by a ferromagnetic object placed in an external magnetic field, which causes the object to line up with the external magnetic field. This force is produced in the motor due to the varying magnetic reluctance along the airgap when varies with tooth width ratio and stator bore. This reluctance force causes high force ripple due to the uneven equivalent air gap in the motor [160].

Figure 6-13 shows the relationship between R_{ext} and the force ripple of the TLPM machine. The minimum point occurs when the external radius is equal to 78 mm.

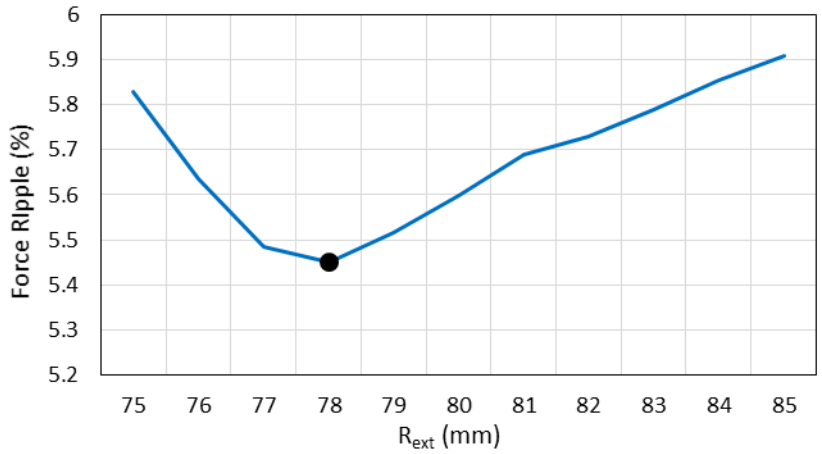


Figure 6-13 ripple factor variation with different R_{ext} at rated current and speed

From the above relationships, it can be understood that the most acceptable value for R_{ext} of the machine for a given R_{in} and τ_{pole} is 80mm.

Slot opening τ_{slot_open} represents the distance between two adjacent tooth faces. And the Slot Opening Ratio (SOR) is the ratio of $\tau_{slot_open}/\tau_{slot}$. This ratio affects the produced force as well as the amplitude of the cogging force and the force ripple. Also, the total harmonic distortion of the phase *back_emf* is influenced by this factor. The best ratio has been chosen equal to 22% of the machine slot pitch. This ratio gives the minimum cogging force and minimum force ripple which is 3.1% as shown in Figure 6-14 and Figure 6-15 respectively, with very acceptable *emf* THD shown in Figure 6-16.

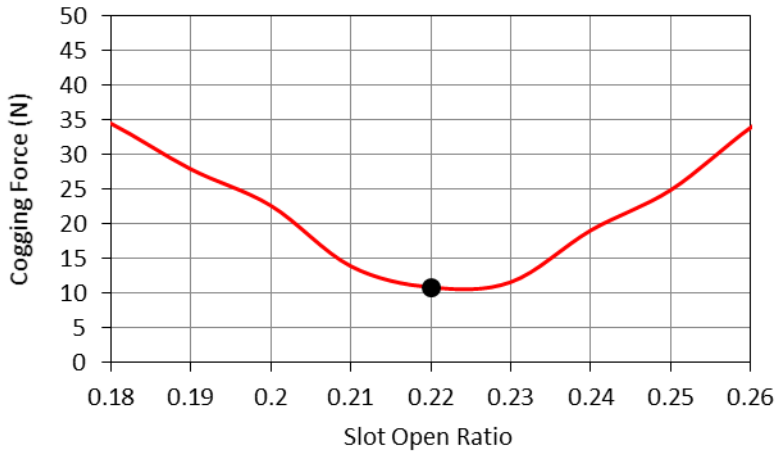


Figure 6-14 Cogging force with different Slot Open Ratio at rated current and speed

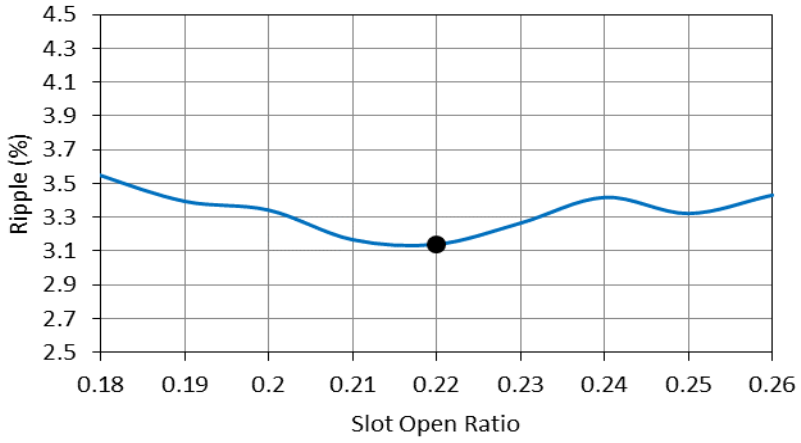


Figure 6-15 Ripple factor with different Slot Open Ratio at rated current and speed

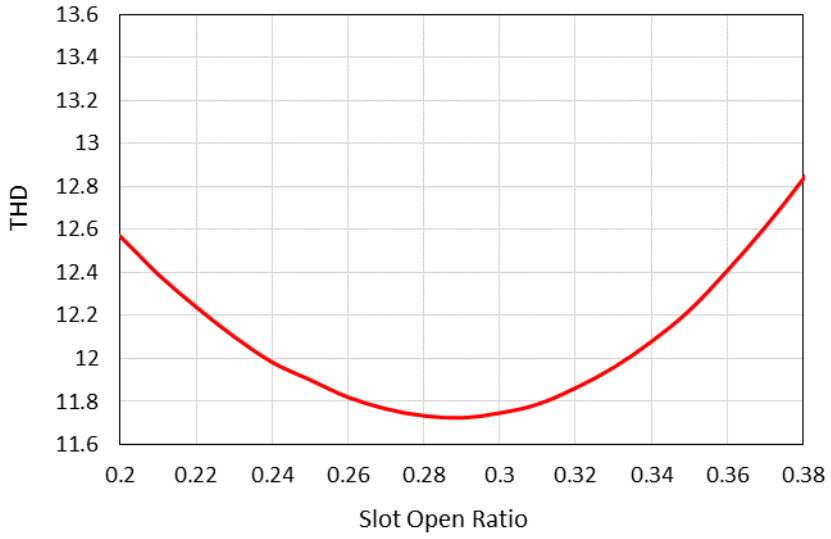


Figure 6-16 the THD of back emf with different Slot Open Ratio at rated current and speed

6.6.2 Other design considerations

6.6.2.1 Finite edge cogging force

Because of the limited length of the TLPM, a static force appears between the mover and the two finite ends of the stator and it is called "Finite edge cogging force" which depends only on the relative axial position between the armature and the mover permanent magnets [95]. The magnitude of net cogging force is the algebraic sum of the axial forces which act on both end faces, hence an extra finite length is required to compensate and minimize this force [161].

Different methods can be used to reduce the end face cogging force, the main techniques are [94, 95]:-

1. Flat end faces.
2. Stepped end faces.
3. Skewed end faces
    a. Skew of complete end face.
    b. Skew of half end face.
    c. Skew of quarter end face.

Each technique has its pros and cons. For flat end faces, the magnitude of all even harmonics are reduced, while, for the stepped end faces technique, only the second, sixth, tenth, ….etc, cogging-force harmonics can be eliminated. Skewing the end faces of the stator core axially by a distance equal to $\tau_{pole}/2$, all even harmonic components of the end face cogging force can be eliminated and the magnitude of the other harmonics reduced.

Using a smooth change in the finite edge length (L_{ext}), the cogging force has been optimized to the minimum value as shown in Figure 6-17. As can be seen, the lowest cogging force appears at (12.98 *mm*) for the longest edge. Figure 6-18 shows a 3D representation of the skewed end face technique.

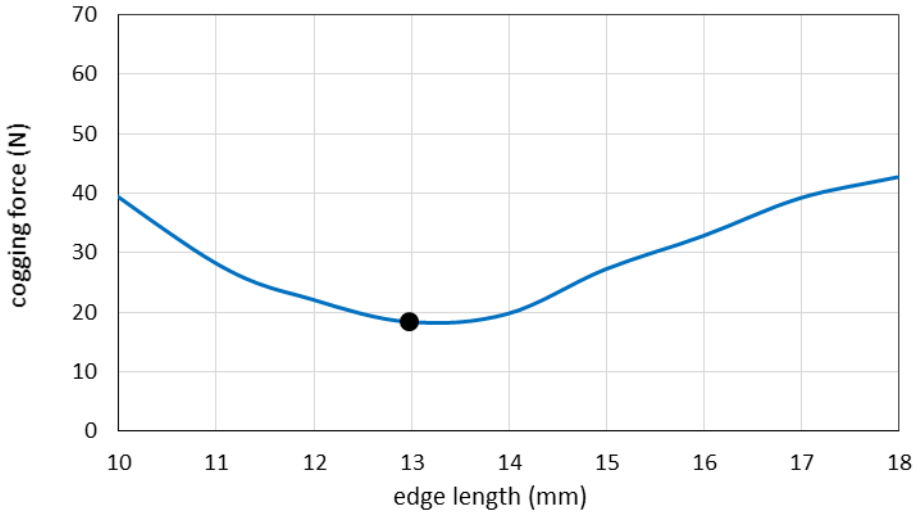


Figure 6-17 end faces force variation with different edge length at rated current and speed

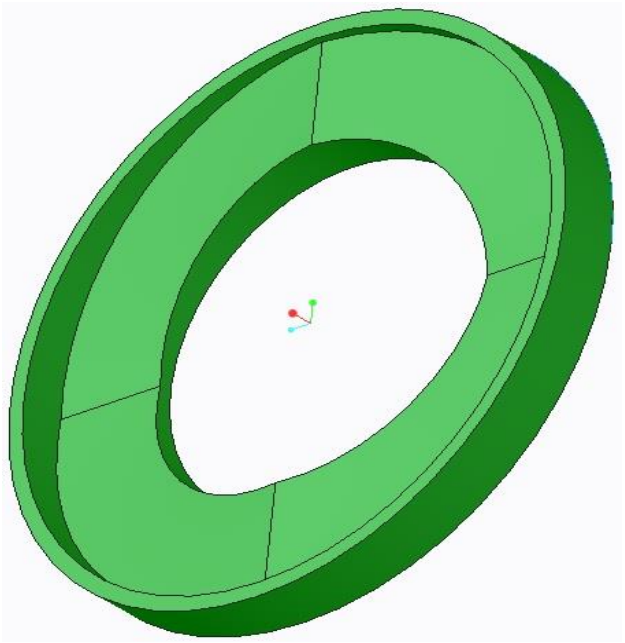


Figure 6-18 single-side skewing end faces

6.6.2.2 Eddy current reduction of solid parts

In Chapter 5, the optimal methods for eddy current reduction for the application at hand were identified to be “Method B” for unidirectional eddy current condition and “Method C” for bidirectional eddy current condition. These methods were implemented into the machine design processes focusing on the magnetic circuit’s solid parts, namely the stator teeth and the finite end parts of the TLPM machine.

The investigation in Chapter 5 proposed the concept of slitting. In this section the concept is implemented on the actual TLPM motor, via the use of a detailed 3D FE analyses. Figure 6-19 represents a 3D FE solid model with 36 slits. Figure 6-20 represents the machine’s performance for different numbers of slits at rated speed of 100 mm/s and rated current density of 17 A/mm^2. As expected and similar to the results in Chapter 5, a higher number of slits results in a lower eddy current loss for the solid stator with slits machine. The generated force is also reduced due to the reduction of the stator material mass and active stator inner area. However, increasing the number of slits will tend to increase the cost and manufacturing complexity of the machine.

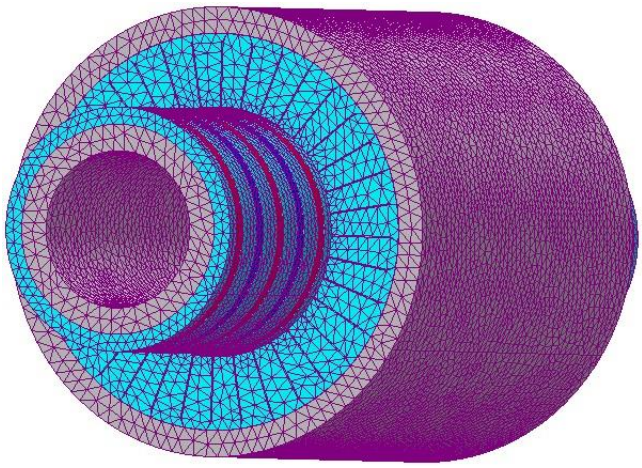


Figure 6-19 3D model for 36 slitted TLPM motor

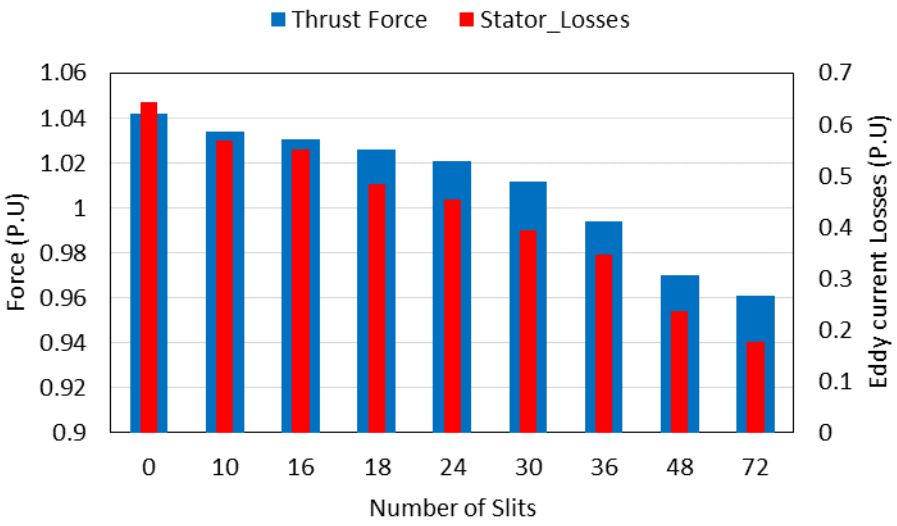


Figure 6-20 force and eddy losses of different slits number

An optimisation procedure based around four models of the machine with a solid stator was then performed. The four models which are shown below in Figure 6-21 are listed below:-

- Model 1 – Solid stator.
- Model 2 - 10 partial long slits.
- Model 3 – 36 partial long slits.
- Model 4 – 100 partial long slits.

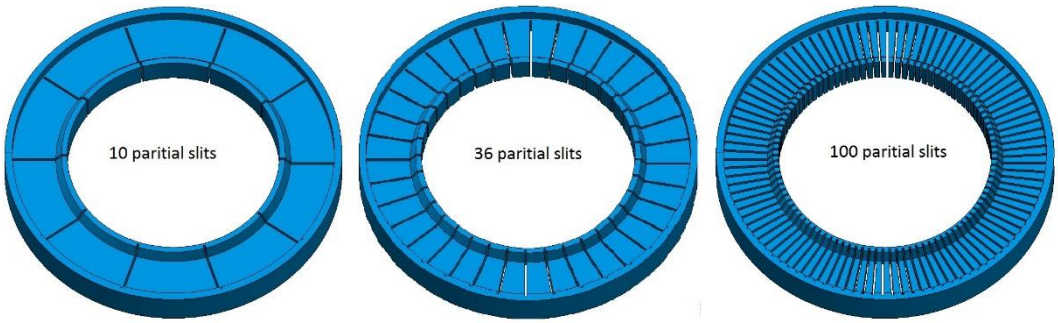


Figure 6-21 TLPM motor with different number of slits

The four models were solved for a range of frequencies corresponding to the mover speed. The results of this analysis are shown in Figure 6-22 and Figure 6-23 for the thrust force and eddy current losses respectively, where the values are obtained at rated condition of those of the original, benchmark machine that comprises a laminated stator.

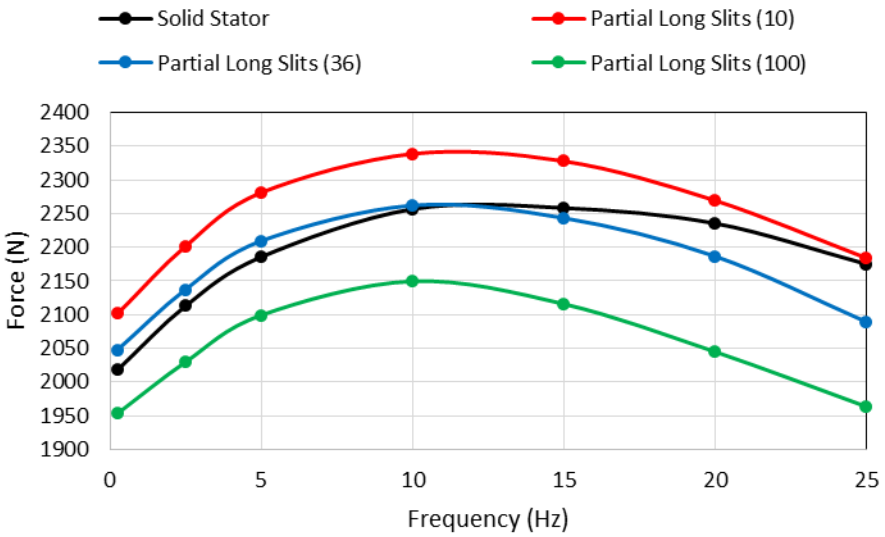


Figure 6-22 produced force for different number of slits

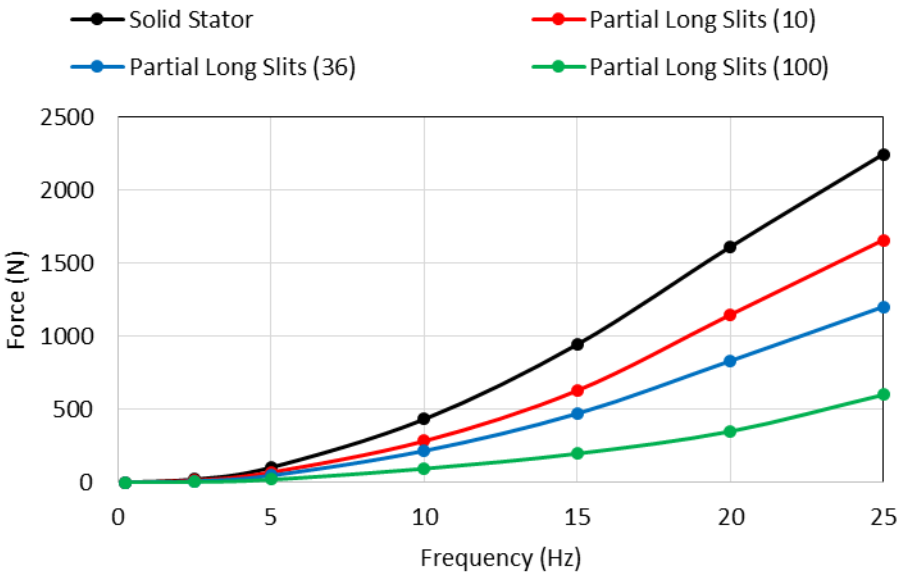


Figure 6-23 Eddy Current Losses for different number of slits

From Figure 6-22 and Figure 6-23, it can be seen that, at very low frequencies, the eddy losses are almost the same, while the generated force is different from each other and changes inversely with the number of slits of the stator. At higher frequencies, the losses are varying inversely with the slitting number.

At low frequencies, a low number of slits might be adequate, while, at higher frequencies, the best performance will be achieved with highest number of slits. In term of *force to losses ratio*, where losses represents the Ohmic losses, i.e. the copper losses and the eddy current losses. It turned out that, at low frequencies (lower than 10Hz), the highest number of slits gives lowest ratio. For frequencies greater than 10 Hz the higher number of slits gives higher ratio at all frequencies greater than 10Hz. as shown in Figure 6-24

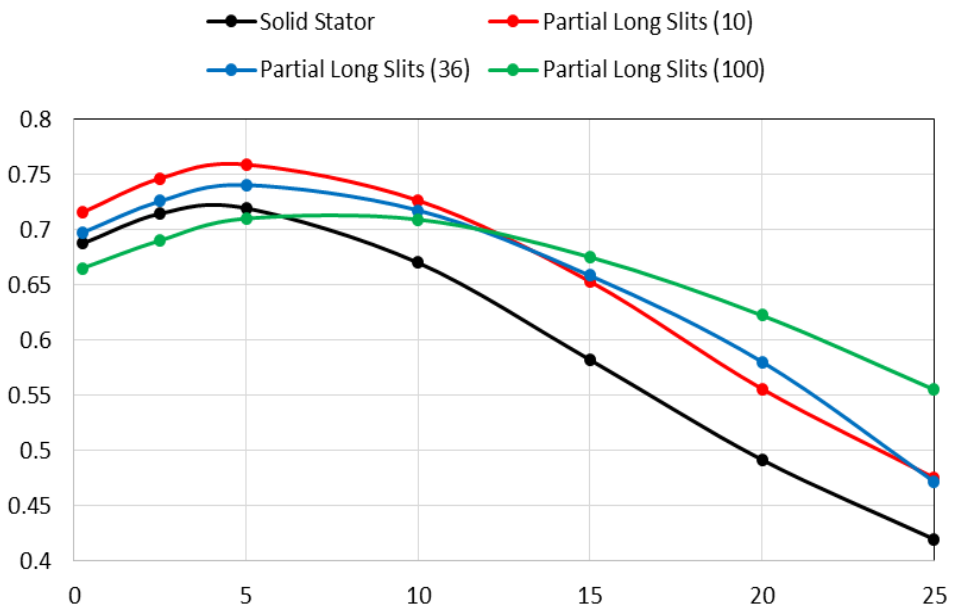


Figure 6-24 Force / Losses Ratio at different frequencies.

All the above indicates that the optimal solution is when the number of slits is 100. This configuration gives the lowest eddy current loss for all the frequencies considered with minimal impact on the generated force.

6.6.3 Thermal Design

The thermal performance of electrical machines and their wound components is a major limiting factor in electrical machine design [8]. An effort to extend the thermal limiting boundary of the tubular machine has been made in [8, 10, 104, 162].

A thermal management technique, proposed and validated in [7, 8, 10], is used in this work. The TLPM motor has been optimized to give the maximum attainable peak current density J_{peak} that satisfies the required thermal limit of the slot windings T_{max}. This has been done by inserting aluminium heat flow paths (HP) so that the thermal resistance of the dominant heat conduction path is reduced, as shown in Figure 6-25, where the thermal conductivity of the aluminium is equal to 204 W/m. ^{o}C.

The thermal network, where the machine has been thermally modelled with axial length equal to one complete slot pitch, is shown in appendix C.

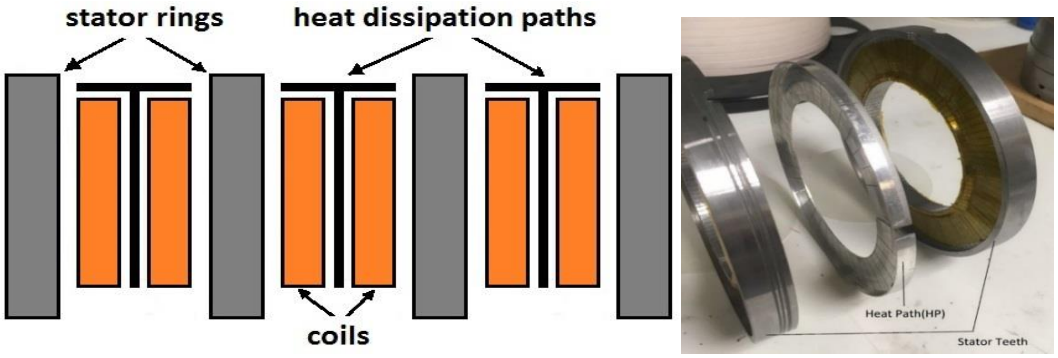


Figure 6-25 Heat path Technique

The thermal management technique used in [7] has been investigated, where the coil temperature is measured with and without the use of a heat path (HP) at different current density and rated speed. The maximum current density has been measured depending on the maximum desired coil temperature which is set to 180°C as in Figure 6-26, where the temperature of the coil with different current densities is presented. The effect of the HP technique can be significantly increased when cooling water (coolant) in the cooling ducts attached to the stator housing is used. The design geometries of the water jacket and related equations for thermal calculation are given critically in [104]. The equivalent thermal conductance for the thermal convection in the boundary layer of water *G*, is defined by (6-17), where α is the heat transfer coefficient (watt/m^2.k), and *A* is the surface involved in this process. Figure 6-27 shows the coil temperature of the cooled TLPM motor with HP solution.

$$G = \alpha \cdot A \tag{6-17}$$

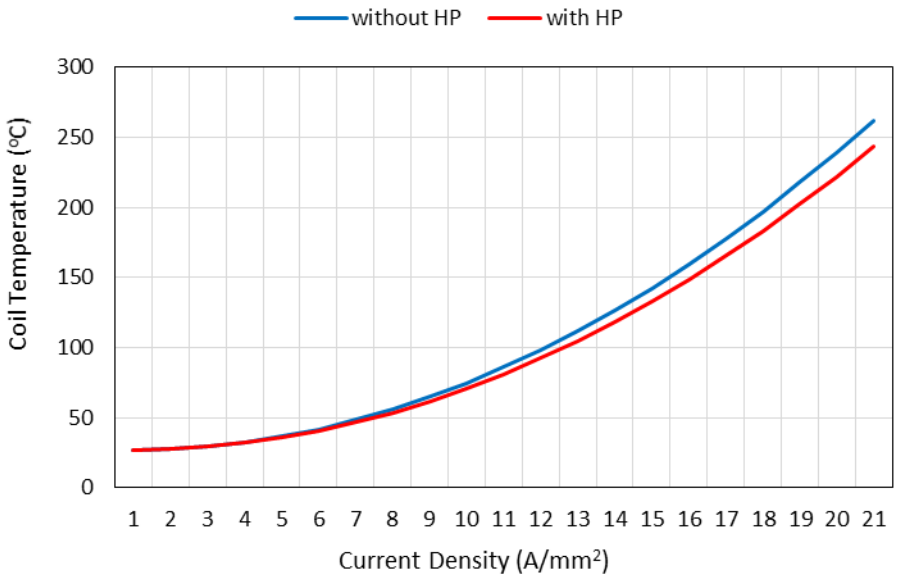


Figure 6-26 coil temperature with natural convection cooling

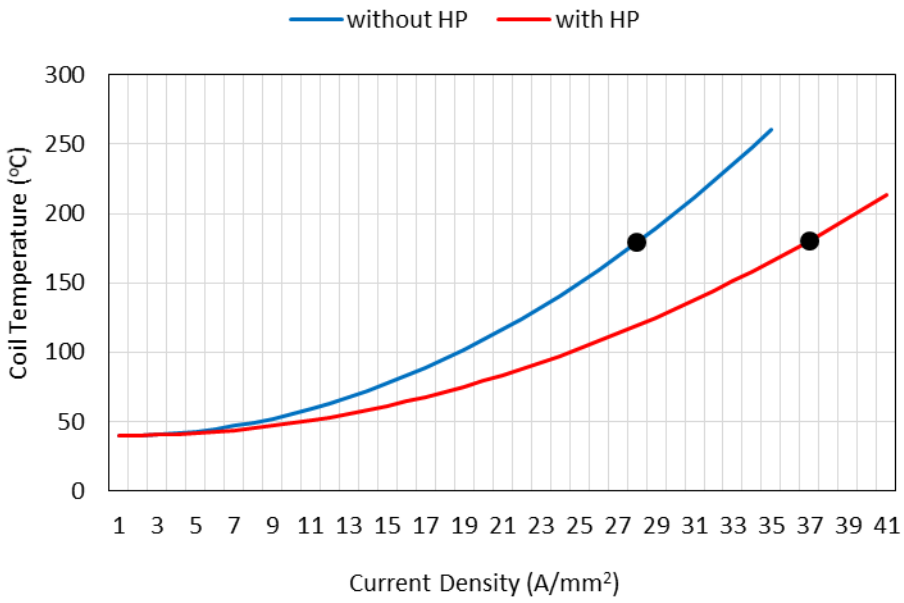


Figure 6-27 coil temperature with water cooled machine

6.6.3.1 Eddy current reduction of HP

Due to the solid nature of the HP and based on the Wiedemann-Franz law [55], it is predicted that the eddy current losses induced in the heat path itself is relatively high. The HP eddy current loss is mainly generated because it is linked by the same flux that links the armature windings. These losses can be described by (6-18), where $\Psi_{(HP)}$ is the flux linking, ω_e is the electrical speed and $\Re_{(HP)}$ is the closed ring HP resistance [10].

$$P_{eddy(HP)} = (\Phi_{(HP)} \times \omega_e)^2 / \Re_{(HP)} \qquad (6\text{-}18)$$

The key problem with the HP is that the eddy current generated inside any solid electrically connective materials is complex to describe and is affected by the shape, in addition to the flux linkage, frequency and resistivity. For low frequency applications (below 10 Hz), eddy current losses are relatively low, while at higher frequencies, these losses will be the main part of machine losses and it may have a

large effect on the machine performance and efficiency. Figure 6-28 shows the eddy current losses of the HPs at different frequencies compared with the Ohmic losses of the machine windings.

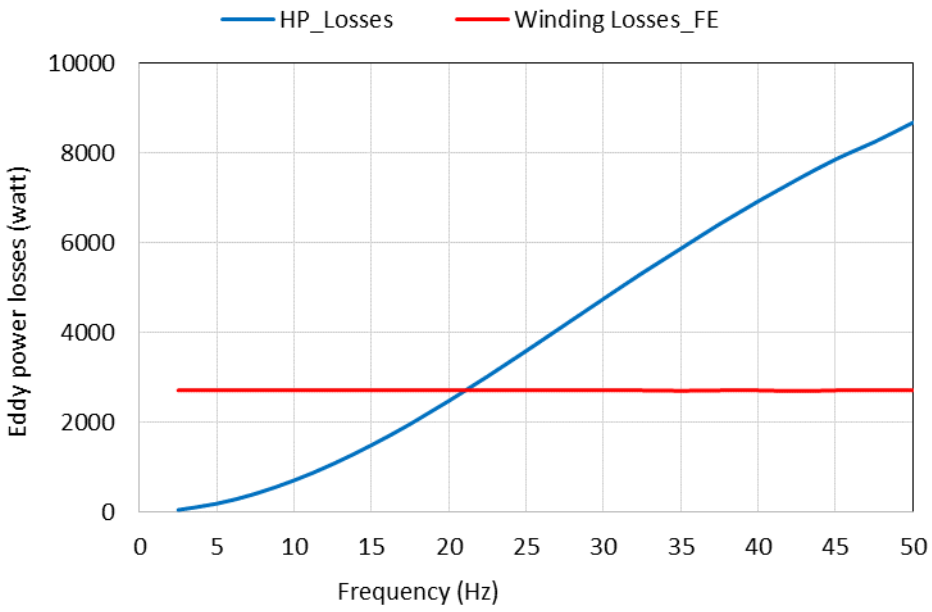


Figure 6-28 HPs eddy current losses at rated load current density

6.7 THE FINAL DESIGN'S PERFORMANCE

The optimisation procedures are done by considering the material characterization and eddy current reduction technique mentioned earlier in Chapter 4 and Chapter5. The optimization has been done under rated condition of speed and load current which they are specified early in this thesis. Based on these rated conditions, Table 6-4 and Table 6-5 represent the final FE design and performance data. The machine thrust performance is shown in Figure 6-29 where the output force has been plotted for the rated current. Figure 6-30 shows the generated force for various load currents and compares them with results from the analytical models.

Table 6-4 TLPM motor, solid stator: final parameters.

Parameter	*Simple*	*Value*	*unit*
Number of poles	N_{pole}	*10*	*-*
Number of slot	N_{slot}	*12*	*-*
Active length	L_{active}	*199.8*	*mm*
Pole_pitch	T_{pole}	*19.98*	*mm*
Slot_pitch	T_{slot}	*16.65*	*mm*
Magnet_pitch (magnet span)	T_m	*6*	*mm*
Air gap length	L_g	*1*	*mm*
Back iron thickness	h_{yoke}	*4*	*mm*
Pole ratio	T_m/τ_{pole}	*0.3*	*-*
Tooth width ratio	T_{tooth}/τ_{slot}	*0.475*	*-*
Split ratio	R_{in}/R_s	*0.62*	*-*
Slot Open Ratio	$T_{slot_open}/\tau_{slot}$	*0.22*	*-*

Table 6-5 TLPM motor, solid stator: final performance

Parameter	*Simple*	*Value*	*unit*
Normal cooling maximum Current density	J_{rms}	*17*	A/mm^2
Rated speed	v_{lin}	*100*	*mm/sec*
Rated frequency	f	*2.5*	*Hz*
Number of turns	N_{turn}	*85*	*-*
Load Current (peak)	I_{peak}	*12.1*	*Amp*
Maximum coil temperature	T_{max}	*159*	^oC
Slot Fill Factor	k_{fill}	*0.48*	*-*
Winding Factor	k_w	*0.933*	*-*
Stator weight	m_{stat}	*23.37*	*kg*
Mover weight	m_{move}	*7.7310*	*kg*
Total machine weight	m_{TLPM}	*35.414*	*kg*
Machine size	V_{TLPM}	*5552*	cm^3
Dynamic Thrust Force (at rated current)	F_{lin}	2397	*N*
Dynamic Force density (at rated current)	-	*102.6*	*N/kg*
Static Thrust Force (at rated current)	F_{lin}	*3414*	*N*
Static Force density (at rated current)	-	*146.1*	*N/kg*
Ripple factor	-	*8.35*	*%*

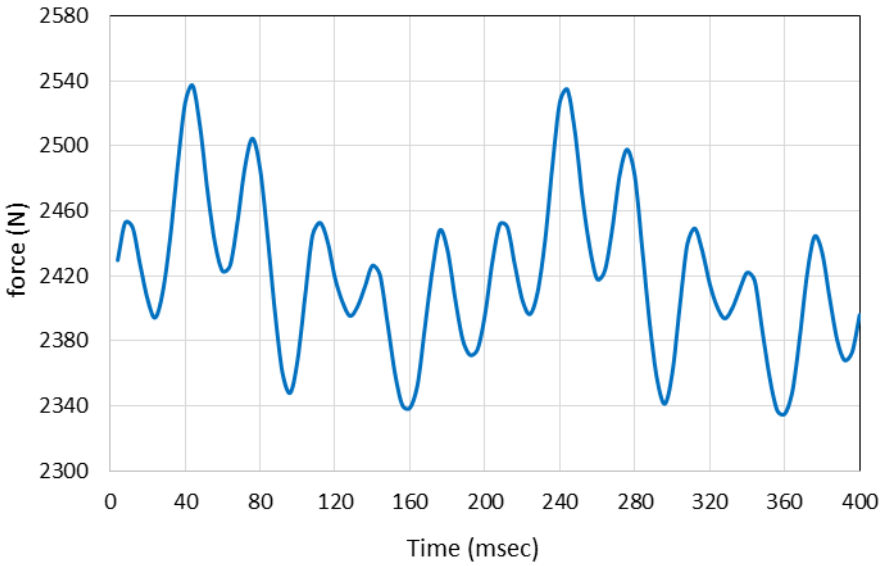


Figure 6-29 TLPM motor : thrust force

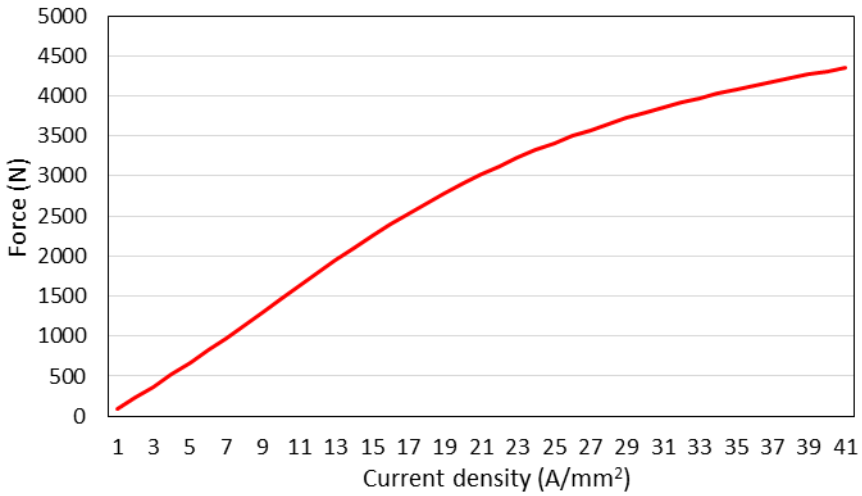


Figure 6-30 TLPM motor: FE force production

6.8 CONCLUSIONS

In this chapter, in-detail procedures on the design and modelling of the TLPM motor with a solid stator are presented. The final results illustrated in this final section of the chapter, show the excellent performance achievable by adopting the analytical and FE models presented above.

A force of 2.4 kN is achieved for a J_{rms} of 17A/mm^2 with normal cooling environment. At total mass of the whole machine of approximately 35kg, the dynamic force density of 102 N/kg and the static force density of 146.1 A/mm^2. The force ripple is less than 8.5% represents an excellent performance against the original machine of laminated version. However the ripple factor is still high, but still represents a significant improvement of 12.5% in force and 22% in ripple over the benchmark, laminated TLPM machine.

The analytical analyses, combined with the accurate characterization data, gives an accurate guide through the machine design procedure, and yield to have a clear start point for the more accurate design stage and optimization stage. Figure 6-31 shows the FE results compare with the predicted values of force production. Table 6-6 shows the machine parameters comparison between the analytical and FE analyses.

Table 6-6 analytical and FE data comparison

parameter	*Analytical*	*FE*
τ_{pole} *ratio*	*0.29*	*0.3*
Tooth width ratio	*0.5*	*0.475*
Split ratio	*0.5*	*0.62*
Back iron thickness	*3mm*	*3.9 mm*
Force (rated)	*2282*	*2397*

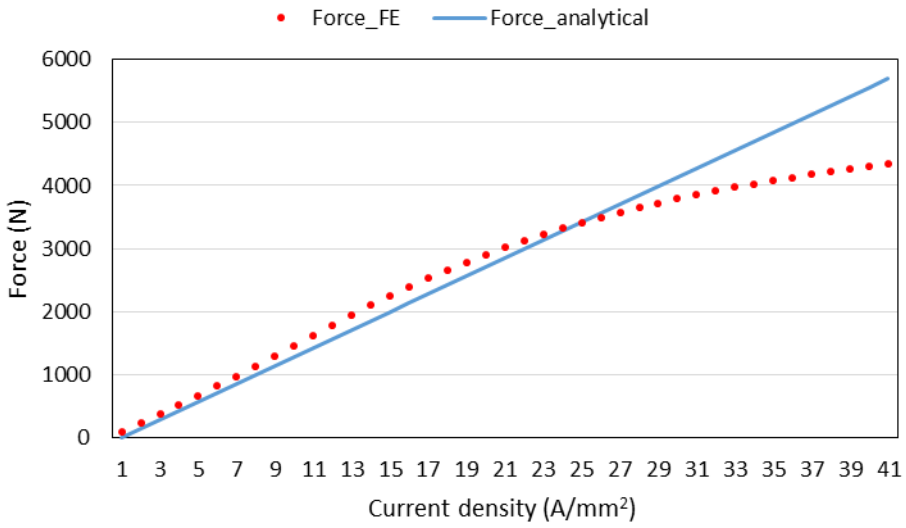


Figure 6-31 TLPM force: comparisonbetween analytical anf FE results

7. MANUFACTURING AND EXPERIMENTAL REALIZATION

7.1 INTRODUCTION

This chapter is focused on describing the prototyping effort related to the motor designed in Chapter 6 and its testing. The specific construction and assembly procedures are presented and where appropriate, various materials and different assembly techniques are investigated. The manufacturing parameters and geometrical dimensions of the TLPM motor are given in Table 6-4. The design procedures shown below are all done relative to these parameters and dimensions.

This chapter describes, in detail, the manufacturing and assembly procedures of this motor. Also, the additional features required to build the machine are included, such as coil forming (moulds), test bed, and cooling system.

7.2 MECHANICAL DESIGN AND MANUFACTURING

7.2.1 Cooling System

To remove heat from the motor, a water cooling system was incorporated into the housing of the machine, via small 8mm holes. . Theses holes are distributed uniformly around the housing periphery, and connected with each other to allow the water to circulate around the machine body at constant temperature, controlled by the water cooling system, as shown in Figure 7-1.

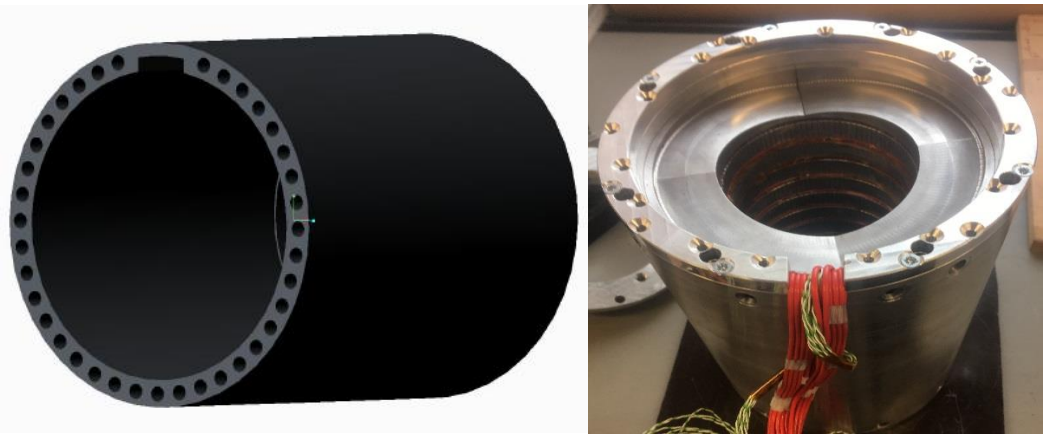


Figure 7-1 TLPM motor: Stator housing design

In this structure, it can be recognized that one of the advantages of the solid stator structure is that it does not need an external structure for lamination support, such as a stator housing, in addition to the water jacket part for the cooling system. In this structure, the stator housing and the water jacket parts are merged in one part, which gives better thermal behaviour.

7.2.2 The coils

Due to the ring shape of the TLPM motor, the coils of the machine can be pre-manufactured and wound individually. Traditionally this can be achieved by manufacturing a specific coil former usually made of aluminium and then wound the coil directly on it. However, considering the high thermal performance that is required from the TLPM motor, it was decided to impregnate the wounded coils with a highly thermally conductive silicon, SC-320, which has high thermal conductivity of (3.2 *watt/m.k*). Also, this material exhibits good electrical insulation properties. The coil mould is shown in Figure 7-2. Figure 7-3 shows the preformed coils before assembling.

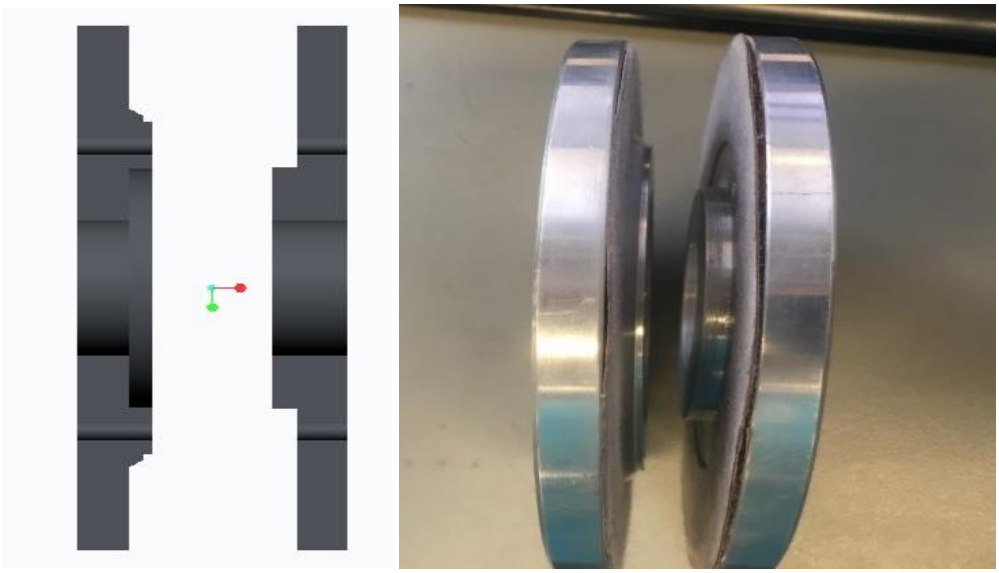


Figure 7-2 coil mould

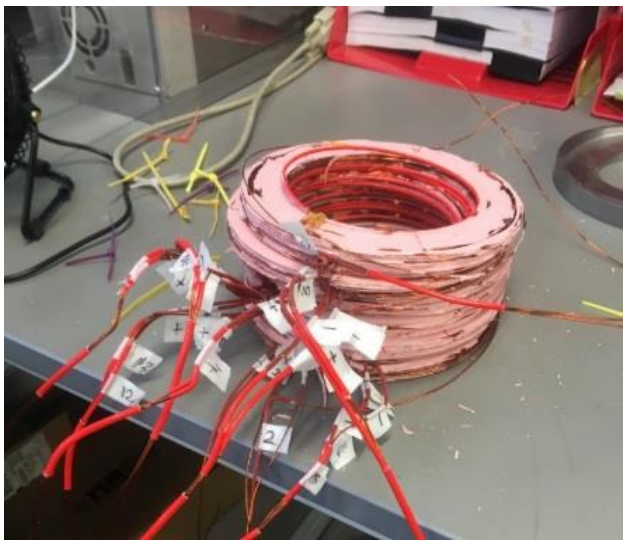


Figure 7-3 pre-formed coils

7.2.3 The stator

The use of solid magnetic material results in considerable reductions (relative to laminated stators) in the cost and construction time. Figure 7-4 shows the solid structure of one TLPM ring section, which is actually one tooth of the machine. The dimensions and the number of slits are given in Chapter 6. Holes are added to provide for external connections for the machine coils and for teeth alignment.

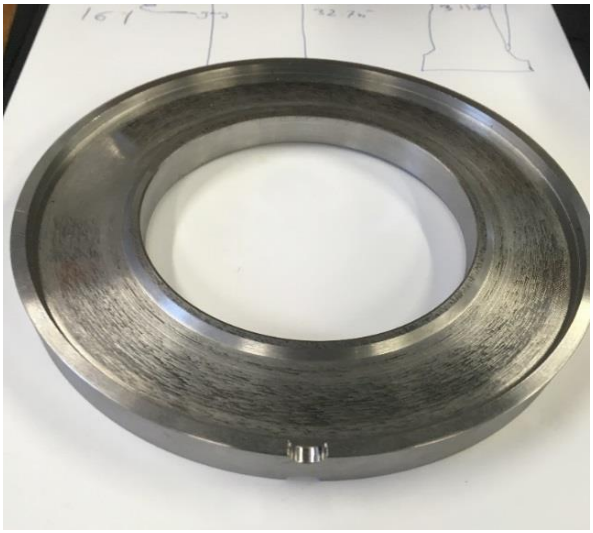


Figure 7-4 stator teeth of the TLPM motor before slitting

7.2.3.1 Solid stator slitting

Figure 7-5 shows the TLPM motor teeth slitted with 100 partial slits. The thickness of the slit was constrained by the machining/cutting process, where the minimum possible value, using an Electro Discharge Machining (EDM) tool, was found to be 0.3 mm.

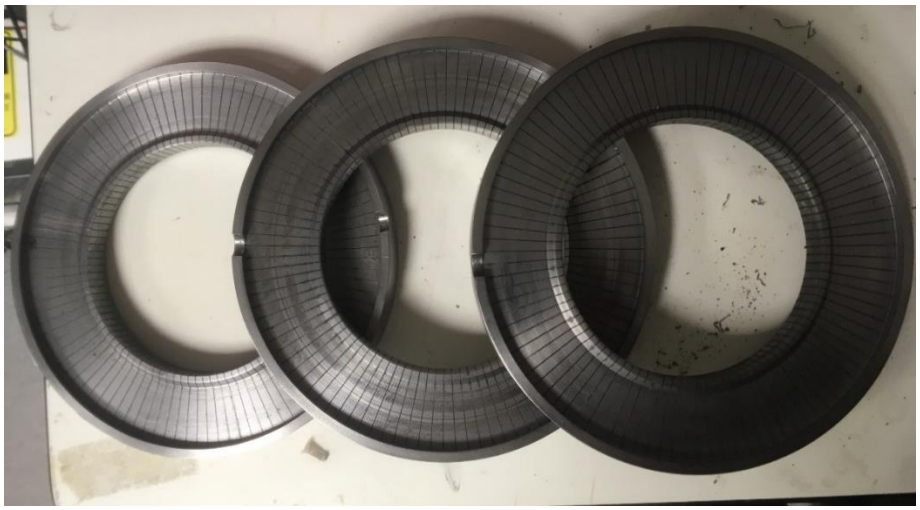


Figure 7-5 Slitted teeth of the TLPM motor

7.2.3.2 Finite end edge slitting

The TLPM motor has two end parts designed to reduce the finite edge cogging force. These two parts are made from solid steel EN8 and located at the two ends of the machine. In these parts, one coil side is located in one side of each part. So that, referring to the eddy current analyses given in section 5.6.2, unidirectional eddy current condition is found in these parts, where "Method B" is used for eddy current reduction. Figure 7-6 shows the end edge arrangement. Figure 7-7 shows the slitting technique used in the finite end edges of the TLPM motor.

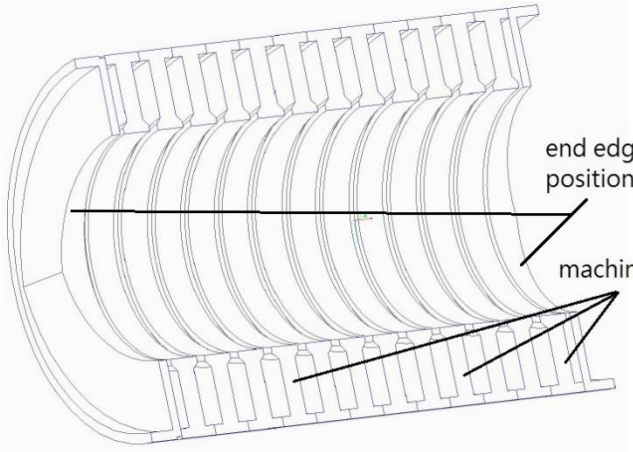


Figure 7-6 teeth and end edges arrangement



Figure 7-7 end edge slitting technique

7.2.3.3 HP slitting

Because of the ring shape of the single turn HP conductor, the proposed solution is similar to the one given by implementing a combination of "Method B", single complete slit and "Method C", one directional partial slits, explained in sections 5.6.2 and 5.6.3. Figure 7-8 shows the eddy current losses of a single HP with and without eddy current reduction normalized to the original solid HP ring. Figure 7-9 shows the final version of the HP parts of the machine.

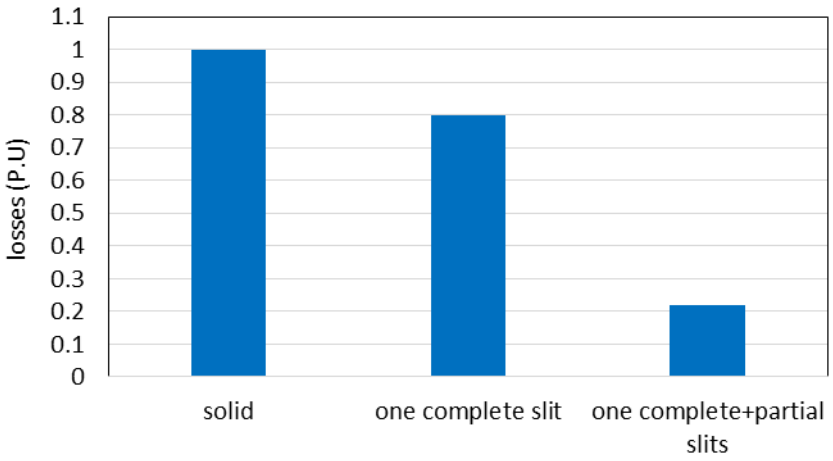


Figure 7-8 HP losses with different models



Figure 7-9 Slited HP (one complete slit + partial slits)

The structure highlighted in Figure 6-25, is used to build the stator teeth, coils, and the HPs in such a sequence so that together they form the complete assembled stator part. This is shown in Figure 7-10.

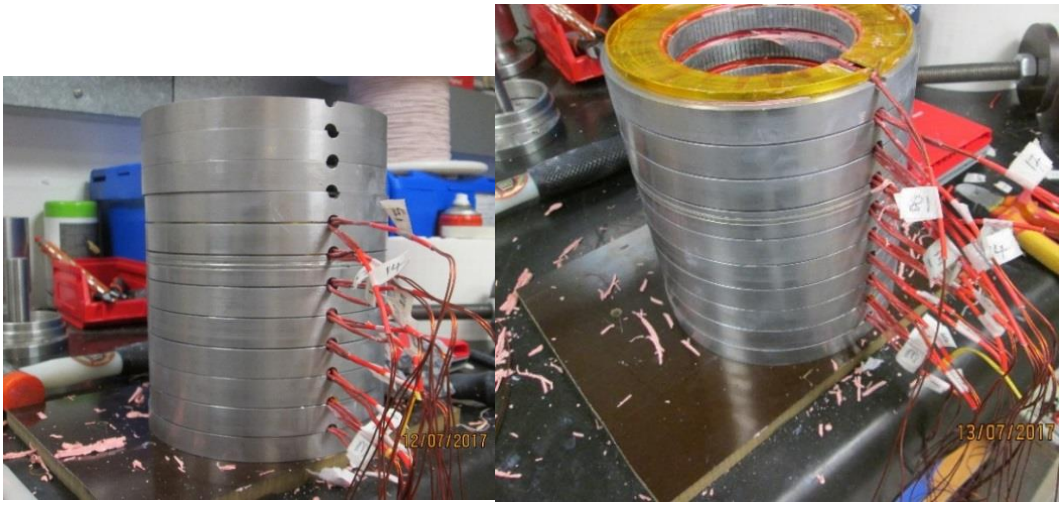


Figure 7-10 stator teeth and coil assembly

Figure 7-11 and Figure 7-12 show the stator assembled inside the stator housing part, which at the same time is used as a water jacket for the machine's cooling. The stator housing is manufactured with a number of axial slots on the inside bore as these provide a path for the windings terminals to the external connection box. An appropriate fit between the inner surface diameter of the stator housing and the outer surface diameter of the stator teeth is required in order to provide good thermal conductivity between the stator and the cooling system.

In each slot, a k-type thermocouple has been accommodated at an appropriate depth inside the stator slot to monitor the coil temperature. The skewed finite edges are also fitted inside the stator housing sides.

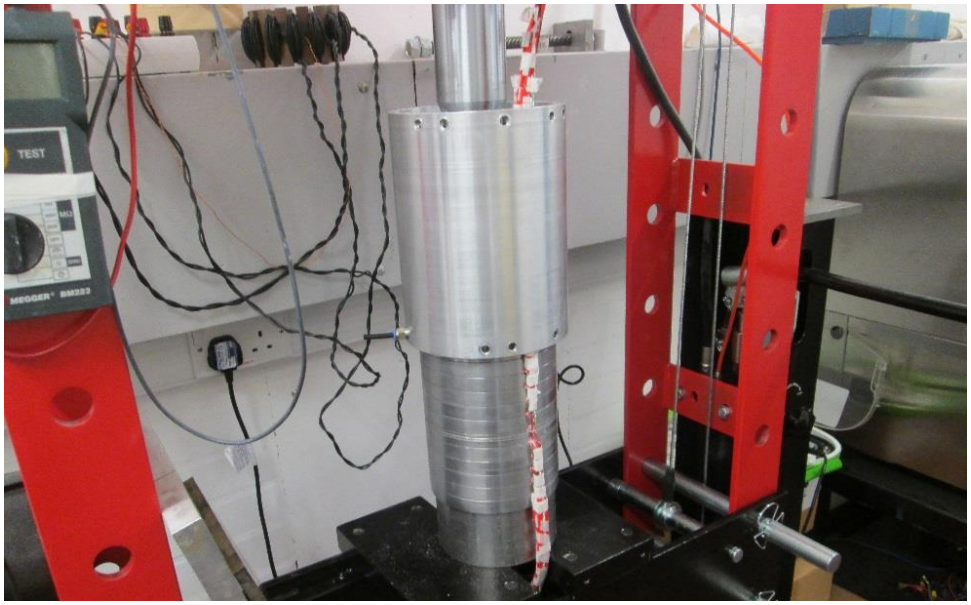


Figure 7-11 stator and housing assembly stage

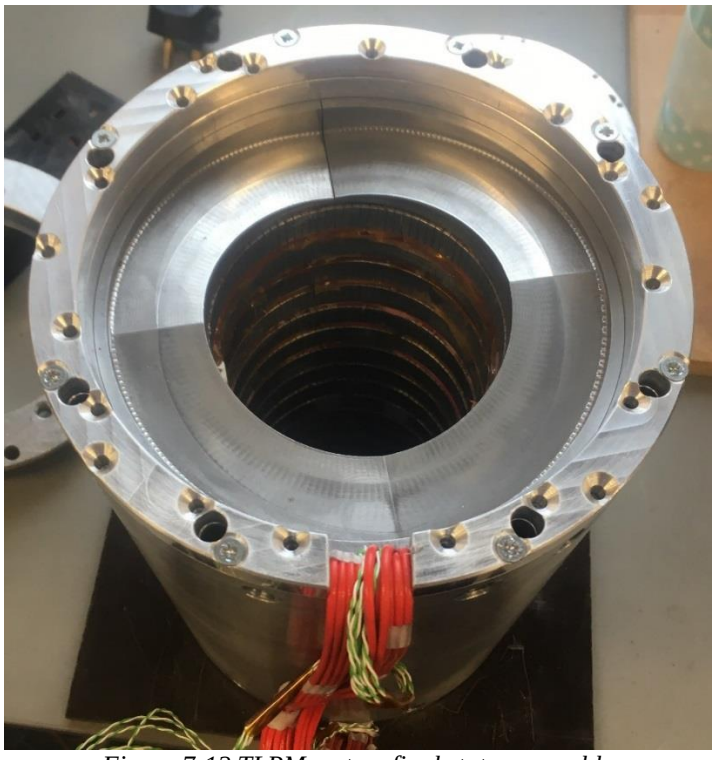


Figure 7-12 TLPM motor: final stator assembly

7.2.4 The mover

For an IPM configuration, the mover consists of the axially magnetised PMs, the flux focusing pieces, the non-ferromagnetic support tube and the shaft. The PMs

and the pieces are simply slid onto the support tube. Figure 7-13 and Figure 7-14 illustrate the mover assembling stage and the final assembled mover respectively.

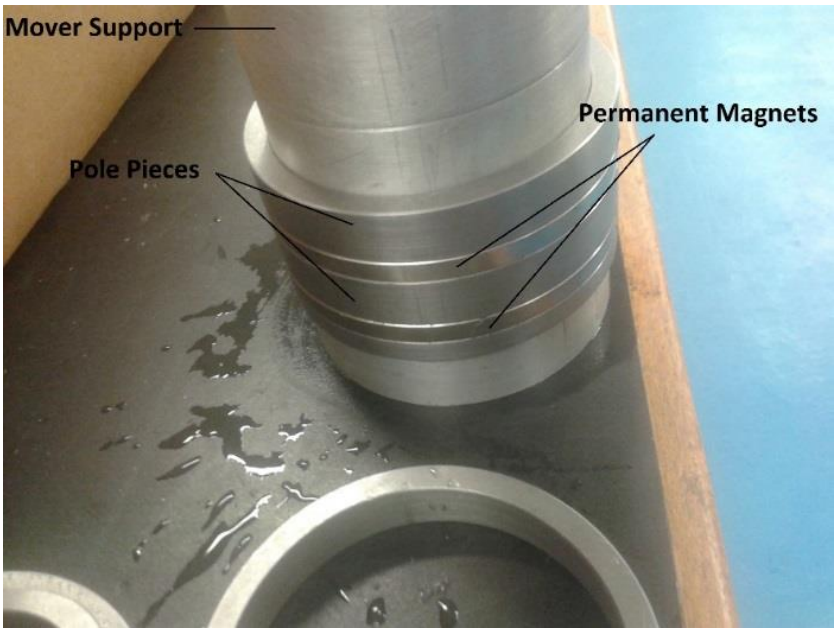


Figure 7-13 TLPM motor: Mover assembling

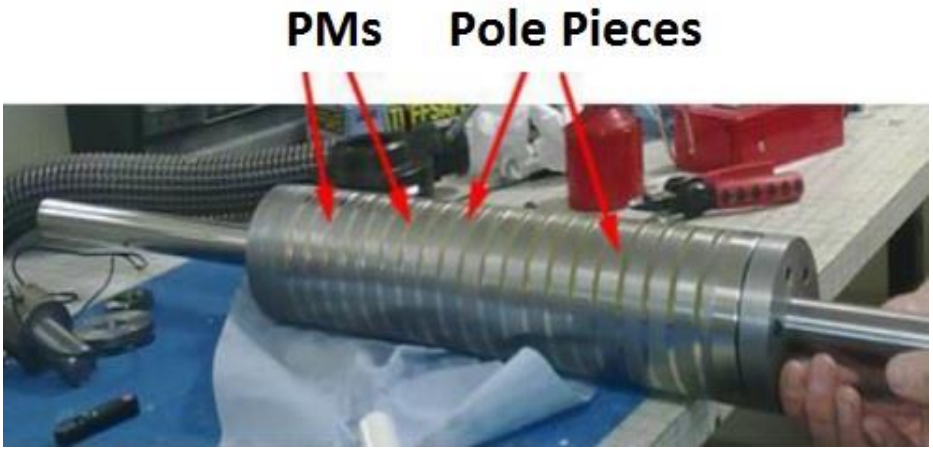


Figure 7-14 TLPM motor: final mover assembly [10]

7.2.5 Final TLPM motor properties

Once the complete machine been assembled, all physical quantities of the machine have been measured. Table 7-1 shows the final physical properties of the TLPM machine comprised with designed values.

Table 7-1 final TLPM motor properties

Quantity	Design Value	Actual Value	Unit
Active Stator Length	*229.8*	*230.4*	*mm*
Active Mover Length	*199.8*	*200.4*	*mm*
Total Stator Length	*290*	*290.6*	*mm*
Total Mover Length	*480*	*479.5*	*mm*
Total Stator Weight	*23.37*	*25.7*	*kg*
Total Mover Weight	*13.14*	*10.7*	*kg*

7.3 OVERALL STRUCTURE AND ASSEMBLY

A general view of the motor test rig is shown in Figure 7-15. The whole motor is assembled on a test-bed that includes all associated features such as linear bearing guides, support plates and a load actuator for testing purposes.

In order to perform a complete set of tests, an industrial 40kW EMA capable of peak force loads up to 17.8kN with a maximum stroke of 100mm at a maximum linear velocity of 313mm/s is used [163]. The EMA is connected to the shaft of the TLPM motor via a high accuracy linear load cell transducer in order to measure the thrust force. Figure 7-16 shows the early stages of test rig set-up and Figure 7-17 shows the complete test rig.

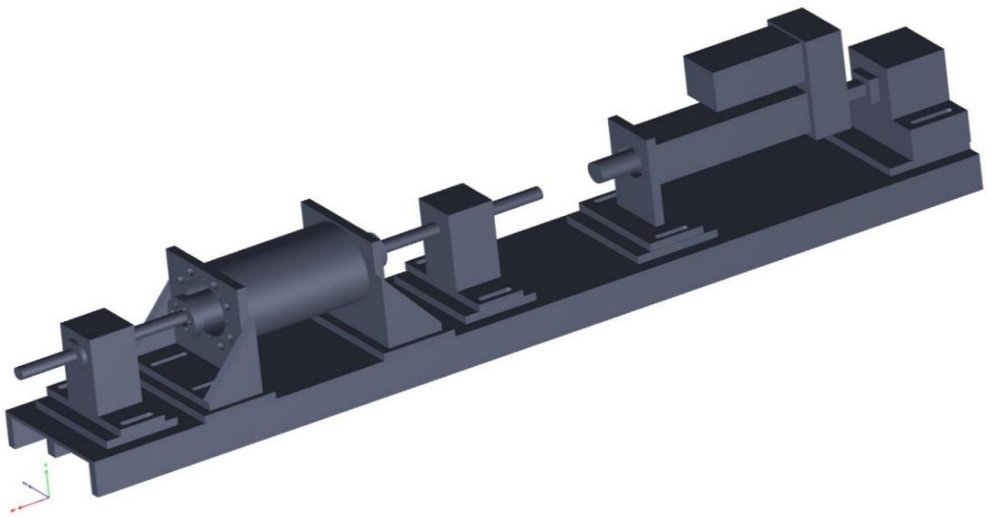


Figure 7-15 TLPM motor: Overall assembled Structure

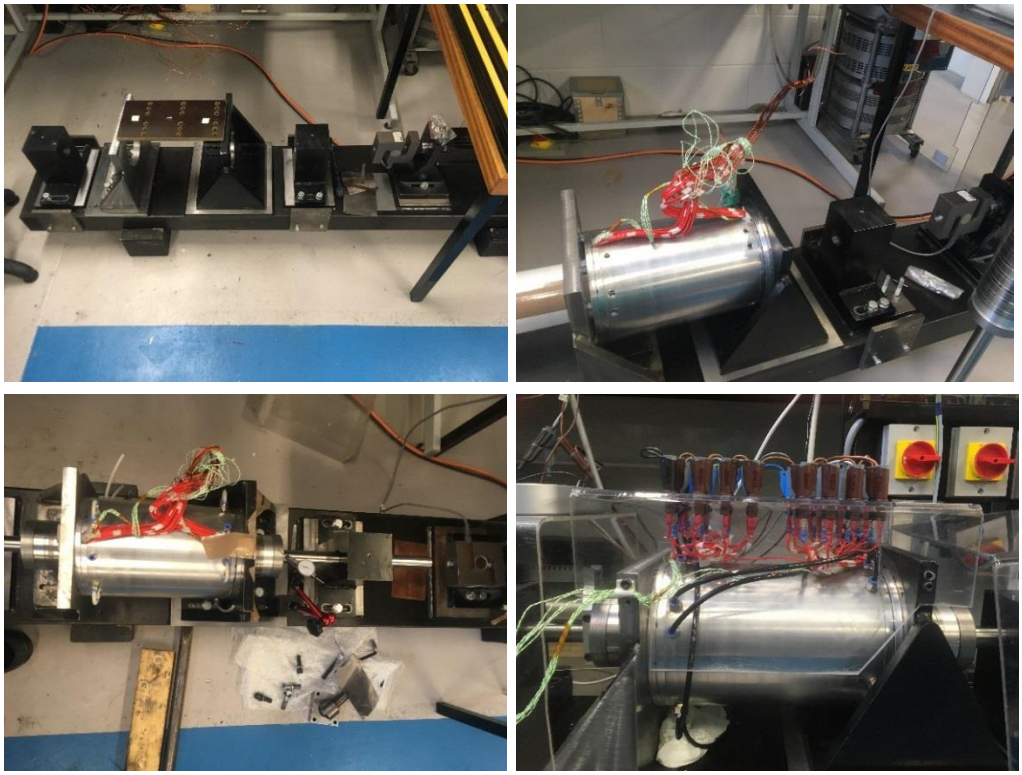


Figure 7-16 TLPM motor: test rig assembling stage

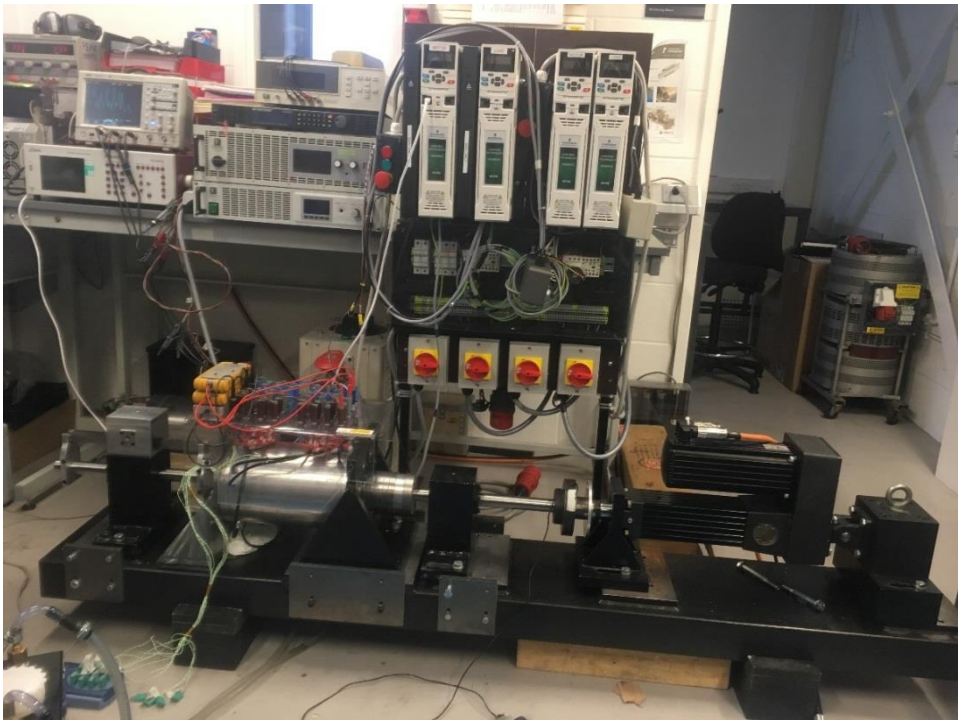


Figure 7-17 TLPM motor: complete structure of the test rig

7.4 DESIGN OF EXPERIMENT

In order to validate the performance of the prototype machine, a series of tests were done. These are presented and described below.

7.4.1 Machine Static Parameters

Having the assembled motor and rig permits the measurement of certain parameters that are critical to the operation of the machine such as static parameters. To check the machine winding static parameters against the predicted values, the d.c. and a.c. resistances of the phase windings have been measured using a 4-wire measurement micro Ohmmeter. The a.c. parameters have been measured at frequency equal to 20Hz and steady state ambient temperature equal to 40^{o}C. Table 7-2 shows the obtained parameters compared with the predicted values.

Table 7-2 static parameters of the machine at 20Hz

parameter	*FE*	*Experimental*	*Error %*	*unit*
R_{phase} *(a.c.)*	*13.4*	*11.65*	*13%*	*Ω*
R_{phase} *(d.c.)*	*11.2*	*10.7*	*4.4%*	*Ω*
L_{d_phase}	*147*	*142*	*3.4%*	*mH*
L_{q_phase}	*104*	*92*	*11%*	*mH*

7.4.2 Short Circuit Fault

Fault calculations are one of the most common types of checks carried out during the design and analysis of electrical machine and drive systems. These calculations involve determining the current flowing through machine windings during abnormal conditions of three phase short circuit fault as shown in Figure 7-18. This test focuses on the winding temperature raise during the abnormal condition, which is very critical in aerospace applications. As it can be seen in Figure 7-19, the coil temperature stays within acceptable limit even after a long fault time.

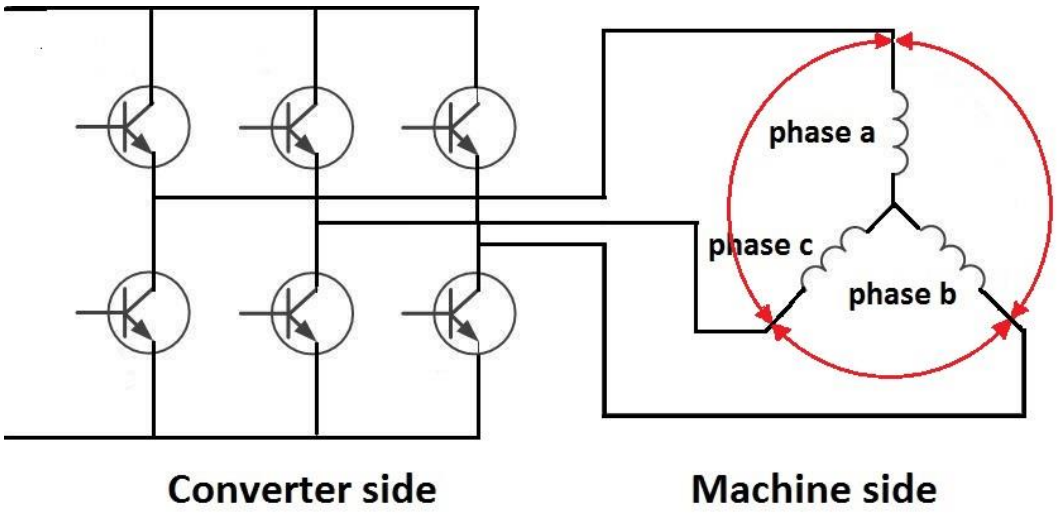


Figure 7-18 three phase short circuit fault

This experimental test can be performed by physically shorting the machine terminals of the TLPM motor and then using the load EMA to translate the mover at a rated velocity of 100 mm/sec and generate short circuit current at rated frequency of 2.5 Hz.

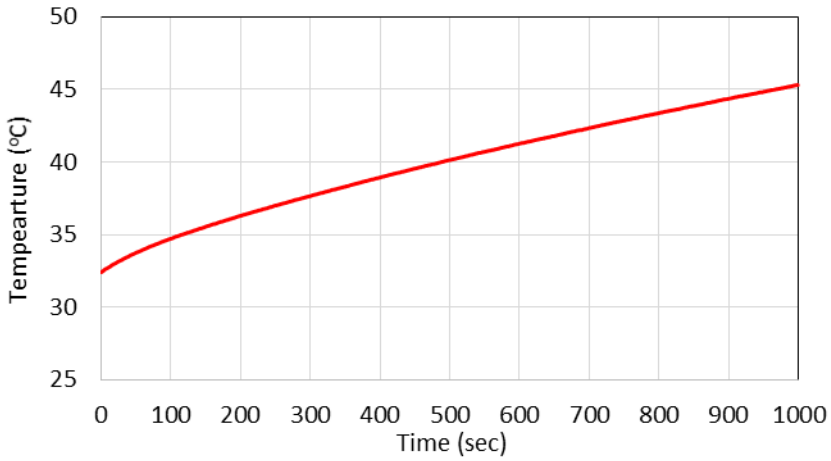


Figure 7-19 TLPM motor: coil temperature under short circuit fault at rated speed

The experimental results of the test are shown in Figure 7-20, where all phase to phase short circuit currents are measured and compared with FE result.

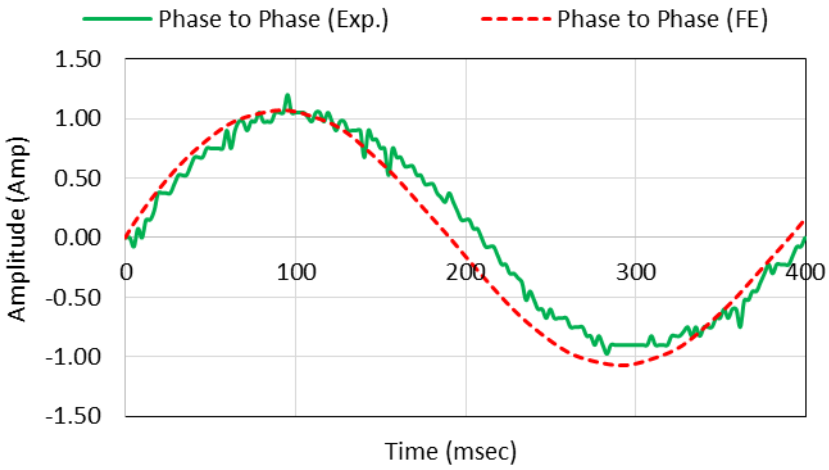


Figure 7-20 TLPM motor: short circuit fault current at rated speed

7.4.3 No load back *emf*

The no load $back_emf$ can be obtained by measuring the voltage induced across the open winding terminals. The objective for this test is:-

1. Check the machine no load generating voltage developed against the design criteria.
2. Check the $back_emf$ voltage balancing.
3. Check the harmonic content of machine back *emf*.

Figure 7-21 shows the measured signal of one phase and also compares it to the predicted back-EMF from the FE results. It can be observed that the experimentally measured voltage is slightly higher in amplitude and harmonic content compared with the predicted analysis, where the maximum error is about 6%. This difference between the signals can be safely attributed to experimental tolerance. Figure 7-22 shows the harmonic content for both results.

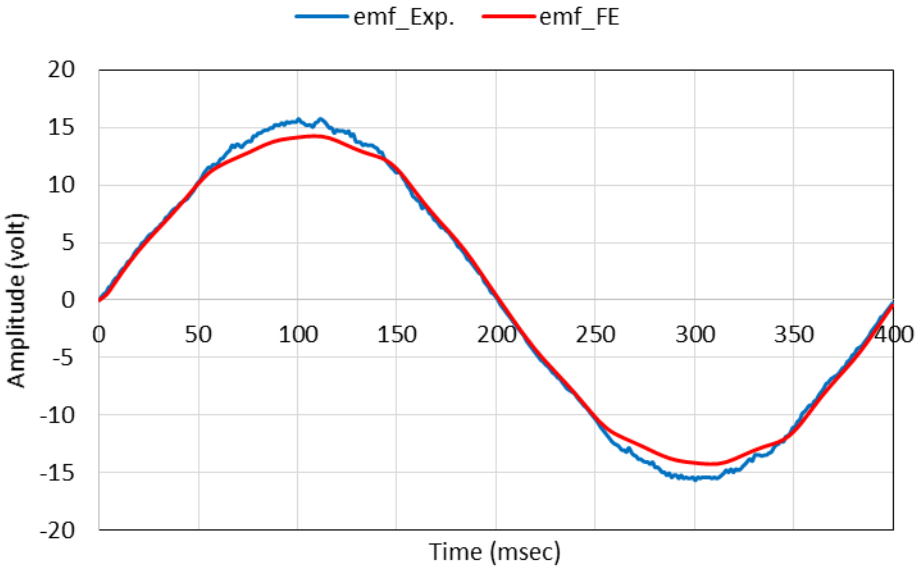


Figure 7-21 TLPM motor: back-EMF, waveform comparison.

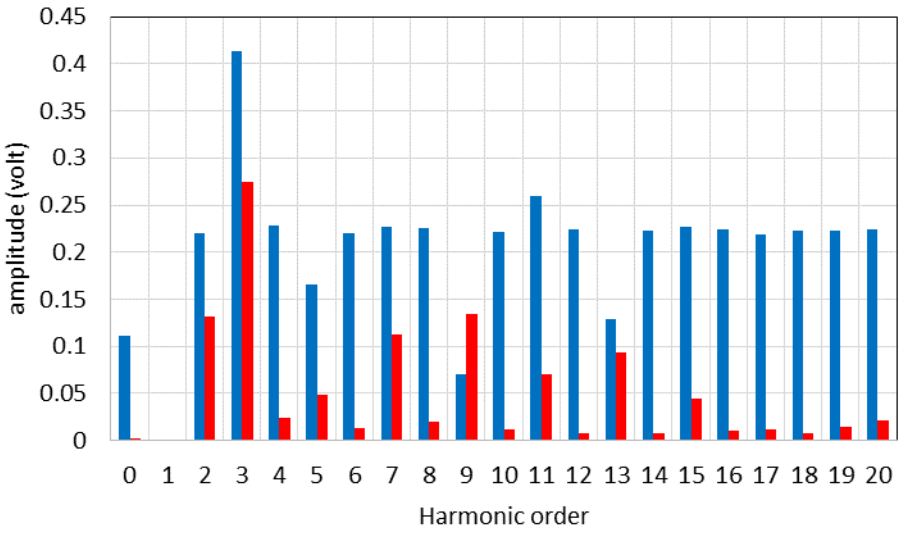


Figure 7-22 TLPM motor: back-EMF, FFT comparison.

7.4.4 Cogging Force

The cogging force has been obtained by driving the mover of the TLPM machine using the EMA unit at low and constant speed (approximately 5 mm/sec) via load cell transducer shown in Figure 7-23.

For the no load condition, the axial force acting on the load cell over an electric cycle is recorded. Figure 7-24 shows the experimental results compared with FE results. It worth mentioning that both cogging force components are included in the obtained results.

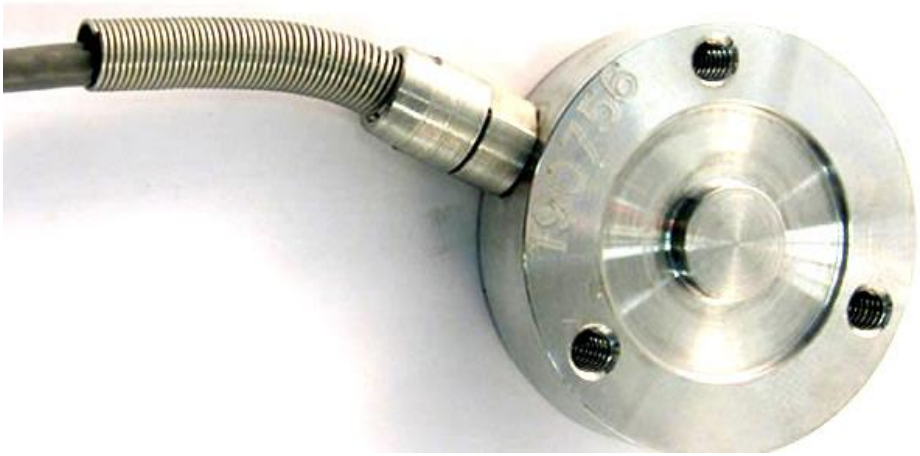


Figure 7-23 linear load cell trancducer

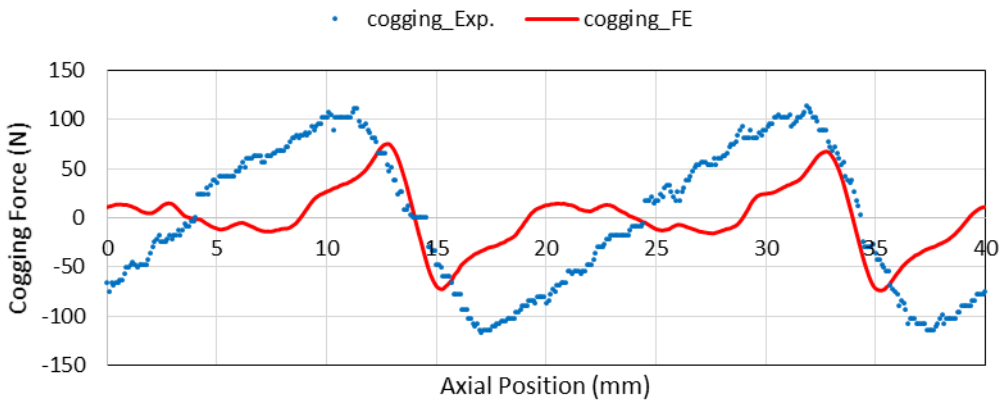


Figure 7-24 TLPM motor: cogging force comparison

7.4.5 Thrust Force

A major point of interest of this experimental section is the force capability of the TLPM motor, as the force and force density capability of the machine is one of the critical targets of the work. The complete structure given in section 7.3 and shown in Figure 7-17 is used to measure the values of the generated linear force. The thrust

force of the TLPM motor is measured with different load currents with water cooling system to maintain the coil temperature at its desired level. The maximum limit of the supply current depends on the maximum allowable temperature inside the slot coil. Figure 7-25 shows the results of the experimental tests and also compares the results with the predicted values. It is important to note that for high values of supply current, mainly values higher than the rated current, the test is done for a very short period of time as at this current value to reduce the thermal stress on the magnets. Generally, this current limit is lower than the predicted value. A very good similarity between the predicted and measured results is achieved. This can be attributed to the accurate 3D modelling and the proposed magnetic material characterisation methods. The force density (N/kg) is also measured and shown in Figure 7-26. Table 7-3 shows the overall performance of the solid version of the TLPM motor.

The predicted and measured values of the force constant K_F are shown in Figure 7-27. It can be seen that the maximum difference between the experimental and FE values is approximately equal to 6 %. The average value of the discrepancy between results is around 0.5%.

Table 7-3 TLPM motor performance chart

Parameter	*Solid version*	*Unit*
Stator Weight	*25.5*	*kg*
Mover weight	*10.7*	*kg*
Stator volume	*5551*	*cm^3*
Stator Outer diameter	*160*	*mm*
Total outer diameter	*188*	*mm*
Rated Current density (rms)	*17*	*A/mm^2*
Rated speed	*100*	*mm/sec*
Static Force	*3310*	*N*
Force density	*129.8*	*N/kg*

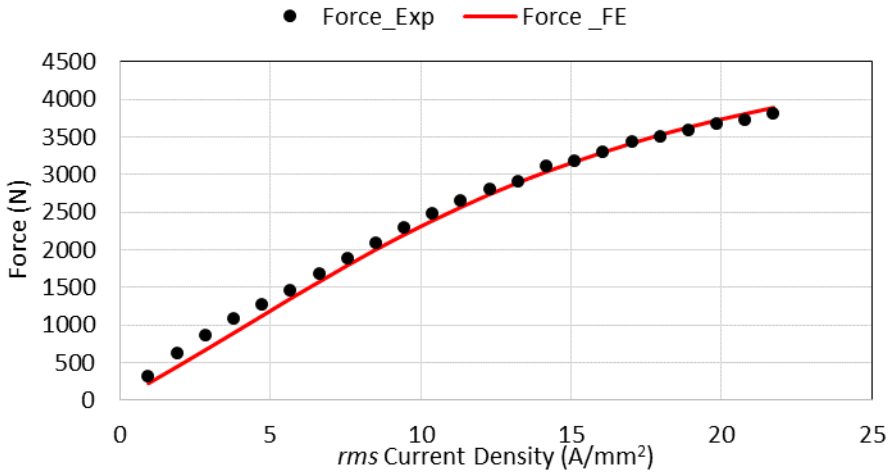


Figure 7-25 TLPM motor: force capability comparison

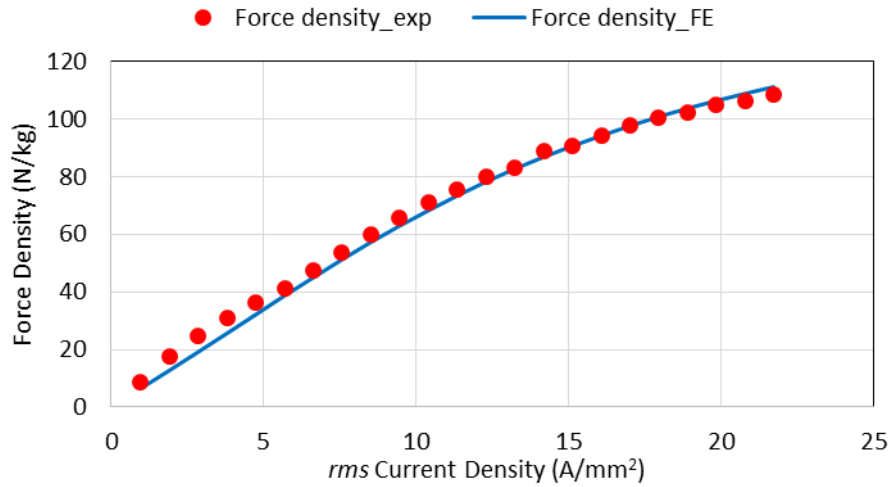


Figure 7-26 TLPM motor: force density

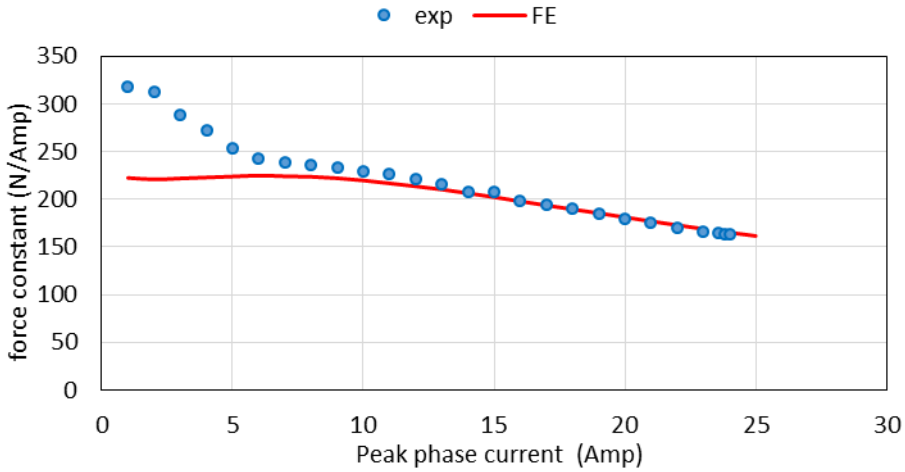


Figure 7-27: Comparison force constant (K_F) of TLPM motor

7.5 CONCLUSION AND COMPARISON TO EXTANT MOTORS

Having fully tested the TLPM motor with a solid stator, a comparison with the original bench mark machine is then done. Examining the motor static force density of both motors, it is clear that the TLPM motor with solid stator performs very well when compared to the benchmark, laminated machine. Table 7-4 shows the comparison between the two models, while Figure 7-28 compare the produced static force for the two models.

Table 7-4 differences between the two versions of the TLPM

Parameter	*Laminated version*	*Solid version*	*Unit*
Stator Weight	*26.3*	*25.5*	*kg*
Mover weight	*10.7*	*10.7*	*kg*
Stator volume	*5600*	*5551*	*cm^3*
Stator Outer diameter	*150*	*160*	*mm*
Total outer diameter	*210*	*188*	*mm*

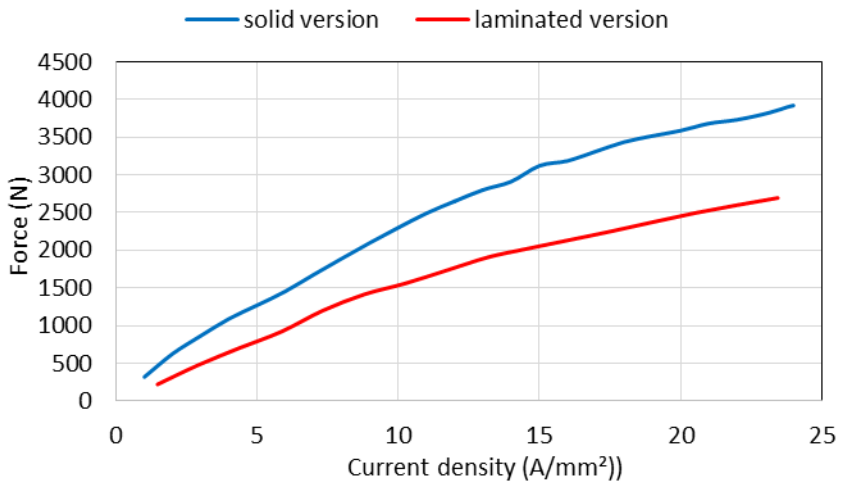


Figure 7-28 produced force for the two versions

Considering all the above, then it is appropriate to state that the proposed solid stator TLPM motor is an optimal solution for the low cost, high performance machine when the operating frequency is relatively low.

Compared with the laminated version of the TLPM motor, the following points explain the advantages of the solid materials in the designing and manufacturing a low speed TLPM motor from manufacturing and performance perspectives:-

1- The modular construction of the machine is easy to be manufactured.
2- Have relatively low production costs.
3- Offer the possibility to realize complex geometrical shape.
4- High material density per unit volume.
5- Good magnetic properties, because high f_{stack} (unity) is achieved.
6- Good thermal properties, because no voids are exist.
7- Isotropic physical and magnetic properties.

The disadvantages of laminated version of the TLPM motor:-

1- Low material density per unit volume, because of the sunshine arrangement of laminations.
2- Low f_{stack} (approximately 0.773)
3- Expensive and time consuming in manufacturing process.
4- misalignment between the lamination sheets of adjacent stator teeth
8- Poor thermal properties.

8. CONCLUSIONS AND FUTURE WORKS

8.1 INTRODUCTION

Machines that can achieve linear actuation and are also relatively mechanical jam free are a very attractive solution for environments where reliability requirements are very important, such as for example in the aerospace industry. However, the lack of any mechanical advantage means that any linear machine employed in such an environment requires excellent values of force density.

While the above is of critical importance, there is also a need to consider the cost and manufacturing aspects of such machines. This thesis has in fact focused a lot of effort on such aspects. In particular this thesis has investigated a feasible manner by which to reduce the manufacturing complexity associated with the laminated structure of the stator of tubular linear machines. The scheme is based around the development of TLPM motor which uses a solid core for its stator.

The main advantage of this solution which was first introduced in Chapter 2 is of course the manufacturing benefits. Machining and processing of solid materials is significantly easier, faster and cheaper than development of machine structures with axial laminations. However contrary to the initial perceptions, this solution has shown that the use of solid materials for the stator core can also affect positively in the machine performance. This is mainly coming from the improvement in terms of the machine's f_{stack} and the excellent resulting thermal behaviour. To validate all this a new TLPM motor with a solid stator core was developed, prototyped and

tested. Excellent results in terms of performance were achieved in comparison to the benchmark machine.

In order to develop this process a 'journey' related to material characterisation, eddy current reduction and machine design and optimisation has been undertaken and presented in this thesis. Discussions on these aspects are given below.

8.1.1 Material characterization

A new approach to develop a more detailed understanding of the magnetic characterization field has been introduced, investigated and validated in Chapter 4. This approach [144] was critical for the project as it resulted in a significant increase in accuracy in terms of the data captured when compared to that of conventional methods of material characterisation. This improvement is mainly related to the fact that a TLPM motor is an electrical machine that has an unconventional magnetic circuits. The proposed method was shown to achieve an accurate map of material losses used in t TLPM machines.

The method was shown to provide more accurate results for losses prediction and accurate characterization of solid magnetic materials. It is therefore ideal for characterizing solid materials used in electrical machines with non-standard flux directions. This method has been mainly developed for TLPM machines in which the flux line directions and eddy current paths are completely different when compared with those of classical rotating machines.

It can be concluded that this new method shows that the eddy current losses of solid materials be significantly higher than predicted by normal methods.

8.1.2 Eddy current reduction techniques

For an electrical machine that comprises solid cores, then it is clear that eddy currents will be a major source of less. In this part of the thesis an investigation related to the eddy current behaviour inside any solid part was done. For the application at hand, it was clear that the direction and the magnitude of the eddy currents were different from tooth to tooth. Thus a suitable eddy current reduction technique was required. Such a technique was proposed and investigated in Chapter 5, based on the material knowledge achieved from Chapter 4.

Various methods for eddy current reduction were implemented. It has been shown that the eddy current and its behaviour is strongly dependent on the current condition inside the slot area. It has also been shown that for the TLPM motor in question, there are two types of typical eddy current patterns, namely a unidirectional and bidirectional one.

8.1.3 Machine design

Employing all the knowledge developed in Chapter 4 and 5, the TLPM motor with a solid core was designed and optimized in Chapter 6. The machine was based on the benchmark TLPM machine and in this chapter the performances of the two machines were analysed and compared. Chapter 7 was focused on the prototyping effort of the TLPM motor and also illustrates the experimental tests done, which show that using an accurate model with accurate material data, excellent similarity between predicted and measured results is achieved. In fact with the FE models equipped with the experimentally measured data, the prediction errors of the models are minimal.

8.2 GENERAL COMPARISON

The performance capabilities of the prototype TLPM motor for the rated current loading are tabulated below in Table 7-3.

The excellent performance of the TLPM motor in terms of its force density relative to the benchmark machine can be appreciated more clearly from Table 8-1. This comparison chart tabulates the force- to-mass performance of the two versions of the TLPM motor.

Table 8-1 performance comparison chart

parameter	*Benchmark machine*	*TLPM with solid stator*	*units*
F_{lin}	*2128.5*	*2397*	*N*
Mass	*26.3*	*25.5*	*kg*
Stator volume	*5600*	*5551*	*cm3*
Force density	*0.38*	*0.432*	*N/cm3*
Force density	*91.51*	*102*	*N/kg*

As a final step in this thesis, the TLPM machine performance is compared to a number of known high performance tubular machines from existing literature. This comparison is given below in, Table 8-2 where it can be easily observed that the final TLPM motor with a solid stator compares excellently with such machines.

Table 8-2 Force density comparison chart

	machine	*Topology*		*Operation*	*Force density (N/cm^3)*
		PMs	*Air-gap*		
1	*Ziegler et al. [164]*	*SMPM*	*Multi*	*Pulsed*	*4.8*
2	*Cavarec et al. [165]*	*IPM*	*Multi*	*Continuous*	*1*
3	*Solid TLPM motor*	*IPM*	*Single*	*static*	*0.432*
4	*Wang et al. [33]*	*Quasi-Halbach*	*Single*	*Continuous*	*0.43*
5	*Galea et al. [7]*	*IPM*	*Single*	*Continuous*	*0.38*
6	*Danson et al. [166]*	*SMPM*	*Double*	*Continuous*	*0.35*
7	*Bianchi et al. [13]*	*SMPM*	*Single*	*Continuous*	*0.35*
8	*Bianchi et al. [13]*	*IPM*	*Single*	*Continuous*	*0.25*

From Table 8-2, it can be observed that apart from the multi air-gap technologies (which however state their performances relative to the active volume and not to the total volume of the machine), solid stator version TLPM motor exceeds all other the TLPM motors performance in terms of force-to-volume ratio.

8.3 FUTURE WORK

Apart from a full and complete characterisation of the TLPM motor, there are several other points that can be identified as interesting targets for future research in order to improve the following areas;-

8.3.1 Motor Design

Investigations of alternative designs of the TLPM motor in an effort to improve the force-to-mass performance capability.

Electrical machines, in general, can be improved against the magnetic limit and thermal limit. An interesting aspect to be considered in the future is an investigation on the effects that the effective air gap area can have on the magnetic limit of the machine. Increasing this air-gap implies improvement in the machine performance without increasing the mass of the volume of the machine. This can be done by using different airgap shapes.

From the circle and ellipse relationship, it can be assume that with the same area, the circumference of the elliptic shape is greater than circle shape [167].

Using this idea, the force density of the TLPM motor can be improved by increasing the effective air gap area using elliptic mover shape, without any increase in the machine weight, complexity and cost. The following point can explain the advantages of this structure:-

1- Theoretically, the machine circumference can be varied from 1 to ∞ times the circular shape. Practically the effective air gap area can be change from 1 to 1.7 times the circular model.
2- Has the same properties of circular tubular motor such as, no end winding, balance radial force, radial heat dissipation path … etc.
3- Solid material can be employed successfully in such design.

8.3.2 Material Characterization

The characterization of magnetic materials is usually arranged as a transformer where the flux density of the alternating magnetic field is building basically a one-dimensional field component. This is usually enough to obtain the magnetization characteristics and core loss.

However, the discrepancy between standard measurements and calculations is usually large when applying this knowledge either to incompletely known materials or unconventional cores. Therefore knowledge of the exact materials that can be used for the design and the estimated character of the magnetic loading is a necessary input for the design process.

The new characterization method, proposed in this work, need to be further improved by accommodating a three phase winding instead of a single phase winding. The three phase winding will generate a translating magnetic field strength in the core specimen. Then, this feature will extend the characterization domain and a rotating magnetic field will be produced instead of pulsating magnetic field.

APPENDIX A

Solution of the airgap subdomain (region I):

The magnetic vector potential ***A*** in the airgap (region I) can be obtained by solving Laplace's and poisson equations as follow:

$$\frac{\partial}{\partial z}\left(\frac{1}{r}\frac{\partial}{\partial z}\left(r\cdot A_{I\theta}\right)\right)+\frac{\partial}{\partial z}\left(\frac{1}{r}\frac{\partial}{\partial r}\left(r\cdot A_{I\theta}\right)\right)=0 \qquad \textit{(A- 1)}$$

$$\frac{\partial}{\partial z}\left(\frac{1}{r}\frac{\partial}{\partial z}\left(r\cdot A_{II\theta}\right)\right)+\frac{\partial}{\partial z}\left(\frac{1}{r}\frac{\partial}{\partial r}\left(r\cdot A_{II\theta}\right)\right)=-\mu_o\nabla\times\vec{M} \qquad \textit{(A- 2)}$$

M is the magnetization vector of the magnets and is given by:-

$$\vec{M}=M_z\,\vec{j}_z \qquad \textit{(A- 3)}$$

Where M_z denotes the magnitude of M in the z direction (for axially magnetized magnet) and j is the unit vector. This vector may be expressed as the furrier series given in:

$$\vec{M}_z=\sum_{n=1,2,\ldots}\frac{4B_{rem}}{\mu_o\pi(2n-1)}\sin\left(\frac{(2n-1)\pi\tau_m}{2\tau_{pole}}\right)\cos(m_n z) \qquad \textit{(A- 4)}$$

The boundary conditions to be satisfied by the solution to (A- 1) are given in [86]. Solving (A- 1) subject to the boundary conditions of [86] yields to following equations:

$$B_{Ir} = \sum_{n=1}^{\infty}\left[a_{In}BI_1(m_n r) + b_{In}BK_1(m_n r)\right]\sin(m_n z) \quad \textit{(A- 5)}$$

$$B_{Iz} = \sum_{n=1}^{\infty}\left[a_{In}BI_0(m_n r) - b_{In}BK_0(m_n r)\right]\cos(m_n z) \quad \textit{(A- 6)}$$

$$B_{IIr} = \sum_{j=1}^{\infty}\left[a_{IIj}BI_1(q_j r) + b_{IIj}BK_1(q_j r)\right]\sin(q_j z) \quad \textit{(A- 7)}$$

$$B_{IIz} = \sum_{j=1}^{\infty}\left[a_{IIj}BI_0(q_j r) - b_{IIj}BK_0(q_j r)\right]\cos(q_j z) \ + B_0 \quad \textit{(A- 8)}$$

$$B_{IIIr} = \sum_{n=1}^{\infty}\left[a_{IIIn}BI_1(m_n r)\right]\sin(m_n z) \quad \textit{(A- 9)}$$

$$B_{IIIz} = \sum_{n=1}^{\infty}\left[a_{IIIn}BI_0(m_n r)\right]\cos(m_n z) \quad \textit{(A- 10)}$$

Where BI_0 and BI_1 are modified Bessel functions of the first kind; BK_0 and BK_1 are modified Bessel functions of the first kind, of order 0 and 1, respectively,

n is the harmonic order of the magnetic field in region I and III, and *j* is the harmonic order of the magnetic field in region II.

In order to solve above equations, let define the following sets of coefficients:-

$$m_n = (2 \cdot n - 1) \cdot \pi / \tau_{pole}$$
$$q_j = (2 \cdot j) \cdot \pi / \tau_m$$

$$c1_n = besseli\ (0, m_n \cdot R_s)$$
$$c2_n = besselk\,(0, m_n \cdot R_s)$$

$$c3_n = besseli\ (1, m_n \cdot R_r)$$
$$c4_n = besseli\ (0, m_n \cdot R_r)$$
$$c5_n = besseli\ (0, m_n \cdot R_m)$$
$$c6_n = besselk\ (0, m_n \cdot R_m)$$
$$c7_n = besseli\ (1, m_n \cdot R_m)$$
$$c8_n = besselk\ (1, m_n \cdot R_m)$$

$$c1_j = besseli\ (1, q_j \cdot R_m)$$
$$c2_j = besselk\ (1, q_j \cdot R_m)$$
$$c3_j = besseli\ (0, q_j \cdot R_m)$$
$$c4_j = besselk\ (0, q_j \cdot R_m)$$
$$c5_j = besseli\ (1, q_j \cdot R_r)$$
$$c6_j = besselk\ (1, q_j \cdot R_r)$$
$$c7_j = besseli\ (0, q_j \cdot R_r)$$
$$c8_j = besselk\ (0, q_j \cdot R_r)$$

$$d1_n = c2_n \times c7_n / c1_n + c8_n$$
$$d2_n = c5_n \times c2_n / c1_n - c6_n$$

$$d1_j = c4_j \times c6_j / c2_j$$
$$d2_j = c8_j \times c6_j / c2_j$$

$$E_n = R_{m\cdot} \cdot d1_n / m_n \cdot \cos(m_n \cdot \tau_m / 2)$$
$$G_n = R_{r\cdot} \cdot c3_n / m_n \cdot \cos(m_n \cdot \tau_m / 2)$$

$$E_j = \cos(q_j \cdot \tau_m / 2) \cdot (c1_j \cdot R_m - c5_j \cdot R_r) / q_j$$
$$G_j = \cos(q_j \cdot \tau_m / 2) \cdot (c2_j \cdot R_m - c6_j \cdot R_r) / q_j$$

$$Q_n = 4 \cdot \sin(m_n \cdot \tau_m / 2) / (\pi \cdot \mu_r * (2.n - 1))$$
$$Q_n = 4 \cdot \sin(m_n \cdot \tau_m / 2) / (\pi \cdot \mu_r * (2.n - 1))$$

$$B_n = B_{rem} \bullet Q_n$$

$$v = (m_n - q_j) \cdot \tau_m / 2$$

$$u = (m_n + q_j) \cdot \tau_m / 2$$

$$F_{jn} = (\sin(v)/v - \sin(u)/u$$

$$F_{nj} = (\sin(v)/v + \sin(u)/u) \cdot \tau_m / (\mu_r \cdot \tau_{pole})$$

$$R_o = (R_m^2 - R_r^2)/2$$

a_{In}, b_{In}, a_{IIj}, b_{IIj}, a_{IIIn}, and B_o are the solution of the instantaneous linear equations, for n = 1, 2, 3,… ∞ and j= 1, 2, 3,… ∞, as shown below:

$$c1_j a_{IIj} + c2_j \cdot b_{IIj} - \sum_n \left[d1_n \cdot F_{jn} \cdot b_{In} \right] = 0$$

$$c5_j a_{IIj} + c6_j \cdot b_{IIj} - \sum_n \left[c3_n \cdot F_{jn} \cdot a_{IIIn} \right] = 0$$

$$\sum_j \left[d1_j \cdot F_{nj} \cdot b_{IIj} \right] - \sum_j \left[c3_j \cdot F_{nj} \cdot a_{IIj} \right] - Q_n \cdot B_o = -B_n$$

$$\sum_j \left[d2_j \cdot F_{nj} \cdot b_{IIj} \right] - \sum_j \left[c7_j \cdot F_{nj} \cdot a_{IIj} \right] + c4_n \cdot a_{IIIn} - Q_n \cdot B_o = -B_n$$

$$\sum_j \left[E_j \cdot a_{IIj} \right] + \sum_j \left[G_j \cdot b_{IIj} \right] - \sum_n \left[E_n \cdot b_{In} \right] + \sum_n \left[G_n \cdot a_{IIIn} \right] + R_o \cdot B_o = 0$$

Then,

$$a_{In} = b_{In} \cdot c2_n / c1_n$$

APPENDIX B

Analytical model for force calculation

The main generation force is consist of three main components; the fundamental component, the positive sequence component and the negative sequence component, as shown in (B_ 1).

$$F = F_1 + \sum_{n}^{\infty} F_n \cos\left[(2n-2)\left(\frac{\pi \cdot z}{\tau_{pole}}\right)\right] + \sum_{h}^{\infty} F_h \cos\left[(2h-5)\left(\frac{\pi \cdot z}{\tau_{pole}}\right)\right] \quad (B_\ 1)$$

$$n = 4, 7, 10, \ldots$$
$$h = 3, 6, 9, \ldots$$

The fundamental component (F_1) can be calculated as in (B_ 2),

$$F_1 = 12 \cdot \sqrt{2} \cdot p \cdot \tau_{pole} \cdot K_{r(1)} \cdot J_{rms} \cdot \sin\left(\frac{\pi}{6}\right) \quad (B_\ 2)$$

The positive sequence (F_{n1}) can be calculated as in (B_ 3)

$$F_n = \sqrt{2} \cdot J_{rms} \cdot \left(\frac{3}{2}\right) \cdot K_{(n)} (-1)^k \quad (B_\ 3)$$

$$n = 3k + 1,$$
$$k = 1, 2, 3, \ldots$$

The negative sequence (F_{n3}) can be calculated as in (B_ 4).

$$F_h = \sqrt{2} \cdot J_{rms} \cdot \left(\frac{3}{2}\right) \cdot K_{(h)} (-1)^{k+1} \quad (B_\ 4)$$

$$h = 3k + 3,$$
$$k = 0, 1, 2, 3, \ldots$$

The harmonic dependence coefficient ($K_{r(n)}$), can be calculated as in (B_ 5)

$$K_{r(n)} = \int_{R_{in}}^{R_s} r\left[a_{In} \cdot besseli(1, m_n) + b_{In} \cdot besselk(1, m_n)\right] dr \qquad (B_5)$$

Where: $$K_{(n)} = -4 \cdot \pi \cdot \tau_w \cdot k_{dp(n)} \cdot k_{r(n)} \qquad (B_6)$$

$$k_{dp(n)} = k_{p(n)} \cdot k_{d(n)} \qquad (B_7)$$

$$k_{p(n)} = \sin\left(\frac{(2n-1)\cdot\pi}{2\cdot m\cdot q}\right) \qquad (B_8)$$

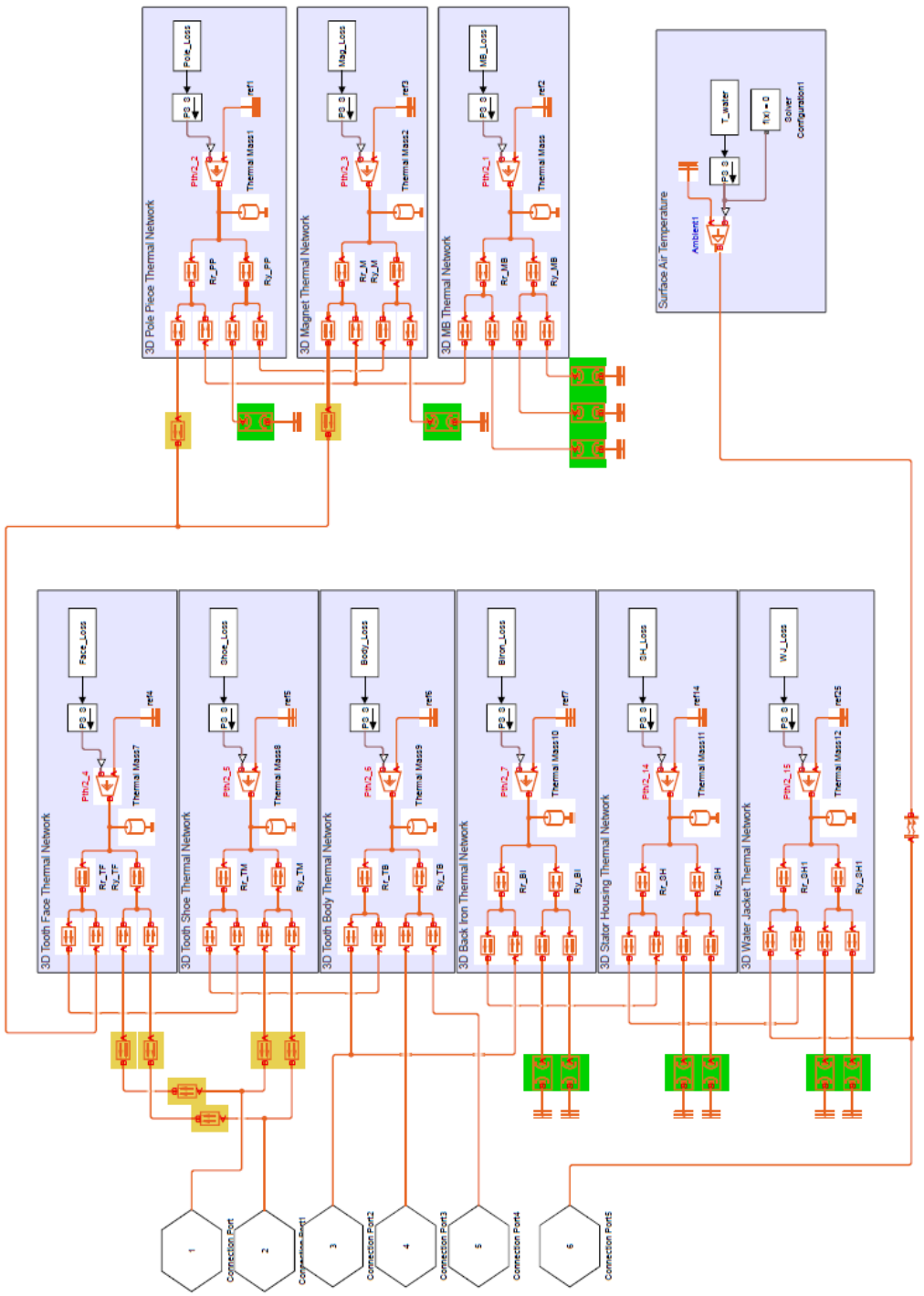
$$k_{d(n)} = \frac{\sin\left(b\cdot\frac{(2n-1)\cdot(m\cdot q-1)\cdot\pi}{2\cdot m\cdot q}\right)}{b\cdot\sin\left(\frac{(2n-1)\cdot(m\cdot q-1)\cdot b\cdot\pi}{2\cdot m\cdot q}\right)} \qquad (B_9)$$

Where q is the number of slot per phase per pole ratio and it is given by (B_ 10) and *b* represents the numerator of this ratio.

$$q = \frac{N_{slot}}{m\cdot N_{pole}} = \frac{b}{c} = \frac{2}{5} = 0.4 \qquad (B_10)$$

APPENDIX C

Thermal model of the TLPM motor



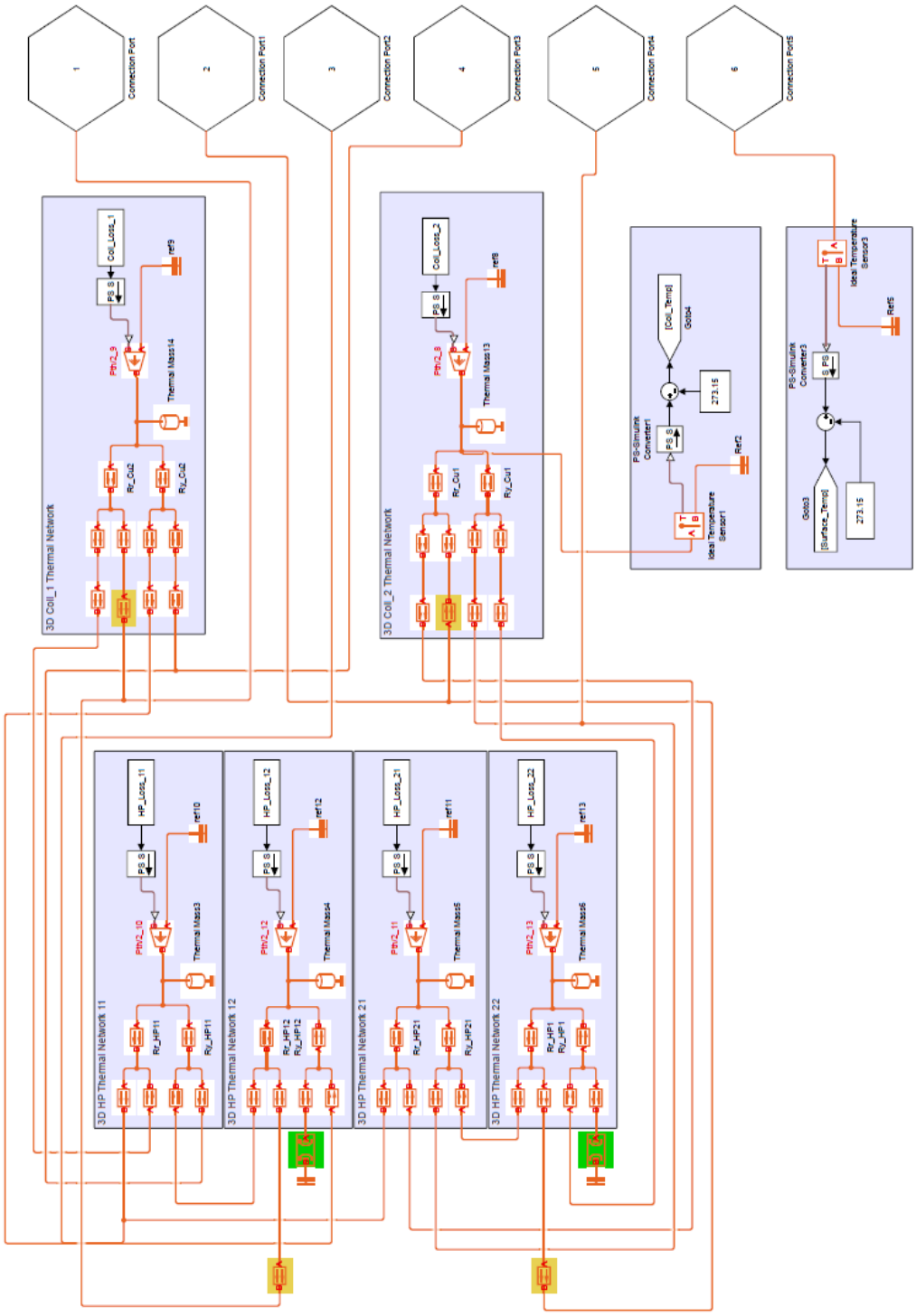


Figure C- 1 TLPM motor: two dimentions thermal netwo

APPENDIX D

Table D- 1 Somaloy 1000 3P Magnetic characteristics

	H (A/m)	B (Tesla)		H (A/m)	B (Tesla)
1	0	0	16	10000	1.6293
2	250	0.2748	17	12000	1.6735
3	500	0.5495	18	14000	1.7135
4	750	0.781	19	16000	1.7497
5	1000	0.9205	20	18000	1.7825
6	1500	1.0868	21	20000	1.8122
7	2000	1.204	22	25000	1.8748
8	2500	1.2854	23	30000	1.9241
9	3000	1.3418	24	35000	1.96
10	4000	1.4119	25	40000	1.995
11	5000	1.4585	26	50000	2.045
12	6000	1.5013	27	60000	2.08
13	7000	1.5432	28	70000	2.105
14	8000	1.5791	29	80000	2.12
15	9000	1.6045	30	90000	2.135

Table D- 2 specification data of (Somaloy 1000 3P)

Properties	*Value*	*Properties*	*Value*
Pressure	800 MPa	Resistivity	7×107 Ω *m
Mass density	7560 Kg /m3	B@10000A/m	1.63 Tesla
B@4000A/m	1.42 Tesla	μ-max	850

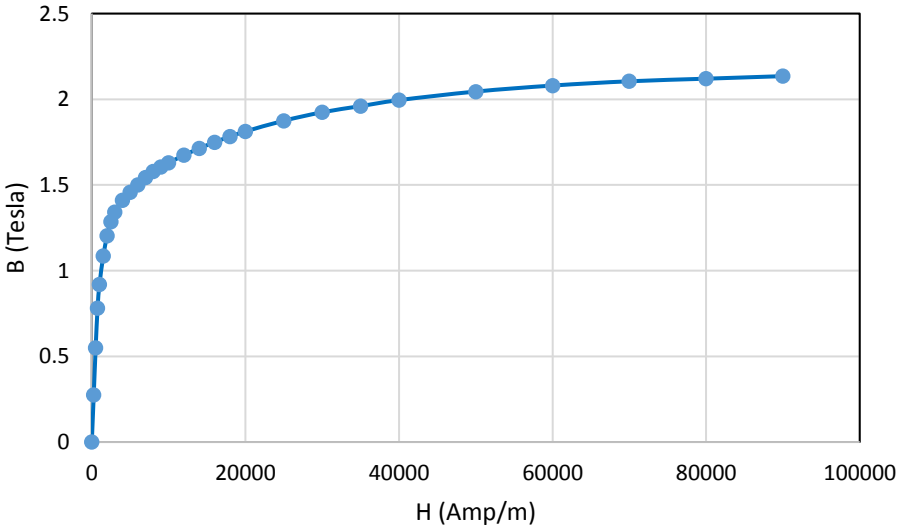


Figure D- 1 Somaloy 1000 3P: B-H curve

Table D- 3 Laminated material (Transil 270-35) Magnetic characteristics

	H (A/m)	B (Tesla)		H (A/m)	B (Tesla)		H (A/m)	B (Tesla)
1	0	0	28	9200.833	1.721017	55	65154.96	2.114424
2	25.43967	0.2364	29	10091.73	1.737177	56	70000	2.127598
3	36.69576	0.33432	30	11015.21	1.753188	57	302.2036	1.22837
4	45.86606	0.409457	31	11974	1.769054	58	325.5886	1.25091
5	54.08085	0.4728	32	12971.45	1.78478	59	351.8729	1.273052
6	61.7799	0.528606	33	14011.45	1.800367	60	381.6521	1.294815
7	69.19377	0.579059	34	15098.46	1.815821	61	415.6861	1.316219
8	76.46549	0.625455	35	16237.52	1.831145	62	454.9567	1.337279
9	83.69493	0.66864	36	17434.32	1.846342	63	500.7492	1.358014
10	90.95862	0.709199	37	18695.22	1.861414	64	554.7681	1.378436
11	98.31995	0.747562	38	20027.34	1.876365	65	619.3032	1.39856
12	105.8349	0.78405	39	21438.63	1.891199	66	697.4637	1.418399
13	113.5559	0.818913	40	22937.92	1.905916	67	793.5031	1.437964
14	121.5341	0.852352	41	24535.05	1.920521	68	913.2397	1.457266
15	129.8217	0.884527	42	26240.93	1.935016	69	1064.523	1.476316
16	138.4732	0.915573	43	28067.61	1.949403	70	1257.546	1.495124
17	147.5472	0.945599	44	30028.33	1.963684	71	1504.529	1.513697
18	157.108	0.974701	45	32137.56	1.977863	72	1818.037	1.532046
19	167.227	1.00296	46	34411	1.99194	73	2207.652	1.550177
20	177.9851	1.030443	47	36865.42	2.005919	74	2676.374	1.568099
21	189.4745	1.057212	48	39518.57	2.019801	75	3219.507	1.585818
22	201.8017	1.08332	49	42388.86	2.033588	76	3827.137	1.603342
23	215.0909	1.108813	50	45494.95	2.047283	77	4488.048	1.620676
24	229.4883	1.133734	51	48855.21	2.060886	78	5192.554	1.637826
25	245.1673	1.158118	52	52487.06	2.0744	79	5933.571	1.654799
26	262.336	1.181999	53	56406.15	2.087827	80	6706.571	1.671599
27	281.2457	1.205407	54	60625.55	2.101168	81	7509.123	1.688232

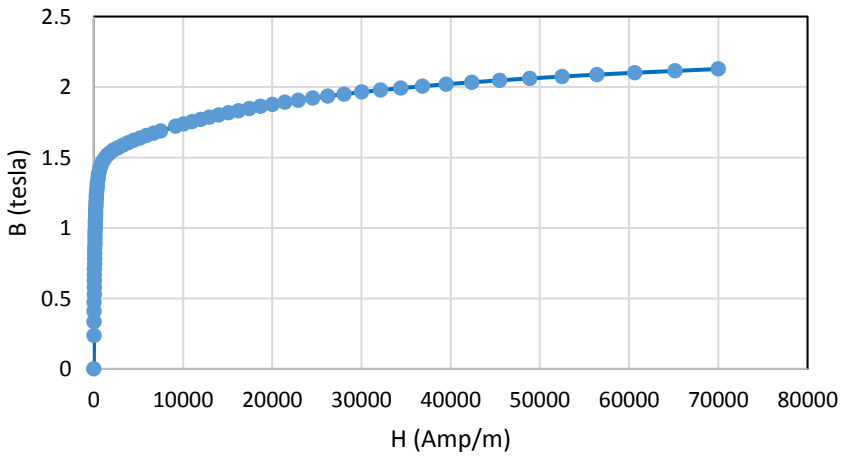


Figure D- 2 Transil 270-35: B-H curve

Table D- 4 Solid material (EN8-080M40) Magnetic characteristics; classical method.

	H (A/m)	B (Tesla)		H (A/m)	B (Tesla)		H (A/m)	B (Tesla)
1	104.0058	0.009887	16	1252.597	0.974533	31	3640.696	1.451692
2	169.0474	0.01852	17	1365.279	1.031808	32	3904.927	1.481892
3	283.0072	0.100625	18	1444.14	1.06339	33	4195.234	1.503695
4	388.8827	0.217085	19	1564.003	1.101233	34	4525.417	1.524723
5	447.3477	0.288177	20	1692.551	1.140233	35	4876.254	1.546105
6	501.7523	0.359699	21	1807.815	1.165534	36	5145.015	1.570876
7	572.2342	0.453994	22	1924.581	1.199654	37	5745.671	1.600195
8	636.8954	0.529319	23	2030.362	1.225934	38	6031.589	1.620292
9	710.4285	0.605887	24	2226.247	1.259692	39	6543.551	1.636627
10	770.9119	0.666347	25	2338.319	1.281612	40	7032.207	1.659772
11	847.5666	0.734234	26	2629.235	1.335447	41	7535.696	1.678321
12	924.761	0.79341	27	2822.468	1.364942	42	8286.329	1.705357
13	993.0367	0.842032	28	3079.048	1.393976	43	9147.157	1.738418
14	1096.143	0.900776	29	3227.076	1.408831	44	9754.338	1.757497
15	1188.593	0.945685	30	3443.615	1.436376	45	10656.15	1.779388

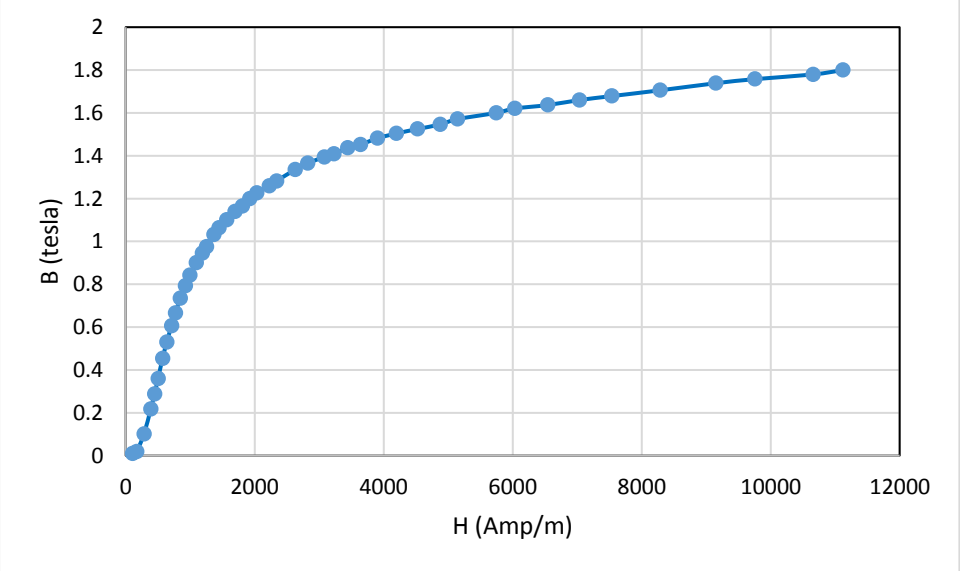


Figure D- 3 Solid material (EN8-080M40) B-H curve

Bibliography

[1] P. K. Budig, "The application of linear motors," in *Proceedings IPEMC 2000. Third International Power Electronics and Motion Control Conference (IEEE Cat. No.00EX435)*, 2000, pp. 1336-1341 vol.3.

[2] Aerotech Inc. *Aerotech Inc, Linear Motors Application Guide, Decicated to the Science of Motion, [online] Available at: https://www.aerotech.com/, [Accessed 2 Feb. 2016]*.

[3] M. Christmann, S. Seemann, and P. Jänker, "Innovative approaches to electromechanical flight control actuators and systems," *Recent Advances in Aerospace Actuation Systems and Components*, pp. 17-23, 2010.

[4] P. Jänker, F. Claeyssen, B. Grohmann, M. Christmann, T. Lorkowski, R. LeLetty, *et al.*, "New Actuators for Aircraft and Space Applications," 2008.

[5] S. Seemann, M. Rottach, S. Bozhko, and C. Schlegel, "Modeling of a fault-tolerant electromechanical actuation system for helicopters using Modelica," in *2012 Electrical Systems for Aircraft, Railway and Ship Propulsion*, 2012, pp. 1-7.

[6] A. Garcia, I. Cusido, J. A. Rosero, J. A. Ortega, and L. Romeral, "Reliable electro-mechanical actuators in aircraft," *IEEE Aerospace and Electronic Systems Magazine*, vol. 23, pp. 19-25, 2008.

[7] M. Galea, G. Buticchi, L. Empringham, L. de Lillo, and C. Gerada, "Design of a High-Force-Density Tubular Motor," *IEEE Transactions on Industry Applications*, vol. 50, pp. 2523-2532, Jul-Aug 2014.

[8] M. Galea, C. Gerada, T. Raminosoa, and P. Wheeler, "A Thermal Improvement Technique for the Phase Windings of Electrical Machines," *IEEE Transactions on Industry Applications*, vol. 48, pp. 79-87, Jan-Feb 2012.

[9] M. Galea, C. Gerada, T. Raminosoa, and P. W. Wheeler, "Considerations for the design of a tubular motor for an aerospace application," in *Electrical Machines and Systems (ICEMS), 2011 International Conference on*, 2011, pp. 1-6.

[10] M. Galea, "High performance, direct drive machines for aerospace applications," University of Nottingham, 2013.

[11] I. Boldea, *Linear Electric Machines, Drives, and MAGLEVs Handbook*: CRC Press, 2013.

[12] J. F. Gieras, Z. J. Piech, and B. Tomczuk, *Linear synchronous motors: transportation and automation systems*, 1st edition ed.: CRC press, 2000.

[13] N. Bianchi, S. Bolognani, D. D. Corte, and F. Tonel, "Tubular linear permanent magnet motors: an overall comparison," *IEEE Transactions on Industry Applications*, vol. 39, pp. 466-475, 2003.

[14] Basak A., *Permanent-Magnet DC Linear Motors*. Oxford, U.K: Clarendon Press, 1996.

[15] S. CHEVAILLER, "comparative study and selection criteria of linear motors," 2006.

[16] J. WANG, D. HOWE, and Z. LIN, "Comparative Studies on Linear Motor Topologies for Reciprocating Vapor Compressors," 2007.

[17] N. Bianchi, S. Bolognani, and J. Corda, "Tubular linear motors: A comparison of brushless PM and SR motors," *International Conference on Power Electronics, Machines and Drives*, pp. 626-631, 2002.

[18] J. F. Gieras, *Permanent Magnet Motor Technolog Design and Applications*, 3rd ed. U.S.A: CRC, Taylor and Francis Group, 2010.

[19] M. J. Melfi, S. Evon, and R. McElveen, "Permanent magnet motors for power density and energy savings in industrial applications," in *Conference Record of 2008 54th Annual Pulp and Paper Industry Technical Conference*, 2008, pp. 218-225.

[20] "automation Inc, "The Linear Motor: How Does It Work?", [online] Available at: https://www.automation.com/automation-news/article/the-linear-motor-how-does-it-work, , [Accessed 10 Feb. 2017].".

[21] P. H. Corporation, "Trilogy Linear Motor and Linear Motor Positioners," 2007.

[22] P. H. Corporation, "linear motor basics," 2005.

[23] T. T. Nguyen, M. Lazar, and H. Butler, "Cancellation of normal parasitic forces in coreless linear motors," in *2015 19th International Conference on System Theory, Control and Computing (ICSTCC)*, 2015, pp. 192-199.

[24] S. G. Min and B. Sarlioglu, "3-D Performance Analysis and Multiobjective Optimization of Coreless-Type PM Linear Synchronous Motors," *IEEE Transactions on Industrial Electronics*, pp. 1-1, 2017.

[25] Y. w. Zhu, L. Sang-geon, and Y. h. Cho, "Optimal design of slotted iron core type permanent magnet linear synchronous motor for ropeless elevator system," in *2010 IEEE International Symposium on Industrial Electronics*, 2010, pp. 1402-1407.

[26] F. Milanesi, "Design optimization and control strategies for PM Multiphase Tubular Linear Actuators," University of Bologna, 2009.

[27] Z. Yu-wu, L. Sang-geon, and C. Yun-hyun, "Topology structure selection of permanent magnet linear synchronous motor for ropeless elevator

system," in *2010 IEEE International Symposium on Industrial Electronics*, 2010, pp. 1523-1528.

[28] I. Boldea and S. A. Nasar, "Linear electric actuators and generators," in *Electric Machines and Drives Conference Record, 1997. IEEE International*, 1997, pp. MA1/1.1-MA1/1.5.

[29] D. Imstepf, F. Baudart, Y. Perriard, and B. Dehez2, "Potential of Flex-PCB Winding in Coreless Tubular Permanent Magnet Synchronous Machines," presented at the Electrical Machines and Systems (ICEMS), 2016 19th International Conference on, Chiba, Japan, 2016.

[30] J. H. Zhao and J. H. Zhang, "Tubular Permanent Magnet Linear Synchronous Motor Thrust Optimization," *Advanced Materials Research*, vol. 383-390, pp. 5640-5647, 2011.

[31] F. Marignetti and M. Scarano, "Comparative analysis and design criteria of permanent magnet tubular actuators," *Electrical Engineering*, vol. 84, pp. 255-264, 2002.

[32] L. Pennander, G. Nord, K. Maezawa, M. Saito, and D. Berchowitz, "Design of soft magnetic composite components for tubular linear motors," in *Motor and Drive Systems Conference, Miami, Florida, US February*, 2006.

[33] J. B. Wang, W. Y. Wang, and K. Atallah, "A Linear Permanent-Magnet Motor for Active Vehicle Suspension," *IEEE Transactions on Vehicular Technology*, vol. 60, pp. 55-63, Jan 2011.

[34] J. Anderson, "Determining manufacturing costs," *CEP*, pp. 27-31, 2009.

[35] D. Montesinos, S. Galceran, A. Sudria, O. Gomis, and F. Blaabjerg, "Low cost sensorless control of permanent magnet motors - an overview and evaluation," in *IEEE International Conference on Electric Machines and Drives, 2005.*, 2005, pp. 1681-1688.

[36] S. A. Nasar, G. Y. Xiong, and Z. X. Fu, "Eddy-Current Losses in a Tubular Linear Induction-Motor," *Ieee Transactions on Magnetics*, vol. 30, pp. 1437-1445, Jul 1994.

[37] G. Cipriani, M. Corpora, V. Di Dio, A. Musolino, R. Rizzo, and L. Sani, "A Comparison among Different Kinds of Stator Lamination in Tubular Linear Machines," *Progress In Electromagnetics Research M*, vol. 50, pp. 95-104, 2016.

[38] H. K. Lee and E. P. Hong, "Stator for linear motor by staggered core lamination," 2000.

[39] G. J. Higham, H. D. Snively, H. G. Nicoll, and G. R. Pruitt, "Cryogenic refrigeration system having an involute laminated stator for its linear drive motor," 1988.

[40] M. A. Farsi and B. Arezoo, "Bending force and spring-back in v-die-bending of perforated sheet-metal components," *Journal of the Brazilian Society of Mechanical Sciences and Engineering,* vol. 33, pp. 45-51, 2011.

[41] J. B. Wang and D. Howe, "Influence of soft magnetic materials on the design and performance of tubular permanent magnet machines," *Ieee Transactions on Magnetics,* vol. 41, pp. 4057-4059, Oct 2005.

[42] A. Mohammed, M. Galea, T. Cox, and C. Gerada, "Considerations for improved design and reduced manufacturing complexity of a PM, Tubular Linear Motor," in *10th International Symposium on Linear Drives for Industry Applications*, Aachen, Germany, 2015.

[43] M. Oono, Q. Yuan, N. Kurita, and T. Ishikawa, "Analysis of a new linear actuator made of Soft Magnetic Composite material with spring," in *2009 International Conference on Electrical Machines and Systems*, 2009, pp. 1-6.

[44] Y. G. Guo and J. G. Zhu, "Application of Soft Magnetic Composite Materials in Electrical Machines: A Review," *Australian Journal of Electrical and Electronics Engineering,* vol. 3, pp. 37-46, 2006.

[45] L. H. O. Andersson, "Advances in Soft Magnetic Composites – Materials and Applications," in *International Conference of Powder Metallurgy Particulate Mater*, Las Vegas, NV, USA, 2009, pp. 1-12.

[46] H. Shokrollahi and K. Janghorban, "Soft magnetic composite materials (SMCs)," *Journal of Materials Processing Technology,* vol. 189, pp. 1-12, 2007.

[47] Y. Dou, Y. Guo, and J. Zhu, "Investigation of motor topologies for SMC application," in *Electrical Machines and Systems, 2007. ICEMS. International Conference on*, 2007, pp. 695-698.

[48] M.-F. Hsieh and K.-H. Hu, "Analysis of a tubular linear motor with soft magnetic composites for reciprocating compressors," *Journal of Applied Physics,* vol. 103, p. 07F112, 2008.

[49] N. Schofield, A. Canova, G. Gruosso, M. Repetto, and M. Ottella, "The application of soft magnetic composites to the design of tubular linear actuators," *International Journal of Applied Electromagnetics and Mechanics*, vol. 19, pp. 225-229, 2004.

[50] J. J. H. Paulides, K. J. Meessen, and E. A. Lomonova, "Eddy-Current Losses in Laminated and Solid Steel Stator Back Iron in a Small Rotary Brushless

Permanent-Magnet Actuator," *Ieee Transactions on Magnetics,* vol. 44, pp. 4373-4376, Nov 2008.

[51] K. Oberretl, "Eddy-Current Losses in Solid Pole Shoes of Synchronous Machines at No-Load and on Load," *Ieee Transactions on Power Apparatus and Systems,* vol. Pa91, pp. 152-&, 1972.

[52] G. G. Sironi and J. R. Vanhulse, "Eddy-Current Losses in Solid Iron Pieces under 3-Dimensional Magnetic-Field," *Ieee Transactions on Magnetics,* vol. 14, pp. 377-379, 1978.

[53] J. Li, D. W. Choi, C. H. Cho, D. H. Koo, and Y. H. Cho, "Eddy-Current Calculation of Solid Components in Fractional Slot Axial Flux Permanent Magnet Synchronous Machines," *Ieee Transactions on Magnetics,* vol. 47, pp. 4254-4257, Oct 2011.

[54] (09-Oct, 2016). *The Metal Store, MILD STEEL, [online] Available at: http://www.themetalstore.co.uk/products/metric-sizes/ [Accessed 09 Oct. 2016]*.

[55] T. Hatakeyama, R. Kibushi, M. Ishizuka, and T. Tomimura, "Fundamental study of surface roughness dependence of thermal and electrical contact resistance," in *2016 15th IEEE Intersociety Conference on Thermal and Thermomechanical Phenomena in Electronic Systems (ITherm)*, 2016, pp. 1078-1082.

[56] G. Knickerbocker and W. Kouwenhoven, "Eddy-current losses in solid and laminated iron," *Circulation Research,* vol. 6, p. 60, 1958.

[57] N. Kesavamurthy and P. K. Rajagopalan, " Eddy currents in solid iron due to alternating magnetic flux," *The Institution of Electrical Engineers,* vol. 106, pp. 207 - 213, Sep-1959 1959.

[58] J. Pyrhonen, Tapani Jokinen, V. Hrabovcov, and H. Niemela, *Design of Rotating Electrical Machines*: JohnWiley & Sons, Ltd, 2008.

[59] P. Thelin and H. Nee, "Calculation of the airgap flux density of PM synchronous motors with buried magnets including axial leakage and teeth saturation," in *1999. Ninth International Conference on Electrical Machines and Drives (Conf. Publ. No. 468)*, 1999, pp. 339-345.

[60] Y. Yang, B. Bilgin, M. Kasprzak, S. Nalakath, M. Preindl, H. Sadek, *et al.*, *Thermal Management of Electric Machines* vol. 7, 2016.

[61] J. Wang, M. West, D. Howe, H. Z. D. L. Parra, and W. M. Arshad, "Design and Experimental Verification of a Linear Permanent Magnet Generator for a Free-Piston Energy Converter," *IEEE Transactions on Energy Conversion,* vol. 22, pp. 299-306, 2007.

[62] W. Soong, "Sizing of Electrical Machines," *Power Engineering Briefing Notes,* pp. 17-18, 2008.

[63] I. Boldea and L. N. Tutelea, *Electric Machines: Steady State, Transients, and Design with MATLAB®*: CRC press, 2009.

[64] P. E. Cavarec, H. B. Ahmed, and B. Multon, "Force density improvements from increasing the number of airgap surfaces in synchronous linear actuators," *IEE Proceedings - Electric Power Applications,* vol. 150, pp. 106-116, 2003.

[65] A. Vagati, G. Pellegrino, and P. Guglielmi, "Comparison between SPM and IPM motor drives for EV application," in *The XIX International Conference on Electrical Machines - ICEM 2010*, 2010, pp. 1-6.

[66] N. Bianchi, S. Bolognani, D. Dalla Corte, and F. Tonel, "Tubular linear permanent magnet motors: An overall comparison," *IEEE Transactions on Industry Applications,* vol. 39, pp. 466-475, Mar-Apr 2003.

[67] N. Bianchi, S. Bolognani, and F. Tonel, "Design criteria of a tubular linear IPM motor," in *Electric Machines and Drives Conference, 2001. IEMDC 2001. IEEE International*, 2001, pp. 1-7.

[68] "On mesh sensitive calculations in 3D finite element modeling of electric machines."

[69] K. Hameyer, F. Henrotte, H. V. Sande, G. Deliège, and H. De Gersem, "Finite element models in electrical machine design," in *Congresso Brasileiro de Eletromagnetismo, CBMAG*, 2002.

[70] P. Ponomarev, J. Keränen, and P. Pasanen, "Electromagnetic transient finite element 3D modelling of electrical machines using open-source tools," in *2016 XXII International Conference on Electrical Machines (ICEM)*, 2016, pp. 1657-1661.

[71] J. KOŁOTA and S. STĘPIEŃ, "Analysis of 2D and 3D finite element approach of a switched reluctance motor," *Przegląd Elektrotechniczny,* vol. 87, pp. 188-190, 2011.

[72] S. J. Salon, *Finite element analysis of electrical machines* vol. 101: Kluwer academic publishers Boston USA, 1995.

[73] J. B. Wang, G. W. Jewell, and D. Howe, "A general framework for the analysis and design of tubular linear permanent magnet machines," *Ieee Transactions on Magnetics,* vol. 35, pp. 1986-2000, May 1999.

[74] L. Liyi, H. Xuzhen, and K. Baoquan, "Calculation and analysis of the magnetic field of a tubular linear motor," in *Digests of the 2010 14th*

Biennial IEEE Conference on Electromagnetic Field Computation, 2010, pp. 1-1.

[75] L. J. Wu, Z. Q. Zhu, D. Staton, M. Popescu, and D. Hawkins, "Analytical prediction of electromagnetic performance of surface-mounted PM machines based on subdomain model accounting for tooth-tips," *IET Electric Power Applications*, vol. 5, p. 597, 2011.

[76] G. Dajaku and D. Gerling, "Determination of air-gap flux density due to magnets using the new analytical model," in *The XIX International Conference on Electrical Machines - ICEM 2010*, 2010, pp. 1-6.

[77] JiabinWang, David Howe, and GeraintW. Jewell, "Analysis and Design Optimization of an Improved Axially Magnetized Tubular Permanent-Magnet Machine," 2004.

[78] L. Wu, Z. Zhu, D. Staton, M. Popescu, and D. Hawkins, "Analytical prediction of electromagnetic performance of surface-mounted PM machines based on subdomain model accounting for tooth-tips," *IET electric power applications*, vol. 5, pp. 597-609, 2011.

[79] K. Boughrara, T. Lubin, and R. Ibtiouen, "General subdomain model for predicting magnetic field in internal and external rotor multiphase flux-switching machines topologies," *IEEE Transactions on Magnetics*, vol. 49, pp. 5310-5325, 2013.

[80] Z. Q. Zhu, D. Howe, E. Bolte, and B. Ackermann, "Instantaneous magnetic field distribution in brushless permanent magnet DC motors. I. Open-circuit field," *IEEE Transactions on Magnetics*, vol. 29, pp. 124-135, 1993.

[81] A. Mohammadpour, A. Gandhi, and L. Parsa, "Winding factor calculation for analysis of back EMF waveform in air-core permanent magnet linear synchronous motors," *IET Electric Power Applications*, vol. 6, pp. 253-259, 2012.

[82] A. Chen, R. Nilssen, and A. Nysveen, "Harmonic analysis and comparison of the back EMFs of four permanent magnet machine with different winding arrangements," in *2008 International Conference on Electrical Machines and Systems*, 2008, pp. 3043-3048.

[83] D. Zhu, X. Qiu, N. Zhou, and Y. Yan, "A comparative study of winding factors between distributed windings and non-overlapping concentrated windings," in *Electric Utility Deregulation and Restructuring and Power Technologies, 2008. DRPT 2008. Third International Conference on*, 2008, pp. 2725-2729.

[84] F. Libert and J. Soulard, "Investigation on pole-slot combinations for permanent-magnet machines with concentrated windings," in *International Conference on Electrical Machines (ICEM 04)*, 2004, pp. 5-8.

[85] J. Wang, "Fractional-slot Tubular Permanent Magnet Machines with Low Space Harmonics," 2015.

[86] W. Jiabin, D. Howe, and G. W. Jewell, "Analysis and design optimization of an improved axially magnetized tubular permanent-magnet machine," *IEEE Transactions on Energy Conversion,* vol. 19, pp. 289-295, 2004.

[87] G. Dajaku and D. Gerling, "Magnetic Radial Force Density of the PM machine with 12-teeth/10-poles Winding Topology," in *Electric Machines and Drives Conference, 2009. IEMDC'09. IEEE International*, 2009, pp. 1715-1720.

[88] Y. Amara, J. B. Wang, and D. Howe, "Analytical prediction of eddy-current loss in modular tubular permanent-magnet machines," *Ieee Transactions on Energy Conversion,* vol. 20, pp. 761-770, Dec 2005.

[89] B. Aslan, E. Semail, J. Korecki, and J. Legranger, "Slot/pole combinations choice for concentrated multiphase machines dedicated to mild-hybrid applications," in *IECON 2011-37th Annual Conference on IEEE Industrial Electronics Society*, 2011, pp. 3698-3703.

[90] S. Skaar, O. Krovel, and R. Nilssen, "Distribution, coil-span and winding factors for PM machines with concentrated windings," *IEEE ICEM September,* 2006.

[91] F. Magnussen and C. Sadarangani, "Winding factors and Joule losses of permanent magnet machines with concentrated windings," in *Electric Machines and Drives Conference, 2003. IEMDC'03. IEEE International*, 2003, pp. 333-339.

[92] Y. Bai, T. Yang, and B. Kou, "Reducing detent force and three-phase magnetic paths unbalance of PM linear synchronous motor using modular primary iron-core structure," in *2014 17th International Conference on Electrical Machines and Systems (ICEMS)*, 2014, pp. 1743-1748.

[93] J. Zhang, C. Wu, X. Lianggen, M. Cheng, and J. Xinmiao, "Optimal design of a tubular linear surface-mounted permanent magnet actuator for high voltage breaker," in *2013 International Conference on Electrical Machines and Systems (ICEMS)*, 2013, pp. 1895-1900.

[94] C. C. Hwang, P. L. Li, and C. T. Liu, "Optimal Design of a Permanent Magnet Linear Synchronous Motor With Low Cogging Force," *Ieee Transactions on Magnetics,* vol. 48, pp. 1039-1042, Feb 2012.

[95] J. Wang, M. Inoue, Y. Amara, and D. Howe, "Cogging-force-reduction techniques for linear permanent-magnet machines," *Iee Proceedings-Electric Power Applications,* vol. 152, pp. 731-738, May 2005.

[96] M. Yoneda, M. Shoji, Y. Kim, and H. Dohmeki, "Novel Selection of the Slot-Pole Ratio of the PMSM for Auxiliary Automobile," in *Industry Applications Conference, 2006. 41st IAS Annual Meeting. Conference Record of the 2006 IEEE*, 006, pp. 8-13.

[97] Z. Q. Zhu, P. J. Hor, D. Howe, and J. Rees-Jones, "Calculation of cogging force in a novel slotted linear tubular brushless permanent magnet motor," *IEEE Transactions on Magnetics,* vol. 33, pp. 4098-4100, 1997.

[98] N. Bianchi, S. Bolognani, and A. D. F. Cappello, "Back EMF improvement and force ripple reduction in PM linear motor drives," in *Power Electronics Specialists Conference, 2004. PESC 04. 2004 IEEE 35th Annual*, 2004, pp. 3372-3377 Vol.5.

[99] S. W. Youn, J. J. Lee, H. S. Yoon, and C. S. Koh, "A new cogging-free permanent-magnet linear motor," *Magnetics, IEEE Transactions on,* vol. 44, pp. 1785-1790, 2008.

[100] G. Qi, J. T. Chen, Z. Q. Zhu, D. Howe, L. B. Zhou, and C. L. Gu, "Influence of Skew and Cross-Coupling on Flux-Weakening Performance of Permanent-Magnet Brushless AC Machines," *IEEE Transactions on Magnetics,* vol. 45, pp. 2110-2117, 2009.

[101] S. Zhu, P. Zheng, B. Yu, L. Cheng, and W. Wang, "Performance Analysis and Modeling of a Tubular Staggered-Tooth Transverse-Flux PM Linear Machine," *Energies,* vol. 9, p. 163, 2016.

[102] J. Wang, G. Jewell, and D. Howe, "Design optimisation and comparison of tubular permanent magnet machine topologies," in *Electric Power Applications, IEE Proceedings-*, 2001, pp. 456-464.

[103] J. Wang and D. Howe, "Analysis of axially magnetised, iron-cored, tubular permanent magnet machines," *IEE Proceedings - Electric Power Applications,* vol. 151, pp. 144-150, 2004.

[104] C. Kral, A. Haumer, and T. Brauml, "Thermal Model and Behavior of a Totally-Enclosed-Water-Cooled Squirrel-Cage Induction Machine for Traction Applications," *Ieee Transactions on Industrial Electronics,* vol. 55, pp. 3555-3565, Oct 2008.

[105] A. Boglietti, A. Cavagnino, D. Staton, M. Shanel, M. Mueller, and C. Mejuto, "Evolution and Modern Approaches for Thermal Analysis of Electrical Machines," *Ieee Transactions on Industrial Electronics,* vol. 56, pp. 871-882, Mar 2009.

[106] R. Wrobel and P. H. Mellor, "A General Cuboidal Element for Three-Dimensional Thermal Modelling," *Ieee Transactions on Magnetics,* vol. 46, pp. 3197-3200, Aug 2010.

[107] T. D. Kefalas and A. G. Kladas, "Finite element transient thermal analysis of PMSM for aerospace applications," in *Electrical Machines (ICEM), 2012 XXth International Conference on*, 2012, pp. 2566-2572.

[108] J. Nerg, M. Rilla, and J. Pyrhonen, "Thermal analysis of radial-flux electrical machines with a high power density," *Industrial Electronics, IEEE Transactions on*, vol. 55, pp. 3543-3554, 2008.

[109] *J. D. Edwared, Infolytica Corporation, Ltd, An Introduction to Magnet for static 2D Modeling, {online] available at : https://www.infolytica.com/secured/customer/elite/docs?id=MagNet%20-%20Introduction.pdf, acces date 1/11/2013.*

.

[110] B. Measurements, "Manual for software operation of the MPG 200 D," ed: Brockhaus Measurements, 2014.

[111] S. Sprague, "Lamination steels third edition A compendium of lamination steel alloys commonly used in electric motors," *The Electric Motor Education and Research Foundation, South Dartmourth, MA, USA*, 2007.

[112] "Catalog - Neodymium-Iron-Boron Magnet Grades, Summary Product List & Reference Guide," in *Neodymium-Iron-Boron Magnet Grades*, ed. NY, USA: Arnold Magnetic Technologies Corp.

[113] E. S. S. D. Association, "Stainless Steel: Tables of technical Properties. Materials and applications Series, 5," ed.

[114] A. Mohammed, M. Galea, and C. Gerada, "Annual PhD. Report,," University of Nottingham (UoN),July 2014.

[115] S. N. Vukosavic, *Electrical machines*: Springer Science & Business Media, 2012.

[116] Ana Alonso Rodríguez, *Eddy Current Approximation of Maxwell Equations* vol. 4. Verlag Italia: Springer, 2010.

[117] H. W. Beaty and J.Kirtley, *Electric Motor Handbook*: The McGraw-Hill Companies., 2004.

[118] B. Standard, "Magnetic materials — Part 4: Methods of measurement of the d.c. magnetic properties of solid steels," in *BS 6404-4*, ed: BSI, 1986.

[119] B. Standard, "Magnetic materials — Part 6: Methods of measurement of the magnetic properties of magnetically soft metallic and powder materials at frequencies in the range 20 Hz to 200 kHz by the use of ring specimens," in *BS 60404-6*, ed: BSI, 2003.

[120] A. J. Clerc and A. Muetze, "Measurement of Stator Core Magnetic Degradation During the Manufacturing Process," *IEEE Transactions on Industry Applications,* vol. 48, pp. 1344-1352, Jul-Aug 2012.

[121] D. Peckner and I. M. Bernstein, *Handbook of stainless steels*: McGraw-Hill New York, NY, 1977.

[122] "Steel Grades, Properties and Global Standards."

[123] B. Koprivica, A. Milovanovic, and M. Djekic, "Effects of wound toroidal core dimensional and geometrical parameters on measured magnetic properties of electrical steel," *Serbian Journal of Electrical Engineering,* vol. 10, pp. 459-471, 2013.

[124] R. J. Tilley, *Understanding solids: the science of materials*: John Wiley & Sons, 2004.

[125] W. Soong, "Bh curve and iron loss measurements for magnetic materials," *Power Engineering Briefing Note Series,* 2008.

[126] B. D. Cullity and C. D. Graham, *Introduction to magnetic materials*: John Wiley & Sons, 2011.

[127] P. K. Lee, K. C. Kuo, C. J. Wu, Z. T. Wong, and J. Y. Yen, "Prediction of iron losses using the modified Steinmetz equation under the sinusoidal waveform," in *Control Conference (ASCC), 2011 8th Asian*, 2011, pp. 579-584.

[128] P.Parthasaradhy and S.V.Ranganayakulu, "Hysteresis and eddy current losses of magnetic material by Epstein frame method novel approach," *The International Journal Of Engineering And Science (IJES),* pp. 85-93, 2014.

[129] Magnetics. (2000, 01-06-2015). *Ferrite Core. Material Selection Guide*.

[130] J. Jamali, "End effect in linear induction and rotating electrical machines," *IEEE Transactions on Energy Conversion,* vol. 18, pp. 440-447, Sep 2003.

[131] K. K. Lim and P. Hammond, "Universal loss chart for the calculation of eddy-current losses in thick steel plates," *Electrical Engineers, Proceedings of the Institution of,* vol. 117, pp. 857-864, 1970.

[132] F. Fiorillo, *Measurement and characterization of magnetic materials*: North-Holland, 2004.

[133] E. J. Woods, "Eddy-Current Losses in Solid Iron with Dc Offset," *Ieee Transactions on Power Apparatus and Systems,* vol. 100, pp. 2241-2248, 1981.

[134] M. D. Abrams and D. H. Gillott, "Numerical Analysis of Hysteresis and Eddy Current Losses in Solid Cylindrical Rods of No 1010 Steel," *Ieee*

Transactions on Power Apparatus and Systems, vol. Pa86, pp. 1077-&, 1967.

[135] W. L. Shevel, "A modified limiting nonlinear theory of eddy-current phenomena in solid iron," *American Institute of Electrical Engineers, Part I: Communication and Electronics, Transactions of the,* vol. 81, pp. 48-55, 1962.

[136] D. O'Kelly, "Flux penetration and core loss in solid iron," *Magnetics, IEEE Transactions on,* vol. 11, pp. 55-60, 1975.

[137] M. A. T.-W. Cores, "Familiarity with the mechanisms underlying magnetic core behavior is essential to (a) optimize the magnetic device design, and (b) properly model its behavior in the circuit application. The Purpose of the Magnetic Core."

[138] K. Zakrzewski and F. Pietras, "Method of calculating the electromagnetic field and power losses in ferromagnetic materials, taking into account magnetic hysteresis," in *Proceedings of the Institution of Electrical Engineers*, 1971, pp. 1679-1685.

[139] S. K. Mukerji, M. George, M. Ramamurthy, and K. Asaduzzaman, "Eddy currents in solid rectangular cores," *Progress In Electromagnetics Research B,* vol. 7, pp. 117-131, 2008.

[140] F. Eastham, T. Cox, P. Leonard, and J. Proverbs, "Linear Induction Motors with Modular Winding Primaries and Wound Rotor Secondaries," *IEEE Transactions on Magnetics*, vol. 44, pp. 4033-4036, 2008.

[141] L. Chong, R. Dutta, and M. F. Rahman, "A comparative study of rotor losses in an IPM with single and double layer concentrated windings," in *Electrical Machines and Systems (ICEMS), 2010 International Conference on*, 2010, pp. 942-946.

[142] M. Kang, J. H. Ji, G. H. Liu, and W. X. Zhao, "A New Tubular Fault-Tolerant Permanent-Magnet Motor for Active Vehicle Suspension," *38th Annual Conference on Ieee Industrial Electronics Society (Iecon 2012)*, pp. 4082-4086, 2012.

[143] T. Cox and J. F. Eastham, "Multi layer planar concentrated windings," in *2011 IEEE International Electric Machines & Drives Conference (IEMDC)*, 2011, pp. 1439-1444.

[144] A. M. Mohammed, T. Cox, M. Galea, and C. Gerada, "A New Method for determining the Magnetic Properties of Solid Materials employed in Unconventional Magnetic Circuits," *IEEE Transactions on Industrial Electronics,* vol. PP, pp. 1-1, 2016.

[145] F. J. H. Kalluf, C. Pompermaier, M. V. F. d. Luz, and A. A. Espindola, "Magnet segmentation in tubular linear motors," in *Electrical Machines (ICEM), 2012 XXth International Conference on*, 2012, pp. 697-701.

[146] K. Weise, M. Carlstedt, M. Ziolkowski, H. Brauer, and H. Toepfer, "Lorentz Force on Permanent Magnet Rings by Moving Electrical Conductors," *IEEE Transactions on Magnetics*, vol. 51, pp. 1-11, 2015.

[147] J. Case and A. H. Chilver, *Strength of materials and structures: an introduction to the mechanics of solids and structures*: Elsevier, 2013.

[148] R. A. Walsh, *Electromechanical design handbook* vol. 8: McGraw-Hill New York City, NY, USA, 2000.

[149] H. Czichos, T. Saito, and L. Smith, *Springer handbook of materials measurement methods* vol. 32: Springer Berlin, 2006.

[150] M. Popescu, T. Jokinen, E. Demeter, and V. Navrapescu, "Magnetic materials in design and construction of electrical motors," in *Electrotechnical Conference, 1998. MELECON 98., 9th Mediterranean*, 1998, pp. 125-128.

[151] Smiths Metal Centres. (2016, 1-Jan-2017). *Technical Datasheet*. Available: www.smithmetal.com/datasheets.htm

[152] I. Dura Magnetics. (2017, 1-July-2017). *Magnet Materials Comparison Guide*. Available: http://www.duramag.com/techtalk/tech-briefs/magnet-materials-comparison-guide/

[153] e-Magnets UK (April. 10, 2017). *Rare Earth Magnet Specialists*. Available: http://e-magnetsuk.com/

[154] "Permanent Magnets Materials and Magnet Systems."

[155] G. H. Wang, "Slot/Pole Ratio Design of Tubular Permanent Magnet Linear Synchronous Motor," *Materials Science and Engineering, Pts 1-2*, vol. 179-180, pp. 1303-1308, 2011.

[156] G. Q. Liu, "Investigation on Slot/Pole Number Combinations for PMSM with Concentrated Fractional Slot Winding," in *Advanced Engineering Forum*, 2011, pp. 512-518.

[157] X. Zhang, X. Wang, X. Xu, and H. Feng, "Slot-pole combinations research of Permanent-Magnet linear synchronous motor with concentrated windings," in *Electrical Machines and Systems (ICEMS), 2014 17th International Conference on*, 2014, pp. 1322-1325.

[158] J. B. Wang and D. Howe, "Tubular modular permanent-magnet machines equipped with quasi-Halbach magnetized magnets - Part II: Armature

reaction and design optimization," *Ieee Transactions on Magnetics*, vol. 41, pp. 2479-2489, Sep 2005.

[159] W. Soong, "Sizing of electrical machines," *Power Engineering Briefing Note Series*, vol. 9, pp. 17-18, 2008.

[160] L. Lavrinovicha, J. Dirba, and R. Dobriyan, "Design of Low-Torque-Ripple Synchronous Reluctance Motor with External Rotor," *Latvian Journal of Physics and Technical Sciences*, vol. 54, pp. 23-30, 2017.

[161] W. Jiabin, D. Howe, and G. W. Jewell, "Fringing in tubular permanent-magnet Machines: part II. Cogging force and its minimization," *IEEE Transactions on Magnetics*, vol. 39, pp. 3517-3522, 2003.

[162] H. Xuzhen, T. Qiang, L. Liyi, and Z. Bo, "Thermal optimization of a tubular permanent magnet linear synchronous motor," in *2014 17th International Symposium on Electromagnetic Launch Technology*, 2014, pp. 1-6.

[163] Moog Inc., "MAXFORCE PRE-ENGINEERED ELECTRIC LINEAR ACTUATION SOLUTION/SIZE 5," in *The Electro Mechanical Solution for High Performance Actuation*, ed, 2007.

[164] N. Ziegler, D.Matt, J.Jac, T. Martire, and P. Enrici, "High force linear actuator for an aeronautical application. Association with a fault tolerant converter. ," presented at the Electrical Machines and Power Electronics, Bodrum, Turkey, 2007.

[165] P. E. Cavarec, H. B. Ahmed, and B. Multon, "New multi-rod linear actuator for direct-drive, wide mechanical band pass applications," in *Conference Record of the 2002 IEEE Industry Applications Conference. 37th IAS Annual Meeting (Cat. No.02CH37344)*, 2002, pp. 369-376 vol.1.

[166] D. M. Joseph and W. A. Cronje, "Design and Analysis of a Double-Sided Tubular Linear Synchronous Generator with Particular Application to Wave-Energy Conversion,," presented at the Power Engineering Society Conference and Exposition in Africa, Johannesburg, South Africa, 2007.

[167] H. Wyatt and M. Lustgarten, *Probing Anterior Segment Kinetics with Focally Applied Mydriatics* vol. 17, 2001.